GDAŃSK UNIVERSITY OF TECHNOLOGY

The author of the doctoral dissertation: Aleksander Mroziński
Scientific discipline: Electronics

DOCTORAL DISSERTATION

Title of doctoral dissertation: Development of iron doped strontium titanates as oxygen electrode for solid oxide fuel cells

Title of doctoral dissertation (in Polish): Tytanian strontu podstawiany żelazem jako elektroda tlenowa w wysokotemperaturowych ogniwach paliwowych

Supervisor *signature*
Prof. dr hab. inż. Piotr Jasiński

Gdańsk, year 2023

GDAŃSK UNIVERSITY OF TECHNOLOGY

STATEMENT

The author of the doctoral dissertation: Aleksander Mroziński

I, the undersigned, declare that I am aware that in accordance with the provisions of Art. 27 (1) and (2) of the Act of 4th February 1994 on Copyright and Related Rights (Journal of Laws of 2021, item 1062), the university may use my doctoral dissertation entitled:
Development of iron doped strontium titanates as oxygen electrode for solid oxide fuel cells
for scientific or didactic purposes.[1]

Gdańsk, 07.07.2023 r. A. Mroziński

signature of the PhD student

Aware of criminal liability for violations of the Act of 4th February 1994 on Copyright and Related Rights and disciplinary actions set out in the Law on Higher Education and Science(Journal of Laws 2021, item 478), as well as civil liability, I declare, that the submitted doctoral dissertation is my own work.

I declare, that the submitted doctoral dissertation is my own work performed under and in cooperation with the supervision of prof. dr hab. Inż. Piotr Jasiński.

This submitted doctoral dissertation has never before been the basis of an official procedure associated with the awarding of a PhD degree.

All the information contained in the above thesis which is derived from written and electronic sources is documented in a list of relevant literature in accordance with Art. 34 of the Copyright and Related Rights Act.

I confirm that this doctoral dissertation is identical to the attached electronic version.

Gdańsk, 07.07.2023 r. A. Mroziński

signature of the PhD student

I, the undersigned, agree * to include an electronic version of the above doctoral dissertation in the open, institutional, digital repository of Gdańsk University of Technology.

Gdańsk, 07.07.2023 r. A. Mroziński

signature of the PhD student

**delete where appropriate*

[1] Art 27. 1. Educational institutions and entities referred to in art. 7 sec. 1 points 1, 2 and 4–8 of the Act of 20 July 2018 – Law on Higher Education and Science, may use the disseminated works in the original and in translation for the purposes of illustrating the content provided for didactic purposes or in order to conduct research activities, and to reproduce for this purpose disseminated minor works or fragments of larger works.

2. If the works are made available to the public in such a way that everyone can have access to them at the place and time selected by them, as referred to in para. 1, is allowed only for a limited group of people learning, teaching or conducting research, identified by the entities listed in paragraph 1.

Acknowledgements

The creation and final shape of my doctoral thesis was influenced by many people whom I would like to thank here.

I thank my promoter professor Piotr Jasiński for all the knowledge passed on to me over the years and all the help, for inspiration, understanding and patience, for valuable comments for all the tips.

I would also like to thank professor Sebastian Molin for his cooperation, for the opportunity to consult, for his time and help in writing the thesis.

I would like to thank PhD Tadeusz Miruszewski, professor Jakub Karczewski and colleagues from the team, as well as all those who helped me in the laboratory.

A separate, equally important, thank you to my wife, who supported me and often relieved me of my home and parental duties, and to my parents, thanks to whom I had the opportunity to learn and gain knowledge, who constantly mobilized and supported me throughout my studies at the Gdańsk University of Technology.

Contents

List of abbreviations and symbols

ABO_3	Perovskite Formula
ASC	Anode Supported Cell
ASR_{pol}	Area Specific (Polarisation) Resistance
CGO	Gadolinium Doped Ceria
DRT	Distribution of Relaxation Times Analysis
ECM	Equivalent Circuit Model
ECR	Electrical Conductivity Relaxation
EIS	Electrochemical Impedance Spectroscopy
ESC	Electrolyte Supported Cell
LSC	$La_{0.6}Sr_{0.4}CoO_{3-\delta}$
LSCF	$La_{0.6}Sr_{0.4}Co_{0.2}Fe_{0.8}O_{3-\delta}$
MIEC	Mixed Ionic and Electronic Conductor
Ni-YSZ	Nickel and Yttria Stabilised Zirconia
NLLS	Non-linear Least-squares Fitting
OCV	Open Circuit Voltage
ORR	Oxygen Reduction Reaction
PEMFC	Polymer Electrolyte Membrane Fuel Cells
pO_2	Oxygen Partial Pressure
SEM	Scanning Electron Microscope
STFx	$SrTi_{1-x}Fe_xO3-\delta$
STF-x	$Sr_xTi_{0.3}Fe_{0.7}O_{3-\delta}$
SOC	Solid Oxide Cell
SOEC	Solid Oxide Electrolysis Cell
SOFC	Solid Oxide Fuel Cell
TEC	Thermal Expansion Coefficient
TMO	Transition Metal Oxides
UN	United Nations Organization
VdP	Van der Pauw method

YSZ	Yttria Stabilised Zirconia
zero-TCR	Zero Temperature Coefficient or Resistivity
A	Surface Area
C	Capacitance
R-CPE	Resistance and parallel Constant Phase Element
d	Thickness of the sample
D*	Chemical Diffusion Coefficient of Oxygen
f	Correlation function
I	Current
k*	Chemical Oxygen Surface Exchange Coefficient
L_0	Inductance
N	Number of collection points
P	Power density
R_{el}	Resistance of equivalent circuit element
R_{ohm}	Ohmic Resistance
R_{pol}	Polarisation Resistance
R_s	Series Resistance
s	EIS sampling frequency
τ	Time scale
U	Voltage
U_{avg}	Average voltage
Z_{DRT}	DRT impedance
λ	Regularisation Parameter
σ_{total}	Total Electrical Conductivity
σ_{el}	Electronic Conductivity
σ_{ion}	Ionic Conductivity
γ	Distribution of Relaxation Times value

Abstract

Producing efficient solid oxide fuel cells (SOFC) without the use of harmful elements is one of the current challenges. Increasing the safety of people and reducing production costs is possible, among others, thanks to the use of iron doped strontium titanates as porous oxygen electrodes. In this thesis, the results of research on iron doped strontium titanates as potential oxygen electrodes for SOFC are presented. The research focused on:

- Solid state reaction synthesis of iron doped strontium titanates with different amounts of substituted iron ($SrTi_{1-x}Fe_xO_{3-\delta}$, STFx) and materials with different nonstoichiometry in the strontium sublattice ($Sr_xTi_{0.3}Fe_{0.7}O_{3-\delta}$, STF-x). Electrical and microstructural studies have proven that these materials can be an alternative to those currently used not only at 800 °C but also at 700 °C.
- Determining the electrochemical processes occurring in the STFx and STF-x materials during the oxygen reduction reaction and distinguishing which process limits the yield depending on the material used. Thanks to electrochemical impedance spectroscopy, a distribution of relaxation times analysis and microstructural studies, it was possible to identify the electrochemical processes occurring in these porous cathodes and indicate which ones limit the efficiency of the electrodes depending on the stoichiometry.

Keywords: oxygen electrode, iron doped strontium titanates, strontium non-stoichiometry, electrochemical impedance spectroscopy, distribution of relaxation times, solid oxide cells.

Chapter 1

Introduction

One of the most important goals declared by the United Nations (**UN**) is to ensure access to affordable, reliable, sustainable and modern energy services for all people (Goal number 7) [1]. According to the UN, access to clean and affordable energy is key to the continued development of industry. Therefore, significant effort is being put into research into the conversion of energy from natural sources. For years, people have been looking for an alternative to the relatively inefficient combustion of fossil fuels, due to the limited amount of raw materials and increasing environmental pollution. One potential solution is the expensive and complex nuclear energy technology. On the other hand, fuel cells, including high-temperature electroceramic cells, e.g.: solid oxide fuel cells (**SOFC**s), show good prospects [2]. Energy is obtained from SOFC as a result of an electrochemical reaction, which is not limited by the Carnot efficiency. The most common reactants used in fuel cells are hydrogen (fuel) and oxygen (oxidiser). As a result of the electrochemical reactions of these two gases, we obtain the desired electrical energy through the electron flow in an external circuit, as well as water (steam) and heat. Both by-products of the electrochemical conversion are harmless and can be used for other needs, such as cogeneration systems and irrigation of plants. The world's currently existing solutions for industrial power plants based on fuel cells are able to exceed the capacity of tens of MW with efficiencies above 60% (e.g. 28 MW in San Jose, California [4]). Figure 1 shows an example of a potential green energy flow using SOFC.

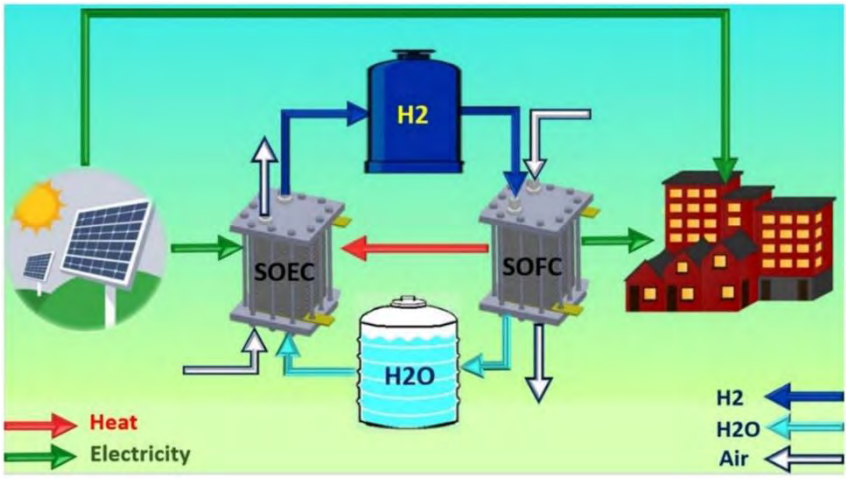

Figure 1. Schematic of proposed thermally self-sustaining energy storage system [3].

SOFC ceramic cells typically require high operating temperatures, i.e. exceeding 800 °C [5]. The high catalytic activity of these materials is often associated with rapid degradation due to enhanced interfacial reactions and corrosion of steel components [6,7]. Therefore, it becomes crucial to search for alternative, cheaper and more stable materials for fuel cells that provide high performance at lower operating temperatures, namely between 600 °C and 800 °C – the so-called intermediate operating temperature range (IT-SOFC).

1.1. Background

In fuel cells, electrical energy can be obtained by oxidising the fuel (hydrogen). The electrodes in fuel cells serve as catalysts for an electrochemical reaction without being a reaction reagent themselves. The most common and simple fuel used for fuel cells is hydrogen. When hydrogen and oxygen (either pure or in air) are used as the working gases, the sum reaction at the electrodes is:

$$O_2 + 2H_2 \rightarrow 2H_2O \qquad \text{(Equation 1)}$$

The sum reaction described by $O_2 + 2H_2 \rightarrow 2H_2O$ (Equation 1 remains the same for most fuel cells utilising hydrogen and oxygen. However, some types of fuel cells can also be alternatively fuelled by other fuels, including hydrocarbons (e.g.: methane) or their derivatives (e.g.: methanol), as well as fuels of natural origin, such

as biogas. Figure 2 compares different types of fuel cells and their most important and distinctive parameters. Hydrogen-only fuel cells include alkaline fuel cells (AFC) [8,9], polymer electrolyte membrane fuel cells (**PEMFC**) [9–11] and phosphoric acid fuel cells (PAFC) [9,12]. SOFCs and molten-carbonate fuel cells (MCFC), operating at elevated temperatures, can be powered by more than one type of fuel [9,13,14].

Despite the relatively low operating temperature of PEMFC cells and the solid form of the electrolyte (polymer), the need to use precious metals (Pt) and electrodes with a large surface area hinders their widespread application. In this perspective, SOFCs based on ceramic solid electrolytes, not requiring noble metals as electrocatalysts and capable of converting various fuels, have become an interesting option. However, to use SOFCs on a larger scale, it is necessary to lower the operating temperature (<800 °C), which will make it possible to reduce the production costs, e.g.: through the use of low-cost steel interconnectors. Nevertheless, due to the thermally activated ion transport in the electrolyte and lowered electrocatalytic reaction rates at the electrodes, lower temperatures currently limit the performance of the existing fuel cells. Typically, operating temperature above 600 °C allow the use of fuels other than pure hydrogen [15]. Although storing large amounts of hydrogen in gaseous form is cumbersome, a combination of solar cells/windmills and solid oxide electrolysers (**SOEC**) may provide a solution, making it possible to generate clean "green" hydrogen during the day to be consumed by a SOFC at a later time. The same electrodes are typically used in both types of solid oxide cell (**SOC**) – used in both the SOFC and SOEC – resulting in a fully reversible SOC.

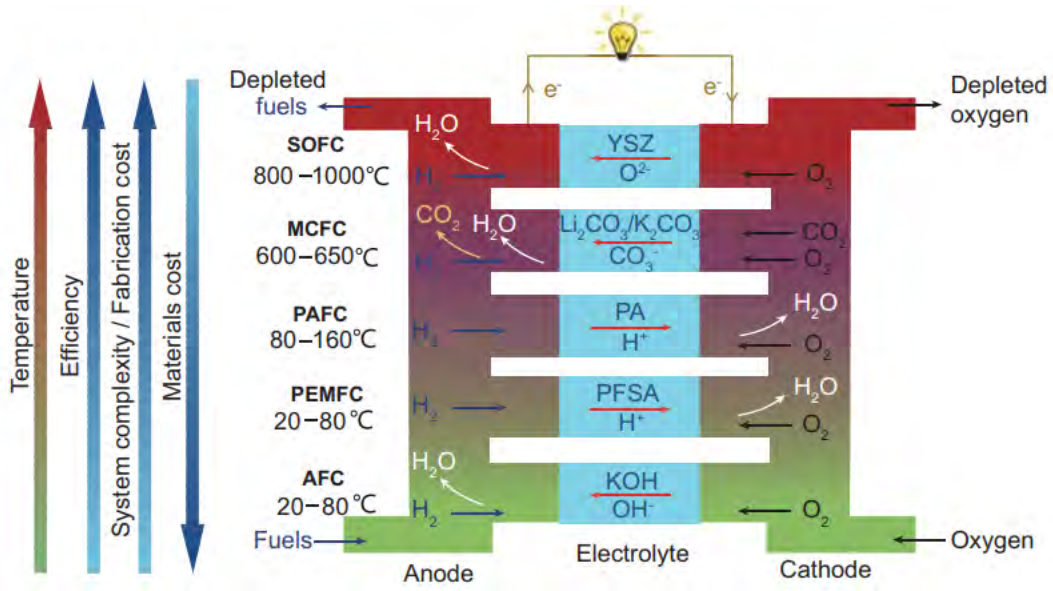

Figure 2. Fuel cell types, showing the general trend in the relationship between the operating temperature, efficiency, system complexity, fabrication cost and materials cost of the FC technologies [2].

1.2. Working principle of SOFC

Figure 3 presents SOFC cells powered by oxygen (oxidant) and hydrogen (fuel), typically made of two porous electrodes (cathode and anode, respectively) separated by an electronically non-conductive but ionically conductive solid electrolyte. On each side of the cell, the supplied gases take part in a different reaction.

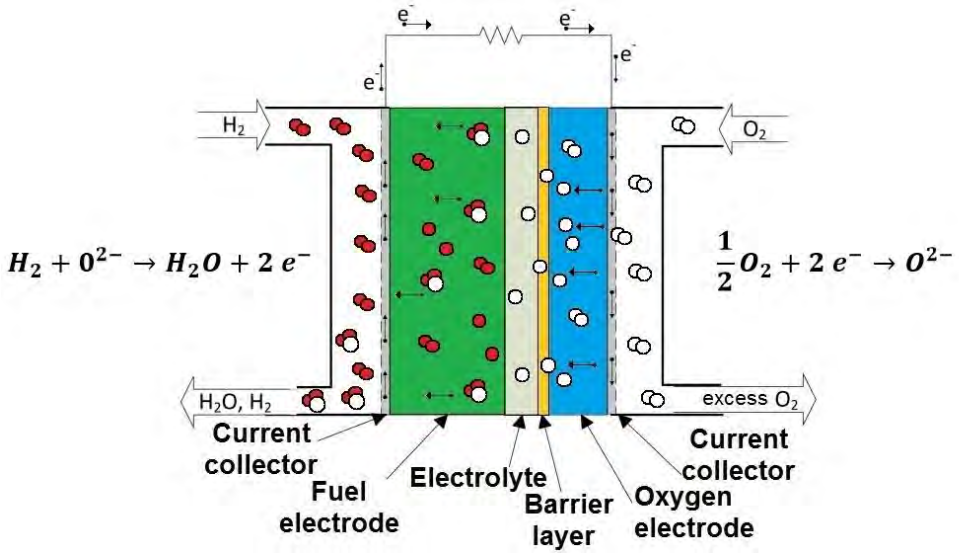

Figure 3. Schematic diagram of a typical SOFC and the total reaction equation on both sides of the cell.

The performance of a SOFC is mainly influenced by the rate of the electrochemical reactions at the electrodes. Typically, during fuel cell operating mode, an oxygen reduction reaction (**ORR**) process occurs on the cathode side of the SOFC. As a result of the ORR reaction, i.e. the formation of doubly negatively charged oxygen ions, the resulting oxygen ions are transported through the purely ionically conducting electrolyte to the anode. The oxygen anions delivered to the anode take part in the hydrogen oxidation reaction. The final products of this process are steam, heat, and an external flow of electrons. The electrons return to the cathode through the external circuit to again take part in the ORR and, on the way, power the connected load. Water in the form of steam is discharged outside the system with the excess hydrogen gas.

1.3. Construction of SOFC

Several configurations of SOFC cells can be prepared [16]. The first possibility is to use the anode as a mechanical support of the cell (**ASC**). The second solution is preparing cells supported on the electrolyte (**ESC**). ASC are characterised by a lower operating temperature and higher performance thanks to their thin electrolyte and cathode [17]. In this case, a thick, porous anode is limited by the diffusion resistance of the fuel gases, which makes it difficult to precisely analyse the results of the development process of the SOFC materials, such as the oxygen electrode. What is more, the porosity can make it difficult to seal the mounted ASC cell well to ensure there is no leakage. In the case of electrolyte-supported cells with a thin anode and cathode, the gas diffusion loses are smaller and there should not be any leakage thanks to the thick, dense electrolyte. Unfortunately, the use of a thick, dense electrolyte has its consequences in the form of much higher ohmic losses. The typical electrolyte thickness of ASC cells is ~10 μm, whereat for ESC, it is >100 μm. This affects the achieved power density value and the need to use a higher operating temperature, which intensifies the degradation process.

An example of a state-of-the-art commercial SOFC (Elcogen, ASC 300 cell) is presented in Figure 4. For many years, the anodes have been based on the composite of nickel and yttria stabilised zirconia (**Ni-YSZ**). At the fabrication step, YSZ is mixed with NiO (green colour), which is then reduced during the startup of the SOFC. Metallic nickel provides high electronic conductivity and is a good hydrogen oxidation electrocatalyst, whereas the YSZ is the ionically conductive phase. In the case of the electrolyte, pure yttria stabilised zirconia (**YSZ**) is usually used [13]. As a result of the composite structure, the hydrogen electrode provides overall a mixed ionic-electronic conductivity, necessary for achieving high electrochemical performance. In the case of an oxygen electrode, the best performance is currently obtained by using $La_{0.6}Sr_{0.4}Co_{0.2}Fe_{0.8}O_{3-\delta}$ (**LSCF**) or $La_{0.6}Sr_{0.4}CoO_{3-\delta}$ (**LSC**) [18]. These materials, though highly active, contain cobalt, which is on the list of carcinogens and is listed as one of the critical raw materials that the EU plans to limit to become more resource independent. In the case of direct contact between the YSZ electrolyte and La/Sr-containing oxygen electrode materials, a reaction between Zr and La/Sr occurs, which results in the formation of a parasitic layer with high resistance. To solve this problem, a gadolinium doped ceria (**CGO**) barrier layer is introduced [19], as also included in Figure 4.

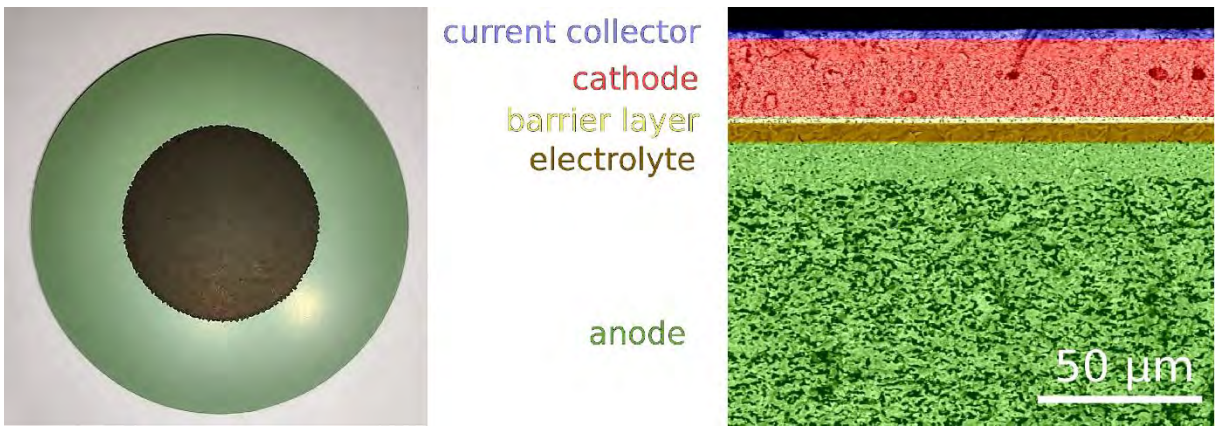

Figure 4. Photo of one of the prepared samples before testing and a SEM picture of a commercially available cell.

1.4. Cathode materials for SOFC

To make SOFC cells as efficient as possible, each layer of the electroceramic cell should be characterised by a low polarisation area specific resistance (**ASR_{pol}**) and series resistance (**R_s**) at SOFC operating temperature. Historically, the main challenge in operating SOCs at lowered temperatures has been the low performance of oxygen electrodes at lowered temperatures [20–22]. Thus, a lot of attention has been directed to searching for novel materials or electrode structures.

In the literature, much attention is devoted to the development of alternative materials for oxygen electrodes [23]. The typical benchmark often used for stating the applicable performance limits is based on the polarisation resistance of the individual electrode not exceeding 100 $m\Omega\ cm^2$ at the designated operating temperature [24]. A large group of materials that meet the requirements are compounds with Mixed Ionic and Electronic Conductivity (**MIEC**), in which the electrochemical reaction could take place throughout the entire volume of the material, in comparison to electronic conductors (Figure 5).

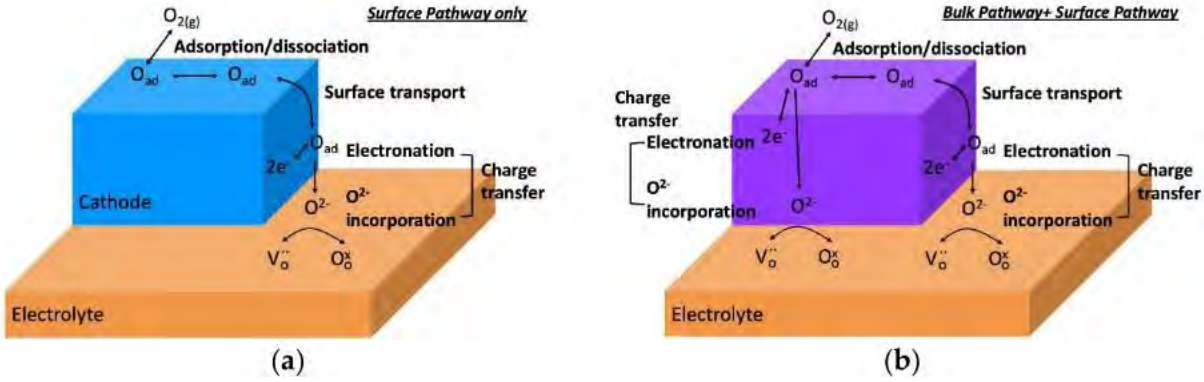

Figure 5. Schematic of possible elementary reaction steps during oxygen reduction reaction (ORR) and possible pathways for two classes of cathode materials; (a) pure electronic conductor and (b) mixed ionic and electronic conducting (MIEC) cathodes [25]**.**

Among the MIEC materials for application as the oxygen electrode, materials belonging to the perovskites group have been the most extensively studied [26–28]. The typical chemical formula of perovskites is ABO_3 (see Figure 6), where A is large cation

(based on rare earth metals) in 12-fold coordination by oxygen anions, and B is a relatively smaller cation (based on transition metal oxides – **TMO**) in the centre of an oxygen-coordinated octahedra (6-fold coordination). What's more, sites A and B can be occupied by more than one type of cation, which results in a strong chance of finding a material that could present low enough ASR_{pol}, not only at 800 °C but also at lower temperatures, e.g.: 700 °C or 600 °C. To increase the performance, the following properties of the electrode materials can be considered and influenced: the microstructure of the electrode (porosity, tortuosity, particle size) [29,30]; intrinsic oxygen activity (Chemical Oxygen Surface Exchange Coefficient **k***, Chemical Diffusion Coefficient of Oxygen **D***) [31,32]; interface between the electrode and electrolyte or the barrier layer [19,33]; matching coefficients of thermal expansion (**TEC**) and the electronic transport properties. The search for new alternative materials among perovskite materials is carried out in several ways, not only by changing the elements in the A or B sublattices but also by changing their stoichiometry or creating composite materials, i.e. chemical and/or microstructural modifications.

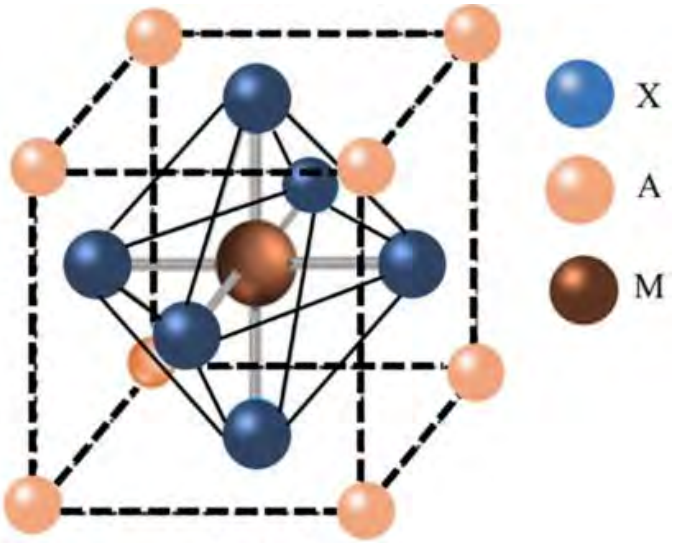

Figure 6. A typical perovskite structure [34]**.**

In addition to materials' bulk modifications, surface modifications, such as infiltration or exsolution, are also intensively studied. Unfortunately, low ASR_{pol} values are obtained mainly by MIEC compounds which contain a large amount of expensive elements such as lanthanum or cobalt (e.g.: LSCF and LSC) [35–39], being also listed on the Critical Raw Materials list (Co) [40]. In the case of state-of-the-art perovskite materials, it is believed that they obtain their efficiency primarily due to the high total electrical conductivity ($\boldsymbol{\sigma_{total}}$) with high ionic transport properties (σ_{ionic}), where σ is in the order of $10^2 \div 10^3$ S cm^{-1}. An example LSCF (σ_{total} ~300 S cm^{-1} at 800 °C, σ_{ionic} 2.6 10^{-4} S cm^{-1} at 800 °C [41]) presents an ASR_{pol} of ~25 mΩ cm^2 at 800 °C for the porous electrode (own result). However, the importance of the individual partial conductivity levels (electronic/ionic) on the electrodes' efficiency is not well recognised, and is currently an active research topic [32,42,43]. In this respect, materials with relatively low total conductivities (or materials with a relatively low electronic-to-ionic conductivity ratio) and good oxygen catalyst properties are very interesting for basic research.

One of the interesting MIEC materials for potential use in SOFC, which has been previously briefly studied by our research group, is doped strontium titanates $SrTi_{1-x}Fe_xO_{3-\delta}$ (**STFx**) [44]. STFx have high ionic conductivity ($\boldsymbol{\sigma_{ion}} \approx 3.5 \cdot 10^{-2}$ S cm^{-1} at 900 °C [45]) but overall, the total conductivity is relatively low (**σ** in the range of $10^{-4} \div 10^{1}$ S cm^{-1} at 800 °C [46]). In comparison, the state-of-the-art $(La_{0.6}Sr_{0.4})_{0.95}Co_{0.2}Fe_{0.8}O_{3-\delta}$ shows ionic conductivity two orders of magnitude lower. Due to their structural versatility, STFx materials have been considered as potential materials for fuel electrodes [47] or oxygen electrodes [48]. However, this group of materials has not yet been well explored. Most of the literature has focused on the properties of dense thin films used as well-defined model MIEC materials [48,49], and the properties of porous electrodes have hardly been studied in a systematic manner. One of the most interesting properties of STFx is the zero temperature

coefficient of resistivity (zero-TCR) for STFx with Fe = 0.35 (σ_{el} ~10^{-1} S cm^{-1}). Zero-TCR is associated with the lack of a significant change in the electrical conductivity of the material in a specific temperature range (700 °C – 900 °C) in the high oxygen partial pressures (**pO_2**) range, see Figure 7 (blue circle). Only the pO_2 changes influence σ_{el}. However, potential changes in the electrochemical mechanisms are not widely studied.

Generally, by varying the iron content in STFx, the total electrical conductivity of STFx can be varied over a large range, which seems interesting to study.

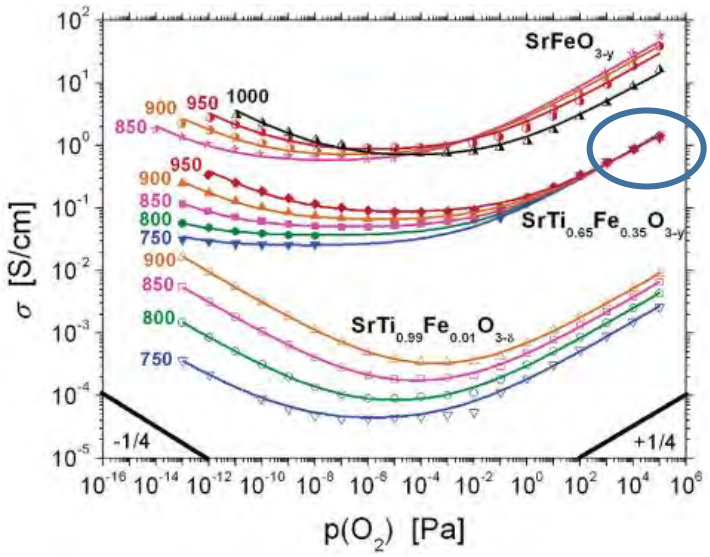

Figure 7. Total conductivity isotherms at different temperatures (750–1000 °C) as a function of oxygen partial pressure (p(O_2)) for STF compositions with 1 mol % (STF01), 35 mol % (STF35), and 100 mol % Fe ($SrFeO_{3-y}$). Experimental data points are represented by symbols, fitted curves by solid lines [46].

1.5. Electrochemical processes occurring at the cathode

As shown in $O_2 + 2H_2 \rightarrow 2H_2O$ (Equation 1, the working principle of the SOFC is based on a simple overall reaction. However, this simple overall reaction has several possible intermediate steps, where rate limitations can occur, so at the molecular level, the electrode process is not so trivial and is still under wide investigation [6,50]. One of the most frequently studied electrochemical processes in SOFC is the oxygen reduction reaction [51]. Several models and mechanism have been reported in the literature due to the overly large number of possible intermediate phases [52–57]. Nevertheless, the

general description of the ORR reaction has not been concisely and unequivocally formulated. It is known that MIEC materials enable electrochemical reactions not only at the interface between the three phase boundaries – gas, electrolyte and electrode (**TPB**) – but also beyond it, across the whole surface of the MIEC electrode. To take full advantage of the good catalytic properties of MIEC materials, porous oxygen electrodes are used, which makes it possible to increase the surface area actively involved in the ORR. Based on the current understanding [57], the most common ORR pathway in MIEC materials consists of the following elementary steps (Figure 8):

- incorporation of oxygen atoms into the crystal lattice (Fig. 8 a);
- adsorption and reduction of gaseous oxygen (O_2) on the surface of the cathode (Fig. 8 b);
- oxygen ion transport at the surface (Fig. 7 d) or in the volume of the cathode (Fig. 8 c);
- oxygen ion exchange through the interface (Fig. 8 e–f);
- one or more of the above-mentioned mechanisms, occurring directly on the electrolyte if it is active in the production and transport of electroactive oxygen species (Fig. 8 g).

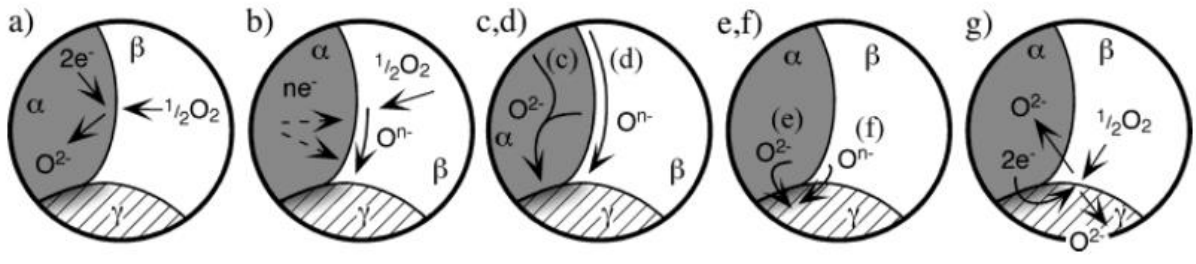

Figure 8. Possible elementary ORR mechanisms in SOFC cathodes. Phases α, β, and γ refer to the electronic, gas, and ionic phases, respectively [57]**.**

Due to the fact that electrode processes are thermally activated, it is difficult to find materials that would provide sufficient reaction efficiency at temperatures not exceeding

600 °C. Moreover, the influence of the physicochemical properties of electrode materials on the kinetic rate of the ORR are partially understood. It is known that, typically, the limitation of MIEC materials is the surface exchange process [48,49,58], but the underlying processes, especially as a function of temperature, are yet to be described in detail.

The most important characterisation and evaluation method of the electrochemical performance is electrochemical impedance spectroscopy (**EIS**) [59,60]. Its proper use, combined with detailed knowledge of the material, can provide a lot of valuable information. Especially using the special case of symmetrical electrode cells, where both electrodes are made of the same material and fed with the same gas, important information about the processes taking place on the electrode can be obtained from the EIS (at OCV). Thus, it is often used to study the effects of material changes on electrochemical processes.

1.6. Investigation of oxygen reduction reaction processes

Proper analysis and interpretation of EIS spectra is a challenge, but the limiting electrochemical processes can be distinguished on its basis [61,62]. Deconvolution of EIS spectra can be performed by physical modelling, electrical circuit modelling (**ECM**) using non-linear square fitting (**NNLS**), and the distribution of relaxation time method (**DRT**) [63]. The first is time-consuming and difficult to implement. The second method is widely used, however ECM is non-trivial, because it requires prior knowledge to select circuit elements that can match the data, and numerous circuit elements can be found to fit the data equally. Recently, DRT has become an increasingly important alternative method because it requires limited prior knowledge during separation and its produces a timescale representation [63–65]. Nevertheless, there are several challenges when interpreting the DRT spectrum.

To describe the electrochemical properties of the electrode materials, typically multiple EIS measurements as a function of experimental conditions are carried out (e.g.: operating temperature, oxygen partial pressure, etc.) and fitted to a proposed equivalent

circuit including electrochemical processes [56,62,66]. The identification of electrochemical processes is easier thanks to the DRT technique, because, as a result of the DRT analysis, we obtain a representation of the spectra with timescales, where the processes with distinct characteristic relaxation times can be differentiated. By combining the ECM and DRT techniques, it is possible to distinguish both quantitatively and qualitatively the electrochemical processes in the tested materials with high probability. It is advisable to use DRT as an indicator in selecting the appropriate equivalent circuit, as in the example shown in Figure 9.

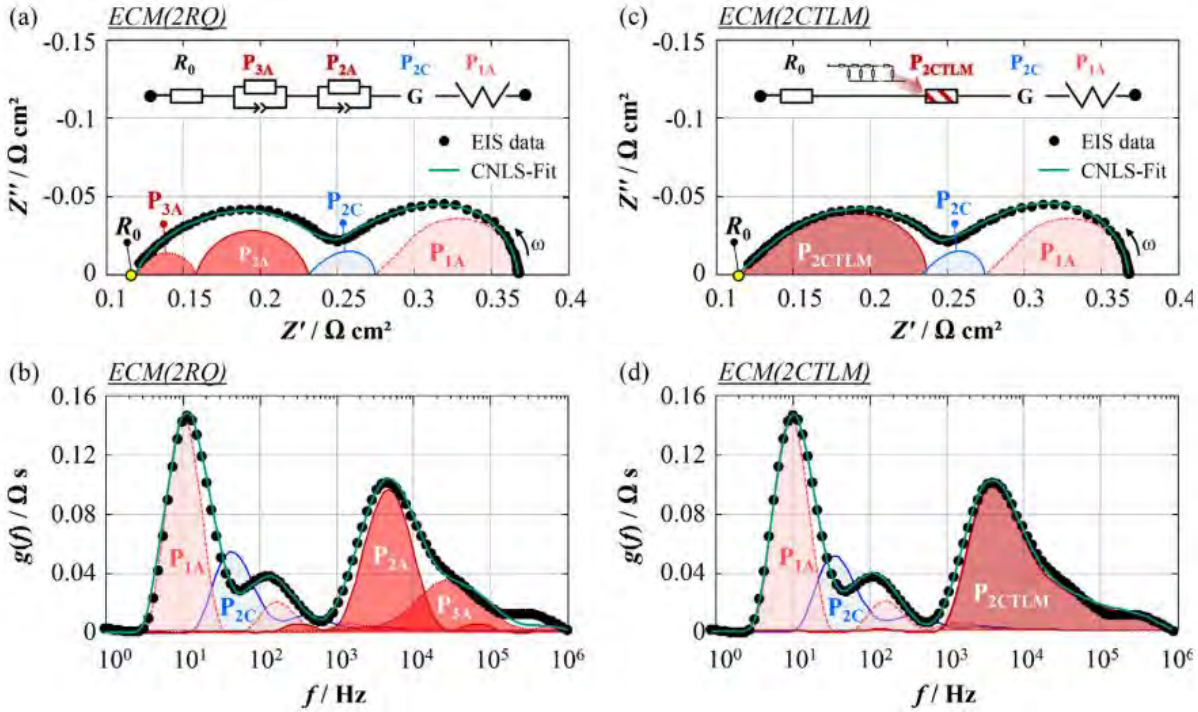

Figure 9. Measured and simulated impedance spectra and DRTs of an anode-supported SOFC based on different equivalent circuit models. Figures (a) and (b) are simulated with the established ECM with two RQ-elements – ECM(2RQ). In (c) and (d), the two RQ-elements are substituted by a physical parametrised TLM model – ECM(2CTLM). The cathode processes are blue and the anode processes are red. The measurement was recorded under OCV-conditions at 720 °C, with 20% humidified hydrogen as fuel and ambient air as oxidant [67].

DRT significantly increases the possibilities of separating the electrochemical processes in the impedance spectra, but several issues must be considered. The quality of the impedance analysis depends on the quality of the EIS spectra, i.e. the quality of the DRT and impedance analysis is largely dependent on the quality of the EIS measurements (e.g.

number of points per decade [68] and the existence of errors/noise [69]). As shown in Figure 10, when the EIS spectrum has too few points per decade (ppd), the DRT analysis is not able to provide reliable information about the number of peaks and their location on a time scale. Moreover, various types of EIS spectra errors can also negatively affect the number of peaks detected and their distribution on the time scale (Figure 11). Therefore, all EIS measurements should be performed with extreme caution.

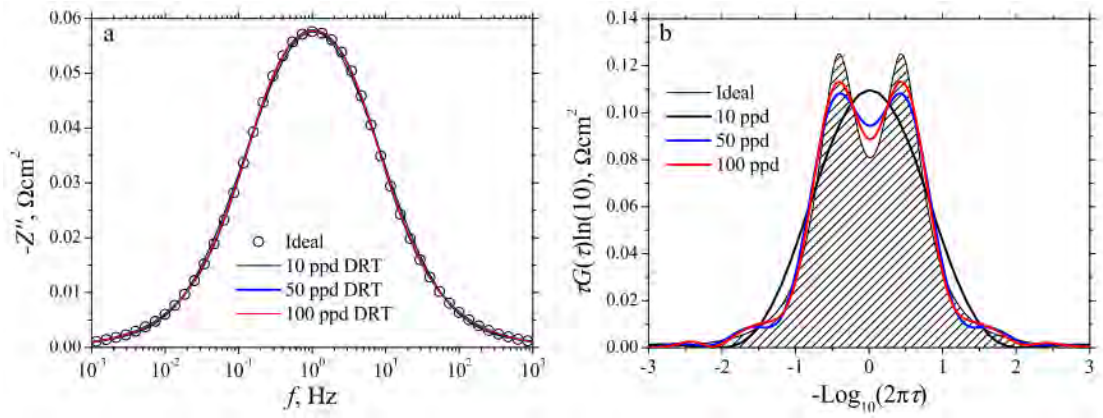

Figure 10. Imaginary impedance of a series circuit consisting of two RQ elements for R_1 = 0.1 Ωcm², Q_1 = 1 sec²/ Ωcm², n_1 = 0.8 and R_2 = 0.1 Ωcm², Q_2 = 5 sec²/ Ωcm², n_2 = 0.8 (a). Scatters in (a) represent the ideal impedance; Solid line represents the reconstructed impedance by using the QP solution of DRT for the 10, 50 and 100 ppd of frequency. (b) shows the analytical solution of DRT (black line with enclosed pattern), and the QP solutions of DRT for the 10, 50 and 100 ppd of frequency (λ = 1) of the series circuit element [70].

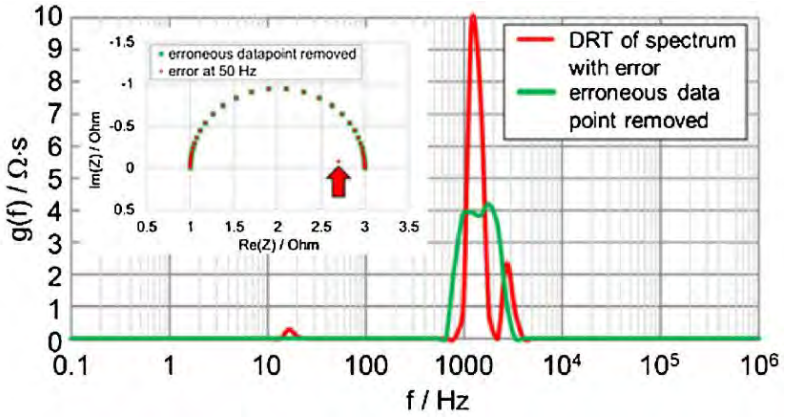

Figure 11. DRTs of a spectrum of two RC-elements (τ_1 = 2 τ_2) with one erroneous data point at 50 Hz (λ= 10^{-8}). Removing this data point from the spectrum removes the errors in the DRT [69].

DRT should not be used as a standalone method as it sometimes cannot distinguish the overlapping processes with a similar time constant, so it should be performed in conjunction with another technique, such as ECM.

In the current work, the DRT technique has been used to distinguish the limiting processes for specific STFx compounds for the first time. Section 3.4 describes the process of DRT analysis in more detail.

1.7. Doped strontium titanates

STFx materials are interesting due to several factors. They do not contain expensive, carcinogenic or critical elements, thus can be a relatively cheap and safe group of MIEC materials with strong potential for use as SOFC oxygen electrode. The example of the crystallographic structure of STFx perovskite with $x = 0.35$ is shown in Figure 12. Depending on the iron content, the most important properties of the cathode material (e.g. electronic conductivity ($\boldsymbol{\sigma_{el}}$), oxygen surface exchange coefficient and oxygen diffusion coefficient) can significantly change [46,71]. So far, it has not been clearly demonstrated how changes in the properties of materials such as k*, D* or σ_{el} can affect the ORR process. Moreover, the use of STFx materials in porous form can significantly improve the results reported earlier [48,49] by increasing the active surface area and number of TPB places.

Thanks to their high ionic conductivity, STFx compounds are well suited as membranes for oxygen separation [72], and materials for resistive oxygen sensors [70]. The high σ_{ion} of STFx is an advantage for SOFC applications, in contrast to the presented levels of electronic conductivity, e.g.: for dense $SrTi_{0.65}Fe_{0.35}O_{3-\delta}$, it is 0.3÷1 S cm^{-1} at 800 °C [49]. Despite the not high σ_{el} of the STFx with x=0.35, there are reports that it has the lowest degree of structural distortion among all STFx, which makes it promising for technical applications [73]. What is more, in STFx materials, σ_{el} can be increased by increasing the Fe/Ti ratio as a result of reducing the band gap and the enthalpies caused by substitution of Ti^{4+} by Fe^{3+}

and also a higher oxygen vacancy concentration [49,70]. The impact of changes in the properties of materials occurring when increasing the iron content on the limiting electrochemical processes in this group of compounds is not known and needs to be investigated. As shown in Figure 13 (and Figure 7), the conductivity of STFx materials is sensitive to the pO_2. This feature can be useful for evaluating the individual contributions of the electrochemical processes in ORR. The pO_2 dependence can be described by the hole concentration equation derived from the oxygen incorporation reaction and the law of mass action [74] (Kröger-Vink notation):

$$p = \left(\frac{K}{[V_{Sr}'']}\right)^{\frac{1}{2}} x\, pO_2^{\frac{1}{4}} \qquad \text{(Equation 2),}$$

where: p denotes the concentration of electron holes, K denotes the chemical reaction constant, $[V_{Sr}'']$ is the concentration of strontium vacancies, and pO_2 is the oxygen partial pressure. As can be seen in Figure 13, at high pO_2, STFx materials are p-type conductors, at low pO_2, they are n-type conductors, and at intermediate pO_2, they become ionic conductors [46]. Therefore, it is advisable to further study these compounds to better understand ORR processes in general.

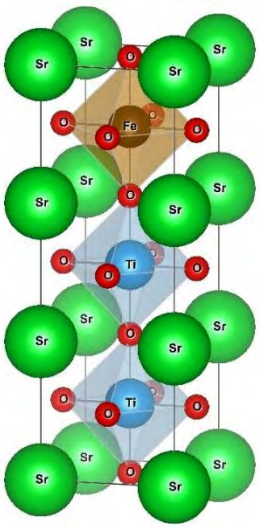

Figure 12. Crystallographic structure of $SrTi_{0.65}Fe_{0.35}O_{3-\delta}$

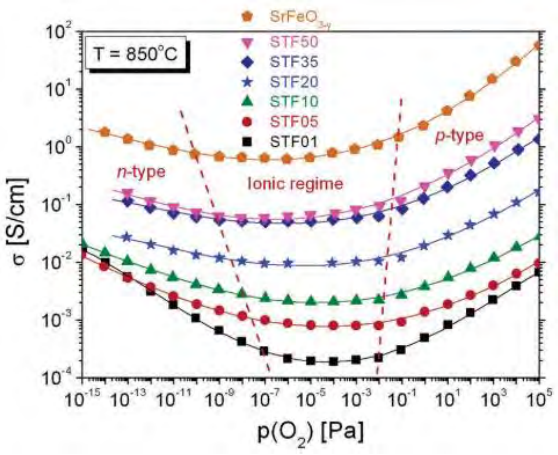

Figure 13. Electrical conductivity (σ) isotherms, at T = 850 °C, as a function of oxygen partial pressure ($p(O_2)$) for different STF compositions with Fe concentrations between 1 mol % (STF01) and 50 mol % (STF50), as well as $SrFeO_{3-y}$ [46].

As can be seen in (Equation 2, by altering the chemical composition, i.e. altering the defects, the electrical conductivity can be increased and indirectly, the electrochemical performance can be altered. The possible chemical modifications can include changes to, e.g., the oxygen vacancy concentration or changes in the A site stoichiometry. By removing Sr from the A sublattice, two possible charge compensation mechanisms could arise, which might change the catalytic activity of the STFx material. (Equation 3 and (Equation 4 show this mechanism on the example of STFx with Fe = 0.70. The first option is when two "virtual" negative charges originated for each Sr^{2+} vacancy are compensated by two "virtual" positive charges originated for each O^{-2} vacancy in the anionic substructure [46,75]:

$$SrTi_{0.3}Fe_{0.7}O_{3-\delta} \rightarrow y\,SrO + Sr_{1-y}(V''_{Sr})_y Ti_{0.3}Fe_{0.7}(V_O^{\bullet\bullet})O_{3-\delta-y} + \frac{y}{2}O_2 \quad \text{(Equation 3).}$$

The second option is a situation where some Fe^{+3} ions are oxidised into Fe^{+4}:

$$SrTi_{0.3}Fe_{0.7}O_{3-\delta} \rightarrow y\,SrO + Sr_{1-y}(V''_{Sr})_y Ti_{0.3}Fe_{0.7-2y}(Fe^{\bullet}_{Fe})_{2y}O_{3-\delta} \quad \text{(Equation 4).}$$

In view of the above, it is reasonable to undertake research on $Sr_xTi_{0.3}Fe_{0.7}O_{3-\delta}$ (**STF-x**) materials and try to better understand the possible differences in material properties that may result from the above equations.

Chapter 2

Knowledge gaps, objectives and hypotheses

As described in the literature review, STFx materials constitute an interesting area for research. Based on the performed review, several knowledge gaps have been identified and served as a basis for the presented PhD work. This chapter presents the objectives, hypothesis and strategy for the implementation of the thesis.

2.1. STF research gaps

Iron doped strontium titanates are perovskite materials with mixed ionic and electronic conductivity, which, in the form of dense thin films, showed promising results applied to SOFC [48,49]. Nevertheless, the materials should be evaluated more broadly in the porous form, i.e. as a porous electrode, which should improve the electrochemical performance at, e.g., 800 °C to be comparable to state-of-the-art materials such as LSCF. It has also been concluded that altering the iron/titanium ratio and/or introducing non-stoichiometry in the A sublattice of the tested materials should lead to a modified defect structure and possibly produce a material with more favourable material properties, such as electrical conductivity, surface exchange coefficient or oxygen diffusion coefficient, which may have a positive effect on the electrochemical performance of SOFCs. These properties have not yet been sufficiently explored and are the basis of the PhD study.

2.2. Objective of the thesis

The aim of the dissertation is to better understand STFx materials from the iron doped strontium titanates family and to determine the limitations of the materials, which can be further improved to make them a viable, Co-free alternative for SOFC oxygen electrode applications even at 700 °C.

To understand the materials behaviour in a structured process, the following research questions have been postulated for the study:

- Is it possible to obtain satisfactory electrochemical electrode parameters (such as low ASR and high power density) comparable to the state-of-the-art materials (e.g.: LSCF) for the materials with low electronic conductivity?
- What electrochemical processes dominate the ORR process of porous $SrTi_{1-x}Fe_xO_{3-\delta}$ electrodes?
- What is the influence of the A-site non-stoichiometry on the microstructural and electrochemical properties of iron doped strontium titanate-based electrodes?
- Is it possible to apply the optimised STFx electrodes in a fuel cell with performance comparable to the LSCF at an intermediate temperature (700 °C)?

2.3. Hypotheses

Based on the above information, the following hypotheses of the PhD thesis have been formulated:

A) For $SrTi_{1-x}Fe_xO_{3-\delta}$ materials (STFx) with low electrical conductivity (below 1 S cm^{-1}), it is possible to obtain porous electrodes with polarisation resistance below 100 mΩ cm^2 in the temperature range 700–750 °C.

B) By using a combination of EIS, DRT and ECM techniques, it is possible to determine quantitatively and qualitatively the electrochemical processes occurring in porous electrodes based on $SrTi_{1-x}Fe_xO_{3-\delta}$ materials.

2.4.Tasks to be performed

As part of the implementation of this dissertation, several research works were carried out in order to prove the assumed hypotheses of the work. For this purpose, the following tasks were performed:

- Selection of materials for the studies based on an analysis of the available literature reports;
- Synthesis of selected materials via the solid-state reaction method;
- Studies of the physicochemical properties of the bulk materials: electrical conductivity, dilatometry studies, surface exchange coefficient, etc.;
- Studies of the electrochemical properties of symmetrical electrodes by the EIS and DRT methods;
- Detailed DRT analysis of a subset of the tested materials under various test conditions, as both symmetric and fuel cell samples.

A description of the experimental methods and the main research methods used to verify the above-mentioned work hypotheses are presented in Chapter 3. The scientific publications containing results confirming the hypotheses are presented in Chapter 4. Chapter 5 presents a summary of the entire work and setting research directions for the future.

Chapter 3

Experimental techniques and analysis methods

This chapter presents the relevant experimental techniques which were used throughout the thesis work. The general block diagram of the tasks grouped according to the order of actions undertaken is presented in **Błąd! Nie można odnaleźć źródła odwołania.**.

3.1. Material and samples preparation

The experimental work performed within the PhD project can be divided into three main parts:

- ceramic processing: preparation of materials: powders, bulk samples, electrode layers for symmetrical and fuel cell measurements;
- electrical/electrochemical measurements: determination of electrical conductivity and electrode performance on symmetrical and in fuel cell studies;
- morphological and structural characterisation of materials: determination of the crystallographic structure of the powders, analysis of the morphology of the powders/layers, etc.

In this chapter, the first two parts are discussed due to their unique features, which are not encountered in many cases. The third part deals with common ways of characterising the basic properties of materials, so it has been omitted.

Powder synthesis

STFx and STF-x powders were obtained by a solid-state reaction method. The substrates used for the synthesis of STFx and STF-x were titanium oxide (TiO_2), strontium carbonate ($SrCO_3$) and iron oxide (Fe_2O_3). The purity of the compounds and their manufacturers varied between publications. In each of the articles, information about the substrates was specifically indicated. The appropriate weight of the starting powders was mixed in a planetary ball mill (Fritsch, Pulverisette 7); pressed into pellets; sintered twice at

a high synthesis temperature (1200 °C or 1100 °C – clearly stated in the articles), with crushing in a mortar between sintering. Finally, the synthesised materials were milled in a ball mill and used for further work. The milling parameters were selected each time so the obtained powders were characterised by a comparable particle size (<300 nm).

Paste preparation and screen printing of electrodes

The powders were prepared into pastes, which were deposited by screen-printing to make symmetrical fuel cell electrodes.

Commercially available compounds from Electro-Science Laboratories (ESL403) and Heraeus (V-006 A) were used as the paste vehicle. The amount of vehicle used required careful selection. To optimise the paste, the STFx material powder was mixed with the vehicle using an agate mortar in various weight ratios (Figure 14 A). The values were selected to ensure the pastes spread well and do not delaminate in the sintering process. Due to the high particle surface area of the milled STFx, to evenly cover the surface, it was found that 60% (w/w) vehicle should be used regardless of the vehicle type. In the next step, it was checked how thick one layer without cracks can be. The limit value of the weight of one wet layer (with 0.5 cm^2 area) was found to be 3.5 mg (Figure 14 B). This weight value was not exceeded during the application of all STFx and STF-x electrodes. In the case of the Article I, the electrode was applied by brush painting, while, for subsequent works, screen printing was used, with appropriate mesh parameters selected based on trials. This change was related to the transition to the screen printing technique. The articles specifically indicated what surface area the electrodes had in given cases.

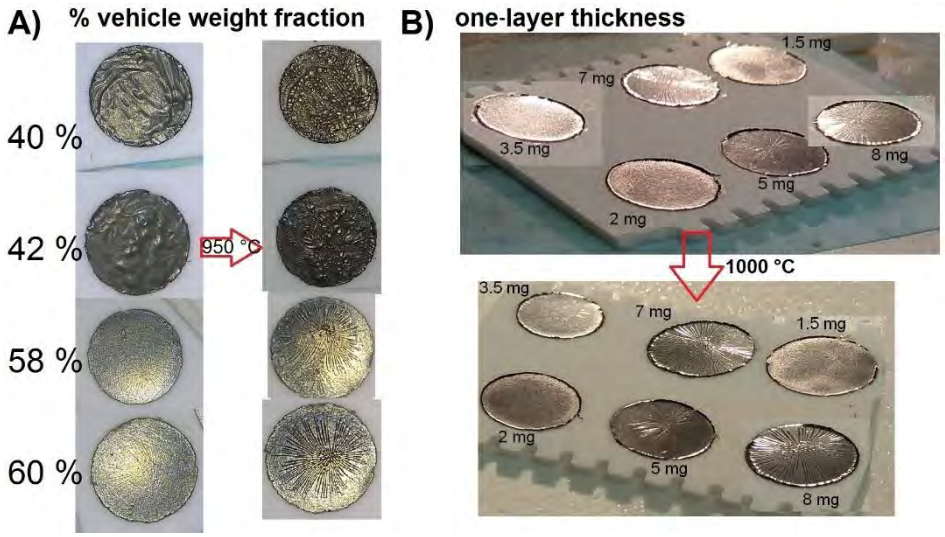

Figure 14. Selected examples of optimising the paste ratio (A) and one-layer thickness (B).

Since the electrodes should have a thickness in the range of 20 ÷ 30 μm, and according to calculations, a sintered electrode with an area equal to 0.5 cm^2 should weigh 3.2 mg, one layer will not provide such thickness, therefore the material should be applied in several stages. Slow drying at 50 °C and 130 °C was required between coats, regardless of the application technique. Without this step, delamination was observed between the layers.

Figure 15 presents scanning electron microscope (**SEM**) images of a polished cross-section of the $SrTi_{0.65}Fe_{0.35}O_{3-\delta}$ with different numbers of layers prepared using selected parameters. All the tested electrodes made of the STFx and STF-x materials that were tested had three or four layers. Each time, during the preparation of a series of samples, the thickness of the electrodes was checked by SEM on a sacrificial sample.

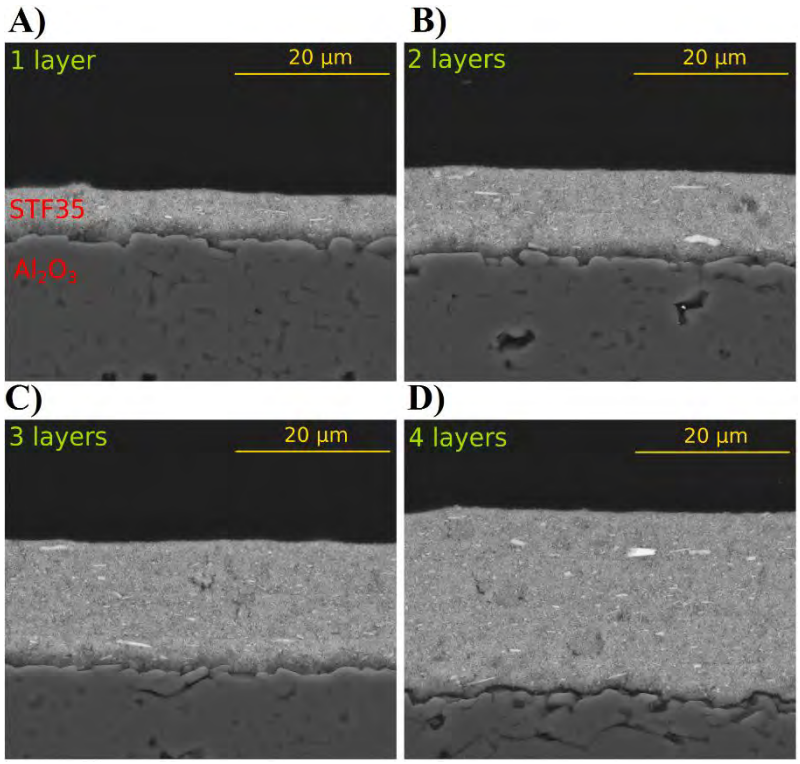

Figure 15. SEM images of a polished cross section of STF35 porous layers sintered at 800 °C with different thicknesses (A–D) on an Al_2O_3 substrate [76].

Figure 16 shows the schematics of the symmetrical samples and fuel cells prepared to study the electrochemical properties of the synthesised STFx and STF-x materials. All the tested symmetrical samples had a substrate made of $Ce_{0.8}Gd_{0.2}O_{1.9}$ (CGO-20). Thanks to the use of CGO-20 as a substrate for the symmetrical samples, we reproduced the interface seen in fuel cells, where CGO-20 is most often used as a barrier layer. In the case of ASC cells, the electrodes were placed on commercially available (Elcogen) half-cells made of YSZ+NiO anode, YSZ electrolyte and CGO-20 barrier layer. Platinum and $La_{0.6}Sr_{0.4}CoO_{3-\delta}$ were used on the surface of the cathode as current collectors of symmetrical samples and ASC, respectively.

The electrode sintering temperature range used in the publications was selected, among others, based on the pellet sinterability test (Figure 17). Since it was noticed that the material starts to sinter at 800 °C, and a dense material is formed from the powder at 1100 °C ÷

1200 °C (regardless of the stoichiometry), it was decided not to exceed the temperature of 1000 °C when sintering the porous electrodes.

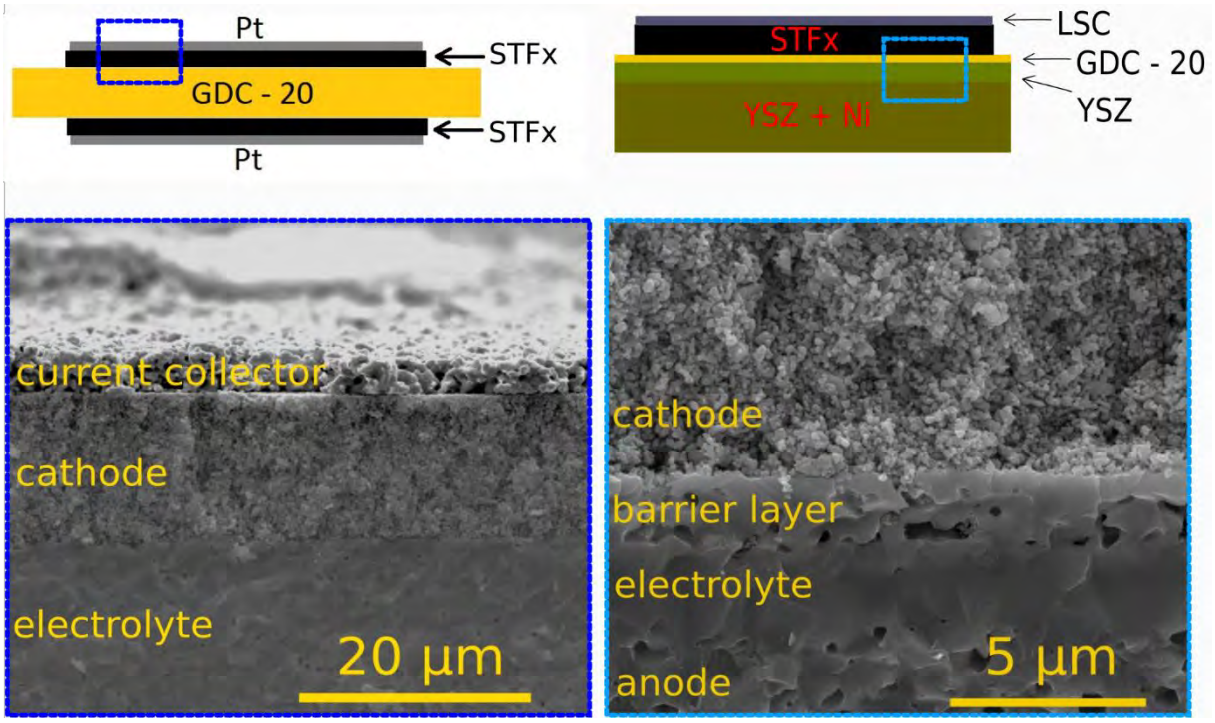

Figure 16. Schematic diagram of symmetrical sample and ASC with SEM images of measured samples.

In contrast to the electrochemical tests of the porous electrodes, all electrical measurements of the STFx and STF-x materials were carried out on dense pellets. In order to obtain dense materials, the compressed powders were sintered at the synthesis temperature for 2 h. Only in the case of the $Sr_{1.05}Ti_{0.30}Fe_{0.50}O_{3-\delta}$ material, the selected temperature was not sufficient to achieve a dense pellet, as appropriately described in Article V.

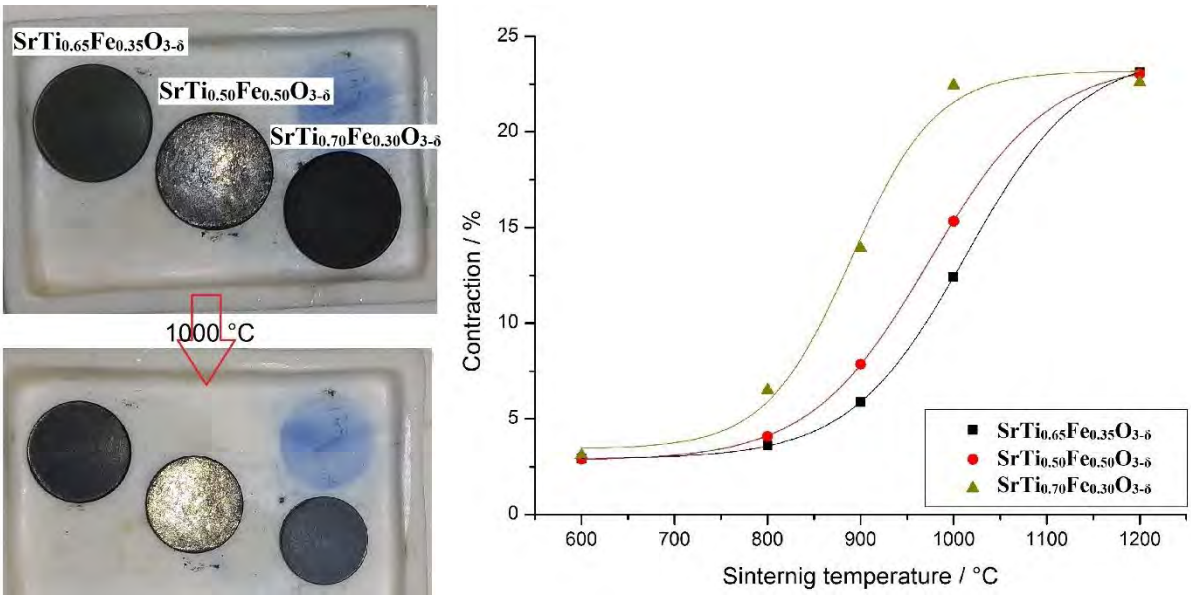

Figure 17. Example of one of the sinterability tests of STFx materials.

3.2. Four point resistance measurement – Van der Pauw technique

Four-point electrical conductivity measurements using the Van der Pauw method (**VdP**) were performed for the STFx and STF-x compounds in the form of dense pellets. The cell placed in a tube furnace had four platinum wires symmetrically connected to the edges on the surface of the sample, as shown in the Figure 18. Silver paste was used each time to ensure a good connection between the sample and the platinum wires. The paste was applied pointwise to keep the contact surface as small as possible. Before mounting the sample, the surface of the pellets was polished to remove any impurities. The samples always had an even thickness. A typical thickness value was ~1 mm. The sample was always on a non-conductive substrate made of Al_2O_3. A type K thermocouple was placed next to the sample, which was used to determine the measurement temperature. Measures were always made in the range of 900 °C – 200 °C with a step of 50 °C. Typically, the tests were performed at 20% oxygen content (synthetic air), but some of the VdP experiments were carried out at a different oxygen partial pressure. A specially written program was used to collect the measurement data.

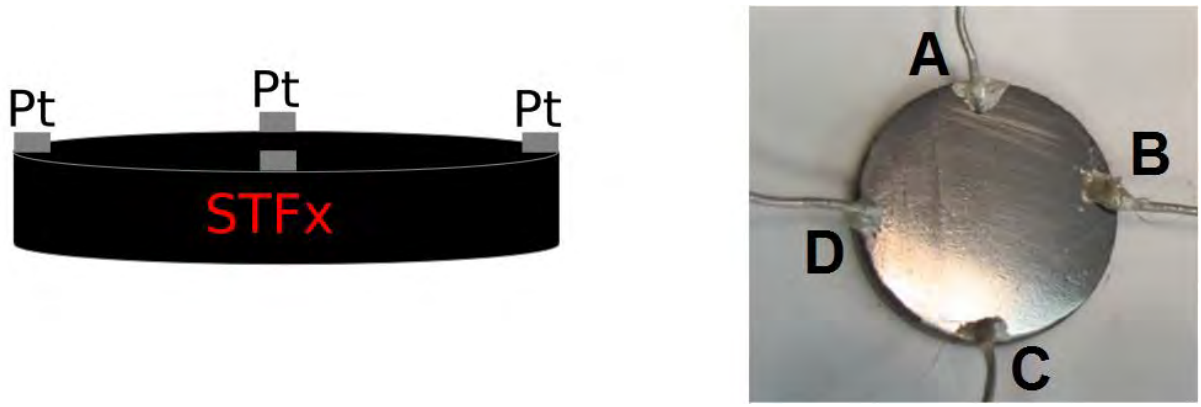

Figure 18. Schematic diagram and example of a mounted sample during VdP measurements.

According to the VdP measurement method, four measurements must be made in order to calculate the conductivity of a sample under given measurement conditions. Voltage measurements should be made in two different configurations (e.g.: perpendicular directions) and by changing the sign of the forced current to reduce thermoelectric phenomena. From both measured voltage values for the different current directions, we calculate the average, and on its basis, we calculate the resistances R_1 and similarly for the other configuration, calculate R_2 according to (Equation 5:

$$R_n = \left|\frac{U_{avg}}{I}\right| \quad \text{(Equation 5)},$$

where: R_n – resistance of each configuration [Ω], U_{avg} – average of measured voltage for configuration n [V], and I – value of forced current [A].

For the measurements performed in our laboratories, the VdP measurements were also performed for the other four configurations. Table 1 summarises all measured configurations. From the obtained resistances, the average R_A was calculated from R_1 and R_4 and also the average R_B from R_2 and R_3.

Table 1 All configurations in which the VdP measurement was performed

	Case 1	Case 2	Case 3	Case 4	Case 5	Case 6	Case 7	Case 8
	Required configurations				Additional configurations			
Resistance	R_1		R_2		R_3		R_4	
Current direction	A→B	B→A	B→C	C→B	A→D	D→A	C→D	D→C
Voltage direction	D→C	C→D	A→D	D→A	B→C	C→B	B→A	A→B

Next, based on the designated R_A and R_B, vales of correlation function and conductivity were calculated (see (Equation 6 and (Equation 7).

$$f\left(\frac{R_A}{R_B}\right) \approx 1 - \left(\frac{R_A - R_B}{R_A + R_B}\right)^2 \frac{ln2}{2} - \left(\frac{R_A - R_B}{R_A + R_B}\right)^4 \left(\frac{(ln2)^2}{4} - \frac{(ln2)^3}{12}\right) \text{ (Equation 6),}$$

$$\sigma = \frac{2\ ln2}{\pi d (R_A + R_B) f\left(\frac{R_A}{R_B}\right)} \text{ (Equation 7),}$$

where: f – correlation function [-], σ – conductivity [S/cm]; and d – thickness of the sample [cm].

3.3. Electrochemical characterisation

EIS measurements carried out as a function of temperature for various oxygen partial pressures of symmetrical samples were the main source of information about electrode ORR processes. The method of EIS measurement originally used by the research team (and Article I) was performed in a symmetrical cell with gold wires glued to the platinum current collector. There were two wires on each side of the symmetrical sample. This form of contact introduced a lot of complications during the sample preparation process and, moreover, the wires sometimes detached during the measurements. As part of the development of the measurement methodology, it was decided to implement a compression cell for measurements, similarly to commercial ASC measurement systems. Porous alumina oxide

sintered in the form of pellets was milled to the size of the electrodes used (0.5 cm^2), thanks to which good contact with the entire electrode was ensured. After the measurements, the electrodes were in good condition, as shown in Figure 19 A). Symmetrical measurements were performed in the range of 800 °C – 400 °C with a step of 50 °C. Typically, the tests were performed at 20% pO_2, but some of the experiments were carried out in different oxygen partial pressures.

ASCs were tested in a commercial Fiaxell OpenFlanges V5 test setup (Figure 19 B), as described in the articles. A nickel mesh was used on the anode side and a gold mesh on the cathode side. The cells were heated slowly to a temperature of 750°C, at which the reduction took place and the temperature was lowered to the measuring temperature of 700°C. In the case of fuel cells, the EIS and current-voltage (DC) measurements were performed under different measuring conditions. The potential range during the measurement was between the Open Circuit Voltage (OCV) and 0.5 V.

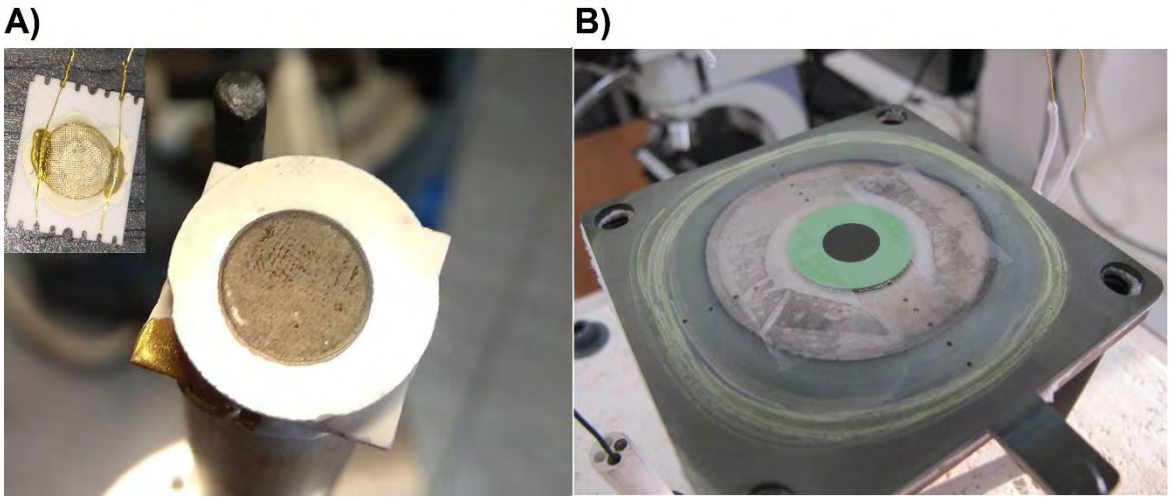

Figure 19. Measuring system for symmetrical samples for EIS tests and SOFC tests in a Fiaxell.

For the purposes of the analyses, ASR_{pol} and R_s were calculated from the measured symmetrical samples according to (Equation 8 and A (Equation 9:

$$ASR_{pol} = \frac{R_{pol} * A}{2} \quad \text{(Equation 8)},$$

$$R_s = R_{ohm} * A \quad \text{(Equation 9)},$$

where: ASR_{pol} – polarisation area specific resistance [Ωcm^2], R_{pol} – polarisation resistance [Ω], A – surface area [cm^2], R_s – series resistance [Ωcm^2], and R_{ohm} – ohmic resistance [Ω].

To prepare the current-voltage and current-power characteristics, the relationship described by (Equation 10 was used.

$$P = U * I \quad \text{(Equation 10)},$$

where: P – power density [W/cm^2], U – voltage [V], and I – current [A].

3.4. Deconvolution of EIS spectra – Distribution of Relaxation Times Analysis

In determining the processes occurring during the ORR, the DRT technique became very helpful and important from the point of view of this doctoral dissertation. Based on the results of the DRT analysis and the results of fundamental material studies, the ECM model was proposed each time and reverse engineering was carried out for verification, which is a much larger scope of verification than can be found in the literature. To analyse the EIS spectra, it was necessary to develop a procedure which is described in more detail in Article IV. It is summarised here with the problems that may arise indicated:

a) Determination and subtraction of series inductance;

b) Conversion per unit area;

c) DRT execution in DRTtools [61,62];

d) EIS spectrum fitting by the Elchemea software [77] with the use of equivalent circuit elements proposed, among others, based on DRT;

e) Reverse engineering of selected cases – DRT of each equivalent circuit element and comparison with the original DRT spectrum for selected measurement conditions;

f) Plotting the resistance values of individual elements as a function of the pO_2 and measurement temperature. Determining the slope of the curve;

g) Based on the obtained slope of the curve, suggest the electrochemical process associated with the exact equivalent circuit elements according to

(Equation 11:

$$\frac{1}{R_{el}} \propto (pO_2)^n \qquad \text{(Equation 11)},$$

where: R_{el} – resistance of equivalent circuit element [Ωcm^2], pO_2 – oxygen partial pressure, and n – slope of the curve.

Depending on the value of n, we can talk about a different process [78]:

- n = 1 oxygen molecule diffusion in pores
- n = 0.5 contribution of atomic oxygen
- n = 3/8 partial reduction of the atomic oxygen
- n = 0.25 diffusion of adsorbed O^{n-} ions on the surface of the cathode
- n = 1/8 reduction of O^- to O^{2-}
- n = 0 diffusion of oxygen ions into the electrolyte

Even though the procedure seems simple, it requires a lot of work and experience in working with both computer programs (DRTools, Elchemea). What is more, as previously mentioned in section 1.6, correct analysis is possible only for high-quality EIS spectra and with particular care when selecting the DRT parameters, which are of great importance for solving (Equation 12:

$$Z_{DRT}(f) = \frac{1}{i2\pi sC} + i2\pi sL_0 + R_{ohm} + \int_{-\infty}^{\infty} \frac{\gamma(\ln \tau)}{1+i2\pi s\tau} d\log\tau \qquad \text{(Equation 12)},$$

where: Z_{DRT} – DRT impedance, s– EIS sampling frequency, L_0 – inductance, R_{ohm} – ohmic resistance, γ – DRT, τ – time scale, and C – capacitance.

There are several computer programs offering to determine the value of γ. One of the widely used is DRTtools. It allows for arbitrary selection of the many parameters on which the solution to the equation strongly depends. Such parameters include the discretisation method and regularisation parameter λ. It is also a challenge to correctly recognise the number of peaks, where overlapping is possible. Therefore, the results from each single sample should be approached individually. Below are brief descriptions of the above-mentioned possible problems with the DRT analysis.

As can be seen in Figure 20, the selection of the discretisation method is a very important issue to correctly determine the number of peaks with high probability. In this case, for a symmetrical sample after infiltration, for which we assume few processes, it can be concluded that Gaussian discretisation will produce an unreliable spectrum due to the many artificial peaks. A much better solution is to use the other two methods (C^4 Matérn and Inverse Quadratic). Each of the discretisation methods is based on a slightly different formula, but, in general, it can be said that some discretisation methods are more sensitive to certain EIS spectral errors that are not visible at first glance.

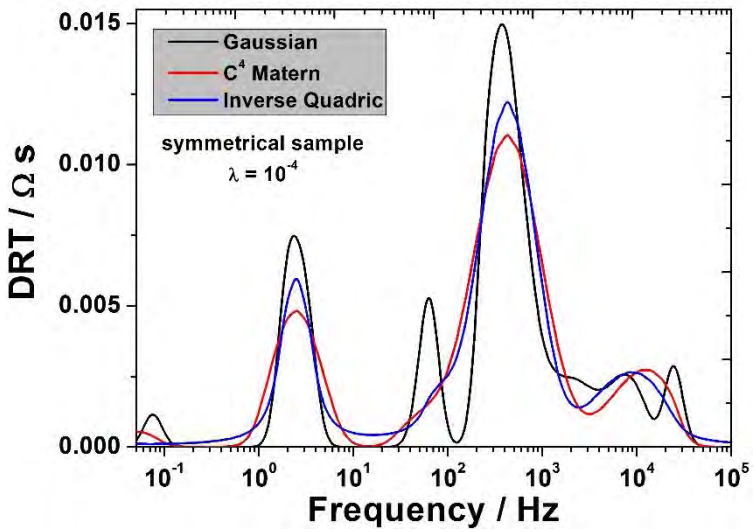

Figure 20. Example of differences in DRT spectra using different discretisation methods.

Another issue affecting the quality of the DRT analysis is the parameter λ. Figure 21 shows the results of the DRT spectra analysis for the measured EIS for four different button cell fuel cells. All analyses presented in the graphs were performed using the C4 Matérn discretisation method. The structure of the cells was very similar. All the cells were tested with the same equipment (Fiaxell setup) and according to the same measurement procedure. Even though the EIS measurement conditions were identical for all cells (700 °C, 3% H^2O and 20% pO_2), we observed that the location and shape of the peaks for all the tested SOFCs differed and strongly depended on the λ parameter. The green arrows in Figure 20 indicate for which lambda value the given DRT analysis seemed to be reliable. In the case of $\lambda = 10^{-4}$, the obtained results were mostly reliable. However, with a type 2 fuel cell, false peaks may occur.

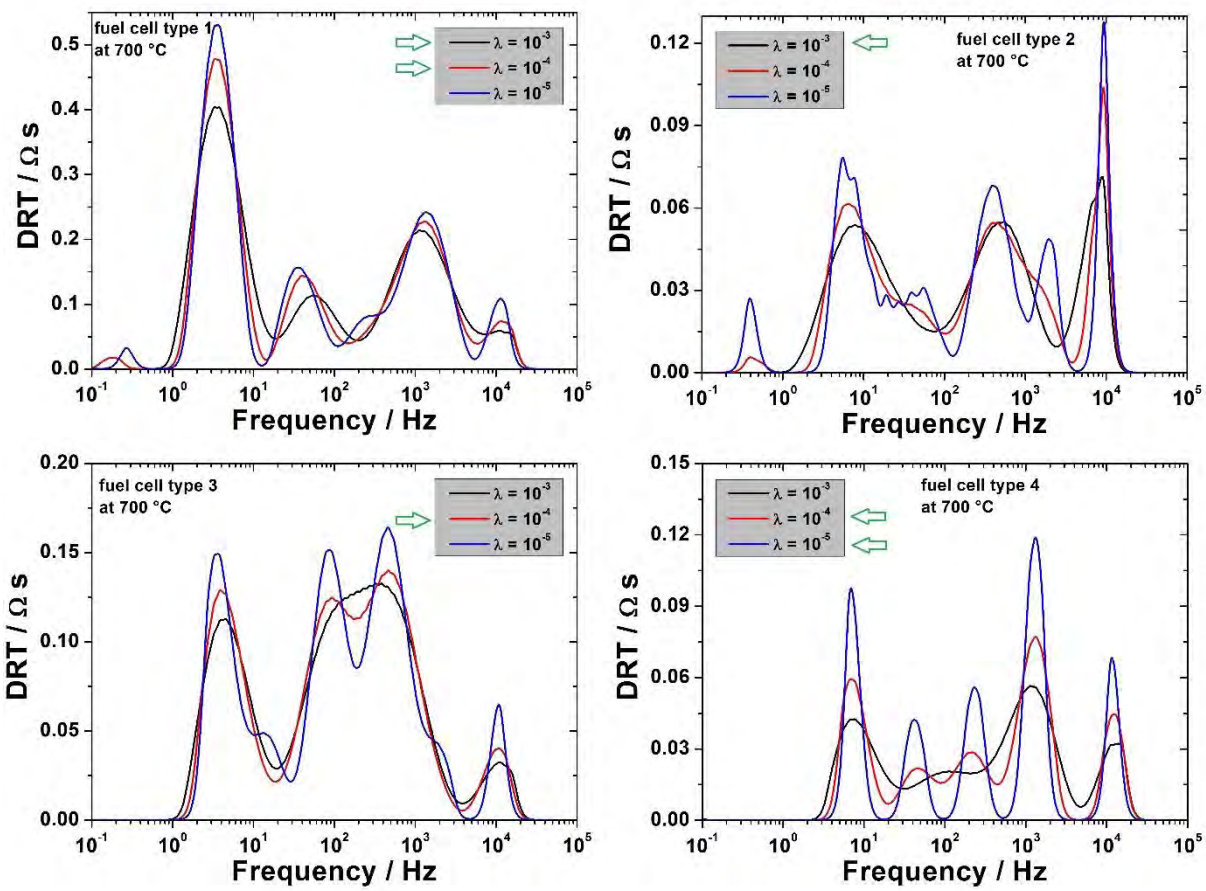

Figure 21. Influence of the regularisation parameter λ on the shape and location of DRT peaks from four solid oxide fuel cells.

Identifying and interpreting DRT peaks for complex systems such as SOFCs is a difficult task, especially when peak overlap occurs (see Figure 22). Therefore, EIS measurements should be performed over a wide range of measurement conditions to identify as many peaks as possible. For example, the EIS and DRT spectra shown in Figure 22 A can be matched with two ECM models (3x and 4x **R-CPE**). It seems that the three R-CPE elements should fit well, but the parameters of the substitute elements of the system for 3xR-CPE have values on the border of acceptability (in the range of 0.75 ÷ 0.80) and raise doubts. Fitting the EIS to 4xR-CPE is a much better solution from the point of view of ECM analysis, but only after a long-term SOFC performance test – ageing (Figure 22 B) the DRT spectrum confirms the assumptions of the ECM model.

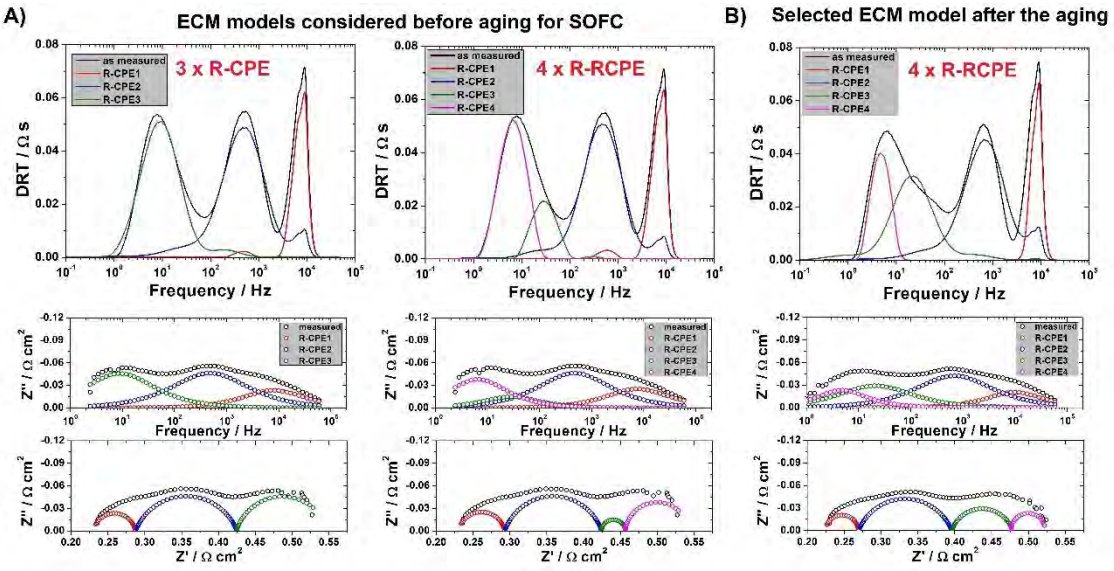

Figure 22. Exemplary problem with overlapping peaks for solid oxide fuel cell.

3.5. Designation of k* and D* – Electrical Conductivity Relaxation technique

To characterise materials properties critical to high electrochemical performance, it was decided to determine the parameters of the chemical oxygen surface exchange coefficient and chemical diffusion coefficient of oxygen. It was decided to use the technique of electrical conductivity relaxation (**ECR**), the results of which are presented in Article V. For these measurements, a special measuring cell was built, which is presented in the Figure 23. The assumption of the method is that the width and height dimensions must be much smaller than the length. For properly selected dimensions of width and height, it is possible to determine both k* and D*. After several trials, it was found that for the ECR studies, dense pellets of STF-x should have the shape of prisms (12 x 1 mm x 2 mm). The samples were cut with a precision tungsten wire saw and then gold wires were attached as in Figure 23 B. Since the main goal of the ECR study is to record the change in the conductivity of the material as a result of a rapid change in the partial pressure of oxygen, a measuring cell with the smallest possible volume was used for the study. The quartz tube had a volume of 64 cm^3. The tests were carried out at the following temperatures: 800 °C, 750 °C, 700 °C, 650 °C and 600 °C. During these studies, the oxygen partial pressure was changed from 20%

to 10% and reversed. Each time, during the pO_2 changes, the four-point single frequency electrochemical impedance spectroscopy (1 Hz) was measured. The impedance was logged every 5 s until sample stabilisation. The recorded impedance-versus-time characteristics were converted into conductivity using Ohm's law, then normalised using

(Equation 13, and then analysed in the ECRTOOLS software.

$$\alpha(t) = \frac{\sigma(t) - \sigma(t_0)}{\sigma(\infty) - \sigma(t_0)} \qquad \text{(Equation 13),}$$

where: α – normalised value [-]; t – a specific point in time; t_0 – onset when the sample was stable before the change in pO_2; and ∞ – point in time when the sample stabilised after the pO_2 change.

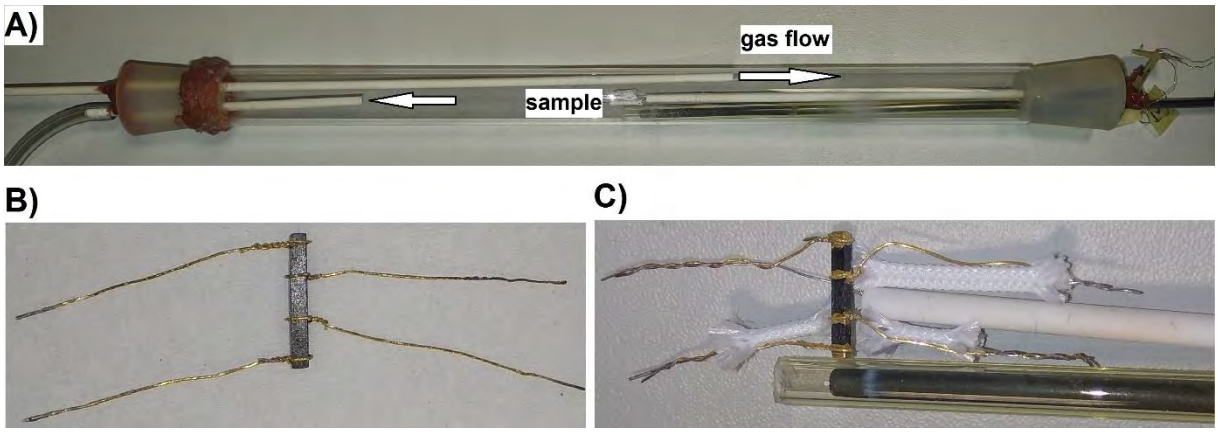

Figure 23. Measurement system for ECR measurement (A), sample prepared for experiment (B), mounted sample in the cell (C).

Chapter 4

List of publications included in the dissertation

4.1. Article I

Title: **Electrochemical properties of porous $Sr_{0.86}Ti_{0.65}Fe_{0.35}O_3$ oxygen electrodes in solid oxide cells: Impedance study of symmetrical electrodes**

Authors: **Aleksander Mroziński**, Sebastian Molin, Jakub Karczewski, Tadeusz Miruszewski, Piotr Jasiński

Journal: International Journal of Hydrogen Energy (2019) vol 44, pages 1827–1838

DOI: 10.1016/j.ijhydene.2018.11.203

Impact Factor (2019): 4.939

The paper evaluates the $Sr_{0.86}Ti_{0.65}Fe_{0.35}O_{3-\delta}$ (STF35) material as a potential porous oxygen electrode for SOFC. The EIS tests of porous electrodes were carried out on symmetrical samples sintered at different temperatures (900 °C, 950 C, 1000 °C and 1050 °C). In order to determine the occurring electrochemical processes, a symmetrical sample sintered at 1000 °C was tested as a function of different temperatures and different pO_2.

My original contribution to this publication was:

- Preparation of high-quality reproducible STF35 symmetrical electrodes.
- Detailed electrical and electrochemical characterisation of the symmetrical electrodes and dense pellets.
- Determination of the electrochemical processes occurring at the electrodes with the application of DRT and clarification of the rate-determining reaction of the porous electrode.

Table 2 CRediT author statement Article I: "Electrochemical properties of porous $Sr_{0.86}Ti_{0.65}Fe_{0.35}O_3$ oxygen electrodes in solid oxide cells: Impedance study of symmetrical electrodes"

Author	CRediT author statement	Signature
Aleksander Mroziński	Investigation; Data curation; Visualization; Writing - original draft	
Sebastian Molin	Methodology; Writing - review & editing; Conceptualization	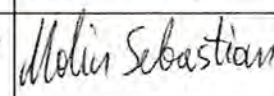
Jakub Karczewski	Investigation (SEM pictures); Writing - review & editing	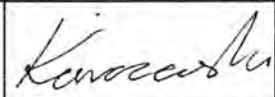
Tadeusz Miruszewski	Investigation (XRD analysis); Writing - review & editing	
Piotr Jasiński	Resources; Writing - review & editing; Supervision; Funding acquisition; Methodology	

Available online at www.sciencedirect.com

ScienceDirect

journal homepage: www.elsevier.com/locate/he

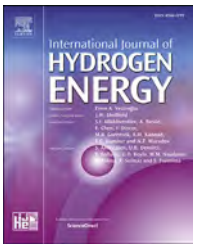

Electrochemical properties of porous $Sr_{0.86}Ti_{0.65}Fe_{0.35}O_3$ oxygen electrodes in solid oxide cells: Impedance study of symmetrical electrodes

A. Mroziński [a,*], S. Molin [a], J. Karczewski [b], T. Miruszewski [b], P. Jasiński [a]

[a] Faculty of Electronics, Telecommunications and Informatics, Gdansk University of Technology, Gdansk, Poland
[b] Faculty of Applied Physics and Mathematics, Gdansk University of Technology, Gdansk, Poland

ARTICLE INFO

Article history:
Received 13 September 2018
Received in revised form
18 November 2018
Accepted 27 November 2018
Available online 17 December 2018

Keywords:
Oxygen electrode
Solid oxide cell
Perovskite
Electrical conductivity

ABSTRACT

This work evaluates porous $Sr_{0.86}Ti_{0.65}Fe_{0.35}O_3$ (STF35) as a possible oxygen electrode material for Solid Oxide Cells. The powder synthesis was performed by solid state method. Characterization included DC electrical conductivity study of sintered bulk samples and impedance spectroscopy study of symmetrical electrodes deposited on gadolinium doped ceria substrates. Measurements were carried out in atmospheres with different pO_2 levels: 0.1%–20% O_2. Detailed equivalent circuit analysis was carried out in order to clarify the reaction pathway on porous electrode, which extends knowledge available for dense model electrodes. At 800 °C in 21% O_2, the DC electrical conductivity of STF35 pellet was 0.6 S cm^{-1} and the polarization resistance of the electrode in the symmetrical cell was ~100 mΩ cm^2. Detailed impedance spectroscopy studies revealed that the largest contribution (~80%) towards the polarization resistance is due to oxygen adsorption, which is limiting the oxygen reduction performance of the porous STF35 electrode. These results show the applicability of advanced impedance analysis methods (e.g. Distribution of Relaxation Times - DRT) for description of complex impedance electrode phenomena of porous electrodes.

Introduction

Solid oxide cells employ porous electrodes for reduction/oxidation of gaseous species. For the hydrogen side electrode a composite of nickel and yttria stabilized zirconia (Ni-YSZ) has been used successfully for many years [1,2], but alternative materials are also sought [3–5]. Electrochemical performance of the cells is often described to be limited by a sluggish oxygen reduction/oxidation reaction [6,7], thus research on the oxygen electrode materials is very active [8–10]. Perovskite materials are dominating the solid oxide cells oxygen electrode materials, where both high ionic and electronic (mixed ionic electronic conductors - MIECs) conductivities are required for highly performing electrodes. Among the perovskites, doped strontium titanates are very versatile materials, which can find use both for the hydrogen and oxygen electrodes in high temperature fuel cells [11–15]. Among the possible Ti substitutions, iron has been studied extensively, especially in the field of resistive oxygen gas sensors [16] and as a model MIEC perovskite. Perovskites with a general formula $SrTi_{1-x}Fe_xO_3$ (STFx) have been studied as model oxygen conductors by group

* *Corresponding author.*
E-mail address: aleksander.mrozinski@pg.edu.pl (A. Mroziński).
https://doi.org/10.1016/j.ijhydene.2018.11.203

of Tuller [17–20] and Ellen-Tiffee [21,22]. STF has high oxygen ion conductivity, even higher than reported for the typical oxygen electrode materials [19]. At 800 °C, oxygen ion conductivity of STF35 is ~0.035 S cm^{-1}, whereas for the state-of-the-art La0.6Sr0.4Co0.2Fe0.8O3 (LSCF) reported ionic conductivity is 0.008 S cm^{-1} [19]. Material with Fe = 0.35 exhibits an interesting property of a zero temperature coefficient of resistivity (zero-TCR). Namely, in a specific temperature range (700 °C-900 °C), electrical conductivity of the material does not depend on the temperature, only on the pO_2, which makes it a very interesting for practical applications for example in lean burn engines exhaust sensors [23,24].

STF has been also evaluated as a possible hydrogen electrode by Nenning et al. [25]. Recently, STF also found use as a mixed-conductor in oxygen permeation membranes [26–28]. Important feature of STF materials is the abundance of the forming elements (Sr, Ti, Fe), thus low price and wide availability. In comparison to other good ionic conductors containing e.g. Co, Ni, it does not contain harmful/carcinogenic elements, which is also considered an important factor [29,30].

Detailed description of the electronic structure of $SrTi_{1-x}Fe_xO_3$ has been given by Rothschild et al. [21]. At high partial pressures of oxygen it is a p-type conductor, at intermediate pO_2 an ionic conductor and at low pO_2 an electronic conductor. The levels of electronic conductivity increase with an increasing Fe/Ti ratio. The results were consistent with the reduced band gap and reduction enthalpies caused by substitution of Ti^{4+} by Fe^{3+}. For 1 at.% Fe doped $SrTiO_3$, total conductivity at 900 °C in air is below 10^{-2} S cm^{-1}, whereas for dense STF35 it is ~1 S cm^{-1} and for pure $SrFeO_3$ > 10 S cm^{-1} [18,31].

One of the possible large disadvantages of using STF35 in fuel cells is its relatively low electronic conductivity. Reported values are between 0.3 and 1 S cm^{-1} at 800 °C, much lower than for LSCF (>300 S cm^{-1}). Thus the practical applicability of STF is questionable, but its physicochemical properties and their influence on electrocatalytic performance are of basic interest [17–19,32,33]. It is still not elucidated to what extent the ionic and electronic conductivities influence the electrocatalytic properties of oxygen electrodes [33]. Yoo and Bouwmeeter evaluated oxygen surface kinetics of STF and concluded, that the ionic conductivity controls the rate of oxygen exchange [34]. Argirusis et al. have evaluated oxygen surface exchange and diffusion of STF, they found that at temperatures below 800 °C the slow oxygen surface exchange was hindering the electrochemical performance [22]. The same conclusion was made by Jung and Tuller [18,19]. Surface exchange limitation is typical for most mixed-ionic electronic conductors, but the underlying processes are yet to be described in details. Most of the basic studies dealt with model dense electrodes, where the contact area was carefully tailored. No studies have analyzed the STF as a possible porous electrode in details, describing what are the effects of the surface exchange limitation on their performance.

STF35 has been studied as a possible cathode material for Solid Oxide Fuel Cells (SOFCs) by our group before [35]. In this case a reasonably good performance of 120 mΩ cm^2 has been achieved on yttria stabilized zirconia (YSZ) electrolyte at 800 °C. The result was reached despite a chemical reaction of STF with YSZ. Formation of a $SrZrO_3$ phase between Sr and Zr containing materials is a well known phenomena [36,37], that leads to reduction in electrochemical performance of the electrodes. This can be mitigated by using doped ceria based electrolytes or application of ceria barrier layers on YSZ electrolytes [38]. Therefore it has been decided to study the electrochemical properties of STF35 on ceria based electrolyte in this work.

Oxygen reduction reaction (ORR) on solid state electrodes is an often studied reaction [39]. Though several decades of research have passed, still no clear and concise general description is available. Due to the large number of possible intermediate species several mechanisms and models have been postulated. Analysis of model compounds like STF35 can deliver new insight into the mechanisms, thus this material has been extensively studied, especially in the form of dense, thin electrodes with well-defined geometrical dimensions [40,41]. A typical general oxygen reduction pathway starts with gaseous oxygen (O_2) that has to be adsorbed on the surface, dissociate into oxygen atoms and then it has to be incorporated into the crystal lattice through the surface. The details of the adsorbate (charge level) and incorporation mechanisms are still subjected to discussions [20,42].

In this work electrochemical properties of porous STF35 electrodes are studied based on CGO electrolyte substrates. Our group has previously studied STF35 electrode on YSZ electrolyte, where chemical reaction between Sr and Zr occured. It is therefore interesting to evaluate the properties of STF35 on CGO, where no reactions take place. In this work, the effect of the sintering temperature on the polarization resistance of symmetrical STF/CGO/STF electrodes is studied. Factors limiting electrochemical performance are evaluated by performing impedance spectroscopy measurements in atmospheres with different oxygen content and at different temperatures. Advanced impedance analyses methods are employed in order to propose physically relevant electrical equivalent circuit. Results obtained in this work are an extension of results obtained on model thin dense electrodes and further clarify the current understanding of the limiting processes.

Materials and methods

Material synthesis

$Sr_{0.86}Ti_{0.65}Fe_{0.35}O_{3-\delta}$ (STF35) powder was prepared by a conventional high temperature solid state reaction method. Strontium carbonate ($SrCO_3$), iron (III) oxide (Fe_2O_3) and titanium dioxide (TiO_2) were used as the starting reagents (purity >99%, all from Sigma-Aldrich, USA). The weighed powders were mixed in a planetary ball mill (Fritsch Pulverisette 7, using 80 ml zirconia container with 5 mm alumina balls) in ethanol for 12 h with rotational speed of 200 rpm. Dried, mixed powders were uniaxially pressed (90 MPa) into pellets, which were sintered at 1200 °C for 15 h (with cooling/heating rate $3° \cdot min^{-1}$). Next, the pellets were re-ground and again pressed for the second sintering step at the same temperature conditions. Finally, the fabricated powder was re-ground and ball milled in two stages using 3 mm YSZ balls. The first milling was conducted with rotational speed of 400 rpm and the second milling with rotational speed of 600 rpm each for 8 h.

Such obtained powder was used throughout the study to prepare the samples for further characterization.

Samples preparation

For the electrical conductivity measurements, STF35 powder was uniaxially pressed into 16 mm diameter pellets under a pressure of 70 MPa. The pellets were sintered at 1200 °C for 2 h (with cooling/heating rate $3^{\circ}\cdot min^{-1}$). The obtained pellets had a diameter of 12 mm with 94% of theoretical density (measured by Archimedes method).

Symmetrical electrodes for impedance analysis were prepared on gadolinium doped ceria (CGO) substrates. CGO pellets were made from a commercial powder (GDC-20K, DKKK Japan), which was compacted under a pressure of 70 MPa and sintered at 1400 °C for 8 h. After the sintering, CGO substrates had diameters of 13 mm and 98% of the theoretical density. The obtained pellets were grinded to approximately 0.6 mm thickness and polished to obtain a smooth surface and remove any contaminants.

STF35 paste for painting of the symmetrical electrodes was made from the fabricated STF35 powder mixed with a paste vehicle system ESL403 (Electro-Science Laboratories, USA). Paste consisted of 65 wt% of powder and 35 wt% of the vehicle mixed in a mortar. Circular STF35 electrodes were brush-painted on both sides of the polished CGO pellets. The thickness of the electrodes was 30 μm with a diameter of 7 mm. Painted electrodes were slowly dried at room temperature and at 60 °C and at 130 °C. Finally, electrodes were sintered for 2 h at 900/950/1000/1050 °C in air with an intermediate dwell step at 600 °C for 1 h to remove the binder (with heating rate $1.5^{\circ}\cdot min^{-1}$ to 600 °C and in the following steps heating/cooling rates $2^{\circ}\cdot min^{-1}$). Surface of the sintered electrodes were coated with platinum current collector (about 5 μm thick) by brush painting Pt paste (ESL 5542, Electro-Science Laboratories, USA). Platinum electrodes were fired at 900 °C for 10 min with heating/cooling rate $3^{\circ}\cdot min^{-1}$.

Compositional and microstructural analysis

The phase composition of the investigated STF35 powder was analyzed by X-ray diffractometry (XRD) at room temperature. XRD spectra of the powder was collected using Philips X'Pert Pro MPD diffractometer with Cu K_{α} (1.542 Å) radiation in a standard 2θ Bragg-Brentano geometry. The diffraction patterns were analysed with the Rietveld refinement method using the HighScore Plus software package [43]. The Pseudo – Voigt peak shape function was used during the refinement. Crystallographic structure of STF35 has been drawn using Vesta software package [44].

Cross sectional images of the symmetric cells samples were obtained using a FEI Quanta FEG 250 Scanning Electron Microscope (SEM) with an accelerating voltage of 10 kV in a high vacuum mode. SEM was operated with a backscattered electron (BSE) detector. Chemical composition of samples was determined using the energy-dispersive X-ray (EDX) spectroscopy using the EDAX Genesis APEX 2i with Apollo X SDD spectrometer at 20 kV.

For SEM imaging of the cross sections of symmetrical cells were embedded in the epoxy resin (EpoFix, Struers, Denmark). The epoxy was polished down to 1 μm diamond suspension finish (Struers, Denmark) and rinsed with isopropanol. The surface of polished epoxy was coated with carbon before imaging.

Electrical and electrochemical performance analysis

DC electrical conductivity measurements were performed on STF35 pellets (~12 mm diameter, ~1 mm thick) by the Van der Pauw method. Prior to measurements, surfaces of the STF35 pellets were slightly polished and silver point contacts (DuPont 4922 N, USA) were painted at the edges. The resistance measurements were performed using Keithley 2400 SourceMeter with custom software (working in the potentiostatic mode at 50 mV). Measurement temperature range was between 900 °C and 200 °C. Studies were performed at different oxygen partial pressures (20%, 1% and 0.1%) under humidified (~4 vol%) gas flow rate of 50 ml min^{-1}.

Area Specific Resistance (ASR) of the prepared symmetrical cells was measured by electrochemical impedance spectroscopy (EIS) using Novocontrol Alpha-A with an excitation amplitude of 25 mV in the frequency range of 1 MHz–50 mHz. Firstly, the evaluation of the effects of the sintering temperature on the resulting ASR was carried out. The measurement temperature range was between 800 °C and 500 °C in stationary air. This temperature range is a typical operating temperature of intermediate-temperature SOFCs. Based on the EIS results, a more detailed analysis of the impedance of symmetrical cells with oxygen electrode sintered at 1000 °C were carried out. Measurements were performed in different oxygen partial pressures (20%, 10%, 5%, 1%, 0.1% and 0.01%) in the temperature range 800 °C - 600 °C. For this purpose Solartron 1287/1260 system was used. Applied measurement conditions were the same as in the previous measurement using Novocontrol. EIS data analysis was performed using Elchemea Analytical (www.elchemea.dk, Technical University of Denmark) software [45]. Distribution of Relaxation Times analysis has been performed by using DRTools Matlab GUI [46–48].

Results and discussion

Analysis of $Sr_{0.86}Ti_{0.65}Fe_{0.35}O_{3-\delta}$ powder

The fabricated STF35 powder was analyzed by XRD in order to confirm the formation of the cubic perovskite oxide phase. The XRD pattern of the STF35 powder, measured at room temperature, is shown in Fig. 1 A.

All the diffraction peaks, except a small one at $2\theta = 25.6^{\circ}$ (*), can be identified as strontium titanate, with a cubic crystal structure ($Pm\bar{3}m$) (Inorganic Crystal Structure Database #186710). The small detected peak (at $2\theta = 25.6^{\circ}$) is related to titanium dioxide TiO_2 in the anatase form (tetragonal, *I41/amd* space group), called also as Magnéli phase. The presence of this phase in the structure is strongly related to the non-stoichiometry of strontium (Sr/Ti < 1 in $SrTiO_3$), what was previously reported in the literature [49–51]. This result indicates the presence of strontium vacancies V''_{Sr} in the sample. XRD pattern was subjected to a Rietveld refinement based on the $Pm\bar{3}m$ cubic space group. Calculated average lattice

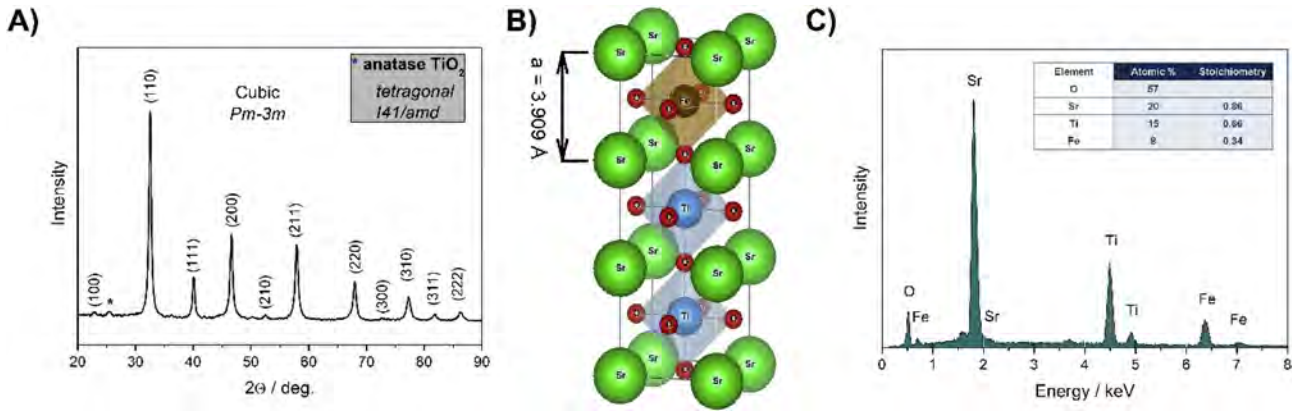

Fig. 1 – X-ray diffractometry of the fabricated powder (A), crystallographic structure of STF35 (B) and energy dispersive x-ray spectra of the sintered pellet used for electrical conductivity study (C).

constant is a = 3.90882(1) Å, with Goodness of Fit parameter (GoF) = 1.37. Crystal structure of STF35 perovskite is shown in Fig. 1 B. Mixed valence Fe cations partially substitute Ti^{4+} ions in the center of oxygen octahedra. For comparison lattice constant of pure $SrFeO_3$ and $SrTiO_3$ is occur a = 3.851 Å and a = 3.905 Å respectively [52,53]. Thus, addition of Fe into $SrTiO_3$ structure caused the lattice should decrease its size. In this work, the obtained lattice parameter slightly deviates from the reported ones and seems to be higher. The observed higher value of average lattice constant than reported for a pure and undoped $SrTiO_3$ is probably caused by appearance of strontium vacancies V''_{Sr} in the structure.

Chemical composition of the bulk STF35 pellet is presented in Fig. 1 C. EDX analysis shows the elements present (Sr, Fe, Ti and O). The averaged atomic percentage of the sintered STF35 pellet is 20% Sr, 15% Ti, 8% Fe and 57% O. Ratio of atoms in the B sublattice (Fe and Ti) is in good agreement with the calculation for STF35. Detected deficiency of Sr atoms in the A sublattice is 0.86. It does not seem to have an effect on the structure, as the perovskite cubic phase is preserved.

The effects of nonstoichiometry on the A-site in the STF35 structure were studied by group of Kharton [54–56]. By using Sr deficient materials, their physicochemical properties seem to be improved: tolerance to CO_2, increased oxygen non-stoichiometry and ionic conductivity with no loss of electronic conductivity. Kharton et al. [55] have shown that the total conductivity of $SrTi_{0.2}Fe_{0.8}O_{3-\delta}$ (STF80) practically does not depend on the presence of a Sr vacancy in the A site between 800 °C and 600 °C. The detected non-stoichiometry of the compound can potentially be responsible for the unit cell size different than reported previously for the stoichiometric compounds, as also noticed by Kharton et al. [55].

The non-stoichiometry on the A-site is an interesting feature in the case of its influence on the oxygen reduction reaction, thus the causes and possible effects of Sr deficiency will be studied separately in our future works.

Electrical conductivity measurements

Electrical conductivity measurement results of sintered pellets are presented in Fig. 2 as a function of temperature (from 900 °C to 200 °C) and in different of pO_2. The conductivity of STF35 decreases with decreasing the oxygen partial pressure, similarly with previous reports [57,58] and the expected p-type conductivity. The highest conductivity (0.59 S cm^{-1}) was obtained at 900 °C in 20% O_2 and is comparable with literature (~1 S cm^{-1}) [18]. As expected, the conductivity is only slightly dependent on temperature between 900 °C and 700 °C. The calculated activation energy (E_a) for this temperature range is 8 kJ mol^{-1}. Below 700 °C, the total conductivity decreases with decreasing temperature and activation energy increases considerably (E_a = 38.5 kJ mol^{-1}) which probably is connected with localization of atomic levels and bandwidth changes [54]. Steinsvik et al. [59] and Rothschild et al. [21] have extensively studied electrical and defect properties of $SrTi_{1-x}Fe_xO_{3-d}$. The electrical conductivity behavior is a complex interplay between the acceptor role of the iron substitution causing a decrease of the band gap and decreased activation energy for oxygen vacancy migration. Interestingly, the electronic transport seems to have a band-like behavior, with decreasing mobilities at high temperatures, rather than the small polaron transport model.

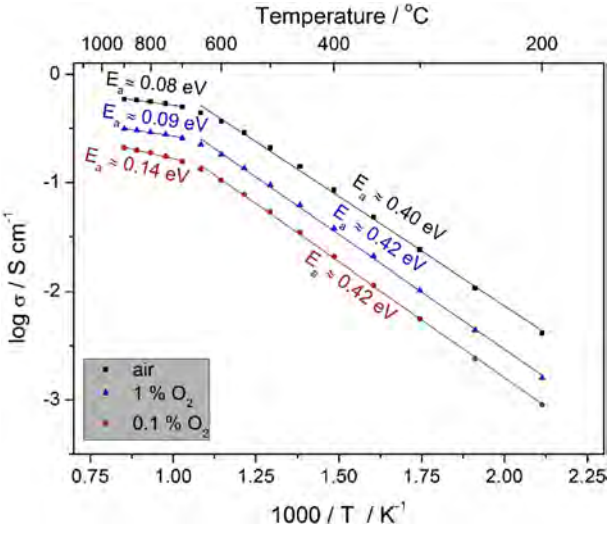

Fig. 2 – Electrical conductivity plots of sintered STF35 pellet in 21%, 1% and 0.1% O_2.

Electrochemical characterization of symmetrical cells

Effects of the electrode sintering temperature on the electrochemical performance were evaluated by impedance spectroscopy of symmetrical electrode samples. Measurements were carried out in air in the temperature range 800 °C-500 °C which is typical for operating temperature of intermediate-temperature SOFCs. Spectra measured at 800 °C are presented in Fig. 3. The lowest sintering temperature (900 °C) resulted in the highest ohmic resistance. Increasing sintering temperature leads to lowering of the ohmic resistance. Interestingly, the polarization resistance seems unaffected by the sintering temperature (R_{pol} ~100 mΩ cm^2). For the sintering temperature of 1050 °C severe cracking of the electrode occurred, caused by electrode shrinkage due to sintering. ASR value is comparable with literature reports for STF with higher amount of Fe (0.85) which seems appealing [60].

Temperature dependence of the ohmic contribution of differently sintered samples is shown in Fig. 4 A. Electrodes with different sintering temperature show different conductivity values (for fixed temperature), as was the case at 800 °C, but have similar activation energy ~65 kJ mol^{-1}. For the sintering temperature of 1000 °C, at 800 °C a resistance of 0.65 Ω cm^2 was obtained and at 500 °C a resistance of 10 Ω cm^2 was measured. Activation energy and the level of resistance are in line with the values reported for doped ceria compounds [61]. Ohmic contribution can be thus ascribed to the series connection of the resistance of the ceria pellet and the resistance of the porous electrode, through which the current is flowing.

Polarization resistance of the STF35 electrode plotted as a function of temperature is shown in Fig. 4 B. Polarization resistance is very similar for all sintering temperatures at all studied temperatures. The activation energy of the polarization resistance is ~136 kJ mol^{-1}. It is much higher than the activation polarization of the electrical conductivity of the bulk material. The obtained value is typical for oxygen electrodes [35,62,63].

Post-mortem SEM

Post-mortem SEM images of cross section of symmetric cells with STF35 electrodes measured by EIS method are presented in Fig. 5 A-C. Representative images of electrodes sintered at 950 °C, 1000 °C and 1050 °C are included for comparison. There is no visible difference in the microstructures of the porous-part

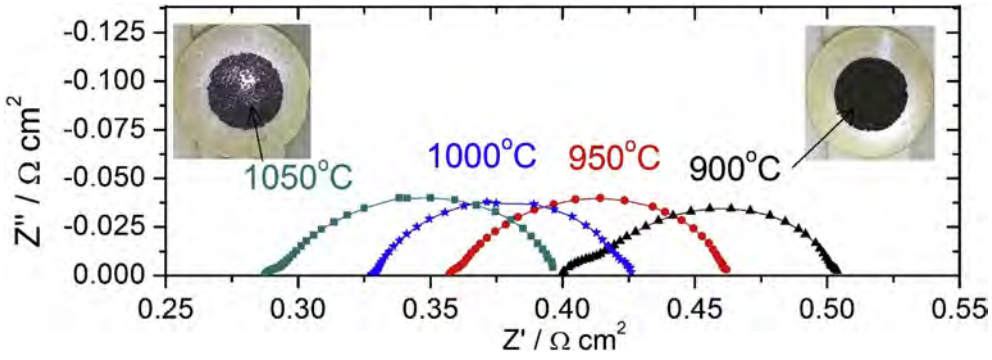

Fig. 3 – Impedance spectra of symmetrical STF35 electrodes sintered at different temperatures measured at 800 °C in air.

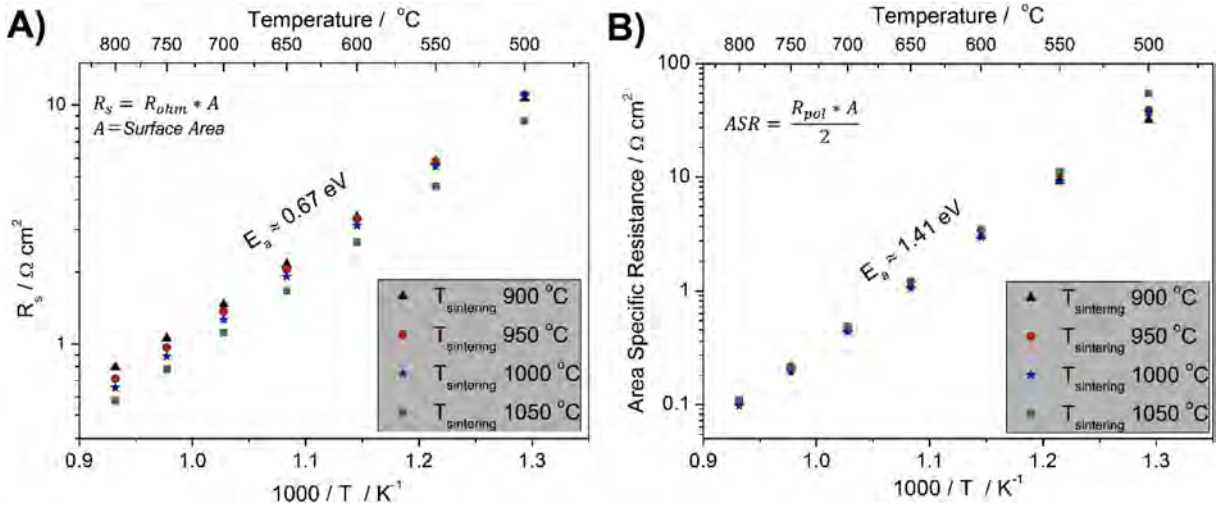

Fig. 4 – Series (A) and polarization (B) resistance of the symmetrical STF35 electrodes sintered at different temperatures as a function of temperature in air.

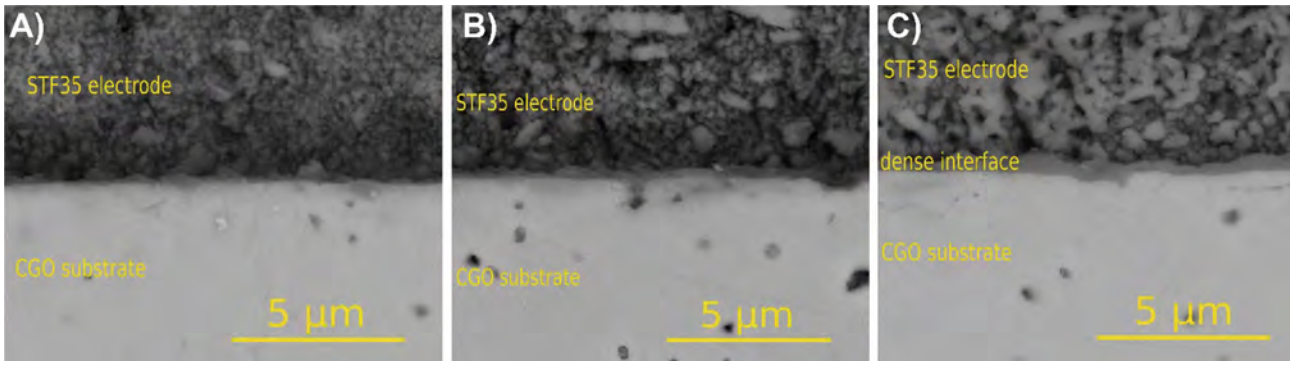

Fig. 5 – SEM images of cross sections of porous STF35 electrodes sintered at 950 °C (A), 1000 °C (B) and 1050 °C (C).

of the STF35 electrode sintered at different temperatures. However the CGO-STF35 interface appears to be considerably influenced by the sintering temperature. A dense interface layer with thickness ~500 nm is formed for electrodes sintered >1000 °C. This layer improves the electrical contact as the ohmic resistance was decreased for these samples (visible in Fig. 3). EDX analysis of the chemical composition (not shown here) of the interface layer did not show any segregation of elements, its chemical composition is similar to the chemical composition of the porous electrode. As we have previously reported, there is no negative reaction (phase forming) between STF35 and CGO [64], thus the interface layer is not expected to negatively influence the electrochemical performance of the porous electrode. As shown in Fig. 3, shrinkage caused by sintering of the electrode above 1000 °C leads to its visible cracking, prohibiting from practical use in real cells. Good electrochemical response of the cracked electrode might be partially due to platinum current collector coverage, filling the cracks and the dense interfacial layer, facilitating oxygen reduction/oxidation reaction at the interface.

Oxygen reduction mechanism

In order to describe electrode properties in more details, a thorough electrochemical evaluation of the electrode sintered at 1000 °C was performed. In order to describe the possible governing physico-chemical processes, measurements were carried out in atmospheres with different oxygen content (20%, 10%, 5%, 1%, 0.1%, 0.01%) in the temperature range 800 °C-600 °C.

Studying electrode resistances as a function of the gas oxygen content can be a powerful tool for determining possible electrode mechanisms. As has been described in the literature [65,66], chemical and electrochemical processes can be distinguished based on their dependency on the pO_2. By plotting polarization resistance contributions as a function of pO_2 in a log-log plot, the slope "n" will be representative for the possible mechanism ($1/R \sim (pO_2)^n$). For n = 1, gas diffusion of molecular oxygen process is expected, n = 0.5 implies the contribution of atomic oxygen. For n = 0.25 a charge transfer/adsorption process is the likely contribution. Thus by careful examination of the impedance data, differentiation between the occurring processes can be made.

For description of the obtained results, first a physically sound equivalent circuit had to be determined. By examination of the spectra it was assumed that it consisted of at least 3 resistive-capacitive elements. For validation of the assumption, a distribution of relaxation times method was used. All measured spectra were analyzed with DRTools script. In Fig. 6 selected, representative DRT spectra are shown. Fig. 6 A

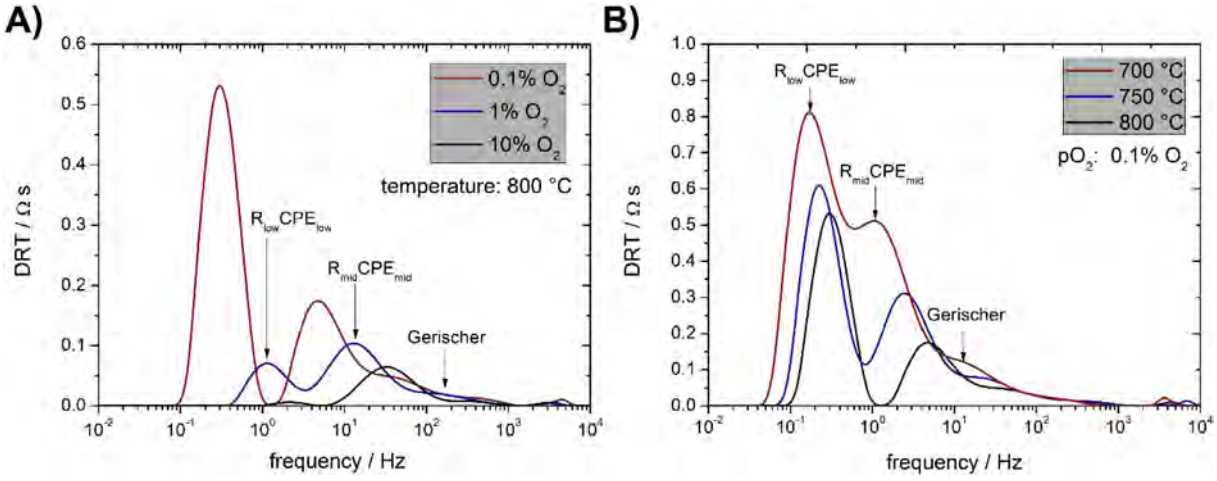

Fig. 6 – Exemplary distribution of relaxation times plots of impedance of a symmetrical STF35 electrodes as a function of the oxygen partial pressure at 800 °C (A) and as a function of temperature at 0.1% O_2 (B).

shows oxygen content dependence of DRT spectra at 800 °C. At lowering of pO_2 a new contribution at low frequency clearly occurs. At mid-frequency pO_2 dependent element is also visible. At high frequencies a relatively smaller contribution can be found. It seems to have a non-symmetrical shape, typically ascribed to Gerischer type elements [67]. Fig. 6 B presents temperature dependence of DRT spectra obtained at 0.1% oxygen content, so that the low frequency contribution is visible. Low- and mid-frequency contributions are clearly present, with a possible Gerischer type element at high frequency (visible at 700 °C). Based on careful DRT analysis at different conditions, an equivalent circuit consisting of R_s-G-($R_{mid}CPE_{mid}$)-($R_{low}CPE_{low}$) was proposed (R_s – series resistance, G – Gerischer element, CPE – Constant Phase Element). At 700 °C in 0.1% O_2 the characteristic frequencies (contributions peak – frequency at highest Z" values) of the contributions are ~17 Hz, ~1 Hz and ~0.2 Hz, as also visible in DRT plots. The obtained fitting had very high quality. Representative impedance spectra (measured at 700 °C and 800 °C at 0.1% oxygen) are shown in Fig. 7 together with the results of the fitting. It should be noted, that also other possible equivalent circuits were initially analyzed and evaluated, e.g. a triple (RCPE) connection, it resulted in visibly worse fitting and higher chi-squared values. For the proposed equivalent circuit chi-squared parameter was mostly $<10^{-5}$, representing a good fit. For some measurement conditions, the contributions became negligibly small, so the parameters were either locked or removed from the analysis. The same equivalent circuit as presented here has been also used by the group of Boukamp [68,69] for analysis of LSCF electrodes. The series resistance typically can be ascribed to the ohmic resistance of the electrolyte substrate, Gerischer element to some surface/solid state diffusion limited phenomena and the two R-CPE elements to possible other phenomena, including for example adsorption, gas diffusion and others, to be determined from detailed impedance measurements.

Based on the measured spectra (as a function of temperature and pO_2) and the selected equivalent circuit, all data was fitted and the results are presented in the following figures. Moreover, all values of the equivalent circuit elements for measurement at 700 °C at different oxygen partial pressures are given in Table 1.

Fig. 8 presents the dependence of the series resistance on the oxygen partial pressure. Temperature dependence was presented in Fig. 4A. Only slight dependence of the resistance on pO_2 is visible, as expected for the ohmic contribution. Electrical conductivity of STF35 depends on the pO_2, thus atmosphere changes will also influence the ohmic contribution of the porous electrodes. Lowering the pO_2 results in increased resistance, in line with the electrical conductivity results presented in Fig. 2.

Dependencies of the Gerischer element on temperature and oxygen content are presented in Fig. 9 A-D. The rate constant parameter "k" is strongly dependent on the temperature with activation energy ~1.55 eV, whereas the admittance parameter "Y" shows only a slight dependence on the temperature (activation energies around ~0.07 eV). In the case of oxygen partial pressure dependence, rate constant parameter increases with an increase of the oxygen content with a ~1/6 slope, whereas the admittance parameter seems not dependent on the oxygen partial pressure. The magnitude of the Gerischer element resistance is roughly ~15 mΩ cm^2 at 800 °C, and it is independent of the oxygen partial pressure. Gerischer type elements are often used in modelling of porous SOFC electrodes – the popular Adler model is based on this element [70,71], often used for modelling of LSCF electrodes. In case of the limiting electrode processes being the chemical surface exchange and/or solid state oxygen diffusion in the bulk, it will be represented as a Gerischer element in the impedance spectra. Hildenbrand and Boukamp used a similar equivalent circuit for description of porous LSCF electrodes [68,69].

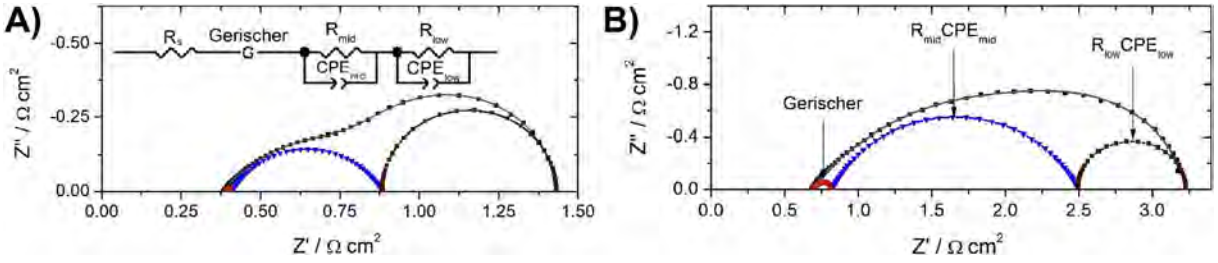

Fig. 7 – Exemplary impedance spectra of a symmetrical STF35 electrode measured at 800 °C (A) and 700 °C (B) in 0.1% O_2 shown with an equivalent circuit and individual contributions of the respective fitting elements.

Table 1 – Calculated parameters for 700 °C in different oxygen partial pressures.

	R_s (Ω cm^2)	Gerischer k parameter (s^{-1})	Gerischer Y parameter (S $s^{0.5}$)	R_{mid} (Ω cm^2)	Equivalent C_{mid} (F cm^{-2})	R_{low} (Ω cm^2)	Equivalent C_{low} (F cm^{-2})
20% O_2	0.59	147.7	1.37	0.37	0.055	0.0055	6.86
10% O_2	0.60	116.7	1.20	0.43	0.061	0.0100	5.26
5% O_2	0.60	103.1	1.09	0.51	0.066	0.0170	3.92
1% O_2	0.63	62.9	0.89	0.92	0.088	0.0750	2.71
0.1% O_2	0.69	59.2	0.89	1.67	0.106	0.7381	1.33
0.01% O_2	0.76	40.2	1.28	3.39	0.165	4.9330	1.00

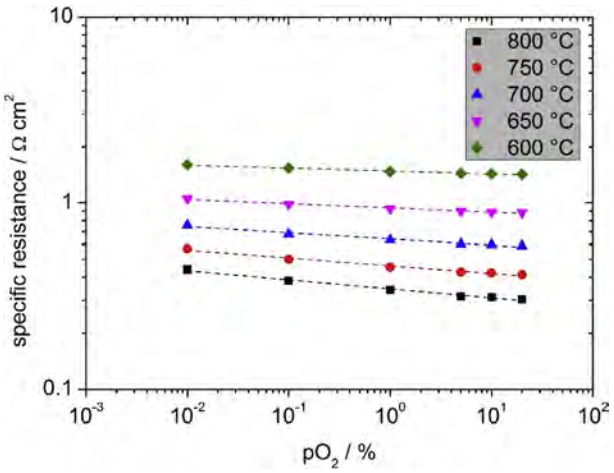

Fig. 8 – pO_2 and temperature dependence of series resistance of symmetrical STF35 electrodes on CGO substrate.

Following the Gerischer element are the two R-CPE elements. The dependencies of their resistance on temperature and oxygen gas content are presented in Fig. 10. Medium frequency resistance is a thermally activated process with E_A~1.45 eV with oxygen dependence of ~0.3. According to theoretical considerations, such pO_2 dependence happens possibly due to adsorption of oxygen and surface exchange (dependence of 0.25). In the case of dissociative adsorption (involvement of atomic oxygen), the expected oxygen dependence is ~0.5. Therefore it seems that the non-dissociative adsorption of oxygen contributes the most to the polarization resistance of the STF35 electrode. At 800 °C in 20% oxygen the resistance of the medium frequency contribution is ~80 mΩ cm^2, which is ~80% of the total polarization resistance at this temperature. Adsorption might be limited by different factors, e.g. slow removal of adsorbed oxygen atoms from the surface caused by slow incorporation into the lattice. Activation energy of the Gerischer rate constant parameter is close to the measured activation energy of the medium frequency contribution, so both elements seem connected together, the rate limiting adsorption determines the bulk diffusion. Equivalent capacitance of this contribution is presented in Fig. 11. With increasing pO_2, capacitance decreases, measured values are between 50 and 100 mF cm^{-2}. Similar capacitances of the medium frequency contributions have been measured by Hildenbrand et al. [69] and Dailly et al. [72]. Values in the range of ~mF cm^{-2} appear typical for adsorption processes [40,73]. Argirusis et al. have measured oxygen incorporation

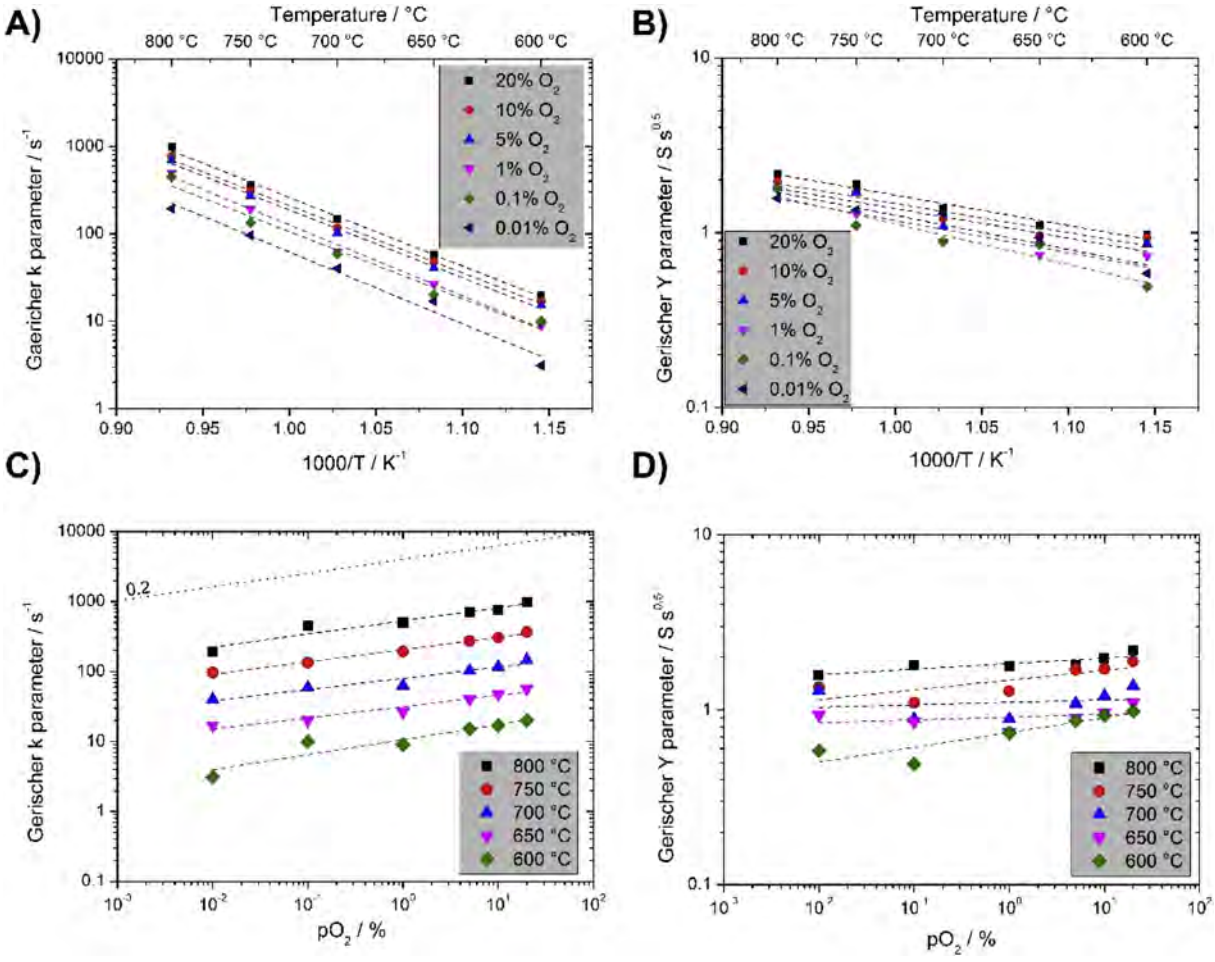

Fig. 9 – Plots of the calculated rate constant k and admittance Y parameters of the high frequency Gerischer element as a function of temperature (A and B respectively for k and Y parameters) and pO2 (C and D respectively for k and Y parameters).

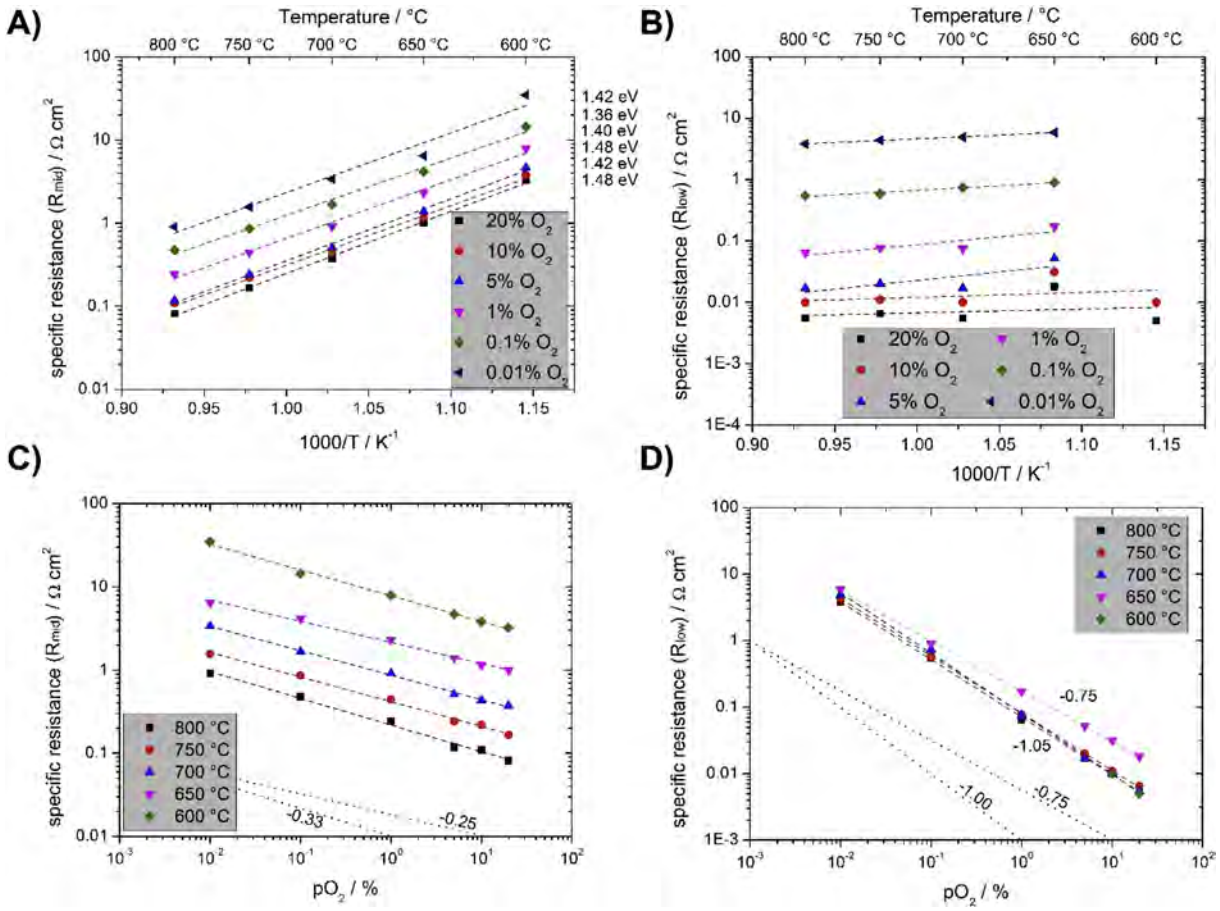

Fig. 10 – Plots of the calculated resistances of the medium and low frequency contributions as a function of temperature (A and B respectively for R_{mid} and R_{low}) and pO2 (C and D respectively for R_{mid} and R_{low}).

and diffusion in STF35 ceramics [22]. They described that at temperatures <750 °C oxygen surface transfer becomes slow. The activation energy of the oxygen surface exchange coefficient k* was determined to be ~1.66 eV, whereas the activation energy of the diffusion coefficient D* was ~0.92 eV. The activation energy of the medium frequency contribution found in this work is thus quite similar to the surface exchange activation energy.

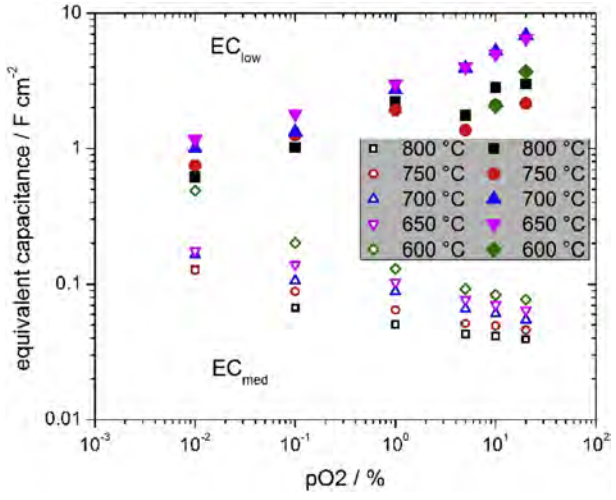

Fig. 11 – Plots of the calculated equivalent capacitances of the medium (open symbols) and low (closed symbols) frequency contributions at different temperatures as a function of the pO_2.

The low frequency R-CPE contribution does not show temperature dependence and shows strong oxygen partial pressure dependence, $1/R \sim pO_2$. These characteristics and measured values are typical for gas diffusion resistance in porous electrodes. This is further evidenced by very high chemical capacitance, as shown in Fig. 11, from 0.4 F cm^{-2} to ~8 F cm^{-2}, similarly to values reported by Hildenbrand [69] and Santos-Gomez et al. [74]. Gas diffusion contribution constitute only a very small contribution to total polarization resistance, R~10 mΩ cm^2 at 800 °C in 20% O_2. If required, gas diffusion resistance can be further minimized by modification of electrode microstructure.

The equivalent circuit presented in Fig. 7 appears to represent all data very well. Physicochemical description of all components seems well justified and comparable with the available literature data. Hypothetically, if the adsorption would be very fast, with only a negligible contribution, and not including gas diffusion resistance, the polarization resistance of the porous STF35 electrode would be only ~15 mΩ cm^2 at 800 °C in 20% O_2, which can be considered very low, similar to polarization resistance of LSCF.

Fig. 12 presents the possible oxygen reduction pathways and rate limiting reactions, as has been determined in this study.

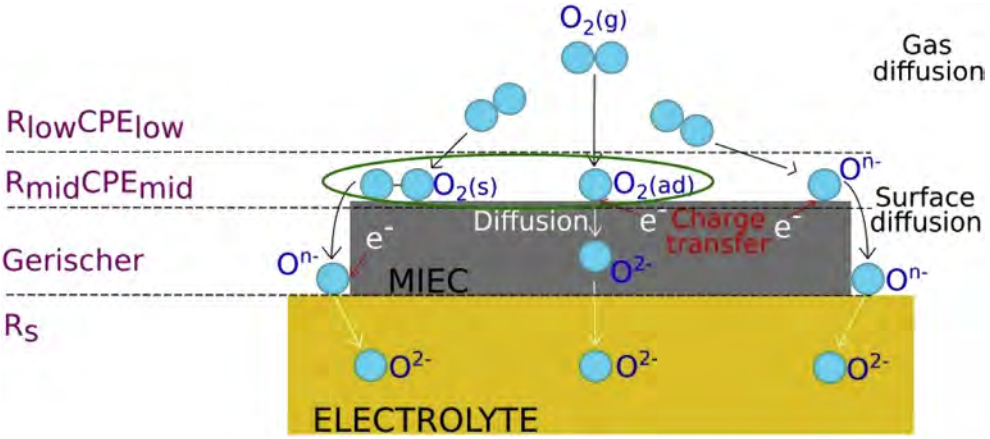

Fig. 12 – Schematic pathways for oxygen reduction reaction.

Performance of porous STF35 electrodes is limited by adsorption of oxygen species, possibly hindered by slow incorporation of oxygen into the lattice. Rate determining reactions are marked with a green circle. Same limiting mechanisms have been determined for STF35 model dense electrodes [18,22]. Future studies will therefore be directed towards use of surface catalysts and studies of their effect on adsorption and surface exchange of the STF35, which has already shown some remarkable possibilities [22]. STF35 electrode, with its clearly defined adsorption limitation seems a very good material to determine possible role of surface modifications/catalysts.

Conclusions

STF35 mixed ionic-electronic conductor perovskite has been fabricated and evaluated for its high temperature electrochemical properties as possible oxygen electrode in solid oxide cells. Studies were performed on symmetrical porous STF35 electrodes, whereas the studies performed so far were focused mainly on dense model electrodes. Detailed impedance spectroscopy study, performed at different temperatures and at different oxygen partial pressures revealed that the performance of the electrode is limited by oxygen adsorption, as has been previously reported for dense STF35 films. Results show that with the use of advanced analysis and appropriate measurement conditions, it is possible to use porous electrodes to study basic physico-chemical properties of materials, typically performed on dense materials fabricated by more advanced processes. It has been shown, that bulk properties of the STF materials are comparable to the state of the art LSCF cathodes. Other processes that were recognized by impedance analysis include a Gerisher type element, possibly connected to gas adsorption and solid state diffusion and gas diffusion resistance. STF35 is a very interesting model material to measure the oxygen reduction processes and its limiting factors.

Acknowledgements

This work was partly supported by project funded by National Science Centre Poland based on decision 2017/25/B/ST8/02275.

This work is partly supported by a statutory grant for research from the Gdańsk University of Technology.

REFERENCES

[1] da Silva FS, de Souza TM. Novel materials for solid oxide fuel cell technologies: A literature review. Int J Hydrogen Energy 2017;42:26020–36. https://doi.org/10.1016/j.ijhydene.2017.08.105.

[2] Goodenough JB, Huang Y-H. Alternative anode materials for solid oxide fuel cells. J Power Sources 2007;173:1–10. https://doi.org/10.1016/j.jpowsour.2007.08.011.

[3] Tian Y, Li J, Liu Y, Yang J, Liu B, Jia L, et al. Preparation and properties of PrBa0.5Sr0.5Co1.5Fe0.5O5+Δas novel oxygen electrode for reversible solid oxide electrochemical cell. Int J Hydrogen Energy 2018;43:12603–9. https://doi.org/10.1016/j.ijhydene.2018.03.187.

[4] Sarno C, Luisetto I, Zurlo F, Licoccia S, Di Bartolomeo E. Lanthanum chromite based composite anodes for dry reforming of methane. Int J Hydrogen Energy 2018;43:14742–50. https://doi.org/10.1016/j.ijhydene.2018.06.021.

[5] Bochentyn B, Karczewski J, Molin S, Klimczuk T, Gazda M, Jasinski P, et al. The comparison of SrTi 0.98Nb 0.02O 3-δ-CeO 2 and SrTi 0.98Nb 0.02O 3-δ-YSZ composites for use in SOFC anodes. J Electroceram 2012;28. https://doi.org/10.1007/s10832-012-9693-8.

[6] Barfod R, Mogensen M, Klemenso T, Hagen A, Liu Y-L, Vang Hendriksen P. Detailed Characterization of Anode-Supported SOFCs by Impedance Spectroscopy. J Electrochem Soc 2007;154:B371. https://doi.org/10.1149/1.2433311.

[7] Hagen A, Liu YL, Barfod R, Hendriksen PV. Assessment of the Cathode Contribution to the Degradation of Anode-Supported Solid Oxide Fuel Cells. J Electrochem Soc 2008;155:B1047. https://doi.org/10.1149/1.2960938.

[8] Niemczyk A, Olszewska A, Du Z, Zhang Z, Świerczek K, Zhao H. Assessment of layered La2-x(Sr,Ba)xCuO4-δoxides as potential cathode materials for SOFCs. Int J Hydrogen Energy 2018;43:15492–504. https://doi.org/10.1016/j.ijhydene.2018.06.119.

[9] Molenda J, Kupecki J, Baron R, Blesznowski M, Brus G, Brylewski T, et al. Status report on high temperature fuel cells in Poland – Recent advances and achievements. Int J Hydrogen Energy 2017;42:4366–403. https://doi.org/10.1016/j.ijhydene.2016.12.087.

[10] Zhang Y, Knibbe R, Sunarso J, Zhong Y, Zhou W, Shao Z, et al. Recent Progress on Advanced Materials for Solid-Oxide Fuel Cells Operating Below 500 °C. Adv Mater 2017. https://doi.org/10.1002/adma.201700132. 1700132:1700132.
[11] Sunarso J, Hashim SS, Zhu N, Zhou W. Perovskite oxides applications in high temperature oxygen separation, solid oxide fuel cell and membrane reactor: A review. Prog Energy Combust Sci 2017;61:57–77. https://doi.org/10.1016/j.pecs.2017.03.003.
[12] Gazda M, Jasinski P, Kusz B, Bochentyn B, Gdula-Kasica K, Lendze T, et al. Perovskites in solid oxide fuel cells, vol. 183; 2012. https://doi.org/10.4028/www.scientific.net/SSP.183.65.
[13] Weber A, Ivers-Tiffée E. Materials and concepts for solid oxide fuel cells (SOFCs) in stationary and mobile applications. J Power Sources 2004;127:273–83. https://doi.org/10.1016/j.jpowsour.2003.09.024.
[14] Haile SM. Fuel cell materials and components. Acta Mater 2003;51:5981–6000. https://doi.org/10.1016/j.actamat.2003.08.004.
[15] Bochentyn B, Karczewski J, Miruszewski T, Krupa A, Gazda M, Jasinski P, et al. Donor-substituted SrTi1 + xO3 - δanodes for SOFC. Solid State Ionics 2012;225:118–23. https://doi.org/10.1016/j.ssi.2012.05.015.
[16] Sarin N, Mishra M, Gupta G, Parkin IP, Luthra V. Elucidating iron doping induced n- to p- characteristics of Strontium titanate based ethanol sensors. Curr Appl Phys 2018;18:246–53. https://doi.org/10.1016/j.cap.2017.11.007.
[17] Litzelman SJ, Rothschild A, Tuller HL. The electrical properties and stability of SrTi0.65Fe0.35O3−δ thin films for automotive oxygen sensor applications. Sensor Actuator B Chem 2005;108:231–7. https://doi.org/10.1016/j.snb.2004.10.040.
[18] Jung W, Tuller HL. Investigation of Cathode Behavior of Model Thin-Film SrTi[sub 1 - x]Fe[sub x]O[sub 3 - delta] (x = 0.35 and 0.5) Mixed Ionic-Electronic Conducting Electrodes. J Electrochem Soc 2008;155:B1194–201. https://doi.org/10.1149/1.2976212.
[19] Jung W, Tuller HL. Impedance study of SrTi(1-x)Fe(x)O(3-delta) (x=0.05 to 0.80) mixed ionic-electronic conducting model cathode. Solid State Ionics 2009;180:843–7. https://doi.org/10.1016/j.ssi.2009.02.008.
[20] Perry NH, Kim JJ, Tuller HL. Oxygen surface exchange kinetics measurement by simultaneous optical transmission relaxation and impedance spectroscopy: Sr(Ti,Fe)O $_{3-x}$ thin film case study. Sci Technol Adv Mater 2018;19:130–41. https://doi.org/10.1080/14686996.2018.1430448.
[21] Rothschild A, Menesklou W, Tuller HL, Ivers-Tiffée E. Electronic structure, defect chemistry, and transport properties of SrTi 1-xFe xO 3-y solid solutions. Chem Mater 2006;18:3651–9. https://doi.org/10.1021/cm052803x.
[22] Argirusis C, Jomard F, Wagner SF, Menesklou W, Ivers-Tiffée E. Study of the oxygen incorporation and diffusion in Sr(Ti 0.65Fe0.35)O3 ceramics. Solid State Ionics 2011;192:9–11. https://doi.org/10.1016/j.ssi.2010.02.016.
[23] Song J-L, Guo X. SrTi0.65Fe0.35O3 nanofibers for oxygen sensing. Solid State Ionics 2015;278:26–31. https://doi.org/10.1016/j.ssi.2015.05.009.
[24] Li HY, Yang H, Guo X. Oxygen sensors based on SrTi0.65Fe0.35O3-δthick film with MgO diffusion barrier for automotive emission control. Sensor Actuator B Chem 2015;213:102–10. https://doi.org/10.1016/j.snb.2015.02.079.
[25] Nenning A, Volgger L, Miller E, Mogni LV, Barnett S, Fleig J. The Electrochemical Properties of Sr(Ti,Fe)O $_{3-\delta}$ for Anodes in Solid Oxide Fuel Cells. J Electrochem Soc 2017;164:F364–71. https://doi.org/10.1149/2.1271704jes.
[26] Oliveira Silva R, Malzbender J, Schulze-Küppers F, Baumann S, Guillon O. Mechanical properties and lifetime predictions of dense SrTi1-xFexO3-δ(x = 0.25, 0.35, 0.5). J Eur Ceram Soc 2017;37:2629–36. https://doi.org/10.1016/j.jeurceramsoc.2017.02.038.
[27] Oliveira Silva R, Malzbender J, Schulze-Küppers F, Baumann S, Krüger M, Guillon O. Microstructure and anisotropic mechanical properties of freeze dried SrTi 0.75 Fe 0.25 O 3-δ for oxygen transport membrane substrates. J Eur Ceram Soc 2018;38:2774–83. https://doi.org/10.1016/j.jeurceramsoc.2018.02.014.
[28] Liu Y, Baumann S, Schulze-Küppers F, Mueller DN, Guillon O. Co and Fe co-doping influence on functional properties of SrTiO3for use as oxygen transport membranes. J Eur Ceram Soc 2018;38:5058–66. https://doi.org/10.1016/j.jeurceramsoc.2018.07.037.
[29] Baharuddin NA, Muchtar A, Somalu MR. Short review on cobalt-free cathodes for solid oxide fuel cells. Int J Hydrogen Energy 2017;42:9149–55. https://doi.org/10.1016/j.ijhydene.2016.04.097.
[30] Liu H, Zhu K, Liu Y, Li W, Cai L, Zhu X, et al. Structure and electrochemical properties of cobalt-free perovskite cathode materials for intermediate-temperature solid oxide fuel cells. Electrochim Acta 2018;279:224–30. https://doi.org/10.1016/j.electacta.2018.05.086.
[31] Rothschild A, Litzelman SJ, Tuller HL, Menesklou W, Schneider T, Ivers-Tiffée E. Temperature-independent resistive oxygen sensors based on SrTi1-xFexO3-δsolid solutions. Sensor Actuator B Chem 2005;108:223–30. https://doi.org/10.1016/j.snb.2004.09.044.
[32] Jung W, Tuller HL. Investigation of surface Sr segregation in model thin film solid oxide fuel cell perovskite electrodes. Energy Environ Sci 2012;5:5370–8. https://doi.org/10.1039/C1EE02762J.
[33] Jung W, Tuller HL. A New Model Describing Solid Oxide Fuel Cell Cathode Kinetics: Model Thin Film SrTi1-xFexO3-δ Mixed Conducting Oxides–a Case Study. Adv Energy Mater 2011;1:1184–91. https://doi.org/10.1002/aenm.201100164.
[34] Yoo C-Y, Bouwmeester HJM. Oxygen surface exchange kinetics of SrTi1−xFexO3−δ mixed conducting oxides. Phys Chem Chem Phys 2012;14:11759. https://doi.org/10.1039/c2cp41923h.
[35] Molin S, Lewandowska-Iwaniak W, Kusz B, Gazda M, Jasinski P. Structural and electrical properties of Sr(Ti, Fe)$O_{3-\delta}$ materials for SOFC cathodes. J Electroceram 2012;28:80–7. https://doi.org/10.1007/s10832-012-9683-x.
[36] Jordan N, Assenmacher W, Uhlenbruck S, Haanappel VAC, Buchkremer HP, Stöver D, et al. Ce0.8Gd0.2O2 − δ protecting layers manufactured by physical vapor deposition for IT-SOFC. Solid State Ionics 2008;179:919–23. https://doi.org/10.1016/j.ssi.2007.12.008.
[37] Wang F, Nishi M, Brito ME, Kishimoto H, Yamaji K, Yokokawa H, et al. Sr and Zr diffusion in LSCF/10GDC/8YSZ triplets for solid oxide fuel cells (SOFCs). J Power Sources 2014;258:281–9. https://doi.org/10.1016/j.jpowsour.2014.02.046.
[38] Szymczewska D, Karczewski J, Chrzan A, Jasinski P. CGO as a barrier layer between LSCF electrodes and YSZ electrolyte fabricated by spray pyrolysis for solid oxide fuel cells. Solid State Ionics 2017;302:113–7. https://doi.org/10.1016/j.ssi.2016.11.008.
[39] Li Y, Gemmen R, Liu X. Oxygen reduction and transportation mechanisms in solid oxide fuel cell cathodes. J Power Sources 2010;195:3345–58. https://doi.org/10.1016/j.jpowsour.2009.12.062.
[40] Baumann FS, Fleig J, Cristiani G, Stuhlhofer B, Habermeier H-U, Maier J. Quantitative Comparison of Mixed Conducting SOFC Cathode Materials by Means of Thin Film Model Electrodes. J Electrochem Soc 2007;154:B931. https://doi.org/10.1149/1.2752974.
[41] Metlenko V, Jung W, Bishop SR, Tuller HL, De Souza RA. Oxygen diffusion and surface exchange in the mixed

conducting oxides SrTi $_{1-y}$ Fe $_{y}$ O $_{3-\delta}$. Phys Chem Chem Phys 2016;18:29495–505. https://doi.org/10.1039/C6CP05756J.
[42] Perry NH, Harrington GF, Tuller HL. Electrochemical ionic interfaces. Elsevier Inc.; 2018. https://doi.org/10.1016/B978-0-12-811166-6.00004-2.
[43] Degen T, Sadki M, Bron E, König U, Nénert G. The high score suite. Powder Diffr 2014;29:S13–8. https://doi.org/10.1017/S0885715614000840.
[44] Momma K, Izumi F. VESTA 3 for three-dimensional visualization of crystal, volumetric and morphology data. J Appl Crystallogr 2011;44:1272–6. https://doi.org/10.1107/S0021889811038970.
[45] Koch S, Graves C, Hansen KV. Elchemea Analytical (Open source free software) http://www.elchemea.dk/n.d.
[46] Ciucci F, Chen C. Analysis of Electrochemical Impedance Spectroscopy Data Using the Distribution of Relaxation Times: A Bayesian and Hierarchical Bayesian Approach. Electrochim Acta 2015;167:439–54. https://doi.org/10.1016/j.electacta.2015.03.123.
[47] Saccoccio M, Wan TH, Chen C, Ciucci F. Optimal regularization in distribution of relaxation times applied to electrochemical impedance spectroscopy: Ridge and Lasso regression methods - A theoretical and experimental Study. Electrochim Acta 2014;147:470–82. https://doi.org/10.1016/j.electacta.2014.09.058.
[48] Wan TH, Saccoccio M, Chen C, Ciucci F. Influence of the Discretization Methods on the Distribution of Relaxation Times Deconvolution: Implementing Radial Basis Functions with DRTtools. Electrochim Acta 2015;184:483–99. https://doi.org/10.1016/j.electacta.2015.09.097.
[49] Bäurer M, Kungl H, Hoffmann MJ. Influence of sr/ti stoichiometry on the densification behavior of strontium titanate. J Am Ceram Soc 2009;92:601–6. https://doi.org/10.1111/j.1551-2916.2008.02920.x.
[50] Horikiri F, Iizawa N, Han LQ, Sato K, Yashiro K, Kawada T, et al. Defect equilibrium and electron transport in the bulk of single crystal SrTi1 - xNbxO3(x = 0.01, 0.001, 0.0002). Solid State Ionics 2008;179:2335–44. https://doi.org/10.1016/j.ssi.2008.10.001.
[51] Horikiri F, Han L, Iizawa N, Sato K, Yashiro K, Kawada T, et al. Electrical Properties of Nb-Doped SrTiO[sub 3] Ceramics with Excess TiO[sub 2] for SOFC Anodes and Interconnects. J Electrochem Soc 2008;155:B16. https://doi.org/10.1149/1.2799733.
[52] Acharya SK, Nallagatla RV, Togibasa O, Lee BW, Liu C, Jung CU, et al. Epitaxial Brownmillerite Oxide Thin Films for Reliable Switching Memory. ACS Appl Mater Interfaces 2016;8:7902–11. https://doi.org/10.1021/acsami.6b00647.
[53] Lytle FW. X-ray diffractometry of low-temperature phase transformations in strontium titanate. J Appl Phys 1964;35:2212–5. https://doi.org/10.1063/1.1702820.
[54] Kharton VV, Kovalevsky AV, Viskup AP, Jurado JR, Figueiredo FM, Naumovich EN, et al. Transport properties and thermal expansion of Sr0.97Ti1-xFexO3-δ(x = 0.2-0.8). J Solid State Chem 2001;156:437–44. https://doi.org/10.1006/jssc.2000.9019.
[55] Kharton VV, Kovalevsky AV, Tsipis EV, Viskup AP, Naumovich EN, Jurado JR, et al. Mixed conductivity and stability of A-site-deficient Sr(Fe,Ti)O 3-δ perovskites. J Solid State Electrochem 2003;7:30–6. https://doi.org/10.1007/s10008-002-0286-3.
[56] Jurado JR, Figueiredo FM, Gharbage B, Frade JR. Electrochemical permeability of Sr-0.7(Ti,Fe)O3-delta materials. Solid State Ionics 1999;118:89–97. https://doi.org/10.1016/s0167-2738(98)00471-8.
[57] Menesklou W, Schreiner H-J, Härdtl KH, Ivers-Tiffée E. High temperature oxygen sensors based on doped SrTiO3. Sensor Actuator B Chem 1999;59:184–9. https://doi.org/10.1016/S0925-4005(99)00218-X.
[58] Moos R, Menesklou W, Schreiner HJ, Härdtl KH. Materials for temperature independent resistive oxygen sensors for combustion exhaust gas control. Sensor Actuator B Chem 2000;67:178–83. https://doi.org/10.1016/S0925-4005(00)00421-4.
[59] Steinsvik S, Bugge R, Gjønnes J, Taftø J, Norby T. The defect structure of SrTi 1−x Fe x O 3−y (x = 0–0.8) investigated by electrical doncutivity measurements and electron energy loss spectroscopy (EELS). J Phys Chem Solid 1997;58:969–76. https://doi.org/10.1016/S0022-3697(96)00200-4.
[60] Yu X, Long W, Jin F, He T. Cobalt-free perovskite cathode materials SrFe1-xTixO3-δand performance optimization for intermediate-temperature solid oxide fuel cells. Electrochim Acta 2014;123:426–34. https://doi.org/10.1016/j.electacta.2014.01.020.
[61] Mogensen M, Sammes NM, Tompsett GA. Physical, chemical and electrochemical properties of pure and doped ceria. Solid State Ionics 2000;129:63–94. https://doi.org/10.1016/S0167-2738(99)00318-5.
[62] Tsipis EV, Kharton VV. Electrode materials and reaction mechanisms in solid oxide fuel cells: a brief review. J Solid State Electrochem 2007;12:1039–60. https://doi.org/10.1007/s10008-007-0468-0.
[63] Chen Y, Zhou W, Ding D, Liu M, Ciucci F, Tade M, et al. Advances in Cathode Materials for Solid Oxide Fuel Cells: Complex Oxides without Alkaline Earth Metal Elements. Adv Energy Mater 2015;5. https://doi.org/10.1002/aenm.201500537. n/a-n/a.
[64] Chrzan A, Gazda M, Szymczewska D, Jasinski P. Interaction of SrTi0.65Fe0.35O3-δ with LaNi0.6Fe0.4O3-δ, La0.6Sr0.4Co0.2Fe0.8O3-δ and Ce0.8Gd0.2O2-δ. Procedia Eng 2014;98:101–4. https://doi.org/10.1016/j.proeng.2014.12.494.
[65] Takeda Y. Cathodic Polarization Phenomena of Perovskite Oxide Electrodes with Stabilized Zirconia. J Electrochem Soc 1987;134:2656. https://doi.org/10.1149/1.2100267.
[66] Esquirol A, Brandon NP, Kilner JA, Mogensen M. Electrochemical Characterization of La[sub 0.6]Sr[sub 0.4]Co[sub 0.2]Fe[sub 0.8]O[sub 3] Cathodes for Intermediate-Temperature SOFCs. J Electrochem Soc 2004;151:A1847. https://doi.org/10.1149/1.1799391.
[67] Boukamp BA, Rolle A. Use of a distribution function of relaxation times (DFRT) in impedance analysis of SOFC electrodes. Solid State Ionics 2018;314:103–11. https://doi.org/10.1016/j.ssi.2017.11.021.
[68] Boukamp B a, Hildenbrand N, Nammensma P, Blank DH a. The impedance of thin dense oxide cathodes. Solid State Ionics 2011;192:404–8. https://doi.org/10.1016/j.ssi.2010.05.037.
[69] Hildenbrand N. Improving the electrolyte - cathode assembly for mt-SOFC. 2011.
[70] Adler SB. Factors governing oxygen reduction in solid oxide fuel cell cathodes. Chem Rev 2004;104:4791–843. https://doi.org/10.1021/cr020724o.
[71] Lu Y, Kreller C, Adler SB. Measurement and Modeling of the Impedance Characteristics of Porous La[sub 1−x]Sr[sub x]CoO[sub 3−δ] Electrodes. J Electrochem Soc 2009;156:B513. https://doi.org/10.1149/1.3079337.
[72] Dailly J, Fourcade S, Largeteau A, Mauvy F, Grenier JC, Marrony M. Perovskite and A2MO4-type oxides as new cathode materials for protonic solid oxide fuel cells. Electrochim Acta 2010;55:5847–53. https://doi.org/10.1016/j.electacta.2010.05.034.
[73] Nenning A, Opitz AK, Huber TM, Fleig J. A novel approach for analyzing electrochemical properties of mixed conducting solid oxide fuel cell anode materials by impedance spectroscopy. Phys Chem Chem Phys 2014;16:22321–36. https://doi.org/10.1039/c4cp02467b.
[74] dos Santos-Gómez L, Porras-Vázquez JM, Losilla ER, Marrero-López D. Improving the efficiency of layered perovskite cathodes by microstructural optimization. J Mater Chem A 2017:7896–904. https://doi.org/10.1039/C6TA10946B.

4.2. Article II

Title: **The influence of Iron Doping on Performance of SrTi1-xFexO3-δ Perovskite Oxygen Electrode for SOFC**

Authors: **Aleksander Mroziński**, Sebastian Molin, Jakub Karczewski, Bartosz Kamecki, Piotr Jasiński

ECS Transactions (2019) vol 91, pages 1299–1307

DOI: 10.1149/09101.1299ecst

In this paper, studies of $SrTi_{1-x}Fe_xO_{3-\delta}$ (STFx) compounds with different iron contents (x = 0.35, 0.50, 0.70) were carried out. The basic material tests, such as four point resistance measurements, dilatometry, XRD and SEM images, were performed. The DC conductivity of STFx materials produced by the solid state reaction were measured in the form of dense pellets and for porous layers of STF50, it was measured as a function of the electrode thickness (1, 2, 3, 4 screen printed layers).

My original contribution to this publication was:

- Preparation of high-quality reproducible STFx material for electrodes.
- Detailed electrical characterisation of STFx material and its chemical composition.

Table 3 CRediT author statement Article II: "The influence of Iron Doping on Performance of SrTi1-xFexO3-δ Perovskite Oxygen Electrode for SOFC"

Author	CRediT author statement	Signature
Aleksander Mroziński	Investigation, Data curation; Visualization; Writing - original draft	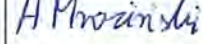
Sebastian Molin	Methodology; Writing - review & editing; Conceptualization	
Jakub Karczewski	Investigation (SEM pictures); Data curation	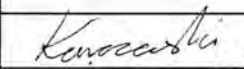
Bartosz Kamecki	Investigation (XRD)	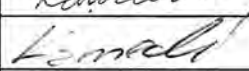
Piotr Jasiński	Resources; Writing - review & editing; Supervision; Funding acquisition; Methodology	

ECS Transactions, 91 (1) 1299-1307 (2019)
10.1149/09101.1299ecst ©The Electrochemical Society

The influence of Iron Doping on Performance of $SrTi_{1-x}Fe_xO_{3-\delta}$ Perovskite Oxygen Electrode for SOFC

A. Mroziński[a], S. Molin[a], J. Karczewski[b], B. Kamecki[b], and P. Jasiński[a]

[a] Laboratory of Functional Materials, Faculty of Electronics, Telecommunications and Informatics, Gdańsk University of Technology, Gdańsk 80-233, Poland
[b] Department of Solid State Physics, Faculty of Applied Physics and Mathematics, Gdańsk University of Technology, Gdańsk 80-233, Poland

Solid Oxide Fuel Cells (SOFC) are based on electrolytes and mixed ionic and electronic conductivity (MIEC) materials. The need to reduce costs causes an increase in interest of new compounds suitable for operating temperatures between 600 °C and 800 °C. The $SrTi_{1-x}Fe_xO_3$ (STF) perovskite material is a perspective material that could be used for the oxygen electrodes. In this work STF materials with different content of iron (x = 0.35, 0.5 and 0.7) have been evaluated. The paper presents synthesis, sintering properties, paste and layer preparation with preliminary electrical measurements. The results show that the electrical conductivity increases with the addition of iron, whereas the activation energy decreases. Based on these results, the applicability of STF as a potential oxygen electrode was discussed.

Introduction

Presently the materials with mixed ionic and electronic conductivity (MIEC) are widely used in different electrochemical systems for energy conversion, e.g. Solid Oxide Fuel Cells (SOFC). Typical operating temperature of the efficient SOFC is above 800 °C and it is caused by the sluggish oxygen reaction rate (ORR) of the cathode material (1). Therefore, high performance new materials for the oxygen electrodes operating at the temperatures range between 600 °C and 800 °C are sought. Most of the investigated MIEC cathodes belongs to the perovskites group including a perspective $SrTi_{1-x}Fe_xO_{3-\delta}$ (STF) (2). Pure undoped $SrTiO_3$ (STO) is a model MIEC material (3) with a low electronic and high oxygen ionic conductivity (4). The defect chemistry of the STO oxide shows that by an iron doping it is possible to increase the electronic conductivity at a cost of ionic conductivity, without changing an oxygen surface exchange mechanism (5,6). Unfortunately pure $SrFeO_3$ (SFO) is not compatible material for SOFC, because of phase transition at about 830 °C. Therefore STF compounds with different amount of iron dopant are gaining more and more interest for evaluation as material for SOFC (7).

One of a common and cheap techniques to synthesize STF frequently utilized in literature is a solid state reaction (SSR) method. The prepared powder can be used in different ways e.g. as an electrode, oxygen sensor or oxygen membrane (8,9). Another possibility to fabricate STF electrode is Pulsed Laser Deposition (PLD). For PLD technique there is needed for a laser beam and pre synthesized target of a metals oxides. By using pulsed laser, metals/metal oxides from target are deposited onto substrates

(10,11). Alternative method for PLD are spin-coating or spray pyrolysis. For these methods nitrates solutions of metals are used as a precursors. From nitrates a STF powder can be prepared as well (12–14). Comparing all this techniques, the traditional SSR method is the easiest and the cheapest one with high repeatability.

This work focuses on the STF compounds with different content of iron dopant (x = 0.35; 0.5; 0.7) made by SSR method. In this study material characterization of the prepared STF and preliminary results of DC electrical conductivity of a dense STF materials and porous STF layers deposited by screen printing method onto Al_2O_3 substrates are shown.

Experimental

Samples fabrication

In this study, the STF material with three different levels of iron (x = 0.35; 0.5 and 0.7) were prepared. The compounds were fabricated by conventional high temperature SSR method. The analytical reagents used for the reaction were strontium carbonate ($SrCO_3$), titanium dioxide (TiO_2) and iron (III) oxide (Fe_2O_3). The first two were purchased from the EuroChem (PL) and third from the Chempur (PL). Syntheses of the STF materials were described in more details in our previous work (2). The obtained $SrTi_{0.65}Fe_{0.35}O_{3-\delta}$ (STF35), $SrTi_{0.5}Fe_{0.5}O_{3-\delta}$ (STF50) and $SrTi_{0.3}Fe_{0.7}O_{3-\delta}$ (STF70) materials, after re-grounding in a mortar were ball milled (Fritsch Pulverisette 7) in ethanol (99.9% purity) with rotational speed of 600 rpm for 15 h using the 5 mm YSZ balls.

The DC electrical conductivity measurements were made on the STF materials in two different forms: pellets and layers. The STF pellets were prepared as shown in our previous work (2). After sintering pellets had diameter of 12 mm and 94% of theoretical density, as measured by Archimedes method. Porous STF layers were fabricated on the aluminum oxide (Al_2O_3) substrates (Rubalit®708 S, CeramTec, DE) using the screen printing method. Before use, Al_2O_3 plates were washed in an acetone by an ultrasound cleaning bath. Screen printing pastes of the STF compounds for were prepared by mixing in ball mill (with 200 rpm) the STF powder and the commercial vehicle system ESL403 (Electro-Science Laboratories, USA). Mass ratio of the powder and the vehicle was 40:60. In order to prevent forming cracks of the layers during paste drying, milled STF powder were thermally processed at 600 °C (with cooling/heating rate 3° min^{-1}) before mixing with vehicle. After screen printing of each layer, pastes were slowly dried at 60 °C and at 130 °C. At the end samples with different number of layers (from n = 1 to n = 4) were sintered at 800 °C in air as shown in previous work (2). The achieved electrodes have diameter of 0.4 cm^2.

Measurements

The X-ray diffractometry (XRD) characterization of STF powders were made at room temperature in air using Bruker D2 PHASER with XE-T detector.

Linear Thermal Expansion measurements were made in air using Netzsch DIL402. The STF compounds were heat up to 1100 °C with heating rate 5° min^{-1}, dwelled for 15 min and then cooled with rate of 3°C min^{-1}.

FEI Quanta FEG 250 Scanning Electron Microscope (SEM) were used for imaging of the STF samples. For imaging of the STF powder SEM were operated with secondary electron (SE) detector, while for polished cross sections with backscattered electron (BSE) detector. An applied accelerating voltage was 20 kV in a high vacuum for all cases.

DC electrical conductivity measurements of the STF pellets and layers were performed as shown in previous work (2) using a Van der Pauw technique.

Results and Discussion

Material characterization

To confirm fabrication of a perovskite cubic oxide phase of STF powders used for screen printing method, XRD analysis was made. The XRD patterns of the STF35, STF50 and STF70 powders measured at room temperature in air are shown in Fig. 1.

Identification of all diffraction peaks for STF50 and STF70 confirm that fabricated compounds has a cubic crystal structure ($Pm\bar{3}m$) (Inorganic Crystal Structure Database #186710) typical for strontium titanate. In case of STF35, beside cubic crystal structure peaks, there is additional one peak at 2θ = 25.6° (*). It was found, that it is related to Magnéli phase (TiO_2). As we reported earlier, this phase is connected with strontium nonstoichiometry (Sr/Ti < 1 in $SrTiO_3$) and does not affect the electronic conductivity of the STF compounds (2).

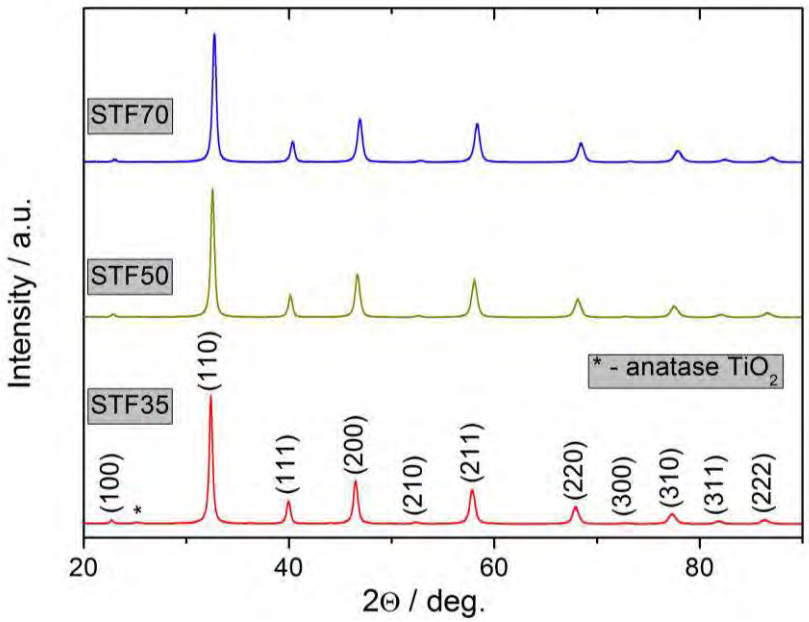

Figure 1. The XRD patterns of the fabricated STF powders for screen printing.

Dilatometry results obtained during heating up to 1100 °C (in air) of the STF powders used for screen printing are shown at Fig. 2A. The shrinkage of 0.36%, 0.38% and 0.45% of the initial length was recorded at 800 °C for STF35, STF50 and STF70, respectively. Figure 2B presents linear thermal expansion during cooling of the STF powders. The calculated thermal expansion coefficient (TEC) in the range from 1000 °C to 20 °C is 16.7 ppm K^{-1}, 17.9 ppm K^{-1} and 23.0 ppm K^{-1} for iron dopant of 0.35, 0.5 and 0.7, respectively. Based on surface morphology of sintered layers (data not shown) at different temperatures (800 °C, 900 °C and 1000 °C), it was found that rate of shrinkage obtained at 800 °C is acceptable for preparing layers without cracks for all evaluated STF compounds, despite of so high TEC value.

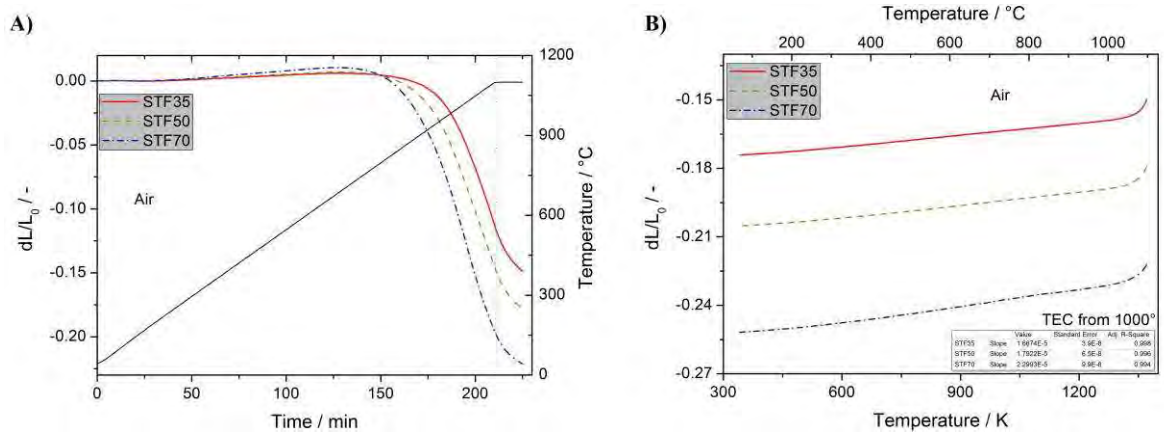

Figure 2. Temperature dependence of relative linear thermal expansion during heating (A) and cooling (B) of the fabricated STF powders.

Figure 3 shows SEM images of the STF powder used for screen printing method. It can be observed that particles of all STF powders look similar. It has been found that diameter of particles is in range from 16 nm to 140 nm. What is more, range of particle size is same as before thermal processing (data not shown), which was made to prevent cracking during drying of the STF paste.

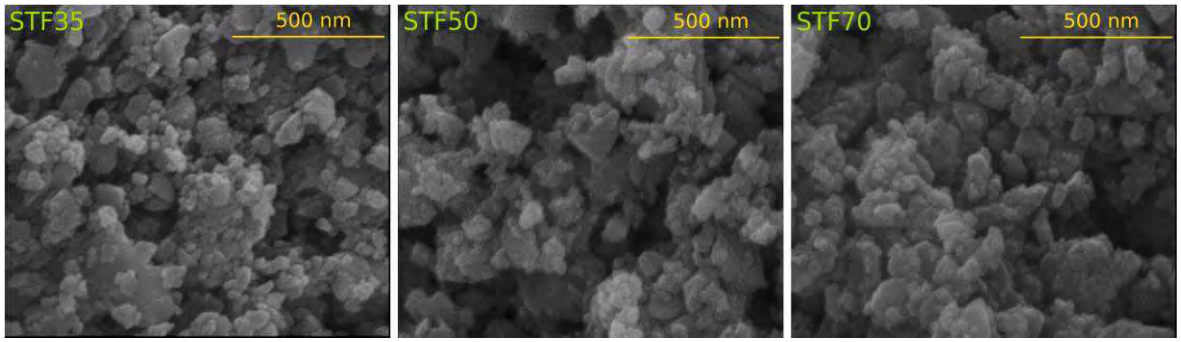

Figure 3. The SEM images of the fabricated STF powder for screen printing.

Results of DC electrical conductivity measurements of the STF dense pellets sintered at 1200 °C, are shown in Fig. 4 as a function of temperature (from 900 °C to 200 °C). The electrical conductivity investigation was conducted in synthetic air (20% O_2). The conductivity of the STF compounds increase with an iron dopant as expected (10). Maximum measured conductivity for STF35, STF50 and STF70 of 0.83 S cm^{-1}, 2.74 S cm^{-1} and 19.8 S cm^{-1} was obtained, respectively. With increasing of iron dopant

there is observed decrease of the temperature at which maximum of conductivity appears. Namely, 850 °C, 650 ° and 600 °C was recorded for iron dopant of 0.35, 0.50 and 0.70, respectively. For the STF35 and STF50 between 900 °C and 700 °C the conductivity only slightly depend on temperature in contrast to STF70 which conductivity increase with decreasing temperature in this temperature range. The calculated activation energy at low temperatures range (between 400 °C and 200 °C) for STF35 and STF50 are similar (E_a = 33.8 kJ mol^{-1} and 32.7 kJ mol^{-1}, respectively) but for STF70 the value is much lower (E_a = 22.6 kJ mol^{-1}).

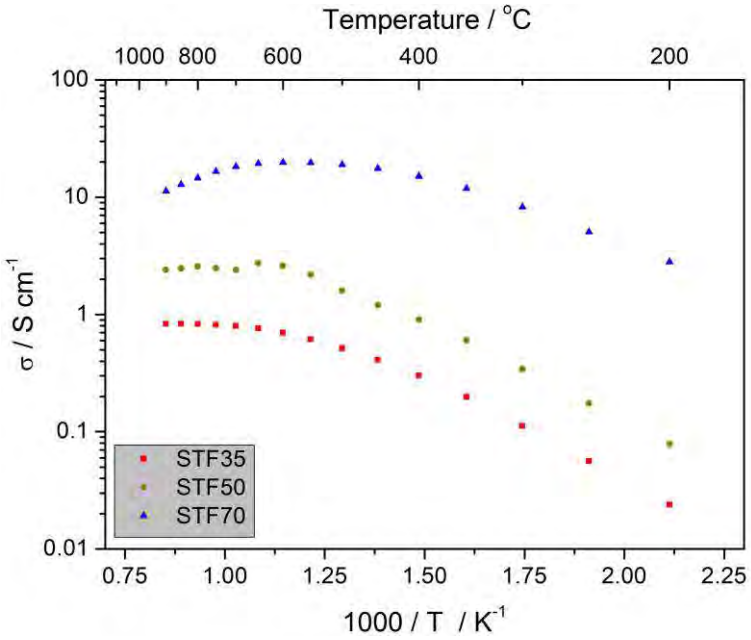

Figure 4. The DC conductivity of the dense STF pellets in function of temperature measured in 20% O_2.

Figure 5A presents post mortem SEM image of polished cross section of dense STF50 pellet used for DC electrical conductivity measurements. The other two STF compounds (STF35 and STF70) looked similarly (data not shown). Using the Archimedes method it was determined that this STF pellets had 94% of theoretical density. Figure 5B shows EDX spectrum of this bulk STF pellets used for conductivity measurements. EDX analysis confirmed chemical composition of investigated materials. Atomic percentage of all presented elements (Sr, Ti, Fe and O), are listed in the Table 1. All STF materials have detected deficiency of Sr atoms in the A sublattice equal 0.93.

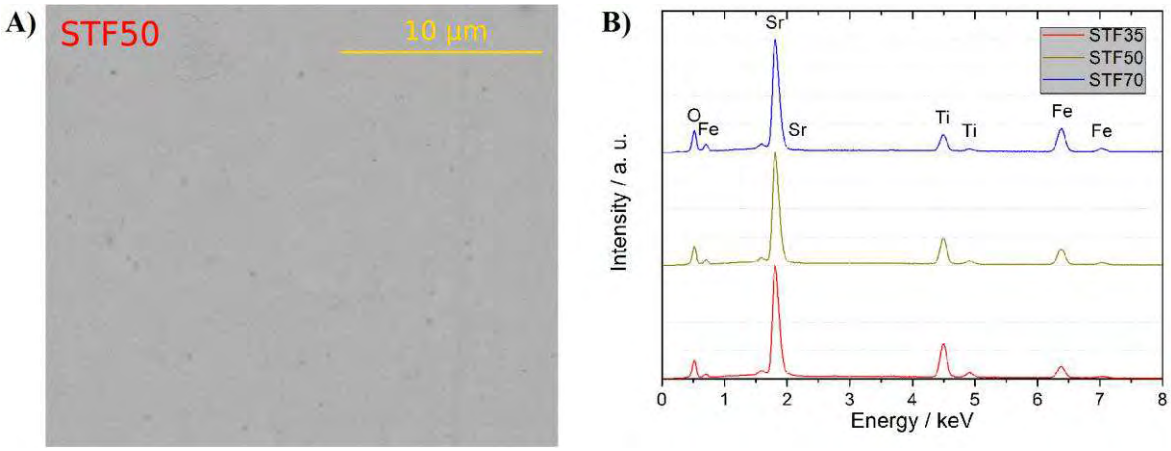

Figure 5. The SEM image of the polished cross section of the dense STF50 pellet (A) and EDX spectra of dense STF pellets used for DC conductivity measurements (B).

TABLE I. Chemical composition (in at.%) of dense STF pellets used for DC electrical conductivity measurements.

	Sr	Ti	Fe	O	Sr/Ti
STF35	20.4	14.4	7.5	57.7	1.42
STF50	20.9	11.3	11.1	56.7	1.85
STF70	21.3	6.8	15.8	56.1	3.13

Porous layers

In order to determine influence of the STF porous electrode thickness on electrical conductivity due to chemical reaction or roughness, a DC electrical conductivity study of the electrode with different thicknesses was performed. Figure 6A shows results of DC electrical conductivity measurements of porous STF50 material in the form of layers with different thicknesses. Layers of STF50 were sintered at 800 °C that can provide little shrinkage (<1%) and at which no cracks are obtained and layers have sufficient mechanical strength. The electrical conductivity was investigated as a function of temperature (from 800 °C to 200 °C) and was conducted in synthetic air (20% O_2). Maximum electronic conductivity for all porous STF50 samples was recorded at 700 °C. The highest value of conductivity was obtained for porous STF50 with four layers and it is 0.11 S cm^{-1}. Up to 400 °C conductivity is slightly increasing with the number of layers ($\Delta\sigma \approx 0.002$ S cm^{-1} n^{-1}). A significant change ($\Delta\sigma = 0.01$ S cm^{-1}) in conductivity at 700 °C is visible between samples with two and three layers. The calculated activation energy between 400 °C and 200 °C is comparable for all thicknesses and it equal $E_a = 22.3$ kJ mol^{-1}. At Fig. 6B is presented comparison of DC electrical conductivity of STF pellet and porous STF50 layer (n = 4). The maximum conductivity occurs almost at the same temperature (between 650 °C and 700 °C) despite of different forms of material and temperatures of calcination. Twenty times higher conductivity for dense STF50 pellet and higher activation energy than for porous layer is probably a consequence of different calcination temperature and porosity.

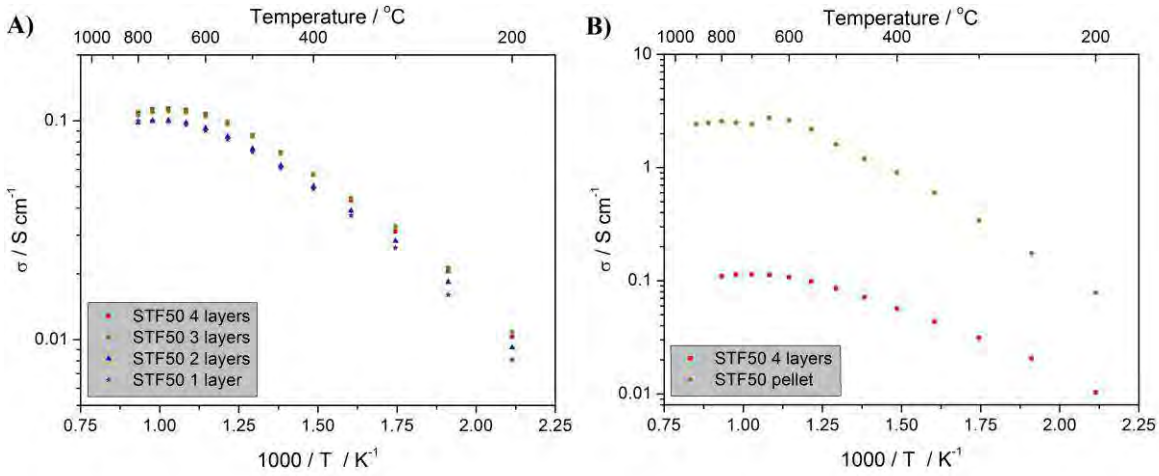

Figure 6. The STF50 DC conductivity of the samples with different number of the layers (A) and comparison with the pellet (B) measured at 21% O_2.

Post mortem SEM images of polished cross sections of porous STF35 layers with different thicknesses (n from 1 to 4) deposited on to Al_2O_3 substrates are shown at Fig. 7. All samples prepared by screen printing method and sintered at 800 °C, look similar. It has been calculated that one layer of screen printed STF compound had ~5.5 µm of thickness after sintering. As presented, sintering at 800 °C reveals porous layer without cracks and with good adhesion to the substrate. It is a good perspective for typical SOFC electrolytes like YSZ, CGO because of smaller TEC mismatch. Namely, the used Al_2O_3 has TEC of 4.6 ppm K^{-1} , while YSZ and CGO have of 10.8 ppm K^{-1} and 12.3 ppm K^{-1}, respectively.

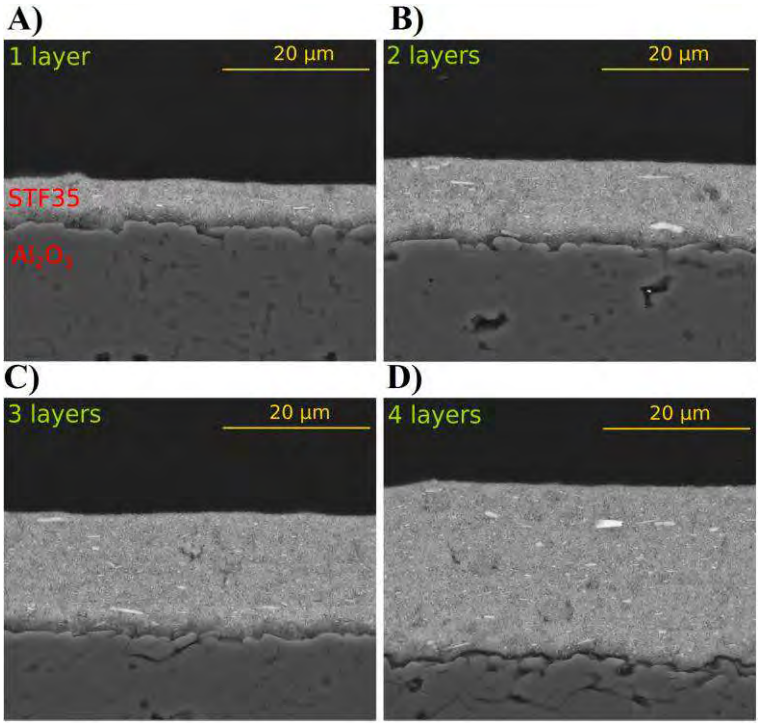

Figure 7. The SEM images of the polished cross section of the sintered at 800 °C STF35 porous layers with different thickness (A-B) on the Al_2O_3 substrate.

Conclusions

For better understanding the role of the iron substitution on the performance of the $SrTi_{1-x}Fe_xO_3$ electrode, STF35, STF50 and STF70 were fabricated in a form of pellet and film and evaluated. All fabricated compounds had regular cubic structure and had no significant differences in size of powder particles or layers morphology (sintered at 800 °C) were observed. It was presented that despite of very high TEC differences of STF and the support, the films without cracks can be obtained.

Preliminary results of DC electrical conductivity measurements show that with increase of iron dopant there is an increase in conductivity and decrease of the activation energy. It was also found that porous layers had lower electronic conductivity than dense material and had lower activation energy. These preliminary results show that STF compounds with different iron dopant requires further electrochemical performance study.

Acknowledgments

This work was supported by project funded by National Science Centre Poland "Understanding and minimization of ohmic and polarization losses in solid oxide cells by nanocrystalline ceramic and cermet functional layers (MiLoSoc)" based on decision 2017/25/B/ST8/02275.

References

1. T. Chen, G. F. Harrington, K. Sasaki, and N. H. Perry, *ECS Trans.*, **75**, 23–31 (2017).
2. A. Mroziński, S. Molin, J. Karczewski, T. Miruszewski, and P. Jasiński, *Int. J. Hydrogen Energy*, **44**, 1827–1838 (2019).
3. R. A. De Souza, J. Fleig, R. Merkle, and J. Maier, *Zeitschrift für Met.*, **94**, 218–225 (2013).
4. R. A. Maier, C. A. Randall, and J. Stevenson, *J. Am. Ceram. Soc.*, **99**, 3350–3359 (2016).
5. V. Metlenko, W. Jung, S. R. Bishop, H. L. Tuller, and R. A. De Souza, *Phys. Chem. Chem. Phys.*, **18**, 29495–29505 (2016).
6. W. Jung and H. L. Tuller, *ECS Trans.*, **25**, 2775–2782 (2009).
7. W. Jung and H. L. Tuller, *ECS Trans.*, **35**, 2129–2136 (2011).
8. X. Yu, W. Long, F. Jin, and T. He, *Electrochim. Acta*, **123**, 426–434 (2014) http://dx.doi.org/10.1016/j.electacta.2014.01.020.
9. X. Yu, J. Fan, and L. Xue, *Ceram. Int.*, **40**, 13627–13634 (2014).
10. W. Jung and H. L. Tuller, *J. Electrochem. Soc.*, **155**, B1194 (2008) http://jes.ecsdl.org/cgi/doi/10.1149/1.2976212.
11. A. Nenning et al., *J. Electrochem. Soc.*, **164**, F364–F371 (2017) http://jes.ecsdl.org/lookup/doi/10.1149/2.1271704jes.
12. N. A. Baharuddin, A. Muchtar, M. R. Somalu, N. S. Kalib, and N. F. Raduwan, *Int. J. Hydrogen Energy* (2018).
13. E. O. Filatova et al., *Solid State Ionics*, **308**, 27–33 (2017) http://dx.doi.org/10.1016/j.ssi.2017.05.016.
14. A. Chrzan, J. Karczewski, M. Gazda, D. Szymczewska, and P. Jasinski, *J. Solid State*

Electrochem., **19**, 1807–1815 (2015).

4.3. Article III

Title: **Effect of sintering temperature on electrochemical performance of porous $SrTi_{1-x}Fe_xO_{3-\delta}$ (x = 0.35, 0.5, 0.7) oxygen electrodes for solid oxide cells**

Authors: **Aleksander Mroziński**, Sebastian Molin, Piotr Jasiński

Journal: Journal of Solid State Electrochemistry (2020) vol 24, pages 873–882

DOI: 10.1007/s10008-020-04534-0

Impact Factor (2020): 2.647

Article number III extends the knowledge from Article II with EIS tests, a SEM analysis and qualitative assessment of differences in the electrochemical processes. The performance of symmetrical samples with porous STFx electrodes sintered at different temperatures was evaluated.

My original contribution to this publication was:

- Preparation of high-quality reproducible STFx symmetrical electrodes.
- Detailed electrochemical characterisation of the symmetrical electrodes.
- Evaluation of chemical composition of STFx material in dense pellets and porous electrodes.
- Determination of the electrochemical processes occurring at the porous electrodes with the application of DRT.

Table 4 CRediT author statement Article III: "Effect of sintering temperature on electrochemical performance of porous $SrTi_{1-x}Fe_xO_{3-\delta}$ (x = 0.35, 0.5, 0.7) oxygen electrodes for solid oxide cells"

Author	CRediT author statement	Signature
Aleksander Mroziński	Investigation; Data curation; Visualization; Writing - original draft	
Sebastian Molin	Methodology; Writing - review & editing; Conceptualization	
Piotr Jasiński	Resources; Writing - review & editing; Supervision; Funding acquisition; Methodology	

Journal of Solid State Electrochemistry (2020) 24:873–882
https://doi.org/10.1007/s10008-020-04534-0

ORIGINAL PAPER

Effect of sintering temperature on electrochemical performance of porous $SrTi_{1-x}Fe_xO_{3-\delta}$ ($x = 0.35, 0.5, 0.7$) oxygen electrodes for solid oxide cells

A. Mroziński[1] · S. Molin[1] · P. Jasiński[1]

Received: 25 November 2019 / Revised: 28 February 2020 / Accepted: 28 February 2020 / Published online: 6 March 2020

Abstract

This work evaluates the effects of the sintering temperature (800 °C, 900 °C, 1000 °C) of $SrTi_{1-x}Fe_xO_{3-\delta}$ ($x = 0.35, 0.5, 0.7$) porous electrodes on their electrochemical performance as potential oxygen electrode materials of solid oxide cells. The materials were prepared by a solid-state reaction method and revealed the expected cubic perovskite structure. After milling, the powders were characterised by a sub-micrometre particle size with high sinter-activity. It was shown that the lowest area specific resistance was achieved after sintering $SrTi_{0.65}Fe_{0.35}O_3$ electrodes at 1000 °C, and $SrTi_{0.5}Fe_{0.5}O_3$ and $SrTi_{0.30}Fe_{0.70}O_3$ electrodes at 800 °C, which can be considered to be a relatively low temperature. In general, EIS measurements showed that increasing the Fe content results in lowered electrode polarisation and a decrease of the series resistance. Even though the studied materials have much lower total conductivities than state-of-the-art electrode materials (e.g. $(La,Sr)(Co,Fe)O_3$), the polarisation resistances obtained in this work can be considered low.

Keywords Strontium titanate · Solid oxide cell · Oxygen electrode · Perovskite · Polarisation resistance

Introduction

Mixed ionic and electronic conducting materials (MIECs) are the main group of materials used for high temperature solid oxide cell (SOC) electrodes [1]. There are several features of porous MIEC materials that have an impact on the performance of the electrode. The microstructure of the electrode (porosity, tortuosity, particle size) [2, 3], intrinsic oxygen activity (surface exchange, oxygen diffusion) [4, 5], interface between the electrode and electrolyte or the barrier layer [6], and the electronic transport properties are all very important. The most studied group of MIEC oxygen electrode materials are the perovskites [7–9]. They are given by the general ABO_3 formula, with A being a large cation in 12-fold coordination by oxygen anions, and B a relatively smaller cation in the centre of an oxygen-coordinated octahedra (6-fold coordination). Typically, the A cation is one of the alkaline earth cations, whereas B is a transition metal cation, e.g. $CaTiO_3$—the archetypical perovskite mineral. In general, the A and B sites can be occupied by more than one cation type, thus providing enormous possibilities to develop new materials. For applications in SOCs, $(La,Sr)(Co,Fe)O_3$, LSCF, and $(La,Sr)CoO_3$, LSC, are the most studied ones [10–14]. Also, other materials groups have been studied: double perovskites, Ruddlesden-Popper-type phases [15], and others [16–21]. Typical electrode materials have high ionic and electronic conductivity levels, with total conductivities exceeding 100 S cm^{-1}; however, the exact role of the influence of the individual partial conductivity levels on the resulting electrode performance is yet to be established, and is currently an active research topic [5, 22, 23]. In this respect, materials with relatively low total conductivities (or materials with a low electronic-to-ionic conductivity ratio) and good oxygen catalyst properties are very interesting for research. Among the interesting materials with relatively low total conductivities (< 10 S cm^{-1} at 800 °C) and high ionic conductivities (comparable with yttria stabilised zirconia or ceria-based materials) are iron doped strontium titanates ($SrTi_{1-x}Fe_xO_{3-\delta}$ (STFx)) [24–27]. Because of their

Electronic supplementary material The online version of this article (https://doi.org/10.1007/s10008-020-04534-0) contains supplementary material, which is available to authorized users.

✉ A. Mroziński
aleksander.mrozinski@pg.edu.pl

[1] Faculty of Electronics, Telecommunications and Informatics, Gdansk University of Technology, ul. G. Narutowicza 11/12, 80-233 Gdansk, Poland

high ionic conductivity (~ 10^{-2} S cm^{-1} at 800 °C) [28], they have found application as oxygen separation membranes [29, 30], catalysts for water electrolysis reactions [31], resistive sensors of oxygen [32] and ethanol [33], and also in solid oxide fuel cell (SOFC) systems as electrodes [34–36] or the functional layer [37]. STFx-based materials show low polarisation resistance and good long term stability, including limited Sr surface segregation [38, 39], which is problematic for LSC/LSCF compounds.

Most studies have focussed on the properties of thin and dense STFx films used as model electrodes [24, 28], whereas the properties of porous electrodes have practically not been studied. Our previous work showed good performance of porous STF35 ($SrTi_{0.65}Fe_{0.35}O_3$) electrodes [40, 41], which has also been confirmed by other authors [38]. The obtained polarisation resistance results were comparable with the well-known LSCF electrode materials. An area specific resistance (ASR) of 0.020 Ω cm^2 at 650 °C [42] has been reported for LSCF, whereas for $SrTi_{0.1}Fe_{0.9}O_3$ (STF90), an ASR of 0.067 Ω cm^2 at 650 °C has been reported [43]. Some reports show that STFx material with $x = 0.35$ has the lowest degree of structural distortions, which makes it promising for technical applications [44] despite its relatively low electronic conductivity (~ 2 S cm^{-1}) and higher ASR values (~ 0.1 Ω cm^2 at 800 °C [40]). In general, there is only a limited number of publications related to STFx performance, and the materials require more studies.

The current work studies the effects of electrode sintering temperature on the electrochemical properties of porous $SrTi_{1-x}Fe_xO_{3-\delta}$ ($x = 0.35$, 0.5, 0.7) electrodes based on symmetrical cells. This work is a continuation of our previous initial study of an STF35 electrode [41].

Materials and methods

Material and samples preparation

$SrTi_{1-x}Fe_xO_{3-\delta}$ (STFx) materials with different Fe substitution levels ($x = 0.35$, 0.5, 0.7) were synthesised from analytical grade (> 99% purity) reagents—strontium carbonate (EuroChem, PL), titanium dioxide (EuroChem, PL), and iron (III) oxide (Chempur, PL)—by the solid-state reaction method, as described in our earlier work [41]. Briefly, stoichiometric amounts of the reagents were re-ground in an agate mortar and were subsequently ball milled (Fritsch Pulverisette 7, ZrO_2 milling container) in absolute ethanol (99.9% purity) with a rotational speed of 600 rpm for 15 h using 5 mm YSZ balls. The obtained STFx powders were further annealed at 600 °C (with a cooling/heating rate of 3 °C min^{-1}). The particle sizes of the prepared STFx powders were similar to what was shown earlier, and all powders had particles in the sub-micron range [45].

Gadolinium doped ceria (CGO) substrates, used for the preparation of the symmetrical cells, were made from a commercial powder (GDC-20 K, DKKK Japan), as presented in our previous work [41]. The surfaces of the sintered CGO substrates were ground and polished to obtain a smooth surface and remove any contaminants. After preparation, the pellets had a thickness of approximately 0.5 mm. Before the deposition of the STFx electrodes, the substrates were cleaned in acetone in an ultrasound cleaning bath.

Porous STFx electrodes were deposited on both sides of the polished CGO substrates using screen printing (DEK 65, UK). For the preparation of the pastes, an ESL403 commercial vehicle system (Electro-Science Laboratories, USA) was mixed with the prepared STFx powders in a ball mill at a mass ratio of 60:40. The mixing of the electrode pastes was carried out with a rotational speed of 200 rpm. The deposited pastes were slowly dried at 60 °C and at 130 °C. To obtain final electrodes with different microstructures, the electrodes were sintered in air at three different temperatures: 800 °C, 900 °C, and 1000 °C in a box furnace (Carbolite RHF1600, UK). Each dried electrode was heated up to 600 °C (for 1 h with a ramp of 1.5 °C min^{-1}) in order to fire the binder, and then dwelled for 2 h at the appropriate temperature, with heating and cooling ramps of 3 °C min^{-1}. The prepared electrodes had an active area of 0.4 cm^2. For electrical contact, the electrodes were brush-painted with Pt paste (ESL 5542, Electro-Science Laboratories, USA), dried, and pre-sintered at 600 °C.

Microstructure and performance analysis

The X-ray diffractometry (XRD) technique was used to determine the phase composition of the fabricated STFx powders. Measurements were performed at room temperature in the air using a Bruker D2 Phaser with an XE-T detector.

The investigation of the linear thermal expansion was carried out using a Netzsch DIL402 dilatometer. The STFx powders were formed into cylinders and heat up to 1100 °C with a heating rate of 5 °C min^{-1}, dwelled for 15 min, and then cooled at a rate of 3 °C min^{-1}. The procedure was carried out in 21% O_2.

A Phenom XL (Thermo Fisher Scientific, the Netherlands) scanning electron microscope (SEM) was used for imaging of the polished cross sections of the symmetrical cells. All SEM images were made using a backscattered electron (BSE) detector with an applied accelerating voltage of 10 kV in a 0.1 Pa vacuum. The chemical compositions of the investigated electrodes were determined via energy-dispersive X-ray (EDX) spectroscopy using an integrated analyser (Thermo Fisher Scientific, 25 mm^2 Silicon Drift Detector) with an accelerating voltage of 20 kV.

Electrochemical impedance spectroscopy (EIS) studies were carried out using a Novocontrol Alpha-A mainframe with a 4-wire ZG4 interface. In order to study, the impact of

the sintering temperature on the ASR, the STFx symmetrical samples were measured in a spring-based compression cell in flowing air. For electrical contact, gold meshes were used for contacting the samples. The measurement parameters were used as described in our previous work [41].

The DRTTools Matlab GUI, available from prof. Ciucci's group, was used for the analysis of the distribution of relaxation times [46, 47].

Results and discussion

Materials characterisation

The phase composition of the powders prepared by the solid-state reaction method was studied using X-ray diffractometry. The XRD of the prepared powders showed the formation of the expected cubic perovskite phase (*Pm*3*m*), in agreement with the crystallographic database (Inorganic Crystal Structure Database #18-6710). The inset of Fig. 1a) shows the change in peak position for powders with different iron contents. With an increasing Fe content, the peaks shift towards higher 2θ angles, indicating the decrease of the unit cell size. The ionic radii (for coordination number 6) of Fe^{3+} was 0.55 Å (in the low spin state), whereas for the Ti^{4+}, it was 0.605 Å.

The general microstructure of an exemplary symmetrical sample (STF50) is presented in Fig. 1b. The low magnification image shows a uniform electrode thickness of ~25–30 μm over the electrolyte surface. On top of the porous electrode, a painted Pt current collector has a thickness of ~10 μm. The CGO substrate has a thickness of ~500 μm, which varies between 450 and 600 μm for all studied samples.

The sintering and thermal expansion properties of STFx materials were evaluated by dilatometry. Figure 1c presents the results of the sintering part of the measurement, whereas the inset shows the thermal expansion part (after the sintering). Upon heating, high thermal expansion of the STF70 compound is visible. The sintering behaviour of the samples is strongly dependent on the iron content. A higher iron content results in lower onset temperature of sintering and higher shrinkage during the dwelling stage (at 1100 °C). The sintering onset temperatures for the STF35 and STF50 were ~690 °C and for the STF70 ~680 °C. The total shrinkages of the pellets after the dilatometry study was 17%, 21%, and ~25% for STF35, STF50, and STF70, respectively.

Thermal expansion coefficients (TEC) were determined based on the cooling stage of dilatometry. For STF35, STF50, and STF70, values of ~16, ~18, and ~23 × 10^{-6} K^{-1} were obtained (in the temperature range 1000 °C–RT), respectively. The addition of iron increases the TEC considerably (possibly including the contribution of chemical expansion), which can make practical application of iron-rich samples troublesome. For example, the TEC of the CGO substrate is ~12–13 × 10^{-6} K^{-1} [48]; therefore, large stresses will be generated between the TEC-dissimilar materials.

The porosities of the cylindrical samples sintered at 1100 °C were measured by the Archimedes method. Porosities of 29%, 23%, and 5% were obtained for STF35, STF50, and STF70, respectively. The dilatometry and porosity measurement results show that increasing the iron content results in improved sinterability, but also results in an increased TEC.

Electrochemical characterisation

For the evaluation of the electrochemical performance towards the oxygen reduction/oxidation reaction (ORR/OER) of the STFx materials, electrochemical impedance spectroscopy (EIS) measurements were carried out. Samples with symmetrical electrodes were prepared on ionic conducting CGO and were sintered at either 800 °C, 900 °C, or 1000 °C. The symmetrical electrodes were measured by EIS in the air in the temperature range of 800 °C to 500 °C with 50 °C decrements. The EIS data were standardised for a specific surface of the electrodes by using the formulas: $R_s = R_{ohm} \times A$ and

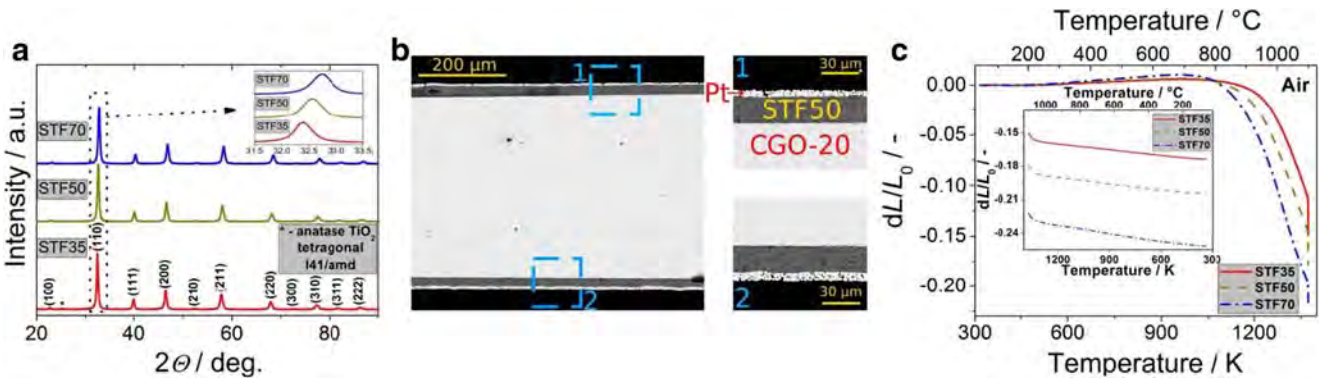

Fig. 1 **a** X-ray diffractometry of the fabricated powders, **b** SEM images of polished cross sections of an exemplary symmetrical cell with porous electrodes, and **c** sintering/thermal expansion curves of STF35, STF50, and STF70

$\mathrm{ASR} = \frac{R_{\mathrm{pol}} \times A}{2}$, where R_s is the series resistance, R_{ohm} is the measured ohmic resistance, R_{pol} is the polarisation resistance, and A is the area of the electrodes (0.4 cm^2).

The electrode responses, given by the ASR values, are directly comparable and represent the electrochemical performance of the electrodes, influenced by the sintering and physico-chemical material properties. In the case of comparison of the R_s values, the values are also influenced by the CGO thickness, which varies between the samples.

It is worth noting that the R_s and ASR values were stable during the few hours of measurement, i.e. no degradation nor activation of the electrodes was noted in the few hours of isothermal holds.

Figure 2 presents the impedance spectra of the differently sintered electrodes measured at 700 °C. A similar plot for the measurement temperature of 800 °C can be found in the Supplementary materials (Fig. S1). Also, Fig. S2 in the Supplementary materials provides the impedance spectra of STFx materials sintered at 800 °C measured at different temperatures (700 °C, 750 °C, and 800 °C). For comparison of the impedance values, the scaling of the axes is the same. The values of R_s and ASR depend on the sintering temperature to different extents, depending on the sample composition. Clearly, there is a visible effect of the sintering temperature on the electrochemical performance of the electrodes. Based on the measured impedance spectra, the values of R_s and ASR were plotted collectively on an Arrhenius scale. The results presented in Fig. 3 are as follows: R_s of STF35, STF50, and STF70 in Fig. 2a–c and ASR in Fig. 3d–f, respectively.

By analysing the R_s values obtained for the three studied materials as a function of the temperature, differences can be observed, which are in-line with the impedance spectra shown in Fig. 2. For STF35 and STF50, increasing the sintering temperature decreases R_s. This effect is strong for the STF35 sample and still noticeable for the STF50. For STF70, a slight increase of R_s is observed. These results might be connected to the electronic conductivity of the materials, and possible current restriction at the interface or ohmic resistance of the porous electrodes. STF70 has the highest total conductivity, so the possible current restriction will be the lowest. A rough calculation of the ohmic contribution of the porous electrodes based on the electrical conductivity of CGO results in relatively low R_s values of STFx, i.e. for the least conductive porous STF35 at 800 °C, the series resistance addition would be only ~ 10 mΩ cm^2. For comparison, the ohmic resistance introduced by a 550 μm thick CGO substrate is estimated to be ~ 400 mΩ cm^2 (based on the $Ce_{0.8}Gd_{0.2}O_{2-\delta}$ conductivity value of 0.140 S cm^{-1} at 800 °C [49, 50]). The activation energy of series resistance for all STFx symmetric samples is ~ 0.67 eV, which is in line with values for doped ceria compounds [51].

Interestingly, the ASR values of the STF35 electrode are practically independent of the sintering temperature and have values of ~ 70 mΩ cm^2 at 800 °C. The same effect was observed in our previous study [41]. For STF50 and STF70, the ASR values are dependent on the sintering temperature, reaching the lowest values for electrodes sintered at 800 °C. Especially for STF70, the increase of the sintering temperature leads to a large increase of the ASR. For STF50 and STF70 electrodes processed and measured at 800 °C, the ASR values are ~ 30 mΩ cm^2 and ~ 22 mΩ cm^2, respectively. The obtained values can be considered very low and are comparable with the best performing mixed conducting oxygen electrodes, such as LSC, LSCF, and others. The very best reported electrodes outperform the STFx electrodes studied in this work, but it is still interesting that electrodes with relatively low total conductivity have such good performance. The activation energy of polarisation resistance is very similar for all STFx materials (~ 1.29–1.24 eV) with a small tendency to decrease with increasing the Fe content.

The polarisation resistances obtained for Co-free cathodes were summarised by Hashim et al. [52]. The lowest reported

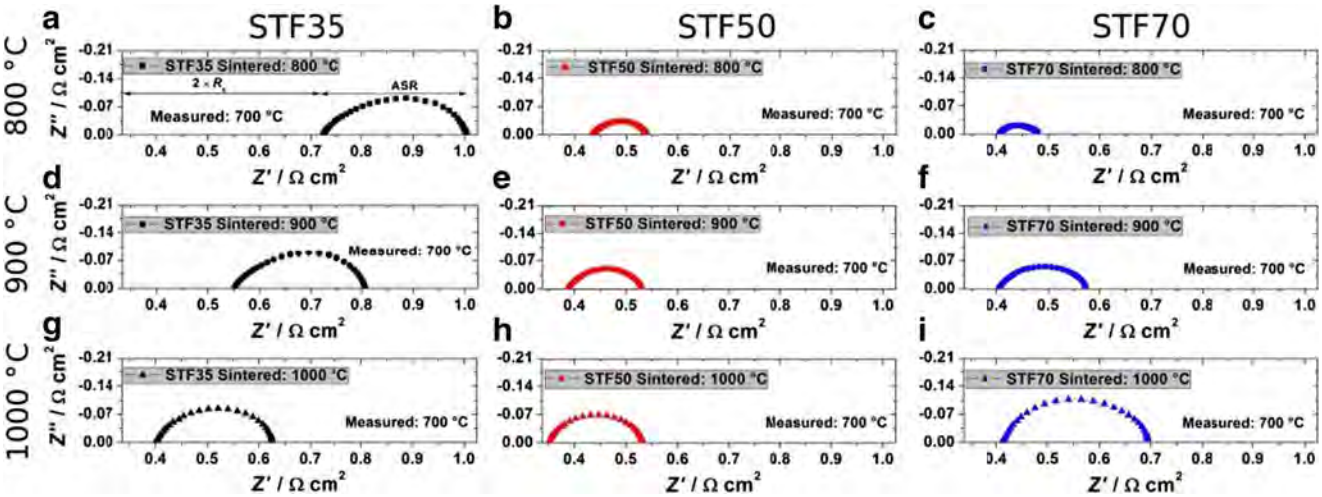

Fig. 2 Impedance spectra of STFx materials sintered at different temperatures (800 °C/900 °C/1000 °C), measured at 700 °C in 21% O_2

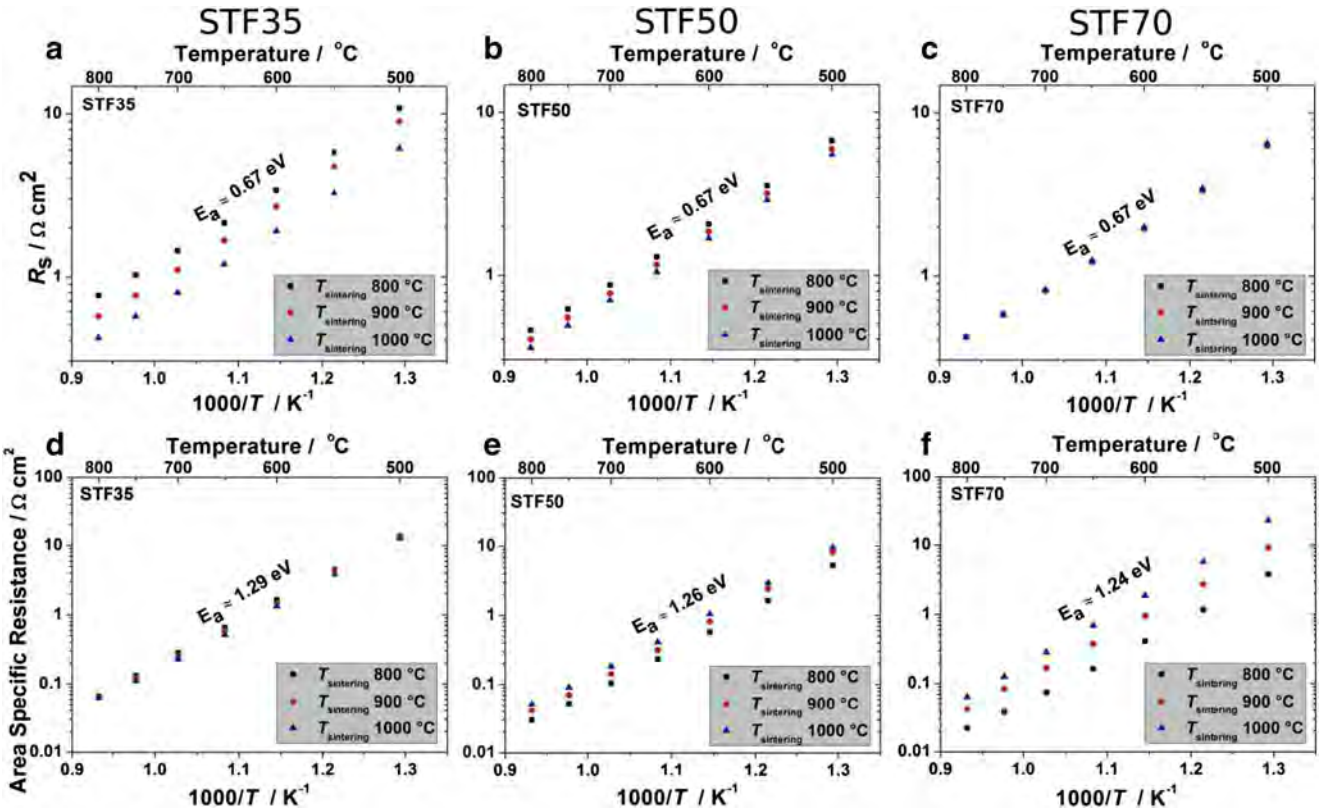

Fig. 3 Series (**a**–**c**) and polarisation (**d**–**f**) resistances of the symmetrical STF35, STF50, and STF70 electrodes, respectively, sintered at different temperatures (800 °C/900 °C/1000 °C) as a function of temperature in 21% O_2

polarisation resistance values were obtained for $PrBa_{0.97}Fe_2O_{5+d}$ and were as low as 0.019 Ω cm^2. The results obtained in this work for STFx lie within the range of the best materials reported. Furthermore, STFx materials can be easily modified to enhance their electrocatalytic activity, e.g. by partial Co substitution [25].

To further evaluate the influence of the sintering temperature on the electrode performances, distribution of relaxation times (DRT) analyses of their spectra were performed. DRT analysis is a powerful tool to investigate electrochemical processes [53–56]. The results of the DRT analysis of the spectra shown in Fig. 2 are presented in Fig. 4. Additionally, the results of the DRT analysis of samples sintered at 800 °C and measured at three different temperatures (700 °C, 750 °C, and 800 °C) are provided in Fig. S3 in the Supplementary materials. These analyses are mostly used to support the selection of the proper sintering temperature of the STFx electrodes and do not fully explain the occurring electrode processes, which will be the aim of our future work.

For all electrodes, increasing the sintering temperature results in a shift of the characteristic frequencies towards lower values. To begin with, all spectra show a distinct high frequency contribution (f_{HF}~1000 Hz). For STF35, it decreases with increased sintering temperature, also shifting towards lower frequencies. STF50 shows quite similar behaviour, but to a smaller extent. For STF70, the contributions do not change much and have a constant characteristic frequency.

Besides the high frequency contribution, which is well separated in the DRT spectra, there are at least two lower frequency contributions that can be analysed. For STF35, the electrode resistance (given the area under the DRT plot) is similar for all temperatures, with a slightly lower value after sintering at 1000 °C. The main difference between the low and high temperature sintered STF35 materials is the medium frequency contribution ($f_{MF(800\ °C)}$~500 Hz), which has the highest resistance for the electrode sintered at 800 °C. Nevertheless, the lower frequency process ($f_{LF(800\ °C)}$~50 Hz) dominates over the entire spectrum. For STF50 and STF70 electrodes, the spectra are very similar for all sintering temperatures, but the magnitude changes. An increase of the sintering temperature results in decreased electrode performance. All electrode processes seem to increase their resistance. For STF50, the dominating contribution is the low frequency process at all temperatures ($f_{LF(800\ °C)}$~80 Hz, $f_{LF(1000\ °C)}$~20 Hz). STF70 shows different behaviour. For electrode sintered at 800 °C, the dominating process is the medium frequency process ($f_{MF(800\ °C)}$~150 Hz), whereas for higher sintering temperatures, the low frequency process dominates ($f_{MF(1000\ °C)}$~10 Hz). For STF70 electrodes sintered at 900 °C and 1000 °C, an additional contribution at even lower

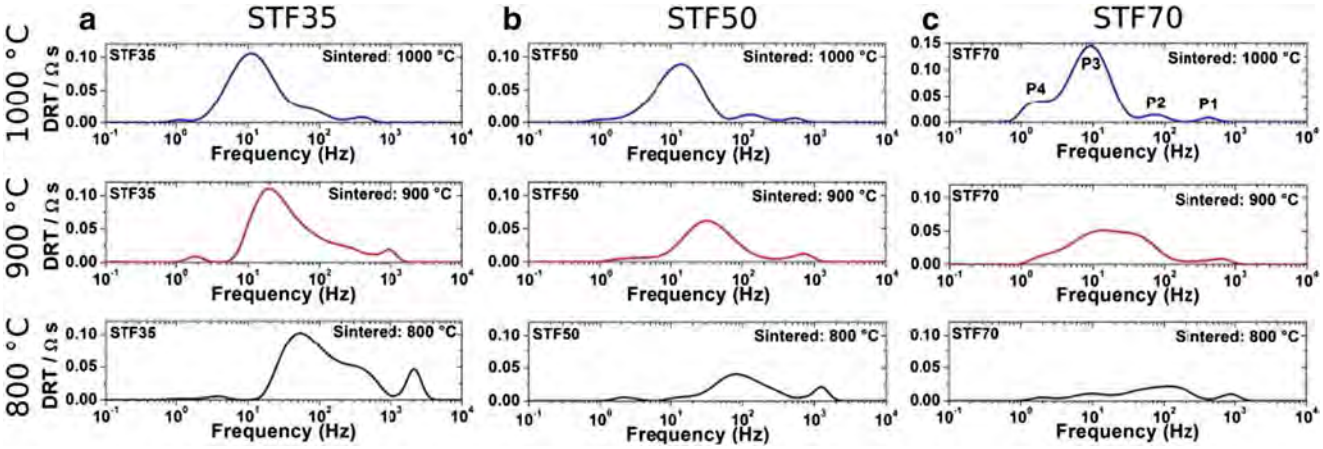

Fig. 4 Exemplary distribution of relaxation times plots of impedance of symmetrical STF35 (**a**), STF50 (**b**), and STF70 (**c**) electrodes measured at 700 °C at 21% O_2, as a function of sintering temperature (800 °C/900 °C/1000 °C)

frequencies becomes apparent. As the electrode microstructure densifies, the porosity becomes lower and the gas diffusion impedance becomes measurable, which agrees well with the characteristic frequency of 1–4 Hz.

The electrochemical processes occurring at the electrodes/interfaces, which have been assigned qualitatively to the peaks from the DRT spectra (based on our previous study and the specific frequencies/capacitances of the processes) are summarised as follows:

P1—(~ 1000 Hz) STFx-CGO interface contribution;
P2—(80–200 Hz) potential Gerischer element: oxygen diffusion in the bulk of the particles;
P3—(10–30 Hz) non-dissociative adsorption/charge transfer;
P4—(~1 Hz) gas diffusion.

The provided description is only a general overview of the possible processes. A more detailed discussion, including studies of the pO_2/temperature dependence of the contributions, will be given in the future. For example, Zhang et al. [38] recently studied STFx materials and used an equivalent circuit consisting of two components. Thus further studies are required to clarify the underlying mechanisms, which are needed to understand the behaviour of mixed ionic-electronic conductors.

In general, the oxygen reduction/oxidation performance increases with increasing iron content. When titanium (Ti^{4+}) is substituted for iron, it can either have a + 3 or + 4 oxidation state. The specific ratio of the cations will depend on the atmosphere and overpotentials. In the case of the formation of Fe^{3+}, charge compensation occurs by the generation of electron holes in the valence bands or, predominantly, by the formation of oxygen vacancies [57]. Either way, both effects should be positive for the performance of mixed ionic-electronic conductors. For Fe-rich compositions, the effective band gap is drastically reduced, the materials become "electron-rich", and the resulting availability of electrons for oxygen reduction is much higher. The surface exchange coefficient for STF70 is orders of magnitude higher than for pure or slightly Fe-doped $SrTiO_3$ [57–59].

As previously reported by Jung and Tuller [28], based on a thin film study, STFx (for x between 0.05 and 0.80) most probably have a common limiting process. The authors describe it as a surface oxygen exchange, occurring at the surface of the electrode materials. This explanation was

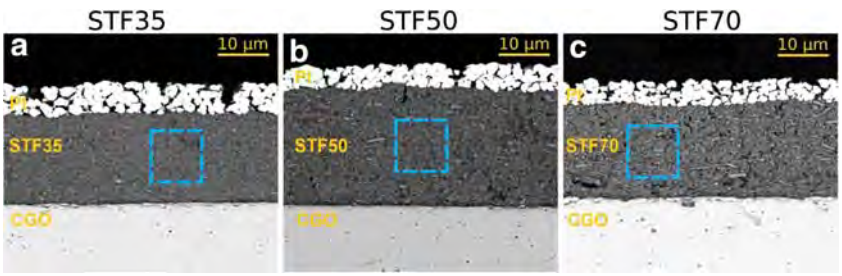

Fig. 5 Post-mortem SEM images of the polished cross section of the symmetrical cells with the STF35 (**a**), STF50 (**b**), and STF70 (**c**) porous electrodes sintered at 800 °C. Regions marked by the dashed squares were analysed by EDS to determine their chemical compositions (results are included in Table 1)

Table 1 EDX results for the STF35, STF50, and STF70 cathodes sintered at 800 °C expressed at percentage of atomic mass

	Sr/%	Ti/%	Fe/%	O/%	Ti: Fe	Sr: (Ti + Fe)
Area STF35	17.7	11.7	6.2	64.4	1.89	0.99
Area STF50	18.7	9.6	9.2	62.5	1.04	0.99
Area STF70	18.8	5.9	13.3	62.1	0.44	0.98
Point 1	15.1	7.1	6.9	71	1.02	1.08
Point 2	16.5	8.5	8.3	66.7	1.03	0.99
STF35 powder	17.1	11.7	5.7	65.5	2.05	0.98
STF50 powder	17.3	9.6	8.1	64.9	1.19	0.98
STF70 powder	14.9	5.1	11.1	68.9	0.46	0.92

further confirmed by subsequent works. Metlenko et al. [60] have studied the oxygen diffusion and surface exchange of STFx materials. They concluded that oxygen diffusion occurs via vacancy migration and that the oxygen diffusivity increases continuously as a function of iron concentration. In addition, the authors support the claim that the oxygen surface exchange occurs by one single mechanism for electron-poor and electron-rich materials. The authors proposed that the energy levels of oxygen adsorbates at the oxide surface, relative to the energy of the conduction-band edge, play a key role in the process.

Comparing the performance of the STFx materials studied in this work with other materials reveals good performance, especially for the Fe-rich compound. The polarisation level achieved for this electrode (~ 20 mΩ cm^2 at 800 °C, ~ 0.41 Ω cm^2 at 600 °C) is comparable with the performance of LSCF (~ 12 mΩ cm^2 at 800 °C); see Fig. S4 in Supplementary materials. State-of-the art LSC electrodes show initial performance at a level of ~ 100 mΩ cm^2 at 600 °C [61, 62], but the results vary greatly. Molin et al. studied STF35 and STF50 deposited on YSZ and reported ASR_{pol} values of ~ 120 mΩ cm^2 at 800 °C [40]. Zhang et al. have shown high performance and stability of STF70 electrodes of 30 mΩ cm^2 at 800 °C and ~ 0.4 Ω cm^2 at 600 °C. Our results, especially for STF70 sintered at 800 °C, thus show very high performance.

Based on the literature findings, it would be interesting to study whether it is possible to further improve the performance of STFx, e.g. by the introduction of surface catalysts (either primarily electronic/ionic, or mixed conducting), for example by an infiltration technique (and to what extent) [63, 64]. This work establishes the selection of sintering conditions and baseline measurements for future work, including infiltration and chemical modification of the compositions.

Microstructure analysis

Post-mortem SEM images of the porous STF35/50/70 electrodes sintered at 800 °C are presented in Fig. 5. A microstructure comparison of the STFx samples sintered at 800 °C, 900 °C, and 1000 °C is provided in Fig. S5 in the Supplementary materials. For each of the electrodes, the chemical composition was analysed using EDS analysis of the centre part of the electrodes (regions marked by dashed squares). The EDX results are presented in Table 1 and are in good agreement with the desired stoichiometries.

As can be seen in Fig. 6, the electrodes have uniform thicknesses between 20 and 30 μm. No cracks or other defects were detected. The morphology of the electrodes is similar: small grains of the synthesised STFx materials result in small pores and a large surface area available for the electrochemical reaction. The prepared Pt contact layer has a thickness of ~ 5–10 μm and serves the role of the current collector. The use of the current collector is required due to the relatively low electronic conductivity of STF35, for which the results have been observed to depend on the contact area of the current collector, indicating current constriction effects. For 20–30 μm thick STFx electrodes, the catalytic activity of the Pt contact layer is negligible; it only serves as a metallic-conducting contact layer.

For the STF50 sample sintered at 800 °C, a linear scan elemental analysis was performed across the Pt/porous electrode/CGO substrate layers. Line scan results, including Pt, Sr, Ti, Fe, Ce, and Gd, are shown in Fig. 6. The strontium profile shows a small but noticeable gradient, with less strontium at

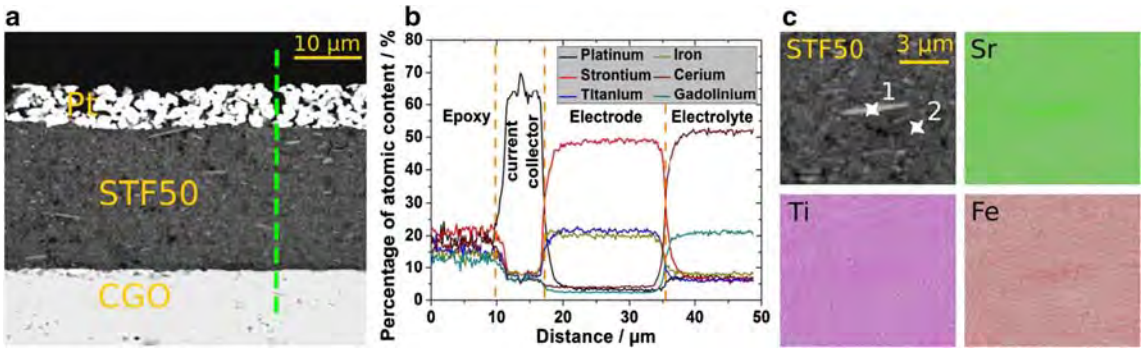

Fig. 6 SEM images of polished cross section of the porous STF50 electrode (**a**) investigated by EDS analysis: line (**b**), point and mapping (**c**)

the CGO/STF50 interface and more at the Pt/STF50 interface. Titanium is distributed uniformly throughout the thickness of the porous electrode; however, at the CGO/STF50 interface, a marked increase of Ti content is detected. The profile of iron shows an opposite trend to strontium; the amount of Fe increases towards the CGO/STF50 interface. Even though the processing and measurement temperature did not exceed a relatively low temperature of 800 °C, there is some visible cation diffusion already causing visible differences in the chemical composition.

Throughout the electrode material, some elongated particles can be seen, especially in the STF50 and STF70 samples. These platelet/rod-like particles were analysed by SEM/EDS in more detail, as presented in Fig. 6c and Fig. S6 in the Supplementary materials. The surrounding regular particles have very small particle sizes, well below 1 μm, whereas the length of this particular elongated particle reaches 10 μm. The chemical composition of the particles was analysed by EDS. Elemental maps (Fig. 6c) did not reveal any noticeable chemical composition difference, confirmed further by point analyses (points 1 and 2 in Fig. 6c), shown in Table 1. A slight increase in Sr in relation to Ti/Fe is the only difference between the particles, but it is possible that this deviation is rather small. The presence of these particles might originate from the mechanical milling step. They were not detected in the as-synthesised powders. Reports exist of STFx powder synthesis by mechanical alloying methods, suggesting their potential for reactions/deformation under mechanical loads. Nonetheless, due to the similar chemical composition, the elongated particles are not supposed to be harmful for the electrode performance.

Conclusions

Three different compositions of $SrTi_{1-x}Fe_xO_{3-\delta}$ ($x = 0.35$, 0.5, 0.7) were fabricated by solid-state reaction method and were analysed for their electrochemical performance depending on the sintering temperature. EIS measurements were analysed in terms of series (ohmic) and polarisation (ASR) contributions. For the three studied electrodes, the lowest ASR values were obtained for STF35 sintered at 1000 °C and for STF50 and STF70 when sintered at only 800 °C. The results show that iron has a strong effect on the electrode performance: the iron-rich sample showed high sinter-activity and low ASR ~ 20 mΩ cm^2 at 800 °C (obtained only for the electrode sintered at 800 °C). DRT analysis of the processes showed that STF70 differs from STF35 and STF50 in terms of the low frequency contribution, attributed to the adsorption of oxygen on the catalyst surface.

This work establishes the optimised sintering conditions of the studied powders. The studies will be further extended with a detailed EIS-DRT analysis, and the effects of surface modifications on the performance will be studied.

Funding information This work was supported by the "Understanding and minimisation of ohmic and polarisation losses in solid oxide cells by nanocrystalline ceramic and cermet functional layers" project funded by the National Science Centre, Poland, based on decision 2017/25/B/ST8/02275.

References

1. Baharuddin NA, Muchtar A, Somalu MR (2017) Short review on cobalt-free cathodes for solid oxide fuel cells. Int J Hydrog Energy 42:9149–9155
2. Rheinheimer W, Phuah XL, Wang H et al (2019) The role of point defects and defect gradients in flash sintering of perovskite oxides. Acta Mater 165:398–408
3. Rolle A, Mohamed HAA, Huo D et al (2016) Ca 3 Co 4 O 9 + δ , a growing potential SOFC cathode material: impact of the layer composition and thickness on the electrochemical properties. Solid State Ionics 294:21–30
4. Rolle A, Boulfrad S, Nagasawa K et al (2011) Optimisation of the solid oxide fuel cell (SOFC) cathode material Ca 3Co4O9-δ. J Power Sources 196:7328–7332
5. Perry NH, Kim JJ, Tuller HL (2018) Oxygen surface exchange kinetics measurement by simultaneous optical transmission relaxation and impedance spectroscopy: Sr(Ti,Fe)O $_{3-x}$ thin film case study. Sci Technol Adv Mater 19(1):130–141
6. Szymczewska D, Karczewski J, Chrzan A, Jasinski P (2017) CGO as a barrier layer between LSCF electrodes and YSZ electrolyte fabricated by spray pyrolysis for solid oxide fuel cells. Solid State Ionics 302:113–117
7. Tsipis EV, Kharton VV (2011) Electrode materials and reaction mechanisms in solid oxide fuel cells: a brief review. III Recent trends and selected methodological aspects. J Solid State Electrochem 15:1007–1040
8. Zhang Y, Knibbe R, Sunarso J et al (2017) Recent progress on advanced materials for solid-oxide fuel cells operating below 500 °C. Adv Mater 29:1–33
9. Zhang WW, Chen M, Povoden-Karadeniz E, Hendriksen PV (2016) Thermodynamic modeling of the Sr-Co-Fe-O system. Solid State Ionics 292:88–97
10. Muhammed Ali SA, Anwar M, Mahmud LS et al (2019) Influence of current collecting and functional layer thickness on the performance stability of La 0.6 Sr 0.4 Co 0.2 Fe 0.8 O 3-δ -Ce 0.8 Sm 0.2 O 1.9 composite cathode. J Solid State Electrochem 23:1155–1164
11. Jiang SP (2019) Development of lanthanum strontium cobalt ferrite perovskite electrodes of solid oxide fuel cells – a review. Int J Hydrog Energy 44:7448–7493

12. Kivi I, Aruväli J, Kirsimäe K et al (2017) Influence of humidified synthetic air feeding conditions on the stoichiometry of $(La_{1-x}Sr_x)_yCoO_{3-\delta}$ and $La_{0.6}Sr_{0.4}Co_{0.2}Fe_{0.8}O_{3-\delta}$ cathodes under applied potential measured by electrochemical in situ high-temperature XRD method. J Solid State Electrochem 21:361–369
13. Kogler S, Nenning A, Rupp GM et al (2015) Comparison of electrochemical properties of La0.6Sr0.4FeO3.δ; thin film electrodes: oxidizing vs. reducing conditions. J Electrochem Soc 162:F317–F326
14. Muhammed Ali SA, Anwar M, Baharuddin NA et al (2018) Enhanced electrochemical performance of LSCF cathode through selection of optimum fabrication parameters. J Solid State Electrochem 22:263–273
15. Garali M, Kahlaoui M, Mohammed B et al (2019) Synthesis, characterization and electrochemical properties of La2-xEuxNiO4+Δ Ruddlesden-Popper-type layered nickelates as cathode materials for SOFC applications. Int J Hydrog Energy 44:11020–11032
16. Nicollet C, Flura A, Vibhu V et al (2016) Preparation and characterization of Pr2NiO4+δ infiltrated into Gd-doped ceria as SOFC cathode. J Solid State Electrochem 20:2071–2078
17. Niemczyk A, Olszewska A, Du Z et al (2018) Assessment of layered La 2-x (Sr,Ba) x CuO 4-Δ oxides as potential cathode materials for SOFCs. Int J Hydrog Energy 43:15492–15504
18. Philippeau B, Mauvy F, Nicollet C et al (2015) Oxygen reduction reaction in Pr2NiO4+δ/Ce0.9Gd0.1O1.95 and La0.6Sr0.4Co0.2Fe0.8O3−δ/La0.8Sr0.2Ga0.8Mg0.2O2.80 half cells: an electrochemical study. J Solid State Electrochem 19:871–882
19. Zhu L, Hong T, Xu C, Cheng J (2019) A novel dual phase BaCe0.5Fe0.5O3-Δ cathode with high oxygen electrocatalysis activity for intermediate temperature solid oxide fuel cells. Int J Hydrog Energy 44:15400–15408
20. Gao Z, Ding X, Ding D et al (2018) Infiltrated Pr2NiO4 as promising bi-electrode for symmetrical solid oxide fuel cells. Int J Hydrog Energy 43:8953–8961
21. Li H, Sun LP, Feng Q et al (2017) Investigation of Pr 2 NiMnO 6 - Ce 0.9 Gd 0.1 O 1.95 composite cathode for intermediate-temperature solid oxide fuel cells. J Solid State Electrochem 21:273–280
22. Yoo C-Y, Bouwmeester HJM (2012) Oxygen surface exchange kinetics of SrTi1−xFexO3−δ mixed conducting oxides. Phys Chem Chem Phys 14:11759
23. Perry NH, Ishihara T (2016) Roles of bulk and surface chemistry in the oxygen exchange kinetics and related properties of mixed conducting perovskite oxide electrodes. Materials (Basel) 9:1–24
24. Jung W, Tuller HL (2008) Investigation of cathode behavior of model thin-film SrTi[sub 1−x]Fe[sub x]O[sub 3−δ] (x=0.35 and 0.5) mixed ionic-electronic conducting electrodes. J Electrochem Soc 155:B1194–B1201
25. Zhang SL, Wang H, Lu MY et al (2018) Cobalt-substituted SrTi0.3Fe0.7O3?d: a stable high-performance oxygen electrode material for intermediate-temperature solid oxide electrochemical cells. Energy Environ Sci 11:1870–1970
26. Yao C, Zhang H, Liu X et al (2019) A niobium and tungsten co-doped SrFeO 3-δ perovskite as cathode for intermediate temperature solid oxide fuel cells. Ceram Int 45:7351–7358
27. Fan L, Zhu B, Su PC, He C (2018) Nanomaterials and technologies for low temperature solid oxide fuel cells: recent advances, challenges and opportunities. Nano Energy 45:148–176
28. Jung W, Tuller HL (2009) Impedance study of SrTi1-xFexO3-δ (x = 0.05 to 0.80) mixed ionic-electronic conducting model cathode. Solid State Ionics 180:843–847
29. Oliveira Silva R, Malzbender J, Schulze-Küppers F et al (2017) Mechanical properties and lifetime predictions of dense SrTi1-xFexO3-δ(x = 0.25, 0.35, 0.5). J Eur Ceram Soc 37:2629–2636
30. Liu Y, Baumann S, Schulze-Küppers F et al (2018) Co and Fe co-doping influence on functional properties of SrTiO3for use as oxygen transport membranes. J Eur Ceram Soc 38:5058–5066
31. Hayden BE, Rogers FK (2018) Oxygen reduction and oxygen evolution on SrTi1 − xFexO3 − y (STFO) perovskite electrocatalysts. J Electroanal Chem 819:275–282
32. Song JL, Guo X (2015) SrTi<inf>0.65</inf>Fe<inf>0.35</inf>O<inf>3</inf> nanofibers for oxygen sensing. Solid State Ionics 278:26–31
33. Sarin N, Mishra M, Gupta G et al (2018) Elucidating iron doping induced n- to p- characteristics of strontium titanate based ethanol sensors. Curr Appl Phys 18:246–253
34. Zhu T, Fowler DE, Poeppelmeier KR et al (2016) Hydrogen oxidation mechanisms on perovskite solid oxide fuel cell anodes. J Electrochem Soc 163:F952–F961
35. Łącz A, Drożdż E (2019) Porous Y and Cr – doped SrTiO 3 materials — electrical and redox properties. J Solid State Electrochem 23:2989–2997
36. Nenning A, Volgger L, Miller E et al (2017) The electrochemical properties of Sr(Ti,Fe)$O_{3-\delta}$ for anodes in solid oxide fuel cells. J Electrochem Soc 164:F364–F371
37. Chrzan A, Karczewski J, Gazda M et al (2015) Investigation of thin perovskite layers between cathode and doped ceria used as buffer layer in solid oxide fuel cells. J Solid State Electrochem 19:1807–1815
38. Zhang S-L, Cox D, Yang H et al (2019) High stability SrTi 1−x Fe x O 3−δ electrodes for oxygen reduction and oxygen evolution reactions. J Mater Chem A:21447–21458
39. Cao Z, Fan L, Zhang G et al (2019) Titanium-substituted ferrite perovskite: an excellent sulfur and coking tolerant anode catalyst for SOFCs. Catal Today 330:217–221
40. Molin S, Lewandowska-Iwaniak W, Kusz B et al (2012) Structural and electrical properties of Sr(Ti, Fe)$O_{3-\delta}$ materials for SOFC cathodes. J Electroceram 28:80–87
41. Mroziński A, Molin S, Karczewski J et al (2019) Electrochemical properties of porous $Sr_{0.86}Ti_{0.65}Fe_{0.35}O_3$ oxygen electrodes in solid oxide cells: impedance study of symmetrical electrodes. Int J Hydrog Energy 44:1827–1838
42. Çelikbilek Ö, Jauffres D, Dessemond L et al (2016) A coupled experimental/numerical approach for tuning high-performing SOFC-cathode. ECS Trans 72:81–92
43. Yang G, Su C, Chen Y et al (2015) Cobalt-free SrFe<inf>0.9</inf>Ti<inf>0.1</inf>O<inf>3-δ</inf> as a high-performance electrode material for oxygen reduction reaction on doped ceria electrolyte with favorable CO<inf>2</inf> tolerance. J Eur Ceram Soc 35:2531–2539
44. Filatova EO, Egorova YV, Galdina KA et al (2017) Effect of Fe content on atomic and electronic structure of complex oxides Sr(Ti, Fe)O3 − δ. Solid State Ionics 308:27–33
45. Mroziński A, Molin S, Karczewski J et al (2019) The influence of iron doping on performance of $SrTi_{1-x}Fe_xO_{3-\delta}$ perovskite oxygen electrode for SOFC. ECS Trans 91:1299–1307
46. Wan TH, Saccoccio M, Chen C, Ciucci F (2015) Influence of the discretization methods on the distribution of relaxation times deconvolution: implementing radial basis functions with DRTtools. Electrochim Acta 184:483–499
47. Ciucci F, Chen C (2015) Analysis of electrochemical impedance spectroscopy data using the distribution of relaxation times: a Bayesian and hierarchical Bayesian approach. Electrochim Acta 167:439–454
48. Zheng K, Świerczek K, Polfus JM et al (2015) Carbon deposition and sulfur poisoning in SrFe<inf>0.75</inf>Mo<inf>0.25</inf>O<inf>3-δ</inf> and SrFe<inf>0.5</inf>Mn<inf>0.25</inf>Mo<inf>0.25</inf>O<inf>3-δ</inf> electrode materials for symmetrical SOFCs. J Electrochem Soc 162:F1078–F1087

49. Molin S, Gazda M, Jasinski P (2009) Conductivity improvement of $Ce_{0.8}Gd_{0.2}O_{1.9}$ solid electrolyte. J Rare Earths 27:655–660
50. Wang S, Kobayashi T, Dokiya M, Hashimoto T (2000) Electrical and ionic conductivity of Gd-doped ceria. J Electrochem Soc 147: 3606
51. Mogensen M, Sammes NM, Tompsett GA (2000) Physical, chemical and electrochemical properties of pure and doped ceria. Solid State Ionics 129:63–94
52. Hashim SS, Liang F, Zhou W, Sunarso J (2019) Cobalt-free perovskite cathodes for solid oxide fuel cells. ChemElectroChem:3549–3569
53. Riegraf M, Costa R, Schiller G et al (2019) Electrochemical impedance analysis of symmetrical Ni/gadolinium-doped ceria (CGO10) electrodes in electrolyte-supported solid oxide cells. J Electrochem Soc 166:F865–F872
54. Boukamp BA, Rolle A (2018) Use of a distribution function of relaxation times (DFRT) in impedance analysis of SOFC electrodes. Solid State Ionics 314:103–111
55. Clematis D, Barbucci A, Presto S et al (2019) Electrocatalytic activity of perovskite-based cathodes for solid oxide fuel cells. Int J Hydrog Energy 44:6212–6222
56. Dogdibegovic E, Guan W, Yan J et al (2016) Activity and stability of (Pr1-xNdx)2NiO4 as cathodes for solid oxide fuel cells: II. Electrochemical performance and performance durability. J Electrochem Soc 163:F1344–F1349
57. Merkle R, Maier J (2008) How is oxygen incorporated into oxides? A comprehensive kinetic study of a simple solid-state reaction with SrTiO3 as a model material. Angew Chem Int Ed 47:3874–3894
58. Rothschild A, Menesklou W, Tuller HL, Ivers-Tiffée E (2006) Electronic structure, defect chemistry, and transport properties of SrTi 1-xFe xO 3-y solid solutions. Chem Mater 18:3651–3659
59. Jung W, Tuller HL (2009) Impedance study of SrTi(1-x)Fe(x)O(3-delta) (x=0.05 to 0.80) mixed ionic-electronic conducting model cathode. Solid State Ionics 180:843–847
60. Metlenko V, Jung W, Bishop SR, Tuller HL, de Souza RA (2016) Oxygen diffusion and surface exchange in the mixed conducting oxides SrTi1-: YFeyO3- δ. Phys Chem Chem Phys 18(42):29495–29505
61. Samson A, Sogaard M, Knibbe R, Bonanos N (2011) High performance cathodes for solid oxide fuel cells prepared by infiltration of La[sub 0.6]Sr[sub 0.4]CoO[sub 3 - delta] into Gd-doped ceria. J Electrochem Soc 158:B650–B659
62. Hjalmarsson P, Søgaard M, Mogensen M (2008) Electrochemical performance and degradation of (La0.6Sr0.4)0.99CoO3 - δ as porous SOFC-cathode. Solid State Ionics 179:1422–1426
63. Ju J, Xie Y, Wang Z et al (2016) Electrical performance of nanostructured La0.6Sr0.4Co0.2Fe0.8O3-δ impregnated onto yttria-stabilized zirconia backbone. J Electrochem Soc 163:F393–F400
64. Cheng Y, Yu AS, Li X et al (2016) Preparation of SOFC cathodes by infiltration into LSF-YSZ composite scaffolds. J Electrochem Soc 163:F54–F58

4.4. Article IV

Title: **Study of Oxygen Electrode Reactions on Symmetrical Porous $SrTi_{0.30}Fe_{0.70}O_{3-\delta}$ Electrodes on $Ce_{0.8}Gd_{0.2}O_{1.9}$ Electrolyte at 800 °C – 500 °C**

Authors: **Aleksander Mroziński**, Sebastian Molin, Piotr Jasiński

Journal: Electrochimica Acta (2020) vol 346, 136285 (Special issue[1])

DOI: 10.1016/j.electacta.2020.136285

Impact Factor (2020): 6.901

In this paper, a detailed qualitative and quantitative evaluation of the occurring electrochemical processes of the STFx (x = 0.70, STF70) material that had the most promising results in Article III was performed. To determine the rate-determining step of the electrochemical reaction, EIS tests of symmetrical samples were performed at different temperatures and pO_2. The DRT analysis was also extended to include selection of the refined parameters.

My original contribution to this publication was:

- Preparation of high-quality reproducible STF70 symmetrical electrodes.
- Detailed electrical and electrochemical characterisation of the symmetrical electrodes.
- Detailed study of the DRT fitting parameters influencing the resulting deconvolution.
- Determination of the electrochemical processes occurring at the electrodes with the application of DRT and clarification of the rate-determining reaction of the porous electrode.

[1] Special issue of Electrochimica Acta titled: Distribution of relaxation time analysis for solid state electrochemistry

Table 5 CRediT author statement Article IV: "Study of Oxygen Electrode Reactions on Symmetrical Porous $SrTi_{0.30}Fe_{0.70}O_{3-\delta}$ Electrodes on $Ce_{0.8}Gd_{0.2}O_{1.9}$ Electrolyte at 800 °C - 500 °C"

Author	CRediT author statement	Signature
Aleksander Mroziński	Investigation; Data curation; Visualization; Writing - review & editing	A. Mroziński
Sebastian Molin	Methodology; Writing - original draft; Conceptualization	Molin Sebastian
Piotr Jasiński	Resources; Writing - review & editing; Supervision; Funding acquisition; Methodology	

Electrochimica Acta 346 (2020) 136285

Contents lists available at ScienceDirect

Electrochimica Acta

journal homepage: www.elsevier.com/locate/electacta

Study of oxygen electrode reactions on symmetrical porous $SrTi_{0.30}Fe_{0.70}O_{3-\delta}$ electrodes on $Ce_{0.8}Gd_{0.2}O_{1.9}$ electrolyte at 800 °C–500 °C

Aleksander Mroziński *, Sebastian Molin , Piotr Jasiński

Laboratory of Functional Materials, Faculty of Electronics, Telecommunications and Informatics, Gdańsk University of Technology, ul. G. Narutowicza 11/12, 80-233, Gdańsk, Poland

ARTICLE INFO

Article history:
Received 15 February 2020
Received in revised form
17 April 2020
Accepted 20 April 2020
Available online 21 April 2020

Keywords:
Solid oxide cells
Oxygen electrodes
Mixed ionic electronic conductor
Impedance spectroscopy
Distribution of relaxation times

ABSTRACT

Iron doped strontium titanates ($SrTi_{1-x}Fe_xO_{3-\delta}$) are an interesting mixed ionic-electronic conductor model used to study basic oxygen reduction/oxidation reactions. In this work, we performed an impedance spectroscopy study on symmetrical porous $SrTi_{0.30}Fe_{0.70}O_{3-\delta}$ (STF70) electrodes on a ceria-based electrolyte. The sample was measured in varying oxygen concentration: from 0.3% to 100% in 800 °C–500 °C temperature range. Low polarisation resistance (e.g. <125 mΩ cm^2 at 600 °C in the air) values were obtained, showing an overall high performance of the STF70 electrode. Impedance data analysis was assisted by the distribution of relaxation times method, which allowed an equivalent electrical circuit to be proposed comprising of two resistance/constant phase element sub-circuits connected in series. The medium frequency contribution, with a characteristic frequency of ~2000 Hz at 800 °C in air, originates most probably from possible surface diffusion followed by charge transfer reaction limitation, whereas the lower frequency contribution (characteristic frequency <10 Hz) is due to gas-phase diffusion.

1. Introduction

Electrochemical impedance spectroscopy (EIS) is a powerful method for the determination of the electrochemical properties of materials in an almost unlimited number of applications. For example, EIS is used extensively to determine the performance of electrodes in solid oxide cells (SOCs) [1–3], in biosensors [4–6], in oxygen sensors [7], in pH sensors [8,9] or determining properties of conductive polymers like polypyrrole [10,11]. In the case of SOCs, the polarisation resistance of the electrodes is usually measured as a function of the materials preparation methodology (e.g. sintering temperature, particle size, resulting porosity), measurement temperature, and oxygen partial pressure. Often, the frequency response (impedance spectra) of the electrodes shows quite a complex result, not easily fitted with simple circuits. Over the years, useful tools have been developed to help in the analysis of these complex phenomena. The method that has been growing in popularity in recent years is the distribution of relaxation times (DRT) analysis [12–18]. It became popular due to the availability of a free software tool developed by the prof. Ciucci group – DRTTools [19–23]. The software offers simple control over the most important parameters required to successfully and reliably use the DRT method.

DRT offers the possibility of differentiation of the measured spectra of several electrochemical processes when characteristic frequencies overlap. Quite a few research groups have used this tool to analyse the electrodes of SOCs. Both the oxygen and fuel electrodes were studied to devise their mechanisms.

Płończak et al. used DRT to determine the electrochemical processes on thin-film dense (La,Sr)$MnO_{3-\delta}$ electrodes. DRT allowed the number of contributing processes to be resolved. For a description of the symmetrical electrode system, three R-CPE elements connected in series were used (with characteristic frequencies at 900 °C of ~1 kHz, ~30 Hz, and 1500 Hz). Clematis et al. analysed $Ba_{0.5}Sr_{0.5}Co_{0.8}Fe_{0.2}O_{3-\delta}$ oxygen electrodes. DRT was used to determine the effects of electrode polarisation in a 3-electrode cell, allowing the polarisation influenced processes to be seen. In addition to the oxygen electrode, fuel electrodes were also studied [15,24–26]. DRT can also be used to study full fuel cells, where

* Corresponding author.
E-mail address: aleksander.mrozinski@pg.edu.pl (A. Mroziński).

https://doi.org/10.1016/j.electacta.2020.136285

there are many simultaneous electrochemical reactions. Chrzan et al. studied a solid oxide cell with infiltrated electrodes and the effects of ageing. As many as 5 different processes were determined [27]. Tong et al. studied large-area cells with $La_{0.6}Sr_{0.4}CoO_{3-\delta}$ electrodes. A full cell model with 5 contributing processes was also devised based on DRT analysis [28]. Also, full polymer electrolyte cells were studied using DRT. The analysis revealed as many as 7 contributions. Moreover, DRT can be used in batteries and other systems [29,30].

Oxygen electrode reactions, including oxygen reduction and oxidation reactions, are one of the most important chemical/electrochemical reactions studied. Even though these processes have been studied for many years, there is still no specific and universal model for the reactions at high temperatures. Due to the complex nature of the process, it is highly dependent on the conditions (temperature, oxygen concentration), as well as on the material and its preparation (defects, particle size, etc). Developing reliable tools for the determination of the electrochemical processes is an important and challenging task.

A reversible oxygen electrode reaction is a complex process consisting of several elementary steps. One possible pathway for the reaction is presented below (according to Kröger-Vink notation) [31,32]:

Step 1) Mass transfer of O_2 molecules in the gas phase and adsorption on the electrode surface: $O_{2(g)} \leftrightarrow O_{2(ads)}$;
Step 2) Dissociation of the adsorbed molecules: $O_{2(ads)} \leftrightarrow 2O_{(ads)}$;
Step 3) Charge transfer to oxide ion electrolyte: $O_{(ads)} + 2e^- + V_{\ddot{O}} \leftrightarrow O_O^x$;
Step 4) Mass transfer of oxide ions in the bulk of the electrode/electrolyte: $V_{\ddot{O}(electrode)} \leftrightarrow V_{\ddot{O}(electrolyte)}$;

To determine the rate-limiting step of the oxygen electrode reaction, the electrode resistance can be studied as a function of both temperature and oxygen partial pressure (pO_2) [33]. The following generalised relation can be used to describe the electrode resistance (R_{el}):

$$\frac{1}{R_{el}} \propto (pO_2)^n \qquad \text{[Equation 1]}$$

Different n-values indicate the type of oxygen species involved in the electrochemical reaction [33–35]. An inverse proportionality relation (n = 1) indicates the molecular oxygen involved (O_2), a $(pO_2)^{0.5}$ dependence indicates the contribution of atomic oxygen (O). The value of n = 3/8 is possibly related to the partial reduction of the atomic oxygen ($O_{(ads)} + e^- \rightarrow O^-_{ads}$). For n = 1/4, the charge transfer reaction has been described as the limiting factor. The studies of electrode polarisation as a function of both the temperature and oxygen concentration are thus a powerful tool to determine the rate-determining reactions. These are however generally complex measurements which can be affected by many factors [36,37], thus the results should be treated with caution.

Iron substituted strontium titanates, with a general formula of $SrTi_{1-x}Fe_xO_{3-\delta}$ are model materials used for studies of mixed ionic-electronic conductors [36,38–40]. Depending on the iron content, the properties of the materials (electrical conductivity, surface exchange, and diffusion coefficient) can be altered and their effects studied [41,42]. These materials have been shown to offer promising performance as catalysts for a number of reactions [43,44], as oxygen electrodes for solid oxide cells [45,46], and found use in resistive oxygen gas sensors [47,48]. Our previous study of the electrochemical processes on porous $SrTi_{0.65}Fe_{0.35}O_{3-\delta}$ (STF35) electrodes revealed three different contributions. For a description of the high-frequency contribution (characteristic frequency of ~200 Hz at 800 °C in air), a diffusion related Gerischer equivalent element was used. It was ascribed to the diffusion of the oxygen ion in the STF35. Based on this work, it is interesting to study the individual contributions for higher Fe-substituted materials, which have higher total electrical conductivities, lower band gaps and higher oxygen vacancy concentrations [36,42,49].

In this work, we study $SrTi_{0.30}Fe_{0.70}O_{3-\delta}$ perovskite for its oxygen electrode reaction processes based on porous symmetrical electrode configurations. STF70 is an interesting electrode material with high ionic conductivity, catalytic activity, and moderate electronic conductivity. By application of electrochemical impedance spectroscopy coupled with the distribution of relaxation times analysis, we determine the equivalent circuit and then obtain the individual contributions and follow their temperature and oxygen concentration dependent behaviour. This allows for the determination of the rate-limiting processes and opens the possibilities to improve the materials in the future.

2. Experimental

$SrTi_{0.30}Fe_{0.70}O_{3-\delta}$ (STF70) powders were fabricated by a solid state reaction method, according to the details in Ref. [46,50]. Stoichiometric amounts of reagent grade $SrCO_3$, TiO_2 (EuroChem, Poland), and Fe_2O_3 powders (Chempur, Poland) were weighed and mixed in a planetary ball mill (Fritsch Pulverisette7). The mixed powders were pressed into a large pellet (diameter of ~3 cm, thickness ~1.5 cm), calcined at 1200 °C for 15 h, followed by crushing, pressing of a new pellet and calcining again at 1200 °C to form the single phase material. To measure the electrical conductivity of the bulk STF70, a pellet was prepared by compacting a powder and sintering at 1200 °C for 2 h. To obtain fine-grained powder for paste preparation, it was milled in a planetary mill with ZrO_2 balls for 12 h and thermally treated at 600 °C. From the powder, the electrode paste was prepared. The powder was mixed with a commercial paste vehicle (403, ESL, USA) in a weight ratio of 2:3. The paste was mixed in a planetary ball mill with zirconia balls.

For symmetrical electrode substrates, $Ce_{0.8}Gd_{0.2}O_{1.9}$ (CGO) pellets were prepared. Commercial CGO powder (DKKG, Japan) was pressed into cylindrical pellets of ~1 mm thickness and 16 mm diameter. No additives were used for pressing. The green pellets were sintered at 1400 °C for 8 h. The porosity of the pellets after the sintering was <4% measured by Archimedes method. After the sintering, the planar surfaces of the CGO pellets were polished using diamond suspensions (particle size ~3 μm). After the polishing step, the individual pellets had a thickness of ~600 μm.

Electrical conductivity measurements of the bulk CGO and STF70 pellets were performed using the van der Pauw method. Platinum wires were fixed to the sample outer edges by silver paste (DuPont 4922 N, USA). The measurement was performed using Keithley 2400 and an automated data logging system in the temperature range of 900–450 °C in 100% O_2, 20% O_2, and 1% O_2 for the STF70 and CGO.

Using the pre-prepared paste and the CGO pellets, symmetrical electrode samples were produced. The electrodes were screen-printed (DEK 65, UK) on the two sides and sintered at 800 °C for 2 h. The resulting electrode area was 0.4 cm^2. For current collection, the surfaces of the electrodes were painted with Pt paste (ESL 5542, USA), dried and fired at 600 °C. The surface roughness of the electrodes was measured using a Keyence laser scanning microscope.

The impedance measurements were performed in a 4-wire compression cell with Au meshes pressed against the STF70/Pt electrodes. The measurement cell was placed inside a sealed quartz tube in order to control the atmosphere. A Novocontrol Alpha-A

with a ZG-4 interface was used for measurement of the impedance spectra. Analyses were carried out at 25 mV amplitude in the frequency range of 3 MHz to 0.05 Hz. The temperatures were 800 °C, 700 °C, 600 °C, and 500 °C. A controlled oxygen concentration (100%, 80%, 50%, 30%, 20%, 15%, 10%, 5%, 2.5%, 1%, 0.3%) was obtained by mixing high precision reference gas mixtures (oxygen in argon): 100%, 20%, 1%, and 0.01% (100 ppm) using mass flow meters (Aalborg, USA).

For plotting and analysis of the impedance data, the obtained impedance spectra were re-calculated for the electrode area (0.4 cm^2). In the case of polarisation resistance, the value was further divided by a factor of 2 to accommodate the two identical, symmetrical interfaces.

Impedance spectra were fitted using the Elchemea Analytical web-tool developed by the Technical University of Denmark (www.elchemea.com, DTU Energy).

The collected impedance spectra were analysed by the distribution of relaxation times method. For this purpose, the freely available DRTTool from the prof. Ciucci group was utilised. Prior to use, the spectra were corrected for the inductance of the rig. Different parameters for the DRT were used to evaluate the spectra, as described in the results section.

The microstructural characterisation of the electrodes was performed by scanning electron microscopy (SEM) using a Thermo Fischer Phenom XL microscope with an integrated energy dispersive x-ray spectrometer. For analysis of the cross-sections, the samples were vacuum embedded (CitoVac, Struers) in epoxy (EpoFix, Struers) and polished down to a 1 μm finish.

3. Results and discussion

3.1. Sample general properties

The microstructure of the symmetrical STF70 electrodes on the CGO electrolyte is shown in Fig. 1A and B. Screen-printing of the electrodes results in a macroscopically uniform microstructure of the electrodes. Higher magnification images reveal the thickness of the electrodes to be ~20 μm, with a porosity of ~35%. The particles visible in the electrodes have sub-micrometre sizes. The surface roughness parameter value, $S_a = 0.41$ μm, confirms a smooth surface. The remnants of the painted Pt current collector are still visible. The thickness of the CGO pellet is ~600 μm, which was also measured with micro-caliper. The sample shown had already undergone the measurement procedure, which included several thermal cycles and many oxygen concentration changes. The microstructure shows no sign of cracks or delamination, which indicates good compatibility of the STF70 with the CGO substrate, even though a mismatch of thermal expansion coefficient (TEC) exists. The previously measured TEC of the bulk STF70 is ~23×10^{-6} K^{-1} [50], whereas the TEC of the CGO is ~13×10^{-6} K^{-1}. The difference in TEC values is high (~10×10^{-6} K^{-1}), but some other electrode materials with such a large TEC mismatch are successfully used (e.g. $La_{0.6}Sr_{0.2}Co_{0.2}Fe_{0.8}O_{3-\delta}$, $La_{0.6}Sr_{0.4}CoO_{3-\delta}$ with TECs >18 [51,52]).

The total electrical conductivities of the bulk CGO and STF70 materials were measured on sintered pellets by the van der Pauw method, and the results are presented in Fig. 2A. The electrical conductivity of ceria, representing purely ionic O^{2-} conduction, is much lower than the conductivity of the iron substituted strontium titanate, which is a mixed ionic-electronic conductor. At 800 °C, the ionic conductivity of ceria is ~100 mS cm^{-1}, and decreases to ~5 mS cm^{-1} at 500 °C, with an activation energy of 0.69 eV. These are typical values for doped ceria electrolytes [53]. The measured total conductivity of STF70 in air is ~16 S cm^{-1} in air at 800 °C. For STF70, the exact ionic and electronic conductivity contributions are not specifically reported. Based on the results of a series of iron substituted strontium titanates, the electronic transference number is ~0.98, with the ionic conductivity at the level of ~40 mS cm^{-1} at 800 °C [54]. As presented in Fig. 2A, the electrical conductivity of CGO, in this oxygen partial pressure range (0.3%—100% O_2), due to the ionic regime of operation, is not dependent on the oxygen concentration [53]. STF70 is a typical p-type conductor, with its electronic conductivity increasing with increasing oxygen content (in the high pO_2 range). According to Ref. [42], in the temperature range 750 °C—1000 °C, based on the defect chemistry description, the total electrical conductivity follows the conductivity ~ $(pO_2)^{1/4}$ behaviour, which indicates that the oxygen vacancy concentration is independent of the partial pressure. Thus the mobility/concentration changes of the majority carriers (p-type) dominate the total conduction of STF70 in the studied oxygen concentration range.

Fig. 2B and C summarise the results obtained from the impedance measurements on the symmetrical electrodes. The data is divided into the ohmic - R_s (Fig. 2B) and polarisation - R_{pol} (Fig. 2C) contributions, shown for three oxygen levels (100%, 20%, and 1%). The spectra and underlying electrochemical processes will be analysed in detail in the following sections. From Fig. 2B and C, it is evident that the oxygen concentration change has a negligible influence on the ohmic part, and a large influence on the polarisation contribution.

3.2. Impedance spectra and distribution of relaxation times analysis

For assistance in the determination of the electrochemical processes occurring on the STF70 electrodes, the DRT method was used for impedance spectra analysis. At the first step, we tried to vary the analysis parameters in order to obtain satisfactory results. A representative spectrum, used as a model example here, measured at 800 °C in 1% O_2 is presented in Fig. 3A. The DRT of the presented spectra is shown in Fig. 3B. Different λ parameters (λ — regularisation parameter) were used for qualitative analysis. A

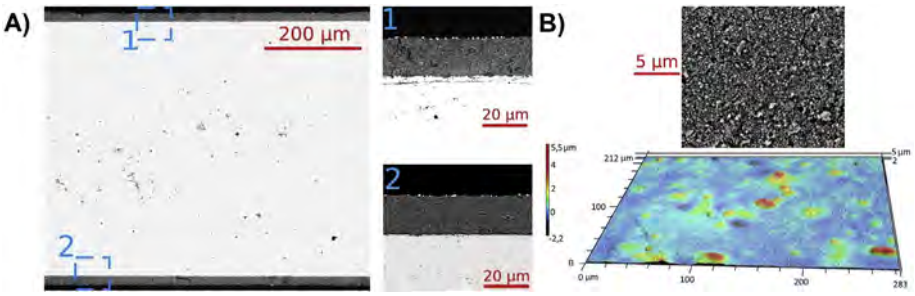

Fig. 1. A) SEM polished cross-section image of the symmetrical STF70 electrodes on CGO electrolyte, B) surface morphology of the STF70 electrode including SEM surface image and laser microscope profilometry.

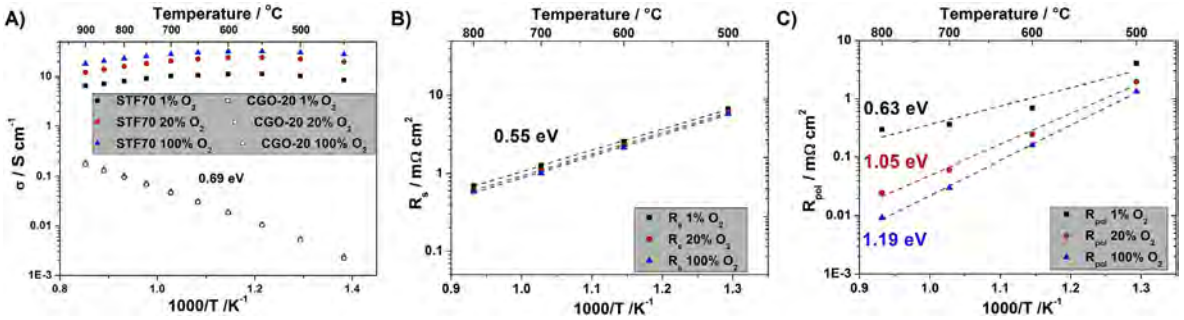

Fig. 2. A) Electrical conductivity of CGO and STF70, B) ohmic, and C) polarisation resistances of the symmetrical STF70 electrodes.

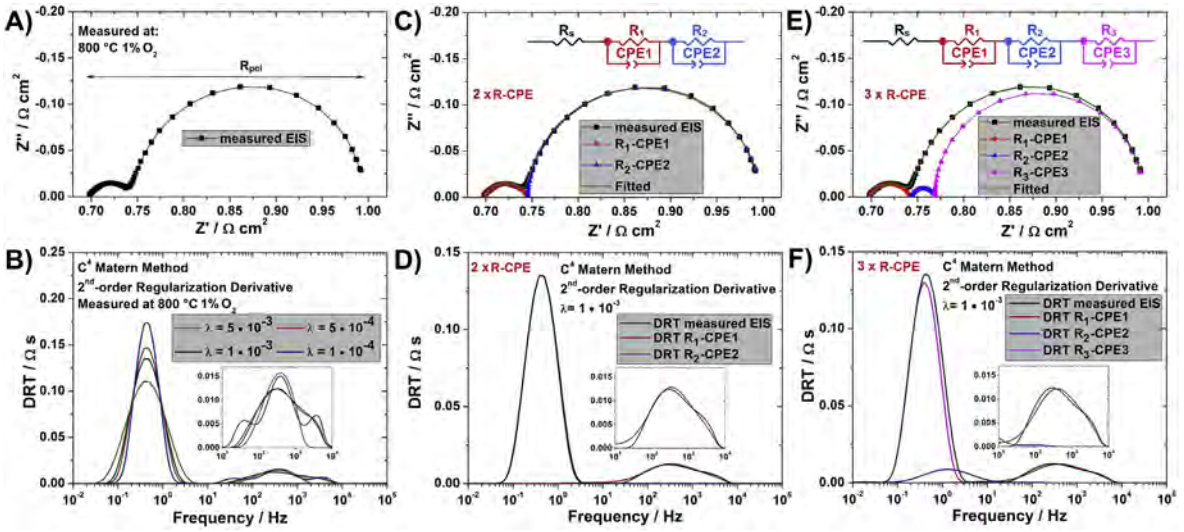

Fig. 3. A) Exemplary impedance spectra measured at 1% O_2 at 800 °C used as a model result, B) the effect of different λ-values on the resulting DRT spectra, C) spectra with fitted two R-CPE elements with D) corresponding DRT analysis, E) spectra with fitted three R-CPE elements with F) corresponding DRT analysis.

change of λ results in the number of "peaks" visible at higher frequencies, and in the lowering and widening of the lower frequency contribution. For $\lambda = 1 \times 10^{-4}$, there are at least three peaks visible around ~300 Hz. Increasing the lambda parameter to 5×10^{-4} and 1×10^{-3} results in a change of shape of the DRT spectra. The process at higher frequencies now seems to have a shoulder at the higher frequencies only. Analysing simulated simple R-CPE elements (not shown here), this broadening of the DRT peaks does not come from another R-CPE contribution, but is just a result of the fitting of a single R-CPE element. For $\lambda = 5 \times 10^{-3}$, only a single broader peak can be found around ~300 Hz. Based on this simple analysis, the selection of λ can have a profound effect on the number of peaks determined by DRT. On the basis of the performed analyses, it was chosen to further study an equivalent circuit consisting of two R-CPE elements connected in series and perform a DRT with $\lambda = 1 \times 10^{-3}$.

Unfortunately, hardly any publications are reporting the specific parameters used for the DRT analysis. For example, Weiß et al. used a value of $\lambda = 1 \times 10^{-5}$, and they obtained and analysed 7 different peaks for a polymer electrolyte cell. For comparison, Heinzmann et al. showed the influence of λ on the resulting DRT spectra for polymer electrolyte membrane cells [55]. They used a value of $\lambda = 1 \times 10^{-3}$, which provided "a compromise between selectivity, low residuals, and oscillation avoidance". For lower λ values, more peaks appeared that were believed to be not true.

Fig. 3C shows the same spectra as Fig. 3A, with added individual contributions calculated according to the developed equivalent circuit consisting of two R-CPE elements. A very good fit is obtained, which is also confirmed by the back-calculation of the DRT based on the fitted R-CPE parameters, as presented in Fig. 3D. To obtain individual R-CPE equivalent circuit values, the complex non-linear least-squares fitting (NLLS) Elchemea software was used. So the DRT was only used to determine the number of equivalent circuit elements. In principle, the DRT can also be used to calculate the contribution resistances (given by the peak area), but this approach is not well proven. As we will briefly show (Fig. 3 and its discussion), DRT transforms the data and can alter it considerably depending on the used parameters, which will influence the fitting procedure results. It would be also problematic for non-trivial elements, for example the Gerischer element, which in DRT is hard to resolve, but is usually well treated by dedicated impedance software. Use of the well-developed impedance fitting tools seems more convenient and much more established at this stage in the authors' opinion. For additional analysis, the spectrum from Fig. 3A was also fitted with three R-CPE elements, as presented in Fig. 3E. The obtained fit is also very good in the Nyquist plot, but the back-calculated DRT spectra, presented in Fig. 3F, shows a clear deviation from the DRT of the measured spectra. A new contribution with a peak frequency of ~1.5 Hz can be noticed between the low and higher frequency peaks. Thus the DRT can also be used as an important validation tool for the fitting procedure, and can assist in selecting the proper equivalent circuits.

Based on the data presented in Fig. 3, we selected the following parameters for the DRT analysis of all of the spectra: regularisation parameter $\lambda = 1 \times 10^{-3}$, C^4 Matérn discretisation method, and the regularisation derivative: 2nd-order. In our experience, for this set of data, these are the most reproducible and dependable parameters, which can also be confirmed by the equivalent circuit fitting and back-calculation of the DRT, and the similarity of the original and back-calculated DRT results.

Below, we show the spectra and their respective DRT analyses for varying oxygen concentrations (5%, 20%, and 100%) at 700 °C (Fig. 4) and for varying temperatures (800 °C, 700 °C, and 600 °C) measured in 15% O_2 (Fig. 5). The separate peaks, corresponding to the two R-CPE equivalent processes, have been deconvoluted and inserted in the spectra figures.

The oxygen content has a clear influence on the lower frequency contribution. This contribution is clearly visible for 5% O_2, still noticeable for 20% O_2, and seems to disappear in pure O_2. Also, the ohmic resistance and the higher frequency contribution seem to change with oxygen concentration, but to a lesser extent. The DRT analysis of the presented spectra shows good agreement between the measured and fitted spectra. The characteristic (peak) frequencies for the processes are ~120 Hz and ~1 Hz for the higher and lower frequency contributions, respectively.

The exponents for the CPE elements (denoted here as γ-values) were relatively constant for the two contributions. For the higher frequency contribution, which is an apparently depressed semicircle, the γ-value was ~0.70–0.80, whereas, for the lower frequency contribution, the γ-value was between 0.90 and 1.00. As a general comment, we would like to note that the measured polarisation resistance values are quite low, i.e. only ~10 mΩ cm^2 in 100% O_2 at 800 °C (measured resistance of ~50 mΩ cm^2).

The influence of temperature on the impedance spectra is presented in Fig. 5. Strong temperature activation is visible, the resistance of the higher frequency contribution (R_1-CPE1) changes from ~15 mΩ cm^2 at 800 °C to >250 mΩ cm^2 at 600 °C. The lower frequency contribution seems constant, so its relative magnitude vs. R_1-CPE1 changes. At high temperatures, even at a relatively high oxygen concentration of 15%, the resistance of the first and second elements are comparable.

Together with an ohmic resistance (R_s), the proposed equivalent circuit, consisting of two R-CPE sub-circuits connected in series, fit well to all of the measured spectra (see Fig. 3C). The full equivalent circuit of the symmetrical porous electrode cell is thus (according to Boukamp's notation [56]): $R_s(R_1\text{-CPE1})(R_2\text{-CPE2})$. The sum of R_1-CPE1 and R_2-CPE2 corresponds to the R_{pol}. The obtained values of the parameters of each equivalent circuit element were calculated (resistances and capacitances) and analysed individually in details as a function of oxygen concentration (0.3%–100% O_2) and

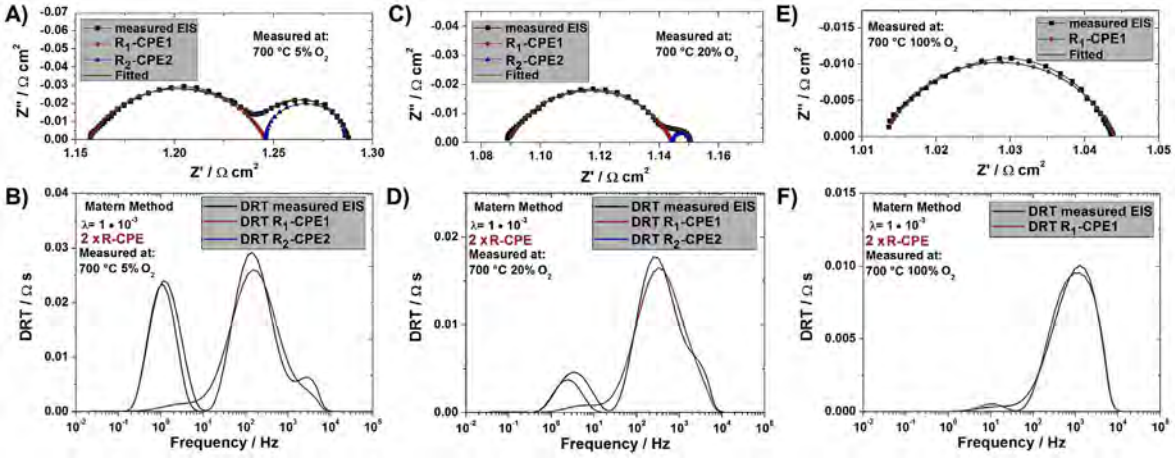

Fig. 4. Impedance spectra measured at 700 °C in different oxygen concentrations and their corresponding DRT plots: A,B) 5% O_2, C,D) 20% O_2, E,F) 100% O_2.

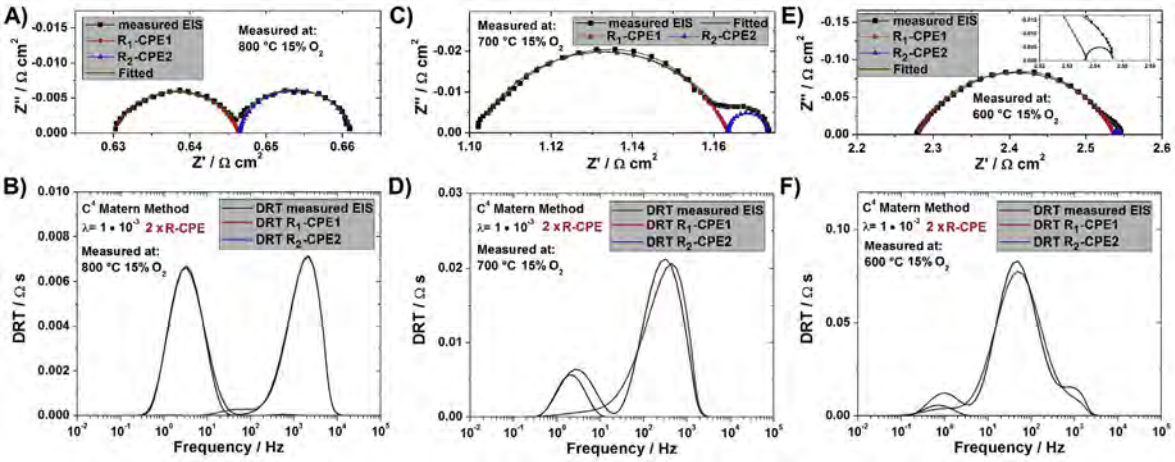

Fig. 5. Impedance spectra measured in 15% O_2 at different temperatures, and their corresponding DRT plots: A,B) 800 °C, C,D) 700 °C, E,F) 600 °C.

temperature (800 °C–500 °C).

3.3. Analysis of ohmic resistance

The ohmic (non-frequency dependent) contribution in the impedance spectra can be the result of several factors. Mainly, it includes the contributions stemming from the electrical conductivity of the thick CGO electrolyte, and of the relatively thin electrodes.

Fig. 6 presents ohmic resistance contribution of the equivalent circuit vs. the oxygen concentration and the temperature. The ohmic resistance changes slightly with the changing oxygen concentration, with a lowering of the resistance at increasing oxygen concentration. This indicates a possible p-type conduction mechanism. The CGO electrolyte, at this pO_2 range, is a pure ionic conductor, so its conductivity can be assumed to be oxygen concentration independent. The electrical conductivity of the STF70 electrode is influenced by the oxygen concentration change, as presented in Fig. 2A. Rothschild et al. showed that the resistivity of STF70 follows the relationship: $R \sim pO_2^{-0.25}$ [42]. Linear fitting of the data shown in Fig. 6 results in slopes in the range −0.03 to −0.05, so much lower than reported for bulk STF70, but it is measured on top of the ceria pellet, which constitutes most of the resistance. Thus the oxygen concentration has a relatively low, but measurable influence on the ohmic resistance of the samples.

The temperature dependence of the conductivity, presented as an Arrhenius plot in Fig. 6B, shows Arrhenius-type temperature-activated behaviour, with activation energy equal to ~0.55 eV. This value is a bit smaller than what was obtained using the van der Pauw method, because the STF70 electrode slightly influences the overall conductivity of the layered structure. This is, however, generally in line with the electrical conductivity activation of ceria-based materials [53,57]. The STF70 has a much lower activation energy and higher conductivity level, and thus the total resistivity is dominated by the CGO.

The ohmic resistance of the CGO at 800 °C, based on the thickness and measured conductivity value (data from Fig. 2A), is ~0.6 Ω cm^2, whereas the ohmic contribution of the STF70 electrodes is only a few mΩ cm^2 at maximum, due to the much higher conductivity and lower thickness. The sum value of ~0.6 Ω cm^2 is very close to the R_s value determined from impedance spectroscopy, which means that no large current constriction/current collection effects take place. The ohmic resistance of the porous electrodes, even in the case of relatively low electric conductivity (assuming a safe, low value of only 10 S cm^{-1} at 800 °C) is very low, below a mΩ cm^2, which represents a negligible value compared to the polarisation resistance, which will dominate the electrode response.

3.4. Analysis of polarisation resistance contributions

Based on the DRT analysis and initial fitting tests, the overall polarisation resistance can be well described by two R-CPE elements for most of oxygen concentrations. For high oxygen content (over 30% O_2), R_2-CPE2 contribution becomes negligible. The relative magnitude of R_1-CPE1 to R_2-CPE2 is very high and fitting by two R-CPE is not possible. In the equivalent circuit used, the higher frequency process, fit to R_1-CPE1, and lower frequency process fit to R_2-CPE2. The determined electrical properties of these elements, determined as a function of oxygen concentration and temperature, are presented in Figs. 7 and 8, respectively.

The higher frequency resistance contribution (R_1) is presented as a function of oxygen concentration in Fig. 7A (see also data in

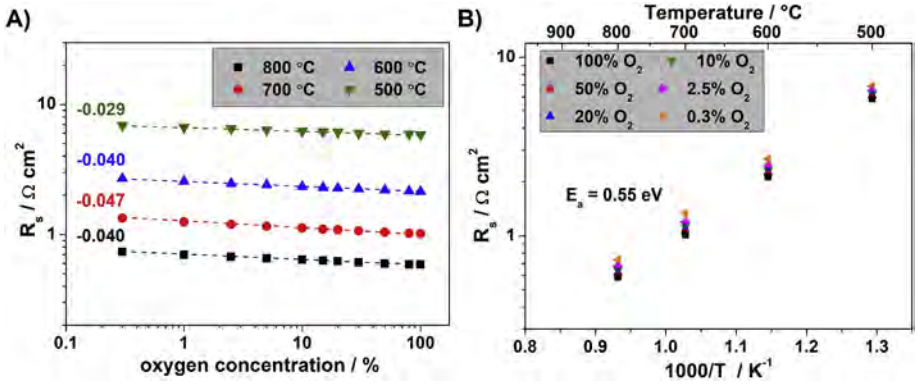

Fig. 6. Ohmic resistance (R_s) of the symmetrical electrodes on CGO as a function of A) oxygen concentration, and B) temperature.

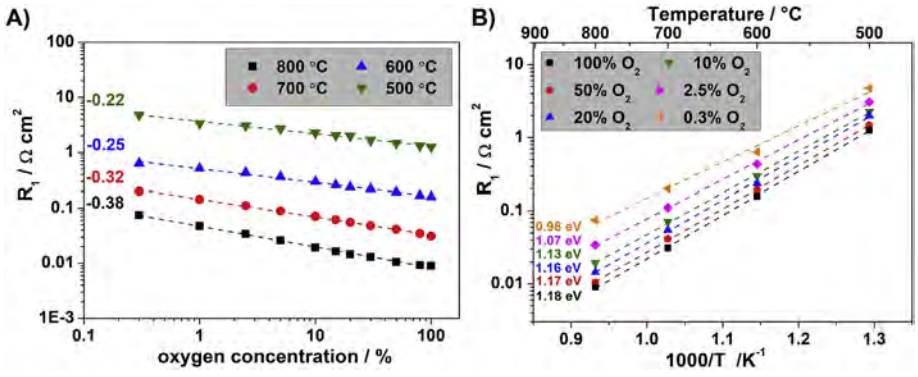

Fig. 7. R_1 resistance values of the symmetrical electrodes on CGO as a function of A) oxygen concentration, and B) temperature.

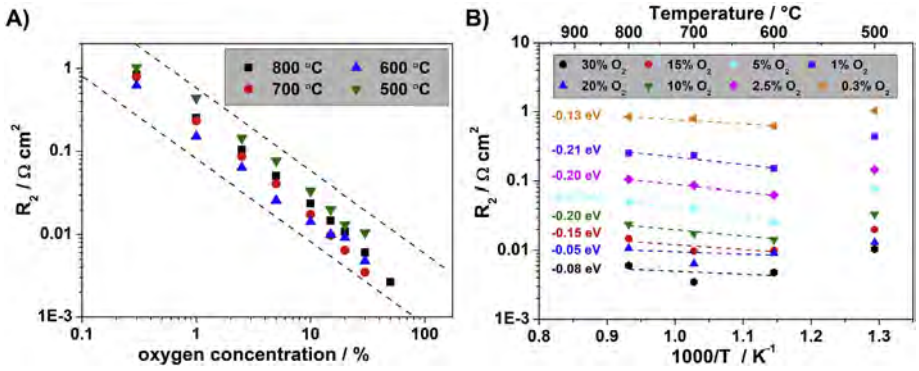

Fig. 8. R_2 resistance values of the symmetrical electrodes on CGO as a function of A) oxygen concentration, and B) temperature.

Table S1). Increasing the oxygen concentration results in decreasing resistance, with the slopes varying in the range $n_{500\ °C} = -0.23$ to $n_{800\ °C} = -0.38$. The dependence on oxygen content can be thus described as moderate. In the lower temperature range (500 °C and 600 °C), the slope values are close to 0.25, which indicates that charge transfer is the rate-determining process (theoretical n = 1/4). For higher temperatures (700 °C and 800 °C), the exponent increases to 0.32–0.38. It is close to a theoretical value of n = 3/8 (0.375) which has been reported to be connected to a reaction controlled by the atomic oxygen diffusion process followed by a charge transfer [58], so a form of intermediate between processes described by n = 1/2 and n = 1/4. The relative change of the limiting processes might be due to different activation energies of the possible contributions (surface diffusion, charge transfer).

Temperature activation of the process described by R_1 is presented in Fig. 7B (see also data in Table S1). The resistance values are dependent on the temperature with an activation energy of ~1.1 eV, slightly dependent on the oxygen concentration. Lowering the oxygen concentration results in lowering the activation energy, from 1.18 eV obtained in 100% O_2 to 0.98 eV in 0.3% O_2.

The obtained data for the R_1 contribution can be compared with our previous results obtained for STF35 [46]. The oxygen dependence slopes were very similar. The resistance magnitude was however higher for the STF35 sample, almost by an order of magnitude. At 800 °C in 20% O_2, the STF35 resistance was ~85 mΩ cm^2, whereas, for the STF70, the resistance was ~14 mΩ cm^2. The lower value of the resistance is due to the faster kinetics of adsorption of oxygen for the iron-richer compound. The temperature effect on the resistance was also stronger for the STF35, for which activation energies ~1.4 eV were reported, considerably higher than the value of 1.1 eV reported here.

The resistance parameters of the second equivalent circuit component, R_2-CPE2, are shown as a function of oxygen concentration in Fig. 8A, and as a function of temperature in Fig. 8B. All results (values of the equivalent circuit parameters) also are collected in Table S1. This is the lowest frequency contribution (characteristic frequency of <5 Hz), clearly noticeable for oxygen concentration < 20%. The strong effect of the oxygen content on the R_2 is visible. The R_2 resistance is directly inversely proportional to the oxygen content. The slope, in the double logarithmic plot, shows inversely proportional behaviour (n = −1). This slope is characteristic for the description of the gas diffusion process in the electrodes. It is thus strongly affected by the oxygen content, but not so much by the temperature, which is evident in Fig. 8B. Due to the relatively low frequency of the process, the fitting at 500 °C can have a relatively large error, thus for the fitting of the activation energy, the three highest temperatures were used. The "activation energy" is negative and has a small magnitude. The values vary between −0.08 and −0.13 eV. If the points at 500 °C were included in the calculation, then the values would be ~0 eV. The low negative temperature effect is also a characteristic feature of the gas diffusion process: in simple theoretical considerations, based on the Nernst equation and gas diffusion laws, Masuda et al. derived a small negative dependence of $T^{-0.5}$ on the gas diffusion overvoltage [59], which is supported experimentally by our results.

To supplement the resistance values, specific pseudo-capacitances and characteristic frequencies of the medium-frequency and low-frequency contributions were calculated, and are presented in Fig. 9A and B, respectively (see also data in Table S2).

For the medium frequency contribution, R_1-CPE1, the specific capacitance (C_1) is in the range 5–144 mF cm^{-2}. Specifically, at

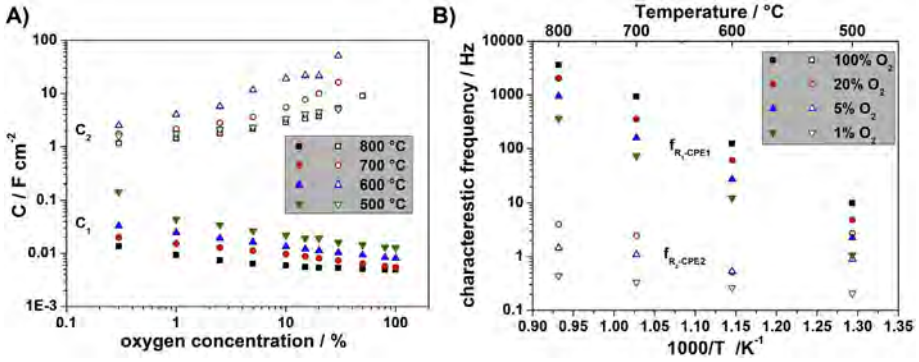

Fig. 9. A) Capacitance, and B) characteristic frequency values calculated from CPE1 and CPE2 contributions.

800 °C, the capacitance varies between 5 and 14 mF cm^{-2} depending on oxygen concentration. The characteristic frequency is strongly affected by the temperature, and also by oxygen concentration. At 800 °C, the characteristic frequency is ~2000 Hz in 20% O_2. Based on the literature, this process can be ascribed to oxygen atom diffusion followed by a charge transfer reaction [58].

For the low-frequency contribution, R_2-CPE2, the specific capacitance shows quite high values. For example, at 500 °C, C_1 varies between ~1.5 F cm^{-2} at 1% O_2, to ~6 F cm^{-2} at 30% O_2. These high capacitance values have a chemical, not electrochemical origin, and are typical for a gas diffusion process. The characteristic frequency of the gas diffusion process is relatively low, ranging from 5 to 0.5 Hz.

Based on the results presented in Figs. 3–9, the values obtained from fitting an equivalent circuit consisting of two R-CPE elements (R_1-CPE1 and R_2-CPE2), corresponding to two possible electrochemical processes, seems valid and well substantiated. The obtained values fit very well with the available literature data reported for mixed ionic electronic conductors.

The porous STF70 electrode shows good electrochemical performance, applicable for practical electrodes for solid oxide cells operating at or above 700 °C, where the polarisation resistance R_{pol} is < 100 mΩ cm^2. This level of polarisation resistance is acceptable for high performance cells, where a polarisation resistance limit of ~150 mΩ cm^2 is often quoted [60]. STF70 is also a Co-free electrode material, which is beneficial from a processing and cost point of view. Also, it has been reported that STF70 has limited Sr surface segregation, so its long-term performance can be favourable [61].

Comparing the obtained results with our previous study of porous STF35 electrodes [46], STF70 shows much higher performance, mostly due to its higher electronic and ionic conductivity, higher surface exchange coefficient (k*) and diffusion coefficient (D*) [36,42]. For STF35, the impedance analysis revealed contributions from the ionic transport in the material (at ~200 Hz) and adsorption (~20 Hz). For STF70, the higher frequency contribution (~2000 Hz at 800 °C) is visible, and the overall polarisation is lower. According to Merkle and Maier, the rate-determining step for Fe-doped $SrTiO_3$ is the dissociation of oxygen, diffusion, and charge transfer, whereas the incorporation into the lattice is a fast process [36]. Clematis et al. analysed the impedance spectra of $Ba_{0.5}Sr_{0.5}Co_{0.8}Fe_{0.2}O_{3-\delta}$ in a 3-electrode setup. The authors describe that at 700 °C, the losses are dominated by ionic conduction and charge transfer at the electrode/electrolyte interface. Oxygen adsorption and bulk diffusion had a minor contribution. The authors did not study the effects of oxygen concentration, but only analysed the polarisation effects. Hjalmarsson and Mogensen analysed symmetrical porous $(La_{0.6}Sr_{0.4})_{0.99}CoO_{3-\delta}$ at different oxygen concentration (2%–100%) [34]. The authors proposed an equivalent circuit consisting of two R-CPE elements in series. The higher frequency contribution (summit frequency of 0.5–5 kHz) showed thermal activation (~1.1 eV), capacitance of ~0.25 mF cm^{-2}, and pO_2 dependence of n = 0.35. The lower frequency contribution was strongly dependent on oxygen concentration and had capacitance values of ~50 mF cm^{-2}, which were ascribed to mass transport limitations (gas diffusion). The origin of a relatively low value of capacitance was unclear. Typically, values of this magnitude are ascribed to molecular adsorption. Wang et al. studied $PrBaCo_2O_{5+x}$ and showed that the major contributions show a charge transfer limitation (n close to 0.25 was obtained) with the characteristic frequency of ~1000 Hz. The polarisation resistance level was quite similar to our work (<125 mΩ cm^2 at 600 °C).

The characteristic frequency value and specific capacitances obtained in this work for the R_1-CPE1 elements differ a bit from the level reported by Escudero et al. [58], but this may be due to much higher performance of the STF70 electrodes, thus shifting the frequency and capacitance values. The activation energy is the same (1.16 eV in the air), and the oxygen concentration dependence is similar.

Our results show that the rate-determining reaction step, at 700 °C and 800 °C is most probably the surface oxygen diffusion process followed by charge transfer. At lower temperatures, i.e. 500 °C and 600 °C, the limiting step is the charge transfer reaction.

4. Conclusions

We studied the electrochemical performance of symmetrical porous $SrTi_{0.30}Fe_{0.70}O_{3-\delta}$ electrodes on a ceria-based electrolyte. Overall, STF70 showed high electrochemical performance (R_{pol} <125 mΩ cm^2 at 600 °C), comparable to state-of-the art materials. We studied a possible electrochemical reaction rate-limiting process by performing impedance measurements as a function of oxygen concentration and temperature. For data analysis, we used the distribution of relaxation times method. The DRT proved to be a useful tool in assisting the selection of a proper equivalent circuit model. Importantly, DRT can also be a very good tool to validate the proposed model by back-calculating the fitted spectra and comparing it with the DRT of the measured one. Based on the analyses, an equivalent circuit composed of two R-CPE elements was selected and fitted to all spectra. The higher frequency process (f_{peak} ~2000 Hz in air at 800 °C), denoted as R_1-CPE1, based on the obtained oxygen concentration dependence of $R \sim pO2^{-0.38}$ was ascribed to originate from surface diffusion of the oxygen species and possible following charge transfer (reduction) reaction. The lower frequency process (R_2-CPE2, f_{peak} ~5 Hz in air at 800 °C) originates from gas diffusion ($R_2 \sim pO_2^{-1}$).

STF70 is a highly performing oxygen electrode material for solid oxide cells, which might find also extensive use in oxygen separation membranes, catalysis, sensors and others. Understanding of the underlying electrochemical processes can lead to further improvement of the material.

This study and the obtained results show that electrochemical impedance spectroscopy, assisted with the distribution of relaxation times data analysis method and extensive temperature and oxygen concentration measurements offer an important insight into the electrochemical processes.

Declaration of competing interest

The authors declare that they have no known competing financial interests or personal relationships that could have appeared to influence the work reported in this paper.

CRediT authorship contribution statement

Aleksander Mroziński: Investigation, Data curation, Visualization, Writing - review & editing. **Sebastian Molin:** Methodology, Writing - original draft, Conceptualization. **Piotr Jasiński:** Resources, Writing - review & editing, Supervision, Funding acquisition, Methodology.

Acknowledgements

This work was partly supported by project funded by National Science Centre Poland based on decision 2017/25/B/ST8/02275. Funding from Statutory Research funds at WETI PG is also acknowledged.

Appendix A. Supplementary data

Supplementary data to this article can be found online at https://doi.org/10.1016/j.electacta.2020.136285.

References

[1] P. Caliandro, A. Nakajo, S. Diethelm, J. Van herle, Model-assisted identification of solid oxide cell elementary processes by electrochemical impedance spectroscopy measurements, J. Power Sources 436 (2019) 226838, https://doi.org/10.1016/j.jpowsour.2019.226838.

[2] A.J. Samson, M. Søgaard, P.V. Hendriksen, Model for solid oxide fuel cell cathodes prepared by infiltration, Electrochim. Acta 229 (2017) 73–95, https://doi.org/10.1016/j.electacta.2017.01.088.

[3] C. Lenser, N.H. Menzler, Impedance characterization of supported oxygen ion conducting electrolytes, Solid State Ionics 334 (2019) 70–81, https://doi.org/10.1016/j.ssi.2019.01.031.

[4] D. Sandil, S. Kumar, K. Arora, S. Srivastava, B.D. Malhotra, S.C. Sharma, N.K. Puri, Biofunctionalized nanostructured tungsten trioxide based sensor for cardiac biomarker detection, Mater. Lett. 186 (2017) 202–205, https://doi.org/10.1016/j.matlet.2016.09.107.

[5] S. Singal, A.K. Srivastava, Rajesh, Electrochemical impedance analysis of biofunctionalized conducting polymer-modified graphene-CNTs nanocomposite for protein detection, Nano-Micro Lett. 9 (2017) 1–9, https://doi.org/10.1007/s40820-016-0108-2.

[6] C. Wei, X. Zou, Q. Liu, S. Li, C. Kang, W. Xiang, A highly sensitive non-enzymatic glucose sensor based on CuS nanosheets modified Cu2O/CuO nanowire arrays, Electrochim. Acta 334 (2020) 135630, https://doi.org/10.1016/j.electacta.2020.135630.

[7] J.L. Song, X. Guo, $SrTi_{0.65}Fe_{0.35}O_3$ nanofibers for oxygen sensing, Solid State Ionics 278 (2015) 26–31, https://doi.org/10.1016/j.ssi.2015.05.009.

[8] L. Folkertsma, L. Gehrenkemper, J. Eijkel, K. Gerritsen, M. Odijk, Reference-electrode free pH sensing using impedance spectroscopy, Proceedings 2 (2018) 742, https://doi.org/10.3390/proceedings2130742.

[9] L. Manjakkal, E. Djurdjic, K. Cvejin, J. Kulawik, K. Zaraska, D. Szwagierczak, Electrochemical impedance spectroscopic analysis of RuO_2 based thick film pH sensors, Electrochim. Acta 168 (2015) 246–255, https://doi.org/10.1016/j.electacta.2015.04.048.

[10] K. Cysewska, L.F. Macía, P. Jasiński, A. Hubin, In-situ odd random phase electrochemical impedance spectroscopy study on the electropolymerization of pyrrole on iron in the presence of sodium salicylate – the influence of the monomer concentration, Electrochim. Acta 290 (2018) 520–532, https://doi.org/10.1016/j.electacta.2018.09.069.

[11] K. Cysewska, M. Gazda, P. Jasiński, Influence of electropolymerization temperature on corrosion, morphological and electrical properties of PPy doped with salicylate on iron, Surf. Coating. Technol. 328 (2017) 248–255, https://doi.org/10.1016/j.surfcoat.2017.08.055.

[12] E. Ivers-Tiffée, A. Weber, Evaluation of electrochemical impedance spectra by the distribution of relaxation times, J. Ceram. Soc. Japan. 125 (2017) 193–201, https://doi.org/10.2109/jcersj2.125.P4-1.

[13] B.A. Boukamp, A. Rolle, Use of a distribution function of relaxation times (DFRT) in impedance analysis of SOFC electrodes, Solid State Ionics 314 (2018) 103–111, https://doi.org/10.1016/j.ssi.2017.11.021.

[14] D. Papurello, D. Menichini, A. Lanzini, Distributed relaxation times technique for the determination of fuel cell losses with an equivalent circuit model to identify physicochemical processes, Electrochim. Acta 258 (2017) 98–109, https://doi.org/10.1016/j.electacta.2017.10.052.

[15] D.A. Osinkin, Complementary effect of ceria on the hydrogen oxidation kinetics on Ni - $Ce_{0.8}Sm_{0.2}O_{2-\delta}$ anode, Electrochim. Acta 330 (2020) 135257, https://doi.org/10.1016/j.electacta.2019.135257.

[16] J. Liu, F. Ciucci, The Gaussian process distribution of relaxation times: a machine learning tool for the analysis and prediction of electrochemical impedance spectroscopy data, Electrochim. Acta 331 (2020) 135316, https://doi.org/10.1016/j.electacta.2019.135316.

[17] X. Li, M. Ahmadi, L. Collins, S.V. Kalinin, Deconvolving distribution of relaxation times, resistances and inductance from electrochemical impedance spectroscopy via statistical model selection: exploiting structural-sparsity regularization and data-driven parameter tuning, Electrochim. Acta 313 (2019) 570–583, https://doi.org/10.1016/j.electacta.2019.05.010.

[18] H. Sumi, H. Shimada, Y. Yamaguchi, T. Yamaguchi, Y. Fujishiro, Degradation evaluation by distribution of relaxation times analysis for microtubular solid oxide fuel cells, Electrochim, Acta 339 (2020) 135913, https://doi.org/10.1016/j.electacta.2020.135913.

[19] F. Ciucci, C. Chen, Analysis of electrochemical impedance spectroscopy data using the distribution of relaxation times: a bayesian and hierarchical bayesian approach, Electrochim. Acta 167 (2015) 439–454, https://doi.org/10.1016/j.electacta.2015.03.123.

[20] M. Saccoccio, T.H. Wan, C. Chen, F. Ciucci, Optimal regularization in distribution of relaxation times applied to electrochemical impedance spectroscopy: ridge and Lasso regression methods - a theoretical and experimental Study, Electrochim. Acta 147 (2014) 470–482, https://doi.org/10.1016/j.electacta.2014.09.058.

[21] T.H. Wan, M. Saccoccio, C. Chen, F. Ciucci, Influence of the discretization methods on the distribution of relaxation times deconvolution: implementing radial basis functions with DRTtools, Electrochim. Acta 184 (2015) 483–499, https://doi.org/10.1016/j.electacta.2015.09.097.

[22] E. Quattrocchi, T.H. Wan, A. Curcio, S. Pepe, M.B. Effat, F. Ciucci, A general model for the impedance of batteries and supercapacitors: the non-linear distribution of diffusion times, Electrochim. Acta 324 (2019) 134853, https://doi.org/10.1016/j.electacta.2019.134853.

[23] F. Ciucci, Modeling electrochemical impedance spectroscopy, Curr. Opin. Electrochem. 13 (2019) 132–139, https://doi.org/10.1016/j.coelec.2018.12.003.

[24] A.P. Tarutin, G.K. Vdovin, D.A. Medvedev, A.A. Yaremchenko, Fluorine-containing oxygen electrodes of the nickelate family for proton-conducting electrochemical cells, Electrochim. Acta 337 (2020) 135808, https://doi.org/10.1016/j.electacta.2020.135808.

[25] S. Wang, H. Jiang, Y. Gu, B. Yin, S. Chen, M. Shen, Y. Zheng, L. Ge, H. Chen, L. Guo, Mo-doped $La_{0.6}Sr_{0.4}Fe_{O3-\delta}$ as an efficient fuel electrode for direct electrolysis of CO_2 in solid oxide electrolysis cells, Electrochim. Acta 337 (2020) 135794, https://doi.org/10.1016/j.electacta.2020.135794.

[26] N. Ortiz-Vitoriano, A. Hauch, I. Ruiz de Larramendi, C. Bernuy-López, R. Knibbe, T. Rojo, Electrochemical characterization of $La_{0.6}Ca_{0.4}Fe_{0.8}Ni_{0.2}O_{3-\delta}$ perovskite cathode for IT-SOFC, J. Power Sources 239 (2013) 196–200, https://doi.org/10.1016/j.jpowsour.2013.03.121.

[27] A. Chrzan, S. Ovtar, P. Jasinski, M. Chen, A. Hauch, High performance $LaNi_{1-x}Co_xO_{3-\delta}$ (x = 0.4 to 0.7) infiltrated oxygen electrodes for reversible solid oxide cells, J. Power Sources 353 (2017) 67–76, https://doi.org/10.1016/j.jpowsour.2017.03.148.

[28] X. Tong, S. Ovtar, K. Brodersen, P.V. Hendriksen, M. Chen, Large-area solid oxide cells with $La_{0.6}Sr_{0.4}CoO_{3-\delta}$ infiltrated oxygen electrodes for electricity generation and hydrogen production, J. Power Sources 451 (2020) 227742, https://doi.org/10.1016/j.jpowsour.2020.227742.

[29] J. Schneider, T. Tichter, P. Khadke, R. Zeis, C. Roth, Deconvolution of electrochemical impedance data for the monitoring of electrode degradation in VRFB, Electrochim. Acta 336 (2019) 135510, https://doi.org/10.1016/j.electacta.2019.135510.

[30] H. Qu, J. Kafle, J. Harris, D. Zheng, J. Koshina, D. Boone, A.M. Drake, C.J. Abegglen, D. Qu, Application of ac impedance as diagnostic tool – low temperature electrolyte for a Li-ion battery, Electrochim. Acta 322 (2019), https://doi.org/10.1016/j.electacta.2019.134755.

[31] S. Sun, Z. Cheng, Electrochemical behaviors for Ag, LSCF and BSCF as oxygen electrodes for proton conducting IT-SOFC, J. Electrochem. Soc. 164 (2017) F3104–F3113, https://doi.org/10.1149/2.0121710jes.

[32] Y. Li, R. Gemmen, X. Liu, Oxygen reduction and transportation mechanisms in solid oxide fuel cell cathodes, J. Power Sources 195 (2010) 3345–3358, https://doi.org/10.1016/j.jpowsour.2009.12.062.

[33] Y. Takeda, Cathodic polarization phenomena of perovskite oxide electrodes with stabilized zirconia, J. Electrochem. Soc. 134 (1987) 2656, https://doi.org/10.1149/1.2100267.

[34] P. Hjalmarsson, M. Søgaard, M. Mogensen, Electrochemical performance and degradation of $(La_{0.6}Sr_{0.4})_{0.99}CoO_{3-\delta}$ as porous SOFC-cathode, Solid State Ionics 179 (2008) 1422–1426, https://doi.org/10.1016/j.ssi.2007.11.010.

[35] L. Navarrete, C. Solís, J.M. Serra, Boosting the oxygen reduction reaction mechanisms in IT-SOFC cathodes by catalytic functionalization, J. Mater. Chem. A. 3 (2015) 16440–16444, https://doi.org/10.1039/c5ta05187h.

[36] R. Merkle, J. Maier, How is oxygen incorporated into oxides? A comprehensive kinetic study of a simple solid-state reaction with SrTiO3 as a model material, Angew. Chem. Int. Ed. 47 (2008) 3874–3894, https://doi.org/10.1002/anie.200700987.

[37] J. Fleig, R. Merkle, J. Maier, The p(O2) dependence of oxygen surface coverage and exchange current density of mixed conducting oxide electrodes: model considerations, Phys. Chem. Chem. Phys. 9 (2007) 2713–2723, https://doi.org/10.1039/b618765j.

[38] W. Jung, H.L. Tuller, Investigation of cathode behavior of model thin-film $SrTi_{1-x}Fe_xO_{3-\delta}$ (x = 0.35 and 0.5) mixed ionic-electronic conducting electrodes, J. Electrochem. Soc. 155 (2008) B1194–B1201, https://doi.org/10.1149/1.2976212.

[39] N.H. Perry, G.F. Harrington, H.L. Tuller, Electrochemical Ionic Interfaces, Elsevier Inc., 2018, pp. 79–106, https://doi.org/10.1016/B978-0-12-811166-6.00004-2.

[40] T. Miruszewski, K. Dzierzgowski, P. Winiarz, S. Wachowski, A. Mielewczyk-Gryń, M. Gazda, Structural properties and water uptake of $STi_{1-x}Fe_xO_{3-x/2-\delta}$, Materials 13 (2020) 965, https://doi.org/10.3390/ma13040965.

[41] S.J. Litzelman, A. Rothschild, H.L. Tuller, The electrical properties and stability of $SrTi_{0.65}Fe_{0.35}O_{3-\delta}$ thin films for automotive oxygen sensor applications, Sensor. Actuator. B Chem. 108 (2005) 231–237, https://doi.org/10.1016/j.snb.2004.10.040.

[42] A. Rothschild, W. Menesklou, H.L. Tuller, E. Ivers-Tiffée, Electronic structure, defect chemistry, and transport properties of $SrTi_{1-x}Fe_xO_{3-y}$ solid solutions, Chem. Mater. 18 (2006) 3651–3659, https://doi.org/10.1021/cm052803x.

[43] P.J. Gellings, H.J.M. Bouwmeester, Ion and mixed conducting oxides as catalysts, Catal. Today 12 (1992) 1–101, https://doi.org/10.1016/0920-5861(92)80046-P.

[44] P.J. Gellings, H.J.M. Bouwmeester, Solid state aspects of oxidation catalysis, Catal. Today 58 (2000) 1–53, https://doi.org/10.1016/S0920-5861(00)00240-6.

[45] S. Molin, W. Lewandowska-Iwaniak, B. Kusz, M. Gazda, P. Jasinski, Structural

and electrical properties of Sr(Ti, Fe)$O_{3-\delta}$ materials for SOFC cathodes, J. Electroceram. 28 (2012) 80–87, https://doi.org/10.1007/s10832-012-9683-x.
[46] A. Mroziński, S. Molin, J. Karczewski, T. Miruszewski, P. Jasiński, Electrochemical properties of porous $Sr_{0.86}Ti_{0.65}Fe_{0.35}O_3$ oxygen electrodes in solid oxide cells: impedance study of symmetrical electrodes, Int. J. Hydrogen Energy 44 (2019) 1827–1838, https://doi.org/10.1016/j.ijhydene.2018.11.203.
[47] R. Moos, W. Menesklou, H.J. Schreiner, K.H. Härdtl, Materials for temperature independent resistive oxygen sensors for combustion exhaust gas control, Sensor. Actuator. B Chem. 67 (2000) 178–183, https://doi.org/10.1016/S0925-4005(00)00421-4.
[48] H.Y. Li, H. Yang, X. Guo, Oxygen sensors based on $SrTi_{0.65}Fe_{0.35}O_{3-\delta}$ thick film with MgO diffusion barrier for automotive emission control, Sensor. Actuator. B Chem. 213 (2015) 102–110, https://doi.org/10.1016/j.snb.2015.02.079.
[49] A. Mroziński, S. Molin, P. Jasiński, Effect of sintering temperature on electrochemical performance of porous $SrTi_{1-x}Fe_xO_{3-\delta}$ (x= 0.35, 0.5, 0.7) oxygen electrodes for solid oxide cells, J. Solid State Electrochem. (2020), https://doi.org/10.1007/s10008-020-04534-0.
[50] A. Mroziński, S. Molin, J. Karczewski, B. Kamecki, P. Jasiński, The influence of iron doping on performance of $SrTi_{1-x}Fe_xO_{3-\delta}$ perovskite oxygen electrode for SOFC, ECS Trans 91 (2019) 1299–1307, https://doi.org/10.1149/09101.1299ecst.
[51] F. Tietz, Thermal expansion of SOFC materials, Ionics 5 (1999) 129–139, https://doi.org/10.1007/BF02375916.
[52] A. Løken, S. Ricote, S. Wachowski, Thermal and chemical expansion in proton ceramic electrolytes and compatible electrodes, Crystals 8 (2018) 365, https://doi.org/10.3390/cryst8090365.
[53] M. Mogensen, N.M. Sammes, G.A. Tompsett, Physical, chemical and electrochemical properties of pure and doped ceria, Solid State Ionics 129 (2000) 63–94, https://doi.org/10.1016/S0167-2738(99)00318-5.
[54] W. Jung, H.L. Tuller, Impedance study of $SrTi_{1-x}Fe_xO_{3-\delta}$ (x = 0.05 to 0.80) mixed ionic-electronic conducting model cathode, Solid State Ionics 180 (2009) 843–847, https://doi.org/10.1016/j.ssi.2009.02.008.
[55] M. Heinzmann, A. Weber, E. Ivers-Tiffée, Advanced impedance study of polymer electrolyte membrane single cells by means of distribution of relaxation times, J. Power Sources 402 (2018) 24–33, https://doi.org/10.1016/j.jpowsour.2018.09.004.
[56] B.A. Boukamp, Electrochemical impedance spectroscopy in solid state ionics: recent advances, Solid State Ionics 169 (2004) 65–73, https://doi.org/10.1016/j.ssi.2003.07.002.
[57] C. Chatzichristodoulou, P.T. Blennow, M. Søgaard, P. V Hendriksen, M.B. Mogensen, Ceria and its use in solid oxide cells and oxygen membranes. Catal. By Ceria Relat. Mater., second ed., 2013, pp. 623–782, https://doi.org/10.1142/9781848169647_0012.
[58] M.J. Escudero, A. Aguadero, J.A. Alonso, L. Daza, A kinetic study of oxygen reduction reaction on La_2NiO_4 cathodes by means of impedance spectroscopy, J. Electroanal. Chem. 611 (2007) 107–116, https://doi.org/10.1016/j.jelechem.2007.08.006.
[59] K. Masuda, A. Kaimai, K. Kawamura, Y. Nigara, T. Kawada, J. Mizusaki, H. Yugami, H. Arashi, Electrochemical reaction kinetics of mixed conducting electrodes on CeO_2-based solid electrolytes, in: Proc. Electrochem. Soc., 1997, pp. 473–482.
[60] B.C.H. Steele, Survey of materials selection for ceramic fuel cells, Solid State Ionics 88 (1996) 1223–1234, https://doi.org/10.1016/0167-2738(96)00291-3.
[61] S.L. Zhang, H. Wang, M.Y. Lu, A.P. Zhang, L.V. Mogni, Q. Liu, C.X. Li, C.J. Li, S.A. Barnett, Cobalt-substituted $SrTi_{0.3}Fe_{0.7}O_{3-\delta}$: a stable high-performance oxygen electrode material for intermediate-temperature solid oxide electrochemical cells, Energy Environ. Sci. 11 (2018) 1870–1970, https://doi.org/10.1039/C8EE00449H.

4.5.Article V

Title: **Impact of Strontium Non-Stoichiometry of $Sr_xTi_{0.3}Fe_{0.7}O_{3-\delta}$ on Structural, Electrical, and Electrochemical Properties for Potential Oxygen Electrode of Intermediate Temperature Solid Oxide Cells**

Authors: **Aleksander Mroziński**, Sebastian Molin, Patryk Błaszczak, Tadeusz Miruszewski, Karolina Górnicka, Jakub Karczewski, Piotr Jasiński

Journal: International Journal of Hydrogen Energy (2023), In Press

DOI: 10.1016/j.ijhydene.2023.05.323

Impact Factor (2022): 7.200

In this publication, a detailed material analysis and an electrical and electrochemical evaluation of the properties of $Sr_{1-x}Ti_{0.30}Fe_{0.70}O_{3-\delta}$ (STF-x) materials are presented in order to find the optimal stoichiometry of the STF70 material presenting the best performance. The work focused on the study of both symmetrical samples and full cells. A detailed analysis of the electrochemical processes depending on strontium stoichiometry was also carried out.

My original contribution to this publication was:

- Preparation of high-quality reproducible STF-x material for application as porous electrodes on symmetrical samples and SOFC.
- Electrical characterisation of the STF-x materials with determination of the k* and D* constants and indication of the changes to k* and D* with strontium content changes in STF-x materials.
- Detailed electrochemical characterisation of symmetrical samples and fuel cells.

- Determination of the electrochemical processes occurring at the electrodes with the application of DRT and clarification of the rate-determining reaction of the porous electrode.

Table 6 CRediT author statement Article V: " Impact of Strontium Non-Stoichiometry of $Sr_xTi_{0.3}Fe_{0.7}O_{3-\delta}$ on Structural, Electrical, and Electrochemical Properties for Potential Oxygen Electrode of Intermediate Temperature Solid Oxide Cells"

Author	CRediT author statement	Signature
Aleksander Mroziński	Investigation; Data curation; Visualization; Writing - original draft	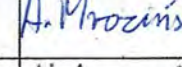
Sebastian Molin	Methodology; Writing - review & editing; Conceptualization	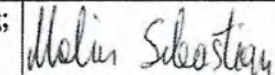
Patryk Błaszczak	Investigation (XPS, H_2-TPR/TPD, SSA); Data curation; Writing - original draft	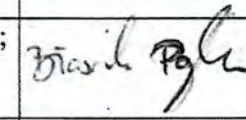
Tadeusz Miruszewski	Conceptualization (ECR); Methodology; Validation	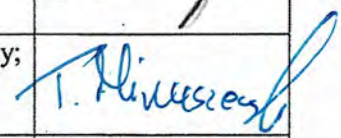
Karolina Górnicka	Investigation (XRD analysis); Data curation	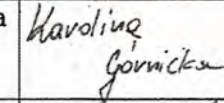
Jakub Karczewski	Investigation (SEM pictures); Data curation	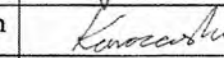
Piotr Jasiński	Resources; Writing - review & editing; Supervision; Funding acquisition; Methodology	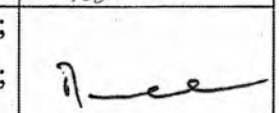

Available online at www.sciencedirect.com

ScienceDirect

journal homepage: www.elsevier.com/locate/he

Impact of strontium non-stoichiometry of $Sr_xTi_{0.3}Fe_{0.7}O_{3-\delta}$ on structural, electrical, and electrochemical properties for potential oxygen electrode of intermediate temperature solid oxide cells

Aleksander Mroziński [a,*], *Sebastian Molin* [a], *Patryk Błaszczak* [b], *Tadeusz Miruszewski* [b], *Karolina Górnicka* [b], *Jakub Karczewski* [b], *Piotr Jasiński* [a]

[a] *Faculty of Electronics, Telecommunications and Informatics and Advanced Materials Center, Gdańsk University of Technology, ul. G. Narutowicza 11/12, 80- 233 Gdańsk, Poland*

[b] *Faculty of Applied Physics and Mathematics and Advanced Materials Center, Gdańsk University of Technology, ul. G. Narutowicza 11/12, 80- 233 Gdańsk, Poland*

HIGHLIGHTS

- Knowledge about the influence of A site non-stoichiometry in STF has been extended.
- The electrochemical characterisation was performed on symmetrical and full cells.
- The DRT technique allowed to distinguish the dominant electrochemical process.
- The non-stoichiometric STF shows improved electrochemical properties.

GRAPHICAL ABSTRACT

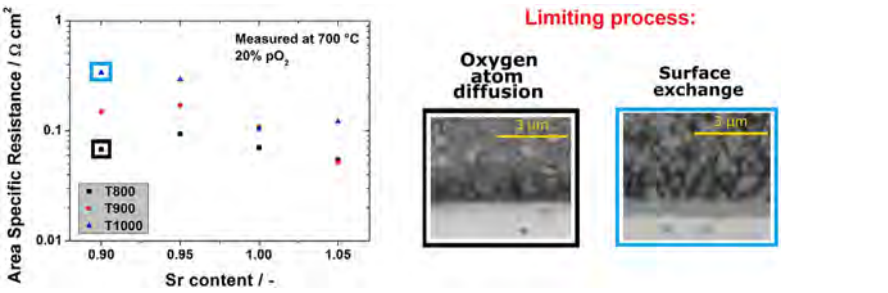

ARTICLE INFO

Article history:
Received 31 March 2023
Received in revised form
14 May 2023
Accepted 29 May 2023
Available online xxx

ABSTRACT

This work presents the results of a comprehensive study on the impact of the A-site non-stoichiometry of $Sr_xTi_{0.3}Fe_{0.7}O_{3-\delta}$ (x = 0.90, 0.95, 1.00, 1.05) ceramics on their physicochemical properties. The materials were fabricated by the conventional solid-state reaction method and their structure was determined by X-ray diffractometry, X-ray photoelectron spectroscopy and electron microscopy. Their sintering and thermal expansion properties were then evaluated. The electrical properties of the materials were determined by electrical conductivity and electrical relaxation measurements (on bulk materials) and by

* *Corresponding author.*
E-mail address: aleksander.mrozinski@pg.edu.pl (A. Mroziński).

https://doi.org/10.1016/j.ijhydene.2023.05.323

Please cite this article as: Mroziński A et al., Impact of strontium non-stoichiometry of $Sr_xTi_{0.3}Fe_{0.7}O_{3-\delta}$ on structural, electrical, and electrochemical properties for potential oxygen electrode of intermediate temperature solid oxide cells, International Journal of Hydrogen Energy, https://doi.org/10.1016/j.ijhydene.2023.05.323

Keywords:
Perovskite
Oxygen electrode
Strontium non-stoichiometry
Distribution of relaxation times
Solid oxide cells

electrochemical impedance spectroscopy (EIS) studies of symmetrical, CGO-electrolyte based, porous electrodes. Finally, fuel cell tests with the non-stoichiometric electrodes were evaluated. To elucidate the electrochemical reaction pathways for oxygen reduction/evolution reaction, EIS measurements were carried out in different pO_2 and were analysed via the distribution of relaxation times method. The results showed a dependence of materials' properties on the A-site non-stoichiometry, which can be used to fine-tune their properties, e.g. increase the surface exchange rate or decrease the thermal expansion coefficient.

Introduction

Solid Oxide Cells (SOCs) are energy conversion devices that can be used for energy generation (SOFCs – Solid Oxide Fuel Cells) and storage (by utilising SOECs – Solid Oxide Electrolysis Cells) [1]. Unfortunately, the performance of SOCs is limited by the electrochemical reactions at the electrodes [2–4], including the oxygen reduction/evolution reaction rate at intermediate temperatures (<700 °C) [5–7]. Therefore, improved and new electrode materials are sought [8–14]. Perovskite oxides (general formula ABO_3) with mixed ionic and electronic conductivity (MIEC) are perspective materials for SOFC electrodes [15–21], which allow for a wide range of compositional tailoring and fine-tuning of their structural and chemical properties. Historically, the most active oxygen electrodes contain Co, which providies high electrochemical activity due to its mixed valence [22–27]. Recent years have however highlighted Co as a problematic material due to its cost and unsustainable mining. Doped strontium titanates seem an interesting Co-free alternative material [28–30]. Doped strontium titanates have been used as oxygen membranes [31,32], resistive random access memory [33], oxygen sensors [34,35], coatings for porous stainless steel [36], fast electronic devices [37,38], quantum devises [39], and electrodes in SOFCs [40–43].

Previous research on the oxygen reduction reaction (ORR) on doped $SrTiO_3$ has focussed on materials with substitution at the A or/and B sublattices [44–49]. For example, Zhang et al. reported excellent electrochemical properties at 700 °C (polarisation resistance 0.043 Ω cm^2) for $SrTiO_3$ substituted at both sublattices, despite much lower electrical conductivity than the conductivity of $La_{0.6}Sr_{0.4}Co_{0.2}Fe_{0.8}O_{3-\delta}$ (~20 S cm^{-1} and ~300 S cm^{-1}, respectively) [43,50].

One of the options for improving perovskite materials is increasing the oxygen vacancies by introducing a non-stoichiometry at the A or B site [51–54]. Several works studying the influence of A-site or B-site deficiency on the properties of doped strontium titanate oxygen electrodes have been published. Ni et al. [55,56] investigated $Sr_{1-x}Ti_{0.3}Fe_{0.6}Ni_{0.1}O_3$ (x = 0, 0.02, 0.05) as an oxygen electrode at 750 °C. They have indicated that Sr deficiency promotes better electrochemical properties because of a higher amount of oxygen vacancies and a smaller thermal expansion coefficient (TEC). The best results in terms of electrochemical performance were obtained for the material with x = 0.05 despite a slight decrease of conductivity. Further research was carried out by Ni et al. [17], who improved the electrochemical properties of $Sr_{0.95}Ti_{0.3}Fe_{0.6}Ni_{0.1}O_3$ by exsolution of (Ni,Fe)O nanoparticles. Zhu et al. proved that the exsoluted $Sr_{0.95}(Ti_{0.3}Fe_{0.63}Ni_{0.07})O_{3-\delta}$ anode has better electrochemical performance than stoichiometric material in the range 700 °C–850 °C. Shan and Guo's [57] research on a $(Y_{0.08}Sr_{0.92})_{1-x}Ti_{0.6}Fe_{0.4}O_{3-d}$ mixed conductor showed a decrease in conductivity when the A-site deficiency increased. Similar behaviour of conductivity was reported for $Sr_{1-x}Fe_{0.8}Ti_{0.2}O_{3-\delta}$ by Kharton et al. [58] and for $Sr_xFe_{0.7}Ti_{0.3}O_{3-\delta}$ by Yang et al. [59]. Opposite behaviour of conductivity was observed by Li et al. for $Sr(Ti_{0.6}Fe_{0.4})_{1-x}O_{3-\delta}$ where B-site deficiency was implemented [60]. Despite the above-mentioned literature reports on non-stoichiometric doped strontium titanates, the influence of the physical and chemical properties of non-stoichiometric materials on the electrochemical performance and electrochemical processes has not been shown.

In our previous work we have identified $SrFe_{0.7}Ti_{0.3}O_{3-\delta}$ as an active catalyst [61]. Therefore, in this work, we study of $Sr_xFe_{0.7}Ti_{0.3}O_{3-\delta}$ (STF-x) with x = 0.90; 0.95; 1.00; 1.05. We report the fundamental material analysis including X-ray diffraction (XRD), particle size distribution (PSD), powder specific surface area (SSA), thermogravimetric analysis (TGA), linear thermal expansion, X-ray photoelectron spectroscopy (XPS), H_2-Thermally Programmed Reduction/Desorption (H_2-TPR/TPD) of STF-x powder and the results of total electrical conductivity and conductivity relaxation of STF-x pellets. Finally, an electrochemical impedance spectroscopy (EIS) study, including a distribution of relaxation times (DRT) analysis, of symmetrical cells under SOC operating conditions and different oxygen partial pressures are demonstrated.

Experimental

Materials synthesis

Stoichiometric $Sr_{1.00}Ti_{0.3}Fe_{0.7}O_{3-\delta}$ (STF-100) and non-stoichiometric $Sr_{0.90}Ti_{0.3}Fe_{0.7}O_{3-\delta}$ (STF-90), $Sr_{0.95}Ti_{0.3}Fe_{0.7}O_{3-\delta}$ (STF-95), and $Sr_{1.05}Ti_{0.3}Fe_{0.7}O_{3-\delta}$ (STF-105) powders were synthesised using the conventional solid state reaction method. Starting reagents: $SrCO_3$ (EuroChem, Poland), TiO_2 (EuroChem, Poland) and Fe_2O_3 (Chempur, Poland) were mixed in a planetary ball mill (Fritsch, Pulverisette 7) for 12 h. All starting powders were >99.9% pure. The mixed reagent

Please cite this article as: Mroziński A et al., Impact of strontium non-stoichiometry of $Sr_xTi_{0.3}Fe_{0.7}O_{3-\delta}$ on structural, electrical, and electrochemical properties for potential oxygen electrode of intermediate temperature solid oxide cells, International Journal of Hydrogen Energy, https://doi.org/10.1016/j.ijhydene.2023.05.323

powders of STF-100 and STF-105 (in the form of pellets) were sintered two times at 1200 °C (for 15 h each time) with an intermediate grinding step between the sinterings. Due to the higher sinterability of strontium-deficient compounds, the synthesis temperature was decreased to 1100 °C for the STF-90 and STF-95. After sintering, STF-x pellets were reground in a mortar and milled in two stages in a planetary ball mill. Firstly, using 3 mm YSZ balls and a rotational speed of 1000 rpm for 1 h and next using 1 mm ZrO_2 balls and 1100 rpm, also for 1 h. Finally, the milled STF-x powders were thermally relaxed at 600 °C as described earlier [62].

Sample preparations

For the electrical conductivity and electrical conductivity relaxation measurements, the synthesised STF-x powders were uniaxially pressed and sintered for 2 h at the same temperature as during synthesis. The achieved pellets were ~1 mm in thickness and ~12 mm in diameter. For the electrical conductivity relaxation studies, pellets were also cut into the shapes of a prisms (12 × 1 mm x 2 mm) using a precision tungsten wire saw.

Porous STF-x electrodes for electrochemical impedance spectroscopy of symmetrical cells were applied on a dense gadolinium-doped ceria (CGO-20, $Ce_{0.8}Gd_{0.2}O_{2-\delta}$) substrate. Commercially available CGO-20 (DKK, Japan) powders were pressed into pellets and sintered at 1400 °C for 8 h. The sintered disks had a diameter of 13 mm and 98% theoretical density. The CGO-20 pellets were polished down to a 3 μm finish and a thickness of 0.6 mm ± 10%. For the application of the STF-x materials on the CGO-20 substrates, the synthesised powders were mixed with a commercial vehicle (Heraeus, V-006 A) at a weight ratio of 2:3 using a planetary ball mill. The STF-x pastes were screen-printed on two sides of the CGO-20. Each side received two layers with a drying step at 130 °C after each application. Symmetrical samples were sintered at 800 °C, 900 °C and 1000 °C for 2 h under an air atmosphere. The produced electrodes had an active surface area equal to 0.5 cm^2 and ~20 μm thickness. As in our previous work, platinum was used as a current collector [61].

For application tests in a SOFC system, selected STF-x (x = 0.95 and 1.05) materials were also screen printed on commercial Elcogen button half cells (ACS-400B) and sintered at 800 °C and 1000 °C, respectively. Finally, for comparison, a reference SOFC with commercially available, state-of-the-art LSCF cathode material (ESL Europe) was sintered at 1050 °C (for 2 h).

Material characterisations

The phase composition of the STF-x powders was characterised by the X-ray diffraction (XRD) technique. Measurements were carried out at room temperature in air using a Bruker D2 Phaser with an XE-T detector equipped with a Cu X-ray anode.

X-ray Photoelectron Spectroscopy analysis (XPS) was performed using an Omicron NanoTechnology X-ray photoelectron spectrometer with a 128-channel collector. The XPS measurements were performed under ultra-high vacuum conditions. Photoelectrons were excited by an Mg-Kα X-ray source with an X-ray anode operated at 15 keV and 300 W. The spectra were deconvoluted using the XPSPEAK software.

The H_2-TPR (temperature programmed reduction) was performed using an apparatus equipped with a TCD detector (Buck Scientific, USA), cold trap, and heated gas transfer line. 100 mg of sample powder was placed in a quartz reactor with an internal measurements of the bed temperature. The STF-x powders were degassed at 200 °C for 20 min in a stream of He prior to the measurements. The samples were reduced under the flow of a 40 ml min^{-1} 5% H_2/Ar gas mixture. The tests were performed up to 900 °C with a heating rate of 10 °C min^{-1}.

O_2-TPD (temperature programmed desorption) was performed using 250 mg of prepared powdered sample with the preparation step as described for the H_2-TPR experiment. After the degassing step and cooling down to 50 °C, the quartz reactor was flushed with pure 4N5 O_2 (40 ml min^{-1}) for 1 h. After that, the gas was switched back to He for 1 h in order to equilibrate. The O_2-TPD was performed up to 900 °C with a heating rate of 10 °C min^{-1}. The profiles were collected using the PeakSimple software with a resolution of 1 Hz.

The specific surface area (SSA) was measured and calculated according to the BET isotherm model using a NovaTouch LX1 physisorption apparatus (Quantachrome, USA). The powder samples were degassed at 300 °C for 3 h under a vacuum prior to the measurement.

The particle size distributions of the powders were obtained using a Zetasizer Nano dynamic light scattering analyser (Malvern Panalytica). Measurements of the STF-x solution in ethanol using backscattering mode (detection angle was 173°) were performed at room temperature after a 20 min ultrasound bath.

The kinetics of the thermal decomposition of the STF-x powders were evaluated using thermogravimetric analysis (TGA). The TGA experiments were carried out using a microbalance (CI Precision MK5) in the temperature range between 900 °C and 200 °C. During the whole measurement procedure, air was fed to the furnace chamber at a flow rate of 40 ml min^{-1}. No baseline correction was made for the change in atmosphere density during heating.

Linear thermal expansion results for the STF-x powders were obtained with a Netzsch DIL 402. Pressed powers in form of cylinder were placed in measuring chamber. The samples were heated up to 1100 °C at a heating rate of 5 °C min^{-1}, and after 15 min of dwelling, were cooled down to room temperature at the rate of 3 °C min^{-1} (all in Synthetic Air).

Electrical and electrochemical performance analysis

DC electrical conductivity measurements of the STF-x pellets between 900 °C and 200 °C, were performed using the van der Pauw technique, as described in previous work [61]. The pellets were ~12 mm in diameter and ~1 mm thick. The conductivity was measured in 20% O_2, 5% O_2 and 1% O_2. Synthetic air was used as the base gas, which was further diluted with 5 N Ar using Brooks thermal mass flow controllers to obtain lower pO_2.

To specify the chemical oxygen surface exchange coefficient (k*) and chemical diffusion coefficient of oxygen (D*), the

Please cite this article as: Mroziński A et al., Impact of strontium non-stoichiometry of $Sr_xTi_{0.3}Fe_{0.7}O_{3-\delta}$ on structural, electrical, and electrochemical properties for potential oxygen electrode of intermediate temperature solid oxide cells, International Journal of Hydrogen Energy, https://doi.org/10.1016/j.ijhydene.2023.05.323

electrical conductivity relaxation (ECR) technique was used [63]. Studies were performed in a small tube furnace (internal diameter ~20 mm) with 64 cm^3 gas volume. The applied temperatures were 800 °C, 750 °C, 700 °C, 650 °C, and 600 °C. During the four-point single frequency electrochemical impedance spectroscopy measurement (1 Hz), the oxygen partial pressures were changed from 20% O_2 to 10% O_2 and the reverse. The impedance was logged every 5 s until sample stabilisation. The gas flow was constant during the measurement (80 ml min^{-1}). After converting the recorded impedance to conductivity (σ), the results were analysed using the ECR-TOOLS software [64].

For electrochemical impedance spectroscopy (EIS) measurements, a Novocontrol Alpha-A with a ZG-4 interface was used. Symmetrical cells were tested in a 4-wire compression cell placed inside a sealed quartz tube. All measurements were at 25 mV amplitude with a frequency range varying from 3 MHz to 0.05 Hz. In the case of the STF-x electrodes sintered at different temperatures evaluated by impedance spectroscopy, each sample was measured in synthetic air between 800 °C and 500 °C. Samples for the selected sintering temperature were tested at 700 °C under a controlled oxygen concentration (100%, 50%, 20%, 10%, 5%, 2.5%, 1%). Appropriate gas mixtures were achieved using a Brooks thermal mass flow controller.

Characterisation of the fuel cells was performed on an Open Flanges™ test setup by Fiaxell. The anode of the tested fuel cell was electrically connected by a nickel mesh. An Au mesh was used to connect the cathode side. A thin layer of LSC (Fiaxell ink paste) was brush painted on all cathodes (STF-x and LSCF) before the test and dried at 70 °C to improve current collection. Alumina felt was used to separate the gases. The Fiaxell setup was placed inside a Kittec temperature controller furnace. The fuel cells were heated up to 750 °C (3 °C min^{-1}) for reduction and then cooled down to 700 °C for the main test after 24 h stabilisation. Reduction of the anode was conducted in H_2 with 3 vol% of steam, while on the cathode side, synthetic air was applied as the oxidant. Electrochemical impedance spectroscopy (at OCV and 3 vol% of steam) and current–voltage plots were measured by a Solartron 1260/1287 frequency analyser. EIS tests with a controlled oxygen concentration (3%, 5%, 10%, 20%, 50%) were performed with 50 vol% of steam. Appropriate oxygen concentration (cathode side) and steam content (anode side) were achieved using a Brooks thermal mass flow controller. High steam content was obtained by mixing hydrogen and oxygen in an external tubular furnace (700 °C) containing a platinum catalyst. All fuel cell tests were conducted with the total flow rates of 100 ml min^{-1} and 200 ml min^{-1} on anode and cathode side, respectively.

In order to designate the Area Specific Resistance (ASR) collected EIS spectra (polarisation resistance) were recalculated for the area of the electrode (0.5 cm^2) and divided by two as the interfaces were identical. Each impedance spectrum was corrected for the inductance of the rig. The data was analysed by the DRTTOOLS software [65] in the same manner as earlier [61]. In the case of tests with different oxygen concentrations, the data were also fitted using the Elchemea Analytical web-tool (www.elchemea.com, DTU Energy).

Post-mortem SEM

Images of the polished cross sections (with a 1 μm finish) of the measured symmetrical cells with STF-x porous electrodes sintered at different temperatures and of dense STF-x pellets were taken by an FEI Quanta FEG 250 Scanning Electron Microscope (SEM) with a backscattered electron detector and 20 kV in high vacuum. Chemical composition of polished cross-section of STF-x pellets was determined using the Thermo Fischer Phenom XL microscope with an integrated energy dispersive x-ray spectrometer (EDX).

Results and discussion

Characterisation of $Sr_xTi_{0.3}Fe_{0.7}O_{3-\delta}$ powders and bulk materials

The crystallographic structure of the prepared powders was characterised by X-ray diffractometry (XRD). All investigated $Sr_xTi_{0.3}Fe_{0.7}O_{3-\delta}$ powders revealed a cubic perovskite structure (*Pm-3m*), i.e. the structure remained stable even though altering the A-site occupation. Fig. 1 A) shows that the measured XRD patterns match well with the $SrTiO_3$ cubic lattice obtained from the crystallographic database. What is more stoichiometry of obtained STF-x materials was confirmed by the EDX analysis of sintered pellets (Table S.1). A small peak on XRD patterns related to the $SrCO_3$ phase could be identified (at 2θ ~24°) for STF-100 and STF-105. Due to high reactivity of doped strontium titanates, on the surface of STF-100 and STF-105 small amount of $SrCO_3$ is forming via reaction of terminating SrO crystal planes with CO_2 from the air, what cannot be avoided during the powder preparation, processing, or storage [66]. The presence of the $SrCO_3$ compound is of no surprise and can be easily explained on the basis of the research on the SrO–CO_2–$SrCO_3$ equilibrium system, where the process of the carbonate formation greatly depends on the partial pressure of the CO_2 and the humidity of the atmosphere under which the powder was prepared. Above 900 °C the $SrCO_3$ is favoured to be decomposed into SrO what was confirmed by firing powders at 950 °C for 24 h in synthetic air (Figure S.2). This indicates that under the working conditions of the cell, where there is no obvious availability of the CO_2 in the gas stream, the surficial $SrCO_3$ is most likely being decomposed nearly fully into SrO [67–69].

The unit cell parameters were calculated each time using Rietveld refining method (GOF <1.8) and plotted as a function of the Sr-content in Fig. 1 B). The unit cell size of the stoichiometric STF-100 was 3.8845 (5) Å, which is in very good agreement with the literature data [28,70]. For the STF-90, STF-95 and STF-105 unit cell size equals to 3.8909 (1) Å, 3.8879 (2) Å and 3.8832 (7) Å, respectively. A good, monotonic correlation between the A-site occupation and the unit cell size is observed. Small deviation from linear trend probably is correlated with $SrCO_3$ formation in case of STF-105. Removal of Sr from the STF results in an increasing unit cell size. Sr^{2+} deficiency can be charge-balanced by the removal of oxygen (O^{2-}) from the lattice (the formation of oxygen vacancies) or via oxidation of iron ions. Such a mechanism was observed *i.a.* by Zhao et al. [71] in yttrium-doped strontium titanate with A-

Please cite this article as: Mroziński A et al., Impact of strontium non-stoichiometry of $Sr_xTi_{0.3}Fe_{0.7}O_{3-\delta}$ on structural, electrical, and electrochemical properties for potential oxygen electrode of intermediate temperature solid oxide cells, International Journal of Hydrogen Energy, https://doi.org/10.1016/j.ijhydene.2023.05.323

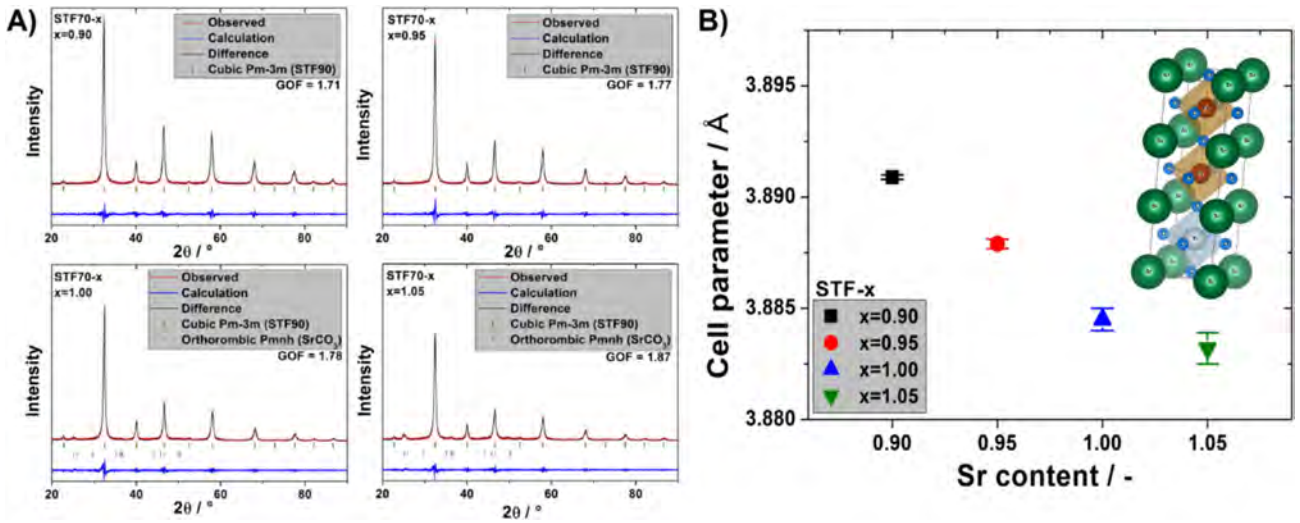

Fig. 1 – X-ray diffractometry spectra of the STF-x powders measured at room temperature (A) and calculated cell parameter value (B).

site deficiency ($(Y_{0.08}Sr_{0.92})_{1-x}TiO_{3-\delta}$). Strontium deficiency in the structure was charge-compensated by both the decrease of Ti^{3+}- ion concentration and the increase of oxygen vacancy concentration. In this work, change of the valence state of iron from 3+ to 4+ induces a large decrease (about 10%) of the ionic radius (0.645 Å vs. 0.585 Å) [72], whereas the observed lattice size change (STF105 vs STF90) is opposite (increase about ~0.2% of the unit cell parameter). Thus the effect of Sr-non-stoichiometry on the lattice must be complex and involve these two compensation mechanisms.

Moreover, the removal of oxygen from the structure and the change in the oxidation state of iron also change the length of the bonds between Fe and O in TiO_6 octahedra. This, in turn, significantly affects the unit cell parameter what was observed in this work. Ward et al. shows that for $Pr_{1-x}Sr_xFeO_{3-\delta}$ with lowering concentration of Sr^{+2} unit cell parameter also increase and with the increase of the oxidation state of iron (smaller ionic radius), Fe–O inter-ion distance leads to lowering of the average Fe–O bonding energy of the redox-active Fe [73]. All facts mentioned above may explain the observed changes in the lattice constant with the changing content of strontium in the structure.

The morphology of the powders was characterised by scanning electron microscopy and particle size measurements, supplemented with specific surface area (SSA) determination.

Fig. 2 A) presents the results of the particle size distribution (PSD) measurements and specific surface area of the STF-x

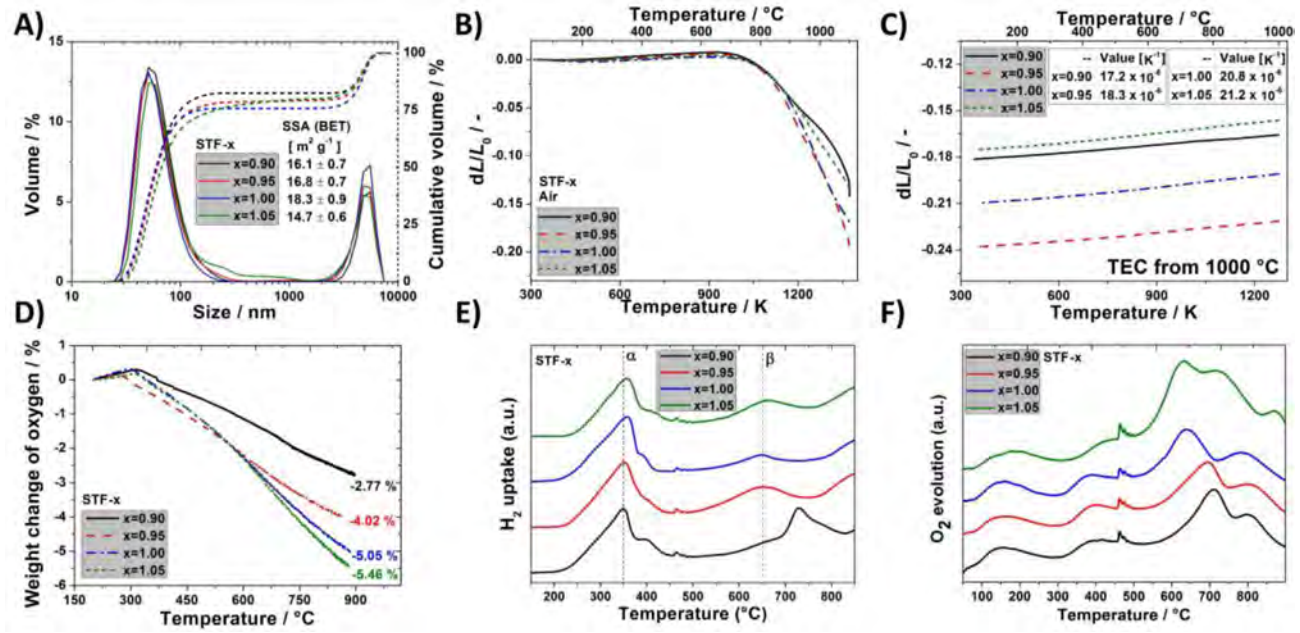

Fig. 2 – Particle size distribution and specific surface area (A), sintering/expansion curves (B–C), thermogravimetric dependence (D), H_2-TPR (E) and O_2-TPD (F) curves for investigated STF-x.

Please cite this article as: Mroziński A et al., Impact of strontium non-stoichiometry of $Sr_xTi_{0.3}Fe_{0.7}O_{3-\delta}$ on structural, electrical, and electrochemical properties for potential oxygen electrode of intermediate temperature solid oxide cells, International Journal of Hydrogen Energy, https://doi.org/10.1016/j.ijhydene.2023.05.323

powders. For all cases, similar particle size distributions and specific surface areas (~15 $m^2\ g^{-1}$) were observed, i.e. no clear effect of the A-site occupation on the powders (e.g. particle coarsening, etc.) could be identified. Approximately 75% of the cumulative volume was formed by particles smaller than 100 nm. PSD measurement showed that ~25% of the cumulative volume was formed by larger particles (~5 μm), whilst the SEM examination (Figure S.1) confirmed presence of only relatively small particles. Interestingly, there was no large aggregates found during the SEM imaging, what may suggest that the presence of the larger particles in PSD result may be caused by the apparatus error due to the upper detection limit. The obtained particle size of the powders can be considered small, which may be advantageous for electrochemical reaction for mixed conducting SOC electrodes. For comparison, Schulze-Kuppers et al. reported preparation of $SrTi_{1-y}Fe_yO_{3-\delta}$- materials also including ball milling. In their case, 90% of the particles had a size lower than a few microns with a resulting much smaller specific surface area (~3 $m_2\ g^{-1}$) [74].

The results of the dilatometry measurements conducted in air are presented in Fig. 2 B)–C). The sintering profile for all STF-x materials looks similar to that reported earlier for the $SrTi_{1-y}Fe_yO_{3-\delta}$ materials [62]. For all of the investigated compounds, the onset of sintering is quite similar: from ~760 °C to ~810 °C. The main differences are observed during heating between 800 °C and 1100 °C. The most Sr-deficient sample, STF-90, shows non-linear bahaviour at high temperatures, whereas the STF-95 and STF-100 show similar sintering profiles.

The TEC values for the STF-x were calculated based on the cooling profiles from dilatometry. Obtained values were ~17, ~18–21, and ~21 × $10^{-6}\ K^{-1}$ for STF-90, STF-95, STF-100, and STF-105, respectively. The differences between the TEC values indicate that the STF-x thermal expansion properties are directly related to the strontium content, possibly caused by different chemical expansion contributions due to oxygen release and different amounts of reducible Fe^{4+} ions, which is consistent with the oxygen loss data (Fig. 2 D). The introduction of Sr-nonstoichiometry can be used to reduce the relatively high TEC value of STF-x. Kharton et al. showed comparable TEC values for $Sr_{0.97}Ti_{1-y}Fe_yO_{3-\delta}$ where y > 0.6 [15]. The values are also comparable with data from Zhang et al. although the TEC profiles reported here are linear in the measurement range RT-900 °C, whereas they reported non-linear behaviour [40]. Despite this relatively high TEC value, the STF-x materials can be successfully used as a SOC oxygen electrode, as is in the case of the state-of-the-art materials, e.g. $La_{0.6}Sr_{0.2}Co_{0.2}Fe_{0.8}O_{3-\delta}$ or $La_{0.6}Sr_{0.4}CoO_{3-\delta}$, with TECs>18 × $10^{-6}\ K^{-1}$ [75,76].

To study the temperature-dependent weight loss properties due to oxygen release caused by the thermal reduction of transition metals, thermogravimetric (TG) measurements were carried out between 200 °C and 900 °C in air. Since the changes in powders' mass during TG measurements were related only to the absorption or release of the oxygen, Fig. 2 D) shows only the change of the mass of oxygen contained within the STF-x compounds as a function of temperature. All samples show weight loss on heating, indicative of lattice oxygen release and the formation of oxygen vacancies. Up to 550 °C, the weight loss followed a similar trend for STF-95/100/105, whereas for the STF-90 sample, smaller weight loss was observed. Above 550 °C, after reaching 900 °C, the weight loss was the highest (>5%) for the samples with high Sr content (STF-105 and STF-100). The lowest weight loss was measured for the most Sr-deficient sample (STF-90: ~2.8%). The oxygen release accompanied by oxygen vacancy formation must be charge balanced to preserve electrical neutrality through the reduction of Fe^{4+} to Fe^{3+}.

The determined weight change, presented in Fig. 2 D), has a similar profile to that reported by Zhang et al. The main difference is the temperature of the inflection point. In this work, the inflection points occur at ~300 °C, while for $SrTi_{1-y}Fe_yO_{3-\delta}$, Zhang obtained the inflection at ~400 °C [40].

The H_2-TPR profiles of the STF-x samples are presented in Fig. 2 E). The reduction profiles in all cases contain two main peaks located at around 350 °C (α) and 650 °C (β) except for the STF-90 sample where the secondary β peak is shifted 100 °C towards higher temperatures. Sr and Ti are assumed not to undergo reduction under the used conditions, so the peaks were assigned to Fe-related processes only. The α peak was associated with the reduction of Fe^{4+} to Fe^{3+}, while the β peak located at higher temperatures was related to the reduction of Fe^{3+} to Fe^{2+}. The additional peak at ~720 °C, visible for the STF-90 sample, could be attributed to the simultaneous reduction of created Fe^{2+} to Fe^0 [77,78]. The existence of metallic Fe^0 in the STF-90 compared to the other compounds was also confirmed through the post-mortem XRD measurements (Figure S.3).

The α peak shifts slightly to a higher temperature with the increasing amount of Sr in the A sublattice. Higher amounts of Sr in the lattice stabilise the STF structure, increasing its reduction temperature presenting also an increase in the concentration of lower valence iron ions.

The oxygen desorption measurements (O_2-TPD) revealed quite similar behaviour of the STF-x samples at low temperatures up to ~550 °C, which can be described by the release of chemisorbed oxygen molecules bound loosely to the sorption centres at the surface of the powders (Fig. 2 F). At high temperatures, the peaks were correlated to the evolution of the bulk lattice oxygen [35]. The STF-100 and STF-105 showed faster onset with the peak position of 640 °C, whereas for the STF-95 and STF-90 the peaks were shifted to 700 °C and 710 °C, respectively. The changed look of the O_2-TPD profile of STF-105 sample in the high temperature region most probably corresponds to the evolution of the CO_2 gas from the $SrCO_3$ secondary phase. O_2-TPD measurements indicate that Sr-deficiency results in a lower tendency of the perovskite to release the oxygen from its structure, which is consistent with the TG results, where the Sr-deficient samples showed decreased thermal reducibility.

The surface composition of the STF-x powders was measured using XPS at room temperature under ultra-high vacuum conditions. Deconvolutions of the Fe2p spectra for all samples are presented in Fig. 3 A). Both Fe^{3+} and Fe^{4+} species were identified in all of the synthesised materials. The doublet peak separated by 134 eV located at around 710 eV was assigned to the Fe^{3+} state of iron, whilst the peak situated at ~712.5 eV corresponded to the coexisting Fe^{4+} ions. This behaviour is very characteristic for this type of the compounds based on the Fe-substituted $SrTiO_3$ [55,79]. The

Please cite this article as: Mroziński A et al., Impact of strontium non-stoichiometry of $Sr_xTi_{0.3}Fe_{0.7}O_{3-\delta}$ on structural, electrical, and electrochemical properties for potential oxygen electrode of intermediate temperature solid oxide cells, International Journal of Hydrogen Energy, https://doi.org/10.1016/j.ijhydene.2023.05.323

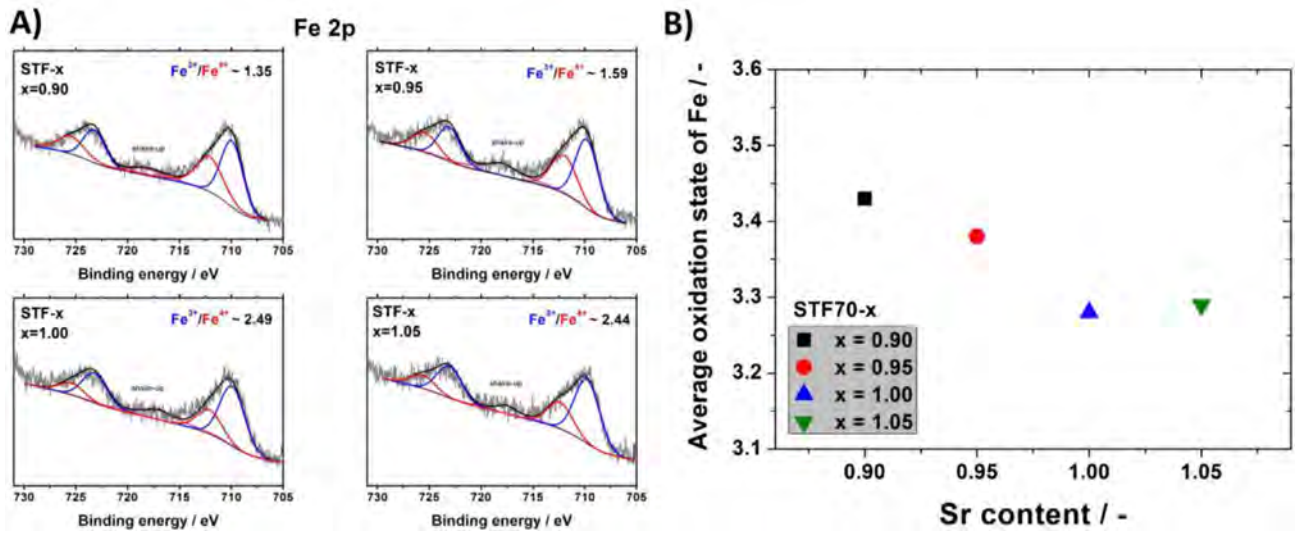

Fig. 3 – Fe 2p spectra (A) and relation of Fe^{+3}/Fe^{+4} ions as a function of Sr content for STF-x powders.

characteristic shake-up lines were also detected, clearly distinguishable mainly for STF-90 and STF-95. It is visible that with the increasing strontium content in the A sublattice, the Fe^{+3}/Fe^{+4} ratio is being elevated. The increase in the Fe mean valence (Fig. 3 B) is considered as one of the mechanism of the charge compensation when A site is being depleted of Sr ions. Despite that the oxygen nonstoichiometry and formation of the oxygen vacancies may have the dominant role, due to the relatively low changes in the increase of the amount of higher valence Fe ions comparing to the removal of the A site cations. Even though the XPS technique surveys just a surface of the materials we can, with high dose of the probability, estimate that similar stoichiometry between Fe^{3+} and Fe^{4+} state is being maintained throughout the material bulk, if the compound is single-phase. It is also proven when looking at the complementary results of the more bulk-related techniques like the temperature-driven oxygen loss (O_2-TPD) and TEC measurements revealing the changes in the Fe oxidation state.

In the case of the Sr3d spectra (Figure S.4), three Sr states were distinguished and associated with the Sr contained within STF-x structure, SrO and $SrCO_3$ (with a characteristic peak at 289.5 eV in C1s spectra) [80–82]. Increasing the Sr content at A sublattice lead to decrease in the relative share of Sr forming the STF-x and increased its participation in the surficial formation of the SrO and, after reacting with atmospheric CO_2, the corresponding carbonate - $SrCO_3$. A superficial effect of the formation of $SrCO_3$ by the exposure for CO_2 was reported earlier and is closely related to the existence of surface SrO terminations in strontium titanates [40,66]. The presence of the $SrCO_3$ was confirmed by the XRD measurement. Based on the XPS, the total surface composition was determined. The introduction of Sr-deficiency leads to lowering of the surface Sr segregation. For Sr-deficient materials, the estimated surficial Sr content vs. (Ti + Fe) content was ~1, what stands for the formation for the non-segregated material or high homogeneity (Figure S.5). At the same time for stoichiometric material, this value reached ~1.3 indicating slight segregation of the Sr towards the surface. For highly Sr enriched materials, the surface Sr ratio peaked at the value of ~2 and thus indicated formation of the highly Sr surface-rich compound. Thus, one can correlate the Sr-stoichiometry in the lattice with the existence of the additional surface segregates of the Sr-base compounds.

After the deconvolution of the Ti2p spectra it was observed that titanium ions generally take up the Ti^{4+} valence (Fig. S.4). Each $2p_{3/2}$ peak of Ti2p spectra was situated at ~457.8 eV with the separation energy of 5.8 eV for the doublet. It clearly correspond to the Fe-doped $SrTiO_3$ lattice, what is in agreement with the previously obtained data by the research of Zhang S. L. et al. [43]. According to the studies on $SrTi_{0.7}Fe_{0.3}O_3$ performed by Nanning A. et al. [83] using Near Ambient Pressure XPS (NAP-XPS) the location of the $Ti2p_{3/2}$ peak depends on the surrounding atmosphere conditions. Under highly reducing conditions the peak is being shifted towards higher bonding energies of ~458.4 eV and while in oxidizing gases it is localized ~457.4 eV. Additionally, the $Ti2p_{1/2}$ peak is broadened, what is a typical behaviour of this feature.

Electrical properties

Total electrical conductivity was investigated as a function of temperature (from 900 °C to 200 °C) in different oxygen concentrations (1%, 5% and 20%). The results of the electrical measurements of the STF-x pellets are presented in Fig. 4 A).

According to the equation derived from the reaction of oxygen incorporation and mass action law [84] (Kröger–Vink notation), a concentration of electron holes can be expressed as:

$$p = \left(\frac{K}{[V''_{Sr}]}\right)^{\frac{1}{2}} x\, pO_2^{\frac{1}{2}} \qquad \text{(equation 1)}$$

where p denotes the concentration of electron holes, K denotes a chemical reaction constant, $[V''_{Sr}]$ is the concentration of strontium vacancies and pO_2 is an oxygen partial pressure. Based on Equation (1), it can be stated that the concentration of electron-holes and thus the conductivity of all STF-x

Please cite this article as: Mroziński A et al., Impact of strontium non-stoichiometry of $Sr_xTi_{0.3}Fe_{0.7}O_{3-\delta}$ on structural, electrical, and electrochemical properties for potential oxygen electrode of intermediate temperature solid oxide cells, International Journal of Hydrogen Energy, https://doi.org/10.1016/j.ijhydene.2023.05.323

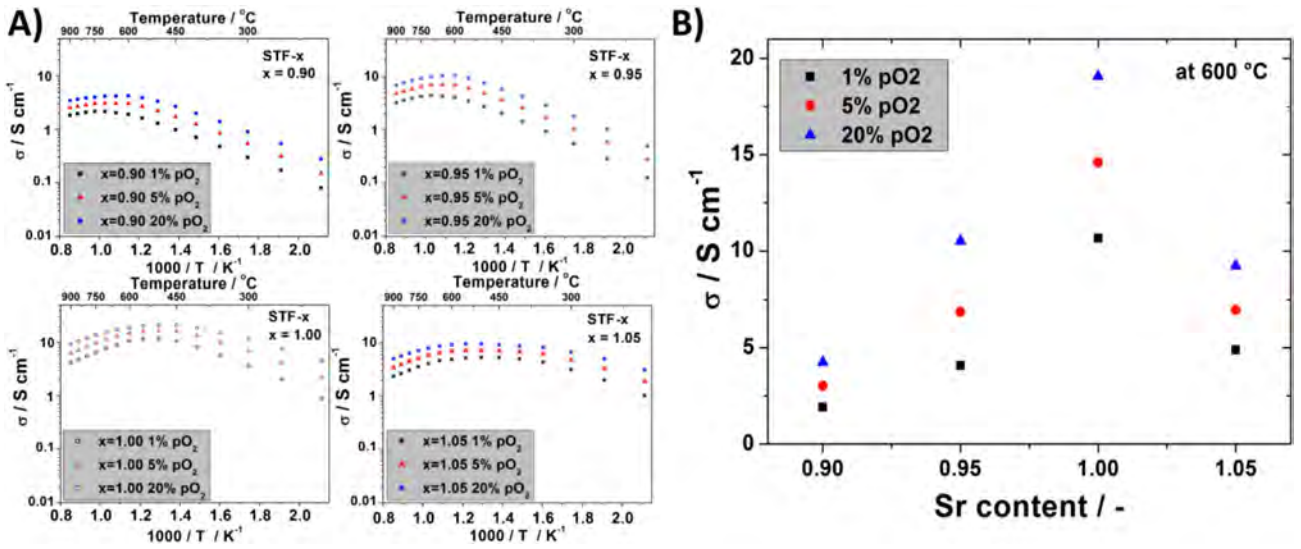

Fig. 4 – Electrical conductivity plots of sintered STF-x pellets measured at 20% O_2, 5% O_2 and 1% O_2 (A) and relation of conductivity at 600 °C as a function of Sr content (B).

decrease with the decreasing oxygen partial pressure. This is in agreement with the experimental results for all investigated samples (see Fig. 4 A). The results of STF-90, STF-95 and STF-100 also indicate a decrease of the conductivity with the increasing strontium deficiency (Fig. 4 B) similar as in the literature [57,58] and in qualitative agreement with equation (1). At 600 °C at 20% oxygen concentration, the conductivity of the STF-90 was ~4 S cm^{-1}, whereas for STF-100 its value was ~18 S cm^{-1}, thus the effect of the Sr-nonstoichiometry is considerable. This behaviour is also in line with equation (1), which relates the concentration of electron-holes inversely to the concentration of strontium vacancies.

The results for STF-105 can be influenced by the sample porosity and presence of secondary phases. As presented in Figure S.6 in the Supplementary materials, the density of STF-90/95/100 was >94%, whereas for the STF-105 the density was ~90%.

The temperature for the maximum conductivity increases slightly for the materials with the higher strontium deficiency (for STF-90 and STF-95 it is ~600 °C, and for STF-100 and STF-105 it is ~500 °C). Ni et al. also reported a slight change of the maximum conductivity temperature, but for their non-stoichiometric $Sr_{1-x}Ti_{0.3}Fe_{0.6}Ni_{0.1}O_{3-\delta}$, the maximum shift was 50 °C [55]. The shift might be correlated with the TG results and O_2-TPD, where the samples with higher Sr-deficiency showed decreased oxygen loss and delayed lattice oxygen evolution and thus decreased formation of charge balancing p-type carriers.

The chemical oxygen surface exchange (k*) and chemical diffusion (D*) coefficients were measured by the electrical conductivity relaxation (ECR) method. Due to the high sample density requirement, D* and k* were determined for STF-90, STF-95 and STF-100. Due to the porosity of the pellets after sintering, the STF-105 sample was not measured by ECR. The typical normalised data as a function of time for STF-90 and STF-100 measured at 700 °C is presented in Fig. 5 A). The total relaxation time at 700 °C was about 3000 s. Qualitatively, for all samples a faster equilibration time occurred during oxygen adsorption and incorporation (change from 10% pO_2 to 20% pO_2) than during desorption of oxygen (change from 20% pO_2 to 10% pO_2), which might indicate good performance of this material when used as an oxygen electrode in fuel cells.

The calculated values of chemical surface exchange coefficient k* and chemical oxygen diffusion coefficient D* are presented in Fig. 5 B)–C). At 700 °C, the values of k* are ~10^{-4} cm s^{-1} and D* from 10^{-5} to 10^{-6} cm^2 s^{-1}. The data is consistent with the values (from an ECR experiment) for STF50 reported by Schulze-Küppers [74]. Moreover, the chemical oxygen surface exchange coefficient of STF-x (at 800 °C) has a higher value than for the state-of-the-art $La_{0.6}Sr_{0.4}Co_{0.2}Fe_{0.8}O_{3-\delta}$ (~1.2×10^{-4}cm s^{-1}) [63].

In this work, k* at 800 °C for all STF-x (<9×10^{-3}cm s^{-1}) are one order of magnitude higher than the values obtained by Zhang et al. for $SrTi_{0.3}Fe_{0.7}O_{3-\delta}$ (~9×10^{-4} cm s^{-1}) [40], who, whoever, based their values on fitting of the electrochemical performance of the electrode to the Adler-Lane-Steele (ALS) model using detailed microstructural 3D analysis. This difference may be influenced by both other research methods for determining the value of k [44,85], as well as differences in the microstructure of the compounds [86] studied by Zhang et al. and in this work.

It was found that with an increasing strontium content, k* decreases (Fig. 5 D), whereas D* has the opposite trend. The calculated D* (~1×10^{-5}cm s^{-1}) for STF-x at 800 °C is similar to those reported for the $La_{0.6}Sr_{0.4}Co_{0.2}Fe_{0.8}O_{3-\delta}$ and $SrTiO_3$ materials [63,87]. In Fig. 5D) shows the relation between the chemical oxygen diffusion coefficient and the Sr content (at 700 °C). According to equation (1), increasing the Sr content increases the concentration of electron-holes, which may increase the chemical oxygen diffusion coefficient D*.

Electrochemical performance of $Sr_xTi_{0.3}Fe_{0.7}O_{3-\delta}$ oxygen electrodes

The results of EIS measurements and DRT analysis for symmetrical STF-x porous electrodes sintered at 800 °C, 900 °C and

Please cite this article as: Mroziński A et al., Impact of strontium non-stoichiometry of $Sr_xTi_{0.3}Fe_{0.7}O_{3-\delta}$ on structural, electrical, and electrochemical properties for potential oxygen electrode of intermediate temperature solid oxide cells, International Journal of Hydrogen Energy, https://doi.org/10.1016/j.ijhydene.2023.05.323

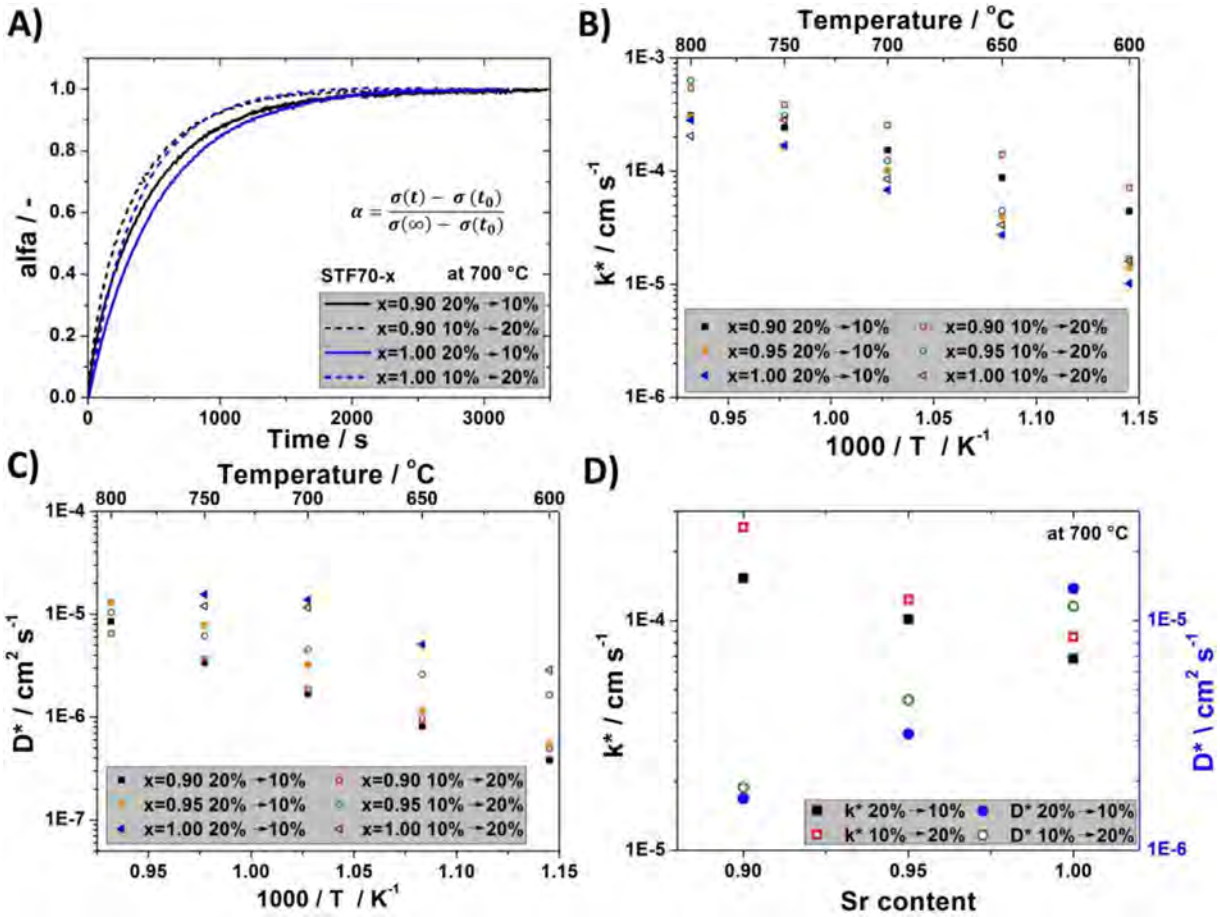

Fig. 5 – Exemplary normalised electrical conductivity relaxation plot of STF-x at 700 °C (A), calculated chemical oxygen surface exchange coefficient (B) and chemical oxygen diffusion coefficient (C) and relation between k* and D* as a function of Sr content at 700 °C.

1000 °C are presented in Fig. 6 A) and D); B) and E); C) and F), respectively.

The STF-x materials showed overall high electrochemical activity for oxygen reduction/evolution reactions. For electrodes sintered at 800 °C, the Area Specific Resistance (ASR) values measured at 700 °C in air were all within the range of ~55–94 mΩ cm^2, and were lower than that reported for $SrTi_{0.3}Fe_{0.7}O_{3-\delta}$ (112 mΩ cm^2) [40] or $Sr_{1-x}Ti_{0.3}Fe_{0.6}Ni_{0.1}O_{3-\delta}$ (~220 mΩ cm^2) [55] obtained in similar conditions. The electrode performance below 150 mΩ cm^2 is promising for high performance SOCs [88]. For the Co-containing $Sr(Ti_{0.3}Fe_{0.7-x}Co_x)O_{3-\delta}$ reported by Zhang et al. ASR values of 40–90 mΩ cm^2 were achieved [43]. For higher sintering temperatures, the Sr-deficient STF-90 and STF-95 show slightly worse performance than the STF-100 and STF-105. Interestingly, the highest performance among the tested electrodes was achieved for the STF-105 sintered at 900 °C. Even though the powder contained traces of strontium carbonate (detected by XRD) and the surface was enriched in strontium (detected by XPS), its ORR/OER performance was the highest, i.e. the polarisation resistance was the lowest (~55 mΩ cm^2 at 700 °C). The specific reasons are not so obvious and are open to future research.

For the sintering temperature of 800 °C, the area specific resistance (ASR) values were comparable for all STF-x electrodes, but as the sintering temperature increased, the differences in electrode performance also increased. The STF-90 was the most sensitive electrode to the effect of the sintering temperature, in contrast to the STF-105 (Figure S.7). For the sintering temperature of 1000 °C, the Sr-deficient compounds (STF-90 and STF-95) have almost twice the value of ASR in comparison to the STF-100 or STF-105. The change in electrochemical performance might come from the formation of a dense, interfacial layer, observed by SEM for STF-90 and STF-95 (Figure S.8). The high Sr content and its surface segregation hinders sintering of the electrodes and has a positive effect on the electrode performance.

The sintering temperature conditions for the preparation of the STF-90, STF-95 and STF-100 electrodes had no significant impact on the ohmic resistance (Figure S.9) as we reported earlier for $SrTi_{0.3}Fe_{0.7}O_{3-\delta}$ [62]. The STF-105 slightly improved contact with the electrolyte with the increasing sintering temperature. Even though the electrical conductivity of the STFx materials is quite low (1–20 S cm^{-1} at 700 °C), this seems sufficient to provide good current collection in the measurements.

These results show, that the electrochemical performance of STFx materials can be tuned by A-site non-stoichiometry and sintering conditions. The obtained ASR values are

Please cite this article as: Mroziński A et al., Impact of strontium non-stoichiometry of $Sr_xTi_{0.3}Fe_{0.7}O_{3-\delta}$ on structural, electrical, and electrochemical properties for potential oxygen electrode of intermediate temperature solid oxide cells, International Journal of Hydrogen Energy, https://doi.org/10.1016/j.ijhydene.2023.05.323

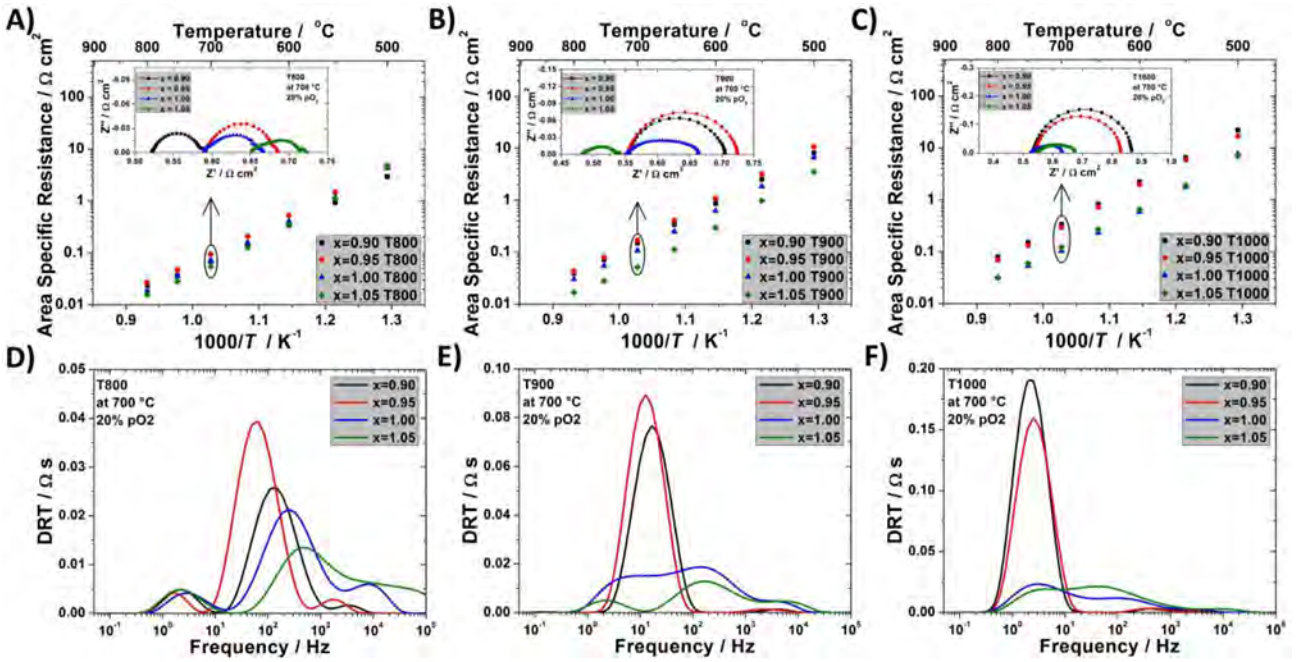

Fig. 6 – Impact of Sr non-stoichiometry on polarisation resistances of symmetrical cells with STF-x electrodes sintered at 800 °C, 900 °C and 1000 °C, respectively (A–C) and corresponding distribution of relaxation times results (D–F) for EIS spectra measured in 20% O_2 at 700 °C.

comparable to typical polarisation values reported for MIEC oxygen electrodes in the intermediate-temperature range [89,90], e.g. 0.1–1 Ωcm2 at 600–700 °C.

Distribution of relaxation times analysis

The results of the DRT analysis (Fig. 6 D)–F)) corresponding to the EIS spectra obtained at 700 °C in air (insets of Fig. 6 A)–C)) indicate differences in electrochemical processes depending on the Sr content.

For all STF-x sintered at the lowest temperature (800C °C), there are possibly two peaks related to two electrochemical processes, as also reported in our previous work for $SrTi_{0.3}Fe_{0.7}O_{3-\delta}$ [61]. The low frequency peak (~1 Hz) is similar for all electrode materials and is most probably connected to gas diffusion within the porous electrodes. The main electrochemical process has a characteristic peak at the frequency of 30–300 Hz (middle frequency), depending on the compound. The lowest contribution and the highest characteristic frequency were obtained for STF-105. The contributions visible as higher frequency "shoulders" of lower magnitude might be indicative of Gerischer-type elements, typically considered for MIEC perovskite electrodes in this frequency range.

As the sintering temperature increased, the spectra changed shape. For the STF-90 and STF-95, only a single process became distinguishable in the DRT spectra (Fig. 6 E) and F)). The shape of the DRT spectrum for STF-100 and STF-105 seems to be insensitive to the sintering temperature and shows the gas diffusion and higher frequency contributions.

To evaluate the electrochemical processes for the STF-90 and STF-95 in more detail, the responses of the electrodes sintered at 900 °C were also investigated at 700 °C as a function of oxygen partial pressure (pO_2). Fig. 7 A)–B) presents the selected EIS spectra and corresponding DRT spectra for the STF-90 at different oxygen concentrations. Similar results were achieved for the STF-95. The EIS measurement data were fitted by an equivalent circuit that consists of two R-CPE elements due to the occurrence of a low frequency contribution visible only at low pO_2 values (<5% O_2).

The ohmic resistance (R_s), low frequency resistance (R_{gas}), middle frequency resistance (R_1) and R-CPE calculated equivalent pseudo capacitances for the STF-90 and STF-95 as a function of oxygen partial pressure are presented in Fig. 7C)–F) and listed in Table S.2 and Table S.3. For pseudo capacitance calculation this formula was used:

$$C = \frac{(R*Y)^{\frac{1}{n}}}{R} \qquad \text{(equation 2)}$$

where C is pseudo capacitance, R resistance of R-CPE element, Y capacitance of R-CPE element and n is dimensionless value. Additionally, for comparison, the results of the pseudo capacitance for the stoichiometric STF-100 at 20% pO_2, reported earlier [61], are presented in Fig. 7F) and measured in this work for the STF-100 in the same conditions.

The fitting results reveal similarities for both Sr-deficient compounds. On the other hand, there are visible differences in comparison to the stoichiometric $SrTi_{0.3}Fe_{0.7}O_{3-\delta}$. Changes of the ohmic resistance in the function of pO_2 are negligible, because the CGO substrates are being practically insensitive for oxygen partial changes under the conditions used within this study [61]. The values for both STF-x compounds are comparable, taking into account the precision of 10% variation in the thickness of the electrolyte. As in our previous work, R_{gas} strongly depends on the oxygen concentration and the slope of the double logarithmic plot (n = −1), suggesting that it is indeed a gas diffusion process. In the case of R_1 and C_1, the value of pseudo capacitance

Please cite this article as: Mroziński A et al., Impact of strontium non-stoichiometry of $Sr_xTi_{0.3}Fe_{0.7}O_{3-\delta}$ on structural, electrical, and electrochemical properties for potential oxygen electrode of intermediate temperature solid oxide cells, International Journal of Hydrogen Energy, https://doi.org/10.1016/j.ijhydene.2023.05.323

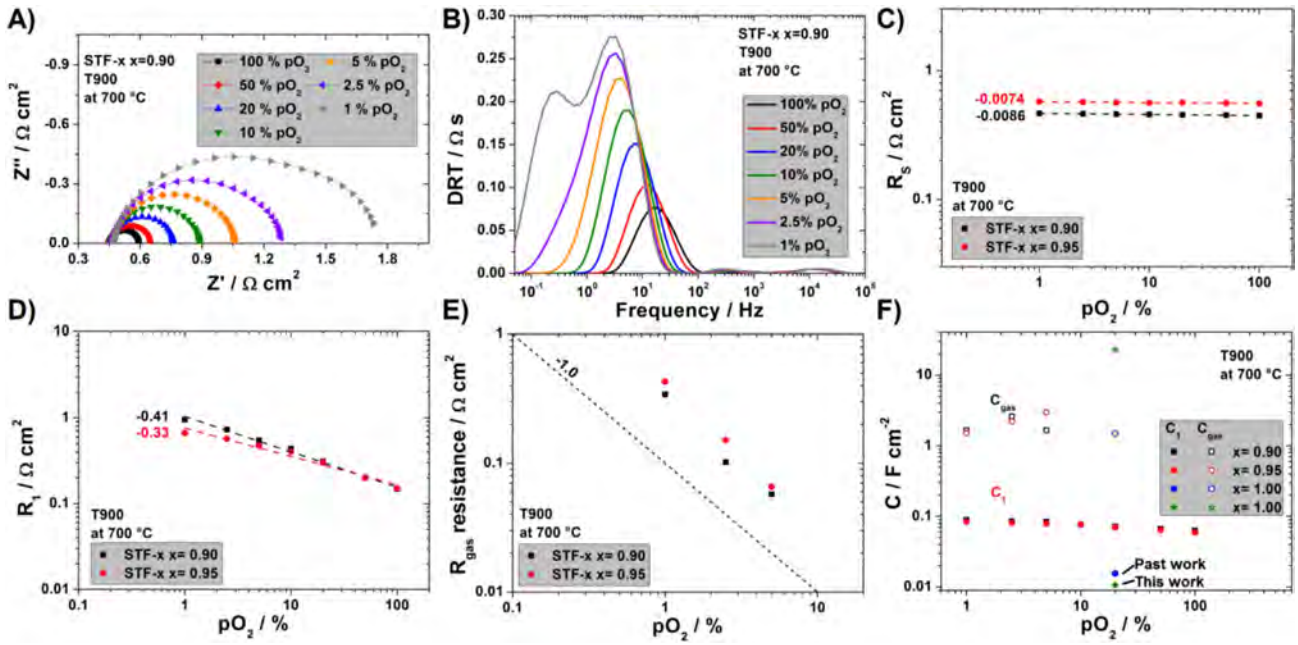

Fig. 7 – Results of EIS measured at 700 °C and different oxygen partial pressures for STF-90 symmetrical cells (A) and corresponding DRT spectra (B), values of calculated contribution of series resistance (C), R1 (D) and R_{gas} (E) and relayed pseudo capacitances (F) as a function of oxygen partial pressure for STF70-90 and STF70-95.

revealed a one order of magnitude increase in relation to the STF-100. The Sr-deficient materials show pseudo capacitance in the range of ~0.1 F cm^{-2}, whereas the stoichiometric STF70 showed a pseudo capacitance of ~0.01 F cm^{-2}, which is probably connected to the formation of a dense interfacial layer at temperatures of 900 °C and above for the Sr-deficient electrode materials and its chemical capacitance due to the accumulation of electro-active oxygen species (oxygen vacancies) in the "bulk" of the thin film structure [91]. This dense layer modifies the ORR/OER process at the interface between the ionic conductor (CGO) and MIEC electrode (STF70).

Solid oxide fuel cell test

The influence of strontium non-stoichiometry on the performance of solid oxide fuel cells at 700 °C was also checked. For the tests, Sr-deficient STF-95 sintered at 800 °C and Sr-enriched STF-105 sintered at 1000 °C were selected. The higher sintering temperature of STF-105 was chosen due to the lower sinterability of this compound. The reference cell with an LSCF cathode was sintered at 1050 °C. Fig. 8 A)–B) shows the current-voltage characteristics (I–V) and EIS for the tested fuel cells. For comparison, the I–V and EIS characteristics for the STF-100 are presented at Figure S.10. The maximum power density for fuels with STF-95, STF-105 and LSCF cathodes were, respectively: 809 mW cm^{-2}, 594 mW cm^{-2}, and 1206 mW cm^{-2}. Although the EIS measurements revealed that all of the materials have different value of polarisation resistance (STF-95 – 276 mΩ cm^2, STF-105 – 337 mΩ cm^2, and LSCF – 237 mΩ cm^2), the electrochemical processes at 700 °C (syn. air and wet H_2) are probably the same, as studied by DRT (presented in Figure S.11 A)). Differences are observed also for the ohmic resistances. The lowest R_s was measured for the LSCF (115 mΩ cm^2), followed by the STF-95 (247 mΩ cm^2), and the STF-105 (261 mΩ cm^2). The increased ohmic resistance originates from the STF materials, which have much lower electronic conductivity than LSCF. Thus, the inferior performance of the cells with STF in comparison to the cells with LSCF is determined by the ohmic resistance. Interestingly, considering only STF-x materials the difference for ASR of symmetrical samples between STF-95 (sintered at 800 °C) and STF-105 (sintered at 1000 °C) was ~29.8% (94 mΩ cm^2 and 122 mΩ cm^2 respectively). In SOFC applications difference of polarisation resistances decrease up to ~22.1%. In the case of ohmic resistance, symmetric samples showed identical value 1.1 Ω cm^2 but in SOFC it slightly change (~5.7%) in favor of STF-95. Which explains the better performance of cells with STF-95 material than with STF-105.

For a more detailed investigation of the influence of Sr non-stoichiometry on electrochemical processes of STF-x materials in fuel cells, EIS measurements as a function of pO_2 were carried out. The results of the DRT analysis corresponding to the EIS data at different pO_2 (Figure S.11 B)–C)) are presented in Fig. 8 C). Three main peaks can be observed. The low-frequency peak (~1 Hz) is probably related to gas diffusion on the cathode and anode side. This low frequency peak looks similar for both cells at 20% and 50% of oxygen partial pressure, but the fuel cell with the STF-105 cathode seems be more sensitive to lowering the pO_2. In contrast, the middle frequency peak (~100 Hz) at low pO_2 (3% pO_2) is comparable for both cells and with the increasing oxygen partial pressure, the fuel cell with the STF-95 cathode decreased more (practically disappearing at 50% of pO_2). This frequency is often attributed to oxygen incorporation and diffusion (e.g. typical Gerischer element). This result is in line with the higher k* value for strontium-deficient materials. For the high frequency peak

Please cite this article as: Mroziński A et al., Impact of strontium non-stoichiometry of $Sr_xTi_{0.3}Fe_{0.7}O_{3-\delta}$ on structural, electrical, and electrochemical properties for potential oxygen electrode of intermediate temperature solid oxide cells, International Journal of Hydrogen Energy, https://doi.org/10.1016/j.ijhydene.2023.05.323

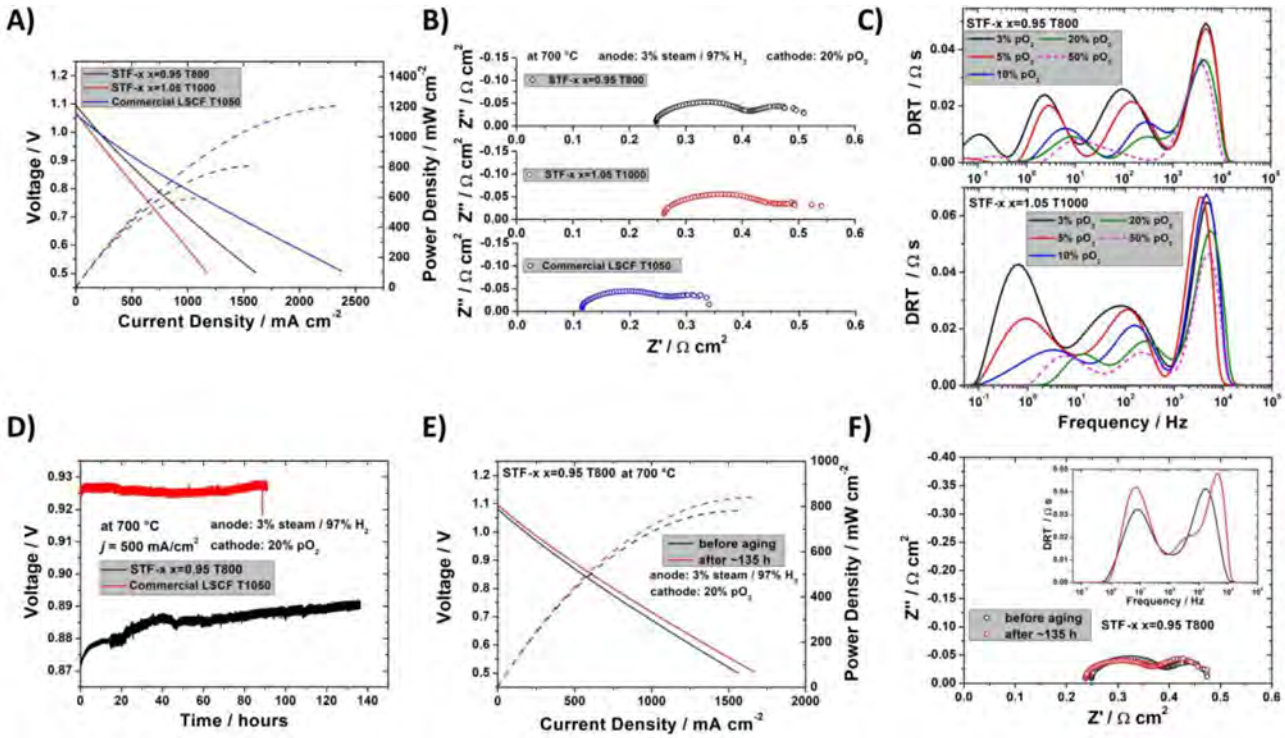

Fig. 8 – I–V characteristic of anode-supported cells (A), Nyquist plots of impedance data measured at OCV (B), DRT analysis of EIS measured as a function of pO_2 for cells with the STF-x cathodes (C), cell stability test under 0.5 A cm^{-2} current load (D) I–V plot before and after ageing of the fuel cell with the STF-95 cathode (E) and corresponding EIS (F).

(~5000 Hz), an observable small decrease of the peak for 20% and 50% of pO_2 in contrast to the rest of the tested conditions can be noticed. Even though the high frequency peak is larger for the cell with the STF-105 cathode, the trend for both cells is comparable, and this peak is probably connected with ion transfer across the cathode/electrolyte.

The performance of the STF-95 and the reference LSCF cathode was evaluated by monitoring the cell voltage output under a constant current load of 0.5 A cm^{-2} (Fig. 8 D) as a function of time. The initial voltages were ~0.87 V and ~0.93 V for the cell with the STF-95 and LSCF cathodes, respectively. During the 136-h the test, the voltage of the cell with the STF-95 cathode steadily increased by 0.02 V and it seems that it did not reach its maximum. In the case of the cell with the LSCF cathode, the voltage was almost stable over the 90 h of the test. The I–V and EIS measurements before and after the ageing test of the cell with the STF-95 cathode revealed improvement of the maximum power density and ohmic resistance with a concurrent small increase of ASR (Fig. 8 E)–F)). Based on the SEM images taken before and after the stability test (Fig. S. 12), there are visible small difference of microstructure between two materials. STF-95 sintered at 800 °C present smaller grains than LSCF sintered at 1050 °C what was to be expected. Interestingly, both materials did not show significant changes in grain size, and no layer formed at the interface. Although the electrical results indicate the advantage of LSCF, STF-95 has the potential to be further modified, for example by infiltration, which will most likely allow it to be taken into account as a potential electrode for SOFCs.

Discussion

Modifications at the A-site sublattice of STF-x material lead to important modifications of the main material properties (e.g. TEC, k*, D*, and σ) which in turn leads to differences in ASR values (Fig. 9A)).

One interesting feature of such modification is that electrochemical performance of the porous Sr-deficient materials can be easily limited by a too-high sintering temperature and the formation of a dense interface layer (Fig. 9 A) blue frame). The thickness of the dense interface layers formed at the sintering temperature of 900 °C for the STF-90 electrode was ~200 nm, whereas for the STF-95 it was slightly thinner (~150 nm). The formation of this dense layer has also been confirmed by Yang et al. [59]. In that case, the layer formed at higher temperatures, probably due to the use of larger particles.

The dense interfacial layer clearly shows a chemical capacitance that depends on the oxygen storage capacity. For example, the chemical capacitance of STF5, STF35 and STF50 thin films was studied by Jung and Tuller [92]. They found a strong dependence of the capacitance on the iron content. For the same thickness of thin films, the capacitance of STF50 was almost an order of magnitude higher than for STF35, for which a value of ~12 mF cm^{-2} for a 160 nm thick layer was reported at 650 °C. Considering the higher content of oxygen vacancies for a higher Fe composition (STF70 instead of STF50) and extra vacancies due to Sr-nonstoichiometry (for lower temperatures), the capacitance of the layer is in reasonable agreement

Please cite this article as: Mroziński A et al., Impact of strontium non-stoichiometry of $Sr_xTi_{0.3}Fe_{0.7}O_{3-\delta}$ on structural, electrical, and electrochemical properties for potential oxygen electrode of intermediate temperature solid oxide cells, International Journal of Hydrogen Energy, https://doi.org/10.1016/j.ijhydene.2023.05.323

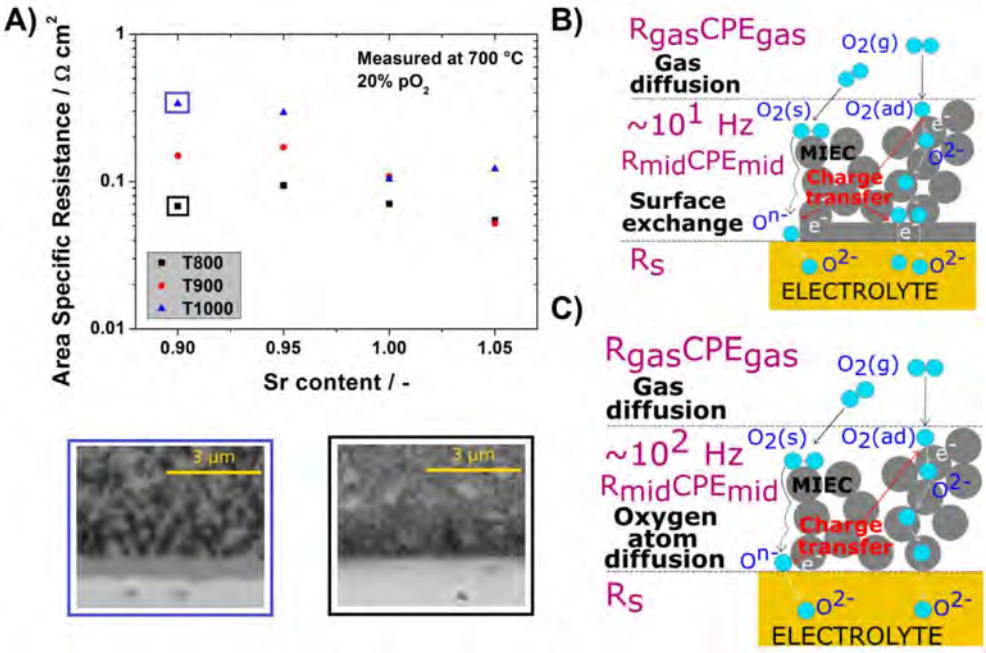

Fig. 9 – ASR as a function of strontium content for different sintering temperatures and SEM pictures of selected materials indicating significant microstructure differences (A), proposed model for porous STF-x cathode (B) and STF-x with a dense layer (C).

with the literature-proposed model for a thin film electrode with surface exchange-limited performance [91,92].

For materials sintered at low temperature (800 °C), characterised by a porous microstructure, the limiting electrochemical step is the process occurring at the middle frequency, identified as the adsorbed oxygen atom surface diffusion followed by a charge transfer reaction and incorporation into the lattice (Fig. 9C)) [61,93]. As presented in Fig. 6 D), the contribution of the middle frequency peaks for the STF-90 and STF-95 is larger than for the STF-100 and STF-105, which is in line with the presented changes of D*. In the case of the STF-90 and STF-95 sintered at higher temperatures (≥900 °C), where Sr-non-stoichiometry induced the formation of a thin interface layer, the limiting electrochemical process changed to a surface exchange/bulk diffusion-limited process due to the lower apparent surface area of the dense layer (Fig. 9 B)). Interestingly, the highest electrochemical performance, measured in the symmetrical cell test, was obtained for the STF-105 electrode, which has a high surface content of Sr confirmed by XPS. It seems that the extra porosity, caused by inferior sinterability, led to the lowest ASR.

The maximum power density of the tested solid oxide fuel cell with STF-95 and STF-105 cathodes with similar microstructures (without a dense layer) differ (809 mW cm^{-2}, 594 mW cm^{-2}), which is in agreement with the results obtained for EIS (94 mΩ cm^2, 122 mΩ cm^2) for the symmetrical cells. The cell with the STF-95 cathode, with higher k*, showed increased performance in the intermediate frequency range (Fig. 8C). The results of the cell performance with the new Co-free oxygen electrode are encouraging. To even further improve the functional properties, it is of interest to increase the total electronic conductivity of the electrode, e.g. by mixing with different material or by infiltration by highly conductive phases.

Summary

In this work, the complex nature of the influence of the Sr-non-stoichiometry on the structural, transport and electrocatalytic properties of the promising $Sr_xTi_{0.7}Fe_{0.3}O_{3-\delta}$-based materials was investigated.

The results showed that modification of the chemical composition by the introduction of non-stoichiometry affects the lattice parameter, i.e. a decrease of the Sr content results in a unit cell parameter increase, which has been connected (via XPS) to the reduction of Fe^{4+} to Fe^{3+} by the charge compensation mechanism and the introduction of oxygen vacancies. Lowering of the concentration of A-site cations (bulk Sr content) lowers the Sr-surface segregation. Based on XPS results, the Sr content is inversely correlated with the Fe^{+3}/Fe^{+4} ratio. Sr-deficient powders contained a lower amount of Fe^{4+} available for thermal reduction at higher temperatures. This was further confirmed by the thermogravimetry (TG), dilatometry (DIL) and temperature programmed (TPx) methods, which revealed changes in weight loss on heating and a lower thermal expansion coefficient due to the lower amount of strontium. One of the issues reported with STF materials with high iron content is their relatively high thermal expansion coefficient. Tailoring the Sr-stoichiometry can limit the TEC from ~21 to ~17, which is a marked improvement for practical applications at intermediate temperature. In accordance with the existing defect model of STF, the introduction of Sr-deficiency results in decreased electronic (p-type) conductivity [65].

The electrocatalytic performance of bulk materials, as determined by the ECR technique, showed a positive influence of the Sr-deficiency on chemical surface exchange

Please cite this article as: Mroziński A et al., Impact of strontium non-stoichiometry of $Sr_xTi_{0.3}Fe_{0.7}O_{3-\delta}$ on structural, electrical, and electrochemical properties for potential oxygen electrode of intermediate temperature solid oxide cells, International Journal of Hydrogen Energy, https://doi.org/10.1016/j.ijhydene.2023.05.323

coefficient (k*), and a negative effect on the chemical diffusion coefficient of oxygen (D*). In the electrochemical evaluation of porous electrodes, a complex trend in materials behaviour was found. Electrodes sintered at 800 °C showed similar electrochemical processes, with at least two clearly separated processes. Due to the small particle size of the synthesised powders and increased sinterability of the Sr-deficient materials, a continuous interfacial layer is formed even at sintering temperatures of 900 °C and above. This layer negatively influenced the electrode performance. Interestingly, the best overall electrode performance (~50 mΩ cm^2 at 700 °C, including the contribution of gas diffusion) was obtained for Sr-rich material (STF-105). Even though the electrical conductivity of this compound was inferior to the stoichiometric one and it showed high surface Sr segregation, its performance was clearly superior. This high performance was attributed to the decreased sinterability of these materials, which restricted grain growth and maintained a high surface area available for oxygen reduction and oxidation processes.

Based on these results, rational design of electrode materials through tailoring A-site non-stoichiometry of the perovskites, based on $Sr_xTi_{0.3}Fe_{0.7}O_{3-\delta}$ (x = 0.90; 0.95; 1.00; 1.05) is possible, but the relation between the basic physicochemical properties of bulk materials and porous electrode materials is complex. Even the well-studied issue of Sr-surface segregation requires further investigation to fully elucidate its effects. Moreover, the solid oxide fuel cell test confirmed that Sr-deficient STF-x materials could be a viable alternative for Co-containing state-of-the-art materials after improvement of the ohmic resistance by, e.g., impregnation.

Availability of data and material

The data that support the findings of this study are openly available in The MOST Wiedzy Open Research Data Catalog at 10.34808/yhx3-f485, reference number [94].

Authors' contributions

A.M.: Investigation; Data curation; Visualization; Writing - original draft.

S.M.: Conceptualization; Methodology; Writing - review & editing.

P.B.: Investigation; Data curation; Writing - original draft;

T.M.: Conceptualization; Methodology; Validation;

K.G.: Investigation; Data curation;

J.K.: Investigation; Data curation;

P.J.: Methodology; Resources; Writing - review & editing; Supervision; Funding acquisition.

Declaration of competing interest

The authors declare that they have no known competing financial interests or personal relationships that could have appeared to influence the work reported in this paper.

Acknowledgements and Funding

This work was supported by a project funded by National Science Centre Poland based on decision 2017/25/B/ST8/02275. Funding from Statutory Research funds at WETI PG is also acknowledged.

Appendix A. Supplementary data

Supplementary data to this article can be found online at https://doi.org/10.1016/j.ijhydene.2023.05.323.

REFERENCES

[1] Ahmad MZ, Ahmad SH, Chen RS, Ismail AF, Hazan R, Baharuddin NA. Review on recent advancement in cathode material for lower and intermediate temperature solid oxide fuel cells application. Int J Hydrogen Energy 2022;47:1103–20. https://doi.org/10.1016/j.ijhydene.2021.10.094.

[2] Zhang Y, Nicholas JD. Updating the notion that poor cathode performance typically dominates overall solid oxide fuel cell response. J Electrochem Soc 2021;168:034513. https://doi.org/10.1149/1945-7111/abed21.

[3] Yan D, Liang L, Yang J, Zhang T, Pu J, Chi B, Li J. Performance degradation and analysis of 10-cell anode-supported SOFC stack with external manifold structure. Energy 2017;125:663–70. https://doi.org/10.1016/j.energy.2016.12.107.

[4] Lee YH, Chang I, Cho GY, Park J, Yu W, Tanveer WH, Cha SW. Thin film solid oxide fuel cells operating below 600°C: a review. Int. J. Precis. Eng. Manuf. - Green Technol. 2018;5:441–53. https://doi.org/10.1007/s40684-018-0047-0.

[5] Hagen A, Liu YL, Barfod R, Hendriksen PV. Assessment of the cathode contribution to the degradation of anode-supported solid oxide fuel cells. J Electrochem Soc 2008;155:B1047. https://doi.org/10.1149/1.2960938.

[6] Zurlo F, Natali Sora I, Felice V, Luisetto I, D'Ottavi C, Licoccia S, Di Bartolomeo E. Copper-doped lanthanum ferrites for symmetric SOFCs. Acta Mater 2016;112:77–83. https://doi.org/10.1016/j.actamat.2016.04.015.

[7] Zhou W, Ran R, Shao Z. Progress in understanding and development of Ba0.5Sr0.5Co0.8Fe0.2O3-δ-based cathodes for intermediate-temperature solid-oxide fuel cells: a review. J Power Sources 2009;192:231–46. https://doi.org/10.1016/j.jpowsour.2009.02.069.

[8] Bai J, Han Z, Zhou D, Zhu X, Wang N, Chen R, He J, Yan W. Preparation of Pr2NiO4+δ-La0.6Sr0.4CoO3-δ as a high-performance cathode material for SOFC by an impregnation method. Int J Hydrogen Energy 2023;48:6076–87. https://doi.org/10.1016/j.ijhydene.2022.11.123.

[9] Zhang Y, Knibbe R, Sunarso J, Zhong Y, Zhou W, Shao Z, Zhu Z. Recent progress on advanced materials for solid-oxide fuel cells operating below 500 °C. Adv Mater 2017;29. https://doi.org/10.1002/adma.201700132.

[10] Irshad M, Idrees R, Siraj K, Shakir I, Rafique M, ul Ain Q, Raza R. Electrochemical evaluation of mixed ionic electronic perovskite cathode LaNi1-xCoxO3-δ for IT-SOFC synthesized by high temperature decomposition. Int J Hydrogen Energy 2021;46:10448–56. https://doi.org/10.1016/j.ijhydene.2020.09.180.

[11] Lee J, Choi M, Lee W. Encapsulation of metal catalysts for stable solid oxide fuel cell cathodes. Int. J. Precis. Eng. Manuf.

- Green Technol. 2021;8:1529–35. https://doi.org/10.1007/s40684-020-00290-8.
[12] Yang Q, Tian D, Liu R, Wu H, Chen Y, Ding Y, Lu X, Lin B. Exploiting rare-earth-abundant layered perovskite cathodes of LnBa0.5Sr0.5Co1.5Fe0.5O5+δ (Ln=La and Nd) for SOFCs. Int J Hydrogen Energy 2021;46:5630–41. https://doi.org/10.1016/j.ijhydene.2020.11.031.
[13] Cai W, Cao D, Zhou M, Yan X, Li Y, Wu Z, Lü S, Mao C, Xie Y, Zhao C, Yu J, Ni M, Liu J, Wang H. Sulfur-tolerant Fe-doped La0·3Sr0·7TiO3 perovskite as anode of direct carbon solid oxide fuel cells. Energy 2020;211:118958. https://doi.org/10.1016/j.energy.2020.118958.
[14] Choi M, Lee J, Lee W. Fluid mechanical approaches for rational design of infiltrated electrodes of solid oxide fuel cells. Int. J. Precis. Eng. Manuf. - Green Technol. 2019;6:53–61. https://doi.org/10.1007/s40684-019-00021-8.
[15] Kharton VV, Figueiredo FM, Kovalevsky AV, Viskup AP, Naumovich EN, Jurado JR, Frade JR. Oxygen diffusion in, and thermal expansionof, $SrTiO_{3-\delta}$- and $CaTiO_{3-\delta}$-Based materials. Defect Diffusion Forum 2000;186–187:119–36. https://doi.org/10.4028/www.scientific.net/ddf.186-187.119.
[16] Niemczyk A, Olszewska A, Du Z, Zhang Z, Świerczek K, Zhao H. Assessment of layered La2-x(Sr,Ba)xCuO4-δoxides as potential cathode materials for SOFCs. Int J Hydrogen Energy 2018;3. https://doi.org/10.1016/j.ijhydene.2018.06.119.
[17] Ni W, Zhu T, Chen X, Jin C, Bu Y, Zhong Q, Han M. Coupling decreased polarization resistance Sr0.95Ti0.3Fe0.6Ni0.1O3-δ cathode with efficient metal supported Solid Oxide Fuel Cell. J Power Sources 2021;489:229490. https://doi.org/10.1016/j.jpowsour.2021.229490.
[18] Li Q, Cao G, Zhang X, Li G. Topology optimization of the microstructure of solid oxide fuel cell cathodes. Acta Mater 2020;201:278–85. https://doi.org/10.1016/j.actamat.2020.10.003.
[19] Morall E. Manganese oxides/LaMnO 3 perovskite materials and their application in the oxygen reduction reaction. Energy 2022;247. https://doi.org/10.1016/j.energy.2022.123456.
[20] Barros Julião PS. A-site cation influences on performance, structure and conductivity of a lanthanide-based perovskite electrode for symmetrical solid oxide fuel cells. J Power Sources 2020;450. https://doi.org/10.1016/j.jpowsour.2020.227723.
[21] Gao J, Ma D, Zhao H, Li Q, Lü Z, Wei B. Synergistically improving electrocatalytic performance and CO2 tolerance of Fe-based cathode catalysts for solid oxide fuel cells. Energy 2022;252:124050. https://doi.org/10.1016/j.energy.2022.124050.
[22] Meng Y, Zhang W, He Z, Liu C, Gao J, Akbar M, Guo R, Zhou S, Ji Y, Wang X, Yang Y. Partially reduced Ni0.8Co0.15Al0.05LiO2-δ for low-temperature SOFC cathode. Int J Hydrogen Energy 2021;46:9874–81. https://doi.org/10.1016/j.ijhydene.2020.05.150.
[23] Khurana S, Johnson S, Karimaghaloo A, Lee MH. Effect of sintering process with Co3O4 on the performance of LSCF-based cathodes for solid oxide fuel cells. Int. J. Precis. Eng. Manuf. - Green Technol. 2018;5:637–42. https://doi.org/10.1007/s40684-018-0066-x.
[24] Lyu Z, Li H, Han M. Electrochemical properties and thermal neutral state of solid oxide fuel cells with direct internal reforming of methane. Int J Hydrogen Energy 2019;44:12151–62. https://doi.org/10.1016/j.ijhydene.2019.03.048.
[25] Chen G, Wang Y, Sunarso J, Liang F, Wang H. A new scandium and niobium co-doped cobalt-free perovskite cathode for intermediate-temperature solid oxide fuel cells. Energy 2016;95:137–43. https://doi.org/10.1016/j.energy.2015.11.061.
[26] Clematis D, Barbucci A, Presto S, Viviani M, Carpanese MP. Electrocatalytic activity of perovskite-based cathodes for solid oxide fuel cells. Int J Hydrogen Energy 2019;44:6212–22. https://doi.org/10.1016/j.ijhydene.2019.01.128.
[27] Yu W, Lee Y, Lee YH, Cho GY, Park T, Tanveer WH, Kim Y, Cha SW. Performance enhancement of thin film LSCF cathodes by gold current collecting layer. Int. J. Precis. Eng. Manuf. - Green Technol. 2016;3:185–8. https://doi.org/10.1007/s40684-016-0024-4.
[28] Baharuddin NA, Mohd Nazrul Aman NA, Muchtar A, Somalu MR, Abdul Samat A, Aznam MI. Structural, morphological, and electrochemical behavior of titanium-doped SrFe 1-x Ti x O 3-δ (x = 0.1–0.5)perovskite as a cobalt-free solid oxide fuel cell cathode. Ceram Int 2019;45:12903–9. https://doi.org/10.1016/j.ceramint.2019.03.216.
[29] Fan W, Sun Z, Bai Y, Wu K, Zhou J, Cheng Y. In situ growth of nanoparticles in A-site deficient ferrite perovskite as an advanced electrode for symmetrical solid oxide fuel cells. J Power Sources 2020;456:228000. https://doi.org/10.1016/j.jpowsour.2020.228000.
[30] Baharuddin NA, Muchtar A, Somalu MR, Kalib NS, Raduwan NF. Synthesis and characterization of cobalt-free SrFe0·8Ti0·2O3-δ cathode powders synthesized through combustion method for solid oxide fuel cells. Int J Hydrogen Energy 2019;44:30682–91. https://doi.org/10.1016/j.ijhydene.2018.11.142.
[31] Liu Y, Motalov V, Baumann S, Sergeev D, Müller M, Sohn YJ, Guillon O. Thermochemical stability of Fe- and co-functionalized perovskite-type SrTiO3 oxygen transport membrane materials in syngas conditions. J Eur Ceram Soc 2019;39:4874–81. https://doi.org/10.1016/j.jeurceramsoc.2019.06.045.
[32] Schulze-Küppers F, Baumann S, Meulenberg WA, Bouwmeester HJM. Influence of support layer resistance on oxygen fluxes through asymmetric membranes based on perovskite-type oxides SrTi1-xFexO3-δ. J Membr Sci 2020;596:117704. https://doi.org/10.1016/j.memsci.2019.117704.
[33] Yin XB, Tan ZH, Yang R, Guo X. Single crystalline SrTiO3 as memristive model system: from materials science to neurological and psychological functions. J Electroceram 2017;39:210–22. https://doi.org/10.1007/s10832-017-0083-0.
[34] Rothschild A, Litzelman SJ, Tuller HL, Menesklou W, Schneider T, Ivers-Tiffée E. Temperature-independent resistive oxygen sensors based on SrTi1-xFexO3-δsolid solutions. Sens Actuators, B 2005;108:223–30. https://doi.org/10.1016/j.snb.2004.09.044.
[35] Li HY, Yang H, Guo X. Oxygen sensors based on SrTi0.65Fe0.35O3-δthick film with MgO diffusion barrier for automotive emission control. Sens Actuators, B 2015;213:102–10. https://doi.org/10.1016/j.snb.2015.02.079.
[36] Dayaghi AM, Kim KJ, Kim SJ, Sung YS, Choi GM. Oxidation of porous stainless-steel coated with donor-doped SrTiO3 in anodic atmosphere of solid oxide fuel cell. J Power Sources 2017;360:488–94. https://doi.org/10.1016/j.jpowsour.2017.06.017.
[37] Tkach A, Okhay O, Almeida A, Vilarinho PM. Giant dielectric permittivity and high tunability in Y-doped SrTiO3 ceramics tailored by sintering atmosphere. Acta Mater 2017;130:249–60. https://doi.org/10.1016/j.actamat.2017.03.051.
[38] Anh LD, Kaneta S, Tokunaga M, Seki M, Tabata H, Tanaka M, Ohya S. High-mobility 2D hole gas at a SrTiO3 interface. Adv Mater 2020;32:1–7. https://doi.org/10.1002/adma.201906003.
[39] Kang KT, Kang H, Park J, Suh D, Choi WS. Quantum conductance probing of oxygen vacancies in SrTiO3 epitaxial thin film using graphene. Adv Mater 2017;29. https://doi.org/10.1002/adma.201700071.
[40] Zhang S-L, Cox D, Yang H, Park B-K, Li C-X, Li C-J, Barnett SA. High stability SrTi 1–x Fe x O 3–δ electrodes for oxygen reduction and oxygen evolution reactions. J Mater Chem A 2019;7:21447–58. https://doi.org/10.1039/C9TA07548H.

Please cite this article as: Mroziński A et al., Impact of strontium non-stoichiometry of $Sr_xTi_{0.3}Fe_{0.7}O_{3-\delta}$ on structural, electrical, and electrochemical properties for potential oxygen electrode of intermediate temperature solid oxide cells, International Journal of Hydrogen Energy, https://doi.org/10.1016/j.ijhydene.2023.05.323

[41] Jia C, Ma Q, Han M, Wang W, Menzler NH, Guillon O. Fabrication and performance of La, Co-substituted SrTiO 3 as cathode materials of solid oxide fuel cell. ECS Trans 2019;91:1291–8. https://doi.org/10.1149/09101.1291ecst.

[42] Zhu T, Troiani H, Mogni LV, Santaya M, Han M, Barnett SA. Exsolution and electrochemistry in perovskite solid oxide fuel cell anodes: role of stoichiometry in Sr(Ti,Fe,Ni)O3. J Power Sources 2019;439:227077. https://doi.org/10.1016/j.jpowsour.2019.227077.

[43] Zhang SL, Wang H, Lu MY, Zhang AP, Mogni LV, Liu Q, Li CX, Li CJ, Barnett SA. Cobalt-substituted SrTi0.3Fe0.7O3-: δ a stable high-performance oxygen electrode material for intermediate-temperature solid oxide electrochemical cells. Energy Environ Sci 2018;11:1870–9. https://doi.org/10.1039/c8ee00449h.

[44] Skiba EJ, Chen T, Perry NH. Simultaneous electrical, electrochemical, and optical relaxation measurements of oxygen surface exchange coefficients: Sr(Ti,Fe)O3-d film crystallization case study. ACS Appl Mater Interfaces 2020;12:48614–30. https://doi.org/10.1021/acsami.0c14265.

[45] Lan C, Luo J, Dou M, Zhao S. First-principles calculations of the oxygen-diffusion mechanism in mixed Fe/Ti perovskites for solid-oxide fuel cells. Ceram Int 2019;45:17646–52. https://doi.org/10.1016/j.ceramint.2019.05.330.

[46] Kuhn M, Kim JJ, Bishop SR, Tuller HL. Oxygen nonstoichiometry and defect chemistry of perovskite-structured BaxSr1-xTi1-yFeyO 3-y/2+δ solid solutions. Chem Mater 2013;25:2970–5. https://doi.org/10.1021/cm400546z.

[47] Ferreira AAL, Abrantes JCC, Jurado JR, Frade JR. Oxygen stoichiometry of Sr0.97(Ti,Fe)O3-δ materials. Solid State Ionics 2000;135:761–4. https://doi.org/10.1016/S0167-2738(00)00375-1.

[48] Yaremchenko AA, Macías J, Kovalevsky AV, Arias-Serrano BI, Frade JR. Electrical conductivity and thermal expansion of Ln-substituted SrTiO3 for solid oxide cell electrodes and interconnects: the effect of rare-earth cation size. J Power Sources 2020;474:228531. https://doi.org/10.1016/j.jpowsour.2020.228531.

[49] Qin M, Gao F, Cizek J, Yang S, Fan X, Zhao L, Xu J, Dong G, Reece M, Yan H. Point defect structure of La-doped SrTiO3 ceramics with colossal permittivity. Acta Mater 2019;164:76–89. https://doi.org/10.1016/j.actamat.2018.10.025.

[50] Jiang SP. Development of lanthanum strontium cobalt ferrite perovskite electrodes of solid oxide fuel cells – a review. Int J Hydrogen Energy 2019;44:7448–93. https://doi.org/10.1016/j.ijhydene.2019.01.212.

[51] Kovalevsky AV, Aguirre MH, Populoh S, Patrício SG, Ferreira NM, Mikhalev SM, Fagg DP, Weidenkaff A, Frade JR. Designing strontium titanate-based thermoelectrics: insight into defect chemistry mechanisms. J Mater Chem A 2017;5:3909–22. https://doi.org/10.1039/c6ta09860f.

[52] Levin I, Krayzman V, Playford HY, Woicik JC, Maier RA, Lu Z, Bruma A, Eremenko M, Tucker MG. The mediation of bond strain by vacancies and displacive disorder in A-site-deficient perovskites. Acta Mater 2021;207. https://doi.org/10.1016/j.actamat.2021.116678.

[53] Li X, Zhao H, Liang J, Luo Y, Chen G, Shi X, Lu S, Gao S, Hu J, Liu Q, Sun X. A-site perovskite oxides: an emerging functional material for electrocatalysis and photocatalysis. J Mater Chem 2021:6650–70. https://doi.org/10.1039/d0ta09756j.

[54] Liang M, Zhu Y, Song Y, Guan D, Luo Z, Yang G, Jiang SP, Zhou W, Ran R, Shao Z. A new durable surface nanoparticles-modified perovskite cathode for protonic ceramic fuel cells from selective cation exsolution under oxidizing atmosphere. Adv Mater 2022;34:1–9. https://doi.org/10.1002/adma.202106379.

[55] Ni W, Zhu T, Chen X, Zhong Q, Ma W. Stable, efficient and cost-competitive Ni-substituted Sr(Ti,Fe)O3 cathode for solid oxide fuel cell: effect of A-site deficiency. J Power Sources 2020;451:227762. https://doi.org/10.1016/j.jpowsour.2020.227762.

[56] Ni W, Ma W, Zhong Q, Zhu T, Han M. Synthesis and electrochemical performance of Ni substituted SrTi0.3Fe0.7O3-δ cathode: effect of A-site deficiency. ECS Trans 2019;91:1535–41.

[57] Shan K, Guo XM. Electrical properties of (Y0.08Sr0.92)1-xTi0.6Fe0.4O3-δ mixed conductor. Electrochim Acta 2015;154:31–4. https://doi.org/10.1016/j.electacta.2014.12.057.

[58] Kharton VV, Kovalevsky AV, Tsipis EV, Viskup AP, Naumovich EN, Jurado JR, Frade JR. Mixed conductivity and stability of A-site-deficient Sr(Fe,Ti)O 3-δ perovskites. J Solid State Electrochem 2003;7:30–6. https://doi.org/10.1007/s10008-002-0286-3.

[59] Yang H, Hanif MB, Zhang SL, Li CJ, Li CX. Sintering behavior and electrochemical performance of A-site deficient SrxTi0.3Fe0·7O3-δ oxygen electrodes for solid oxide electrochemical cells. Ceram Int 2021;47:25051–8. https://doi.org/10.1016/j.ceramint.2021.05.235.

[60] Li R, Liu F, Zhang C, Liu J, Zhou J, Xu L. Electrical properties of Fe-doped SrTiO3 with B-site-deficient for SOFC anodes. Ceram Int 2019;45:21684–7. https://doi.org/10.1016/j.ceramint.2019.07.167.

[61] Mroziński A, Molin S, Jasiński P. Study of oxygen electrode reactions on symmetrical porous SrTi0.30Fe0.70O3-δ electrodes on Ce0.8Gd0.2O1.9 electrolyte at 800 °C–500 °C. Electrochim Acta 2020;346:136285. https://doi.org/10.1016/j.electacta.2020.136285.

[62] Mroziński A, Molin S, Jasiński P. Effect of sintering temperature on electrochemical performance of porous SrTi1-xFexO3-δ (x = 0.35, 0.5, 0.7) oxygen electrodes for solid oxide cells. J Solid State Electrochem 2020;24:873–82. https://doi.org/10.1007/s10008-020-04534-0.

[63] Li Y, Gerdes K, Horita T, Liu X. Surface exchange and bulk diffusivity of LSCF as SOFC cathode: electrical conductivity relaxation and isotope exchange characterizations. J Electrochem Soc 2013;160:F343. https://doi.org/10.1149/2.044304jes. –F350.

[64] Ciucci F. Electrical conductivity relaxation measurements: statistical investigations using sensitivity analysis, optimal experimental design and ECRTOOLS. Solid State Ionics 2013;239:28–40. https://doi.org/10.1016/j.ssi.2013.03.020.

[65] Wan TH, Saccoccio M, Chen C, Ciucci F. Influence of the discretization methods on the distribution of relaxation times deconvolution: implementing radial basis functions with DRTtools. Electrochim Acta 2015;184:483–99. https://doi.org/10.1016/j.electacta.2015.09.097.

[66] Staykov A, Fukumori S, Yoshizawa K, Sato K, Ishihara T, Kilner J. Interaction of SrO-terminated SrTiO3 surface with oxygen, carbon dioxide, and water. J Mater Chem A 2018;6:22662–72. https://doi.org/10.1039/c8ta05177a.

[67] Rhodes NR, Barde A, Randhir K, Li L, Hahn DW, Mei R, Klausner JF, Auyeung N. Solar thermochemical energy storage through carbonation cycles of SrCO3/SrO supported on SrZrO3. ChemSusChem 2015;8:3793–8. https://doi.org/10.1002/cssc.201501023.

[68] Bagherisereshki E, Tran J, Lei F, AuYeung N. Investigation into SrO/SrCO3 for high temperature thermochemical energy storage. Sol Energy 2018;160:85–93. https://doi.org/10.1016/j.solener.2017.11.073.

[69] Mizera A, Kowalczyk A, Chmielarz L, Drożdż E. Catalysts based on strontium titanate doped with Ni/Co/Cu for dry reforming of methane. Materials 2021;14. https://doi.org/10.3390/ma14237227.

Please cite this article as: Mroziński A et al., Impact of strontium non-stoichiometry of $Sr_xTi_{0.3}Fe_{0.7}O_{3-\delta}$ on structural, electrical, and electrochemical properties for potential oxygen electrode of intermediate temperature solid oxide cells, International Journal of Hydrogen Energy, https://doi.org/10.1016/j.ijhydene.2023.05.323

[70] Miruszewski T, Dzierzgowski K, Winiarz P, Wachowski SL, Mielewczyk–Gryń A, Gazda M. Structural properties and water uptake of SrTi1-xFexO3-x/2-δ. Materials 2020;13:1–16. https://doi.org/10.3390/ma13040965.
[71] Zhao H, Gao F, Li X, Zhang C, Zhao Y. Electrical properties of yttrium doped strontium titanate with A-site deficiency as potential anode materials for solid oxide fuel cells. Solid State Ionics 2009;180:193–7. https://doi.org/10.1016/j.ssi.2008.11.018.
[72] Shannon RD. Revised effective ionic radii and systematic studies of interatomic distances in halides and chalcogenides. Acta Crystallogr A 1976;32:751–67. https://doi.org/10.1107/S0567739476001551.
[73] Ward S, Isaacs MA, Gupta G, Mamlouk M, Pramana SS. Boosting the oxygen evolution activity in non-stoichiometric praseodymium ferrite-based perovskites by A site substitution for alkaline electrolyser anodes. Sustain Energy Fuels 2021;5:154–65. https://doi.org/10.1039/d0se01278e.
[74] Schulze-Küppers F, Ten Donkelaar SFP, Baumann S, Prigorodov P, Sohn YJ, Bouwmeester HJM, Meulenberg WA, Guillon O. Structural and functional properties of SrTi1-xFexO3-δ ($0 \leq x \leq 1$) for the use as oxygen transport membrane. Sep Purif Technol 2015;147:414–21. https://doi.org/10.1016/j.seppur.2014.12.020.
[75] Tietz F. Thermal expansion of SOFC materials. Ionics 1999;5:129–39. https://doi.org/10.1007/BF02375916.
[76] Løken A, Ricote S, Wachowski S. Thermal and chemical expansion in proton ceramic electrolytes and compatible electrodes. Crystals 2018;8:365. https://doi.org/10.3390/cryst8090365.
[77] Zaza F, Frangini S, Leoncini J, Luisetto I, Masci A, Pasquali M, Tuti S. Temperature-independent sensors based on perovskite-type oxides. AIP Conf Proc 2014;1603:53–61. https://doi.org/10.1063/1.4883042.
[78] Zhang X, Li H, Li Y, Shen W. Structural properties and catalytic activity of Sr-substituted LaFeO3 perovskite. Cuihua Xuebao/Chinese J. Catal. 2012;33:1109–14. https://doi.org/10.1016/S1872-2067(11)60388-4.
[79] Biesinger MC, Payne BP, Grosvenor AP, Lau LWM, Gerson AR, Smart RSC. Resolving surface chemical states in XPS analysis of first row transition metals, oxides and hydroxides: Cr, Mn, Fe, Co and Ni. Appl Surf Sci 2011;257:2717–30. https://doi.org/10.1016/j.apsusc.2010.10.051.
[80] Link C, Opitz AK, Rameshan C, Kubicek M, Rupp GM, Nenning A. The chemical evolution of the -La0.6Sr0.4CoO3–δ surface under SOFC operating conditions and its implications for electrochemical oxygen exchange activity. Top Catal 2019;61:2129–41. https://doi.org/10.1007/s11244-018-1068-1.
[81] Chen Y, Jung W, Cai Z, Kim JJ, Tuller HL, Yildiz B. Impact of Sr segregation on the electronic structure and oxygen reduction activity of SrTi1-xFexO3 surfaces. Energy Environ Sci 2012;5:7979–88. https://doi.org/10.1039/c2ee21463f.
[82] Murakami R, Tanaka H, Shinotsuka H, Nagata K, Shouno H, Yoshikawa H. Development of multiple core-level XPS spectra decomposition method based on the Bayesian information criterion. J Electron Spectrosc Relat Phenom 2020;245:147003. https://doi.org/10.1016/j.elspec.2020.147003.
[83] Nenning A, Opitz AK, Rameshan C, Rameshan R, Blume R, Hävecker M, Knop-Gericke A, Rupprechter G, Klötzer B, Fleig J. Ambient pressure XPS study of mixed conducting perovskite-type SOFC cathode and anode materials under well-defined electrochemical polarization. J Phys Chem C 2016;120:1461–71. https://doi.org/10.1021/acs.jpcc.5b08596.
[84] Merkle R, Maier J. Oxygen incorporation into Fe-doped SrTiO3: mechanistic interpretation of the surface reaction. Phys Chem Chem Phys 2002;4:4140–8. https://doi.org/10.1039/b204032h.
[85] Goel V, Cox D, Barnett SA, Thornton K. Simulation of the electrochemical impedance in a three-dimensional, complex microstructure of solid oxide fuel cell cathode and its application in the microstructure characterization. Front Chem 2021;9:1–14. https://doi.org/10.3389/fchem.2021.627699.
[86] Merkle R, Maier J. How is oxygen incorporated into oxides? A comprehensive kinetic study of a simple solid-state reaction with SrTiO3 as a model material. Angew Chem Int Ed 2008;47:3874–94. https://doi.org/10.1002/anie.200700987.
[87] Siebenhofer M, Huber T, Artner W, Fleig J, Kubicek M. Substrate stoichiometry changes during pulsed laser deposition: a case study on SrTiO3. Acta Mater 2021;203. https://doi.org/10.1016/j.actamat.2020.10.077.
[88] Steele BCH. Survey of materials selection for ceramic fuel cells. Solid State Ionics 1996;88:1223–34.
[89] Md Harashid MA, Chen RS, Ahmad SH, Ismail AF, Baharuddin NA. Recent advances in electrode material for symmetrical solid oxide fuel cells and way forward sustainability based on local mineral resources. Int J Energy Res 2022;46:22188–221. https://doi.org/10.1002/er.8579.
[90] Muhammed Ali SA, Anwar M, Baharuddin NA, Somalu MR, Muchtar A. Enhanced electrochemical performance of LSCF cathode through selection of optimum fabrication parameters. J Solid State Electrochem 2018;22:263–73. https://doi.org/10.1007/s10008-017-3754-5.
[91] Jung W, Tuller HL. Investigation of cathode behavior of model thin-film SrTi[sub 1–x]Fe[sub x]O[sub 3–δ] (x=0.35 and 0.5) mixed ionic-electronic conducting electrodes. J Electrochem Soc 2008;155:B1194. https://doi.org/10.1149/1.2976212. –B1201.
[92] Jung W, Tuller HL. Impedance study of SrTi1-xFexO3-δ (x = 0.05 to 0.80) mixed ionic-electronic conducting model cathode. Solid State Ionics 2009;180:843–7. https://doi.org/10.1016/j.ssi.2009.02.008.
[93] Escudero MJ, Aguadero A, Alonso JA, Daza L. A kinetic study of oxygen reduction reaction on La2NiO4 cathodes by means of impedance spectroscopy. J Electroanal Chem 2007;611:107–16. https://doi.org/10.1016/j.jelechem.2007.08.006.
[94] Mroziński A, Błaszczak P, Górnicka K, Miruszewski T, Karczewski J, Molin S, Jasiński P. Impact of strontium non-stoichiometry of SrxTi0.3Fe0, 7O3-δ; 2022. https://doi.org/10.34808/yhx3-f485.

Please cite this article as: Mroziński A et al., Impact of strontium non-stoichiometry of $Sr_xTi_{0.3}Fe_{0.7}O_{3-\delta}$ on structural, electrical, and electrochemical properties for potential oxygen electrode of intermediate temperature solid oxide cells, International Journal of Hydrogen Energy, https://doi.org/10.1016/j.ijhydene.2023.05.323

Chapter 5

Summary and conclusions

5.1. General conclusions from doctoral dissertation

This work presents the results of research on materials from the group of iron doped strontium titanates in application as a porous cathode in SOFC.

The tested materials – $SrTi_{1-x}Fe_xO_{3-\delta}$ (STFx) and $Sr_{1-x}Ti_{0.30}Fe_{0.70}O_{3-\delta}$ (STF-x) – were produced by the solid-state reaction method within the PhD project framework. The structural parameters of the materials were studied in detail.

In the studies on STFx and STF-x used as porous electrodes, it was shown that they can be alternatives to the commercially used materials, such as LSCF. A series of tests of symmetrical samples and fuel cells clearly determined that these materials perform well at an operating temperature range 700 °C÷800 °C. The first part of the work concerned research on finding the best STFx stoichiometry to work at 800 °C **Despite the relatively low electronic conductivity of STFx compounds, ASR_{pol} results of <100 mΩ cm^2 at 800 °C were obtained repeatedly. Among the tested STFx materials, the $SrTi_{0.30}Fe_{0.70}O_{3-\delta}$ electrode performed best and shows ASR_{pol} <100 mΩ cm^2 even at 700 °C.** Further work on optimising the stoichiometry showed that by reducing the strontium content in the A-sublattice, even better results could be achieved and for the $Sr_{0.95}Ti_{0.30}Fe_{0.70}O_{3-\delta}$, boasts a power density of ~800 mW cm^{-2} at 700 °C.

During the work on finding the optimal stoichiometry of iron-doped strontium titanates materials, efforts were made to obtain as much information as possible about the electrochemical processes occurring in the individual compounds. **Using the EIS, DRT and ECM techniques, what processes occur and which of these limit the work of porous cathodes made of STFx and STF-x materials were determined.** The subject matter is

very interesting, which is evidenced by the invitation of a PhD candidate to publish one of the papers in a special issue of the Electrochimica Acta Journal concerning the application of the DRT analysis method,[2] the invitation to participate in a workshop concerning DRT[3] and co-authoring the review publication with some of the most recognised scientists within the DRT field.[4]

5.2. Original contributions in the doctoral dissertation

The main contribution of the PhD student presented in the doctoral dissertation is the development and demonstration that materials from the group of iron doped strontium titanates are a promising candidate for use as a cathode in SOFC.

The specific contributions introduced in the doctoral dissertation are as follows:

- Optimisation of the solid-state reaction process parameters for the production of materials from the group of iron doped strontium titanates with different stoichiometry in the A and B sublattices with nanometric sizes.
- Optimisation of the procedure for preparing low-temperature sintered (800 °C÷1000 °C) efficient porous STFx and STF-x electrodes.
- Demonstration of a series of materials from the group of iron doped strontium titanates, which in the form of porous electrodes, present ASR_{pol} lower than 100 mΩ cm^2 at 800 °C.
- Development of a procedure for precise analysis of EIS spectra using the DRT technique, thanks to which it is possible to quantitatively and qualitatively determine the electrochemical processes taking place in the cathodes.

[2] Special issue of Electrochimica Acta titled: "Distribution of relaxation time analysis for solid state electrochemistry"
[3] The Hong Kong University of Science and Technology – MAE HKPFS Workshop: "The distribution of relaxation times, an application of machine learning in electrochemistry"
[4] Manuscript in the edition titled: "The Distribution of Relaxation Times: A Blueprint for Developing New Methods"

- Study and matching the contribution of the occurring electrochemical processes with the stoichiometry of the iron doped strontium titanates cathodes and their microstructure.
- Indication of the most favourable stoichiometry for iron doped strontium titanates materials based on the physicochemical requirements.
- Investigation and demonstration of the influence of stoichiometry changes in the A sublattice of $Sr_xTi_{0.30}Fe_{0.70}O_{3-\delta}$ on the materials constants k* and D*, which are crucial from the point of view of the SOFC cathode.
- Obtaining a high power density (809 mW cm^{-2}) at 700 C for the $Sr_{0.95}Ti_{0.30}Fe_{0.70}O_{3-\delta}$ material in a working fuel cell.

5.3.Future research directions

Based on the performed tasks, several aspects of the STF materials development should be further studied in the future to drive the technology and our understanding forward:

- The performance of the porous electrodes could be increased considerably by the infiltration of additional, catalytically active phases, which seems an interesting study direction to even further lower the ASR of the electrode.
- Due to the high thermal expansion coefficients of the STFx materials, formation of the composite with an electronically or ionically conducting backbone can lead to improvement in the stability and performance of the electrodes.
- Demonstration of the long-term performance (>1000 h) of the electrodes, including work in a real stack system, would be required to further show the materials' applicability in operating devices.
- Introduction of chemical modifications to increase electrocatalytic activity: partial substitution of Fe/Ti on the B-site by another element may be a strategy to further

optimise the performance. Even though substitution by Co has already been studied [79], certain other elements, especially outside of the CRM group materials, should be tested.

These points show that even though STF has already been studied for several years and by several groups, it still remains a very interesting material, which has potential in application in operating devices in the future.

List of Figures

References

[1] United Nations, Leveraging energy action for advancing the sustainable development goals, (2021) 237. https://sdgs.un.org/sites/default/files/2021-06/2021-UN_POLICY BRIEFS-063021.pdf.

[2] S. Wang, S.P. Jiang, Evolving strategies for tumor immunotherapy: Enhancing the enhancer and suppressing the suppressor. Prospects of fuel cell technologies, Natl. Sci. Rev. 4 (2017) 161–163. doi:10.1093/nsr/nwx032.

[3] P. Mottaghizadeh, M. Fardadi, F. Jabbari, J. Brouwer, Dynamics and control of a thermally self-sustaining energy storage system using integrated solid oxide cells for an islanded building, Int. J. Hydrogen Energy. 46 (2021) 24891–24908. doi:10.1016/j.ijhydene.2021.03.136.

[4] Bloom Energy and SK E&C Announce 28-Megawatt Deployment of Fuel Cell Technology to Power South Korea's Historic Hwasung and Paju Cities, (2020). https://www.bloomenergy.com/news/bloom-energy-and-sk-ec-announce-28-megawatt-deployment-of-fuel-cell-technology-to-power-south-koreas-historic-hwasung-and-paju-cities/.

[5] R.A. Evrin, I. Dincer, Development and evaluation of an integrated solid oxide fuel cell system for medium airplanes, Int. J. Energy Res. 44 (2020) 9674–9685. doi:10.1002/er.5525.

[6] S. Zarabi Golkhatmi, M.I. Asghar, P.D. Lund, A review on solid oxide fuel cell durability: Latest progress, mechanisms, and study tools, Renew. Sustain. Energy Rev. 161 (2022) 112339. doi:10.1016/j.rser.2022.112339.

[7] M.C. Tucker, Durability of symmetric-structured metal-supported solid oxide fuel cells, J. Power Sources. 369 (2017) 6–12. doi:10.1016/j.jpowsour.2017.09.075.

[8] G. Merle, M. Wessling, K. Nijmeijer, Anion exchange membranes for alkaline fuel cells: A review, J. Memb. Sci. 377 (2011) 1–35. doi:https://doi.org/10.1016/j.memsci.2011.04.043.

[9] O.Z. Sharaf, M.F. Orhan, An overview of fuel cell technology: Fundamentals and applications, Renew. Sustain. Energy Rev. 32 (2014) 810–853. doi:10.1016/j.rser.2014.01.012.

[10] Y. Wang, K.S. Chen, J. Mishler, S.C. Cho, X.C. Adroher, A review of polymer electrolyte membrane fuel cells: Technology, applications, and needs on fundamental research, Appl. Energy. 88 (2011) 981–1007. doi:https://doi.org/10.1016/j.apenergy.2010.09.030.

[11] H.-W. Wu, A review of recent development: Transport and performance modeling of PEM fuel cells, Appl. Energy. 165 (2016) 81–106. doi:https://doi.org/10.1016/j.apenergy.2015.12.075.

[12] V. Neburchilov, J. Martin, H. Wang, J. Zhang, A review of polymer electrolyte membranes for direct methanol fuel cells, J. Power Sources. 169 (2007) 221–238. doi:https://doi.org/10.1016/j.jpowsour.2007.03.044.

[13] N. Mahato, A. Banerjee, A. Gupta, S. Omar, K. Balani, Progress in material selection for solid oxide fuel cell technology: A review, Prog. Mater. Sci. 72 (2015) 141–337. doi:10.1016/j.pmatsci.2015.01.001.

[14] J. Molenda, J. Kupecki, R. Baron, M. Blesznowski, G. Brus, T. Brylewski, M. Bucko, J. Chmielowiec, K. Cwieka, M. Gazda, A. Gil, P. Jasinski, Z. Jaworski, J. Karczewski, M. Kawalec, R. Kluczowski, M. Krauz, F. Krok, B. Lukasik, M. Malys, A. Mazur, A. Mielewczyk-Gryn, J. Milewski, S. Molin, G. Mordarski, M. Mosialek, K. Motylinski, E.N. Naumovich, P. Nowak, G. Pasciak, P. Pianko-Oprych, D. Pomykalska, M. Rekas, A. Sciazko, K. Swierczek, J. Szmyd, S. Wachowski, T. Wejrzanowski, W. Wrobel, K. Zagorski, W. Zajac, A. Zurawska, Status report on high temperature fuel cells in Poland – Recent advances and achievements, Int. J. Hydrogen Energy. 42 (2017) 4366–4403. doi:10.1016/j.ijhydene.2016.12.087.

[15] A. Hagen, H. Langnickel, X. Sun, Operation of solid oxide fuel cells with alternative hydrogen carriers, Int. J. Hydrogen Energy. 44 (2019) 18382–18392. doi:10.1016/j.ijhydene.2019.05.065.

[16] C. Mendonça, A. Ferreira, D.M.F. Santos, Towards the Commercialization of Solid Oxide Fuel Cells: Recent Advances in Materials and Integration Strategies, Fuels. 2 (2021) 393–419. doi:10.3390/fuels2040023.

[17] A.K. Padinjarethil, F.R. Bianchi, B. Bosio, A. Hagen, Electrochemical Characterization and Modelling of Anode and Electrolyte Supported Solid Oxide Fuel Cells, Front. Energy Res. 9 (2021) 1–19. doi:10.3389/fenrg.2021.668964.

[18] J. Hayd, L. Dieterle, U. Guntow, D. Gerthsen, E. Ivers-Tiffée, Nanoscaled La0.6Sr0.4CoO3-δ as intermediate temperature solid oxide fuel cell cathode: Microstructure and electrochemical performance, J. Power Sources. 196 (2011) 7263–7270. doi:10.1016/j.jpowsour.2010.11.147.

[19] D. Szymczewska, J. Karczewski, A. Chrzan, P. Jasinski, CGO as a barrier layer between LSCF electrodes and YSZ electrolyte fabricated by spray pyrolysis for solid oxide fuel cells, Solid State Ionics. 302 (2017) 113–117. doi:10.1016/j.ssi.2016.11.008.

[20] G. Yang, C. Su, H. Shi, Y. Zhu, Y. Song, W. Zhou, Z. Shao, Toward reducing the operation temperature of solid oxide fuel cells: Our past 15 years of efforts in cathode development, Energy and Fuels. 34 (2020) 15169–15194. doi:10.1021/acs.energyfuels.0c01887.

[21] A. Ndubuisi, S. Abouali, K. Singh, V. Thangadurai, Recent advances, practical challenges, and perspectives of intermediate temperature solid oxide fuel cell cathodes, J. Mater. Chem. A. 10 (2022) 2196–2227. doi:10.1039/d1ta08475e.

[22] S. Hu, J. Li, Y. Zeng, J. Pu, B. Chi, A mini review of the recent progress of electrode materials for low-temperature solid oxide fuel cells, Phys. Chem. Chem. Phys. 25 (2023) 5926–5941. doi:10.1039/d2cp05133h.

[23] M.Z. Ahmad, S.H. Ahmad, R.S. Chen, A.F. Ismail, R. Hazan, N.A. Baharuddin, Review on recent advancement in cathode material for lower and intermediate temperature solid oxide fuel cells application, Int. J. Hydrogen Energy. 47 (2022) 1103–1120. doi:10.1016/j.ijhydene.2021.10.094.

[24] B.C.H. Steele, Survey of materials selection for ceramic fuel cells: II. Cathodes and anodes, Solid State Ionics. 86–88 (1996) 1223–1234. doi:10.1016/0167-2738(96)00291-3.

[25] G. Yang, W. Jung, S.J. Ahn, D. Lee, Controlling the oxygen electrocatalysis on

perovskite and layered oxide thin films for solid oxide fuel cell cathodes, Appl. Sci. 9 (2019). doi:10.3390/app9051030.

[26] E. V. Tsipis, V. V. Kharton, Electrode materials and reaction mechanisms in solid oxide fuel cells: A brief review. III. Recent trends and selected methodological aspects, J. Solid State Electrochem. 15 (2011) 1007–1040. doi:10.1007/s10008-011-1341-8.

[27] Y. Zhang, R. Knibbe, J. Sunarso, Y. Zhong, W. Zhou, Z. Shao, Z. Zhu, Recent Progress on Advanced Materials for Solid-Oxide Fuel Cells Operating Below 500 °C, Adv. Mater. 29 (2017) 1–33. doi:10.1002/adma.201700132.

[28] W.W. Zhang, M. Chen, E. Povoden-Karadeniz, P.V. Hendriksen, Thermodynamic modeling of the Sr-Co-Fe-O system, Solid State Ionics. 292 (2016) 88–97. doi:10.1016/j.ssi.2016.05.011.

[29] W. Rheinheimer, X.L. Phuah, H. Wang, F. Lemke, M.J. Hoffmann, H. Wang, The role of point defects and defect gradients in flash sintering of perovskite oxides, Acta Mater. 165 (2019) 398–408. doi:10.1016/j.actamat.2018.12.007.

[30] A. Rolle, H.A.A. Mohamed, D. Huo, E. Capoen, O. Mentré, R.N. Vannier, S. Daviero-Minaud, B.A. Boukamp, Ca 3 Co 4 O 9 + δ, a growing potential SOFC cathode material: Impact of the layer composition and thickness on the electrochemical properties, Solid State Ionics. 294 (2016) 21–30. doi:10.1016/j.ssi.2016.06.001.

[31] A. Rolle, S. Boulfrad, K. Nagasawa, H. Nakatsugawa, O. Mentré, J. Irvine, S. Daviero-Minaud, Optimisation of the Solid Oxide Fuel Cell (SOFC) cathode material Ca 3Co4O9-δ, J. Power Sources. 196 (2011) 7328–7332. doi:10.1016/j.jpowsour.2011.02.030.

[32] N.H. Perry, J.J. Kim, H.L. Tuller, Oxygen surface exchange kinetics measurement by simultaneous optical transmission relaxation and impedance spectroscopy: $Sr(Ti,Fe)O_{3-x}$ thin film case study, Sci. Technol. Adv. Mater. 19 (2018) 130–141. doi:10.1080/14686996.2018.1430448.

[33] A. Chrzan, J. Karczewski, D. Szymczewska, P. Jasinski, Nanocrystalline cathode functional layer for SOFC, Electrochim. Acta. 225 (2017) 168–174. doi:10.1016/j.electacta.2016.12.128.

[34] M.S. Hasan, J. Alom, M. Asaduzzaman, M.B. Ahmed, M.D. Hossain, A.S.M. Saem, J. Masud, J. Thakare, M.A. Hossain, Recent Criterion on Stability Enhancement of Perovskite Solar Cells, Processes. 10 (2022). doi:10.3390/pr10071408.

[35] S.A. Muhammed Ali, M. Anwar, L.S. Mahmud, N.S. Kalib, A. Muchtar, M.R. Somalu, Influence of current collecting and functional layer thickness on the performance stability of La 0.6 Sr 0.4 Co 0.2 Fe 0.8 O 3-δ -Ce 0.8 Sm 0.2 O 1.9 composite cathode, J. Solid State Electrochem. 23 (2019) 1155–1164. doi:10.1007/s10008-019-04208-6.

[36] S.P. Jiang, Development of lanthanum strontium cobalt ferrite perovskite electrodes of solid oxide fuel cells – A review, Int. J. Hydrogen Energy. 44 (2019) 7448–7493. doi:10.1016/j.ijhydene.2019.01.212.

[37] I. Kivi, J. Aruväli, K. Kirsimäe, P. Möller, A. Heinsaar, G. Nurk, E. Lust, Influence

of humidified synthetic air feeding conditions on the stoichiometry of (La1-xSrx)yCoO3−δ and La0.6Sr0.4Co0.2Fe0.8O3−δ cathodes under applied potential measured by electrochemical in situ high-temperature XRD method, J. Solid State Electrochem. 21 (2017) 361–369. doi:10.1007/s10008-016-3379-0.

[38] S. Kogler, A. Nenning, G.M. Rupp, A.K. Opitz, J. Fleig, Comparison of electrochemical properties of La0.6Sr0.4FeO3.δ; Thin film electrodes: Oxidizing vs. reducing conditions, J. Electrochem. Soc. 162 (2015) F317–F326. doi:10.1149/2.0731503jes.

[39] S.A. Muhammed Ali, M. Anwar, N.A. Baharuddin, M.R. Somalu, A. Muchtar, Enhanced electrochemical performance of LSCF cathode through selection of optimum fabrication parameters, J. Solid State Electrochem. 22 (2018) 263–273. doi:10.1007/s10008-017-3754-5.

[40] R. Major, P. Morton, EU Commission publishes proposal for Critical Raw Materials Act, (n.d.). https://hsfnotes.com/mining/2023/03/23/eu-commission-publishes-proposal-for-critical-raw-materials-act/.

[41] C. Lei, M.F. Simpson, A. V. Virkar, Investigation of Ion and Electron Conduction in the Mixed Ionic-Electronic Conductor- La-Sr-Co-Fe-Oxide (LSCF) Using Alternating Current (AC) and Direct Current (DC) Techniques, J. Electrochem. Soc. 169 (2022) 014506. doi:10.1149/1945-7111/ac43d8.

[42] C.-Y. Yoo, H.J.M. Bouwmeester, Oxygen surface exchange kinetics of SrTi1−xFexO3−δ mixed conducting oxides, Phys. Chem. Chem. Phys. 14 (2012) 11759. doi:10.1039/c2cp41923h.

[43] N.H. Perry, T. Ishihara, Roles of bulk and surface chemistry in the oxygen exchange kinetics and related properties of mixed conducting perovskite oxide electrodes, Materials (Basel). 9 (2016) 1–24. doi:10.3390/ma9100858.

[44] S. Molin, W. Lewandowska-Iwaniak, B. Kusz, M. Gazda, P. Jasinski, Structural and electrical properties of Sr(Ti, Fe)$O_{3-\delta}$ materials for SOFC cathodes, J. Electroceramics. 28 (2012) 80–87. doi:10.1007/s10832-012-9683-x.

[45] V. V. Kharton, A. V. Kovalevsky, E. V. Tsipis, A.P. Viskup, E.N. Naumovich, J.R. Jurado, J.R. Frade, Mixed conductivity and stability of A-site-deficient Sr(Fe,Ti)O 3-δ perovskites, J. Solid State Electrochem. 7 (2003) 30–36. doi:10.1007/s10008-002-0286-3.

[46] A. Rothschild, W. Menesklou, H.L. Tuller, E. Ivers-Tiffée, Electronic structure, defect chemistry, and transport properties of SrTi 1-xFe xO 3-y solid solutions, Chem. Mater. 18 (2006) 3651–3659. doi:10.1021/cm052803x.

[47] B. Bochentyn, J. Karczewski, T. Miruszewski, A. Krupa, M. Gazda, P. Jasinski, B. Kusz, Donor-substituted SrTi1 + xO3 - δanodes for SOFC, Solid State Ionics. 225 (2012) 118–123. doi:10.1016/j.ssi.2012.05.015.

[48] W. Jung, H.L. Tuller, Impedance study of SrTi(1-x)Fe(x)O(3-delta) (x=0.05 to 0.80) mixed ionic-electronic conducting model cathode, Solid State Ionics. 180 (2009) 843–847. doi:10.1016/j.ssi.2009.02.008.

[49] W. Jung, H.L. Tuller, Investigation of Cathode Behavior of Model Thin-Film SrTi[sub 1 - x]Fe[sub x]O[sub 3 - delta] (x = 0.35 and 0.5) Mixed Ionic-Electronic

Conducting Electrodes, J. Electrochem. Soc. 155 (2008) B1194–B1201. doi:10.1149/1.2976212.

[50] C.E. Beall, E. Fabbri, T.J. Schmidt, Perovskite Oxide Based Electrodes for the Oxygen Reduction and Evolution Reactions: The Underlying Mechanism, ACS Catal. 11 (2021) 3094–3114. doi:10.1021/acscatal.0c04473.

[51] H.Y. Li, H. Yang, X. Guo, Oxygen sensors based on SrTi0.65Fe0.35O3-δthick film with MgO diffusion barrier for automotive emission control, Sensors Actuators, B Chem. 213 (2015) 102–110. doi:10.1016/j.snb.2015.02.079.

[52] S.B. Adler, Mechanism and kinetics of oxygen reduction on porous La1−xSrxCoO3−δ electrodes, Solid State Ionics. 111 (1998) 125–134. doi:10.1016/S0167-2738(98)00179-9.

[53] F. V. Heuveln, H.J.M. Bouwmeester, Electrode Properties of Sr-Doped LaMnO3, J. Electrochem. Soc. (1997).

[54] E. V. Tsipis, V. V. Kharton, Electrode materials and reaction mechanisms in solid oxide fuel cells: A brief review : I Performance-determining factors, J. Solid State Electrochem. 12 (2008) 1039–1060. doi:10.1007/s10008-007-0468-0.

[55] H. Xu, H. Zhang, A. Chu, An investigation of oxygen reduction mechanism in nano-sized LSCF-SDC composite cathodes, Int. J. Hydrogen Energy. 41 (2016) 22415–22421. doi:10.1016/j.ijhydene.2016.09.153.

[56] H. Schichlein, H. Schichlein, E. Ivers-tiffe, E. Ivers-tiffe, M. Voigts, A. Kru, H. Schichlein, A.C. Mu, A. Müller, M. Voigts, Deconvolution of electrochemical impedance spectra for the identification of electrode reaction mechanisms in solid oxide fuel cells, J. Appl. Electrochem. 32 (2002) 875–882. doi:10.1023/A:1020599525160.

[57] S.B. Adler, Factors governing oxygen reduction in solid oxide fuel cell cathodes, Chem. Rev. 104 (2004) 4791–4843. doi:10.1021/cr020724o.

[58] C. Argirusis, F. Jomard, S.F. Wagner, W. Menesklou, E. Ivers-Tiffée, Study of the oxygen incorporation and diffusion in Sr(Ti 0.65Fe0.35)O3 ceramics, Solid State Ionics. 192 (2011) 9–11. doi:10.1016/j.ssi.2010.02.016.

[59] B.A. Boukamp, Electrochemical impedance spectroscopy in solid state ionics: Recent advances, Solid State Ionics. 169 (2004) 65–73. doi:10.1016/j.ssi.2003.07.002.

[60] J. Huang, Z. Li, B.Y. Liaw, J. Zhang, Graphical analysis of electrochemical impedance spectroscopy data in Bode and Nyquist representations, J. Power Sources. 309 (2016) 82–98. doi:10.1016/j.jpowsour.2016.01.073.

[61] F. Ciucci, C. Chen, Analysis of Electrochemical Impedance Spectroscopy Data Using the Distribution of Relaxation Times: A Bayesian and Hierarchical Bayesian Approach, Electrochim. Acta. 167 (2015) 439–454. doi:10.1016/j.electacta.2015.03.123.

[62] T.H. Wan, M. Saccoccio, C. Chen, F. Ciucci, Influence of the Discretization Methods on the Distribution of Relaxation Times Deconvolution: Implementing Radial Basis Functions with DRTtools, Electrochim. Acta. 184 (2015) 483–499. doi:10.1016/j.electacta.2015.09.097.

[63] B.A. Boukamp, A. Rolle, Use of a distribution function of relaxation times (DFRT) in impedance analysis of SOFC electrodes, Solid State Ionics. 314 (2018) 103–111. doi:10.1016/j.ssi.2017.11.021.

[64] D. Papurello, D. Menichini, A. Lanzini, Distributed relaxation times technique for the determination of fuel cell losses with an equivalent circuit model to identify physicochemical processes, Electrochim. Acta. 258 (2017) 98–109. doi:10.1016/j.electacta.2017.10.052.

[65] J. Bartoszek, Y.-X. Liu, J. Karczewski, S.-F. Wang, A. Mrozinski, P. Jasinski, Distribution of relaxation times as a method of separation and identification of complex processes measured by impedance spectroscopy, in: EMPC 2017 - 21st Eur. Microelectron. Packag. Conf. Exhib., 2018. doi:10.23919/EMPC.2017.8346901.

[66] D. Burnat, G. Nasdaurk, L. Holzer, M. Kopecki, A. Heel, Lanthanum doped strontium titanate - ceria anodes: deconvolution of impedance spectra and relationship with composition and microstructure, J. Power Sources. 385 (2018) 62–75. doi:10.1016/j.jpowsour.2018.03.024.

[67] S. Dierickx, A. Weber, E. Ivers-Tiffée, How the distribution of relaxation times enhances complex equivalent circuit models for fuel cells, Electrochim. Acta. 355 (2020) 136764. doi:10.1016/j.electacta.2020.136764.

[68] Y. Zhang, Y. Chen, M. Yan, F. Chen, Reconstruction of relaxation time distribution from linear electrochemical impedance spectroscopy, J. Power Sources. 283 (2015) 464–477. doi:10.1016/j.jpowsour.2015.02.107.

[69] E. Ivers-Tiffée, A. Weber, Evaluation of electrochemical impedance spectra by the distribution of relaxation times, J. Ceram. Soc. Japan. 125 (2017) 193–201. doi:10.2109/jcersj2.125.P4-1.

[70] A. Rothschild, S.J. Litzelman, H.L. Tuller, W. Menesklou, T. Schneider, E. Ivers-Tiffée, Temperature-independent resistive oxygen sensors based on SrTi1-xFexO3-δsolid solutions, Sensors Actuators, B Chem. 108 (2005) 223–230. doi:10.1016/j.snb.2004.09.044.

[71] S.J. Litzelman, A. Rothschild, H.L. Tuller, The electrical properties and stability of SrTi0.65Fe 0.35O3-δ thin films for automotive oxygen sensor applications, Sensors Actuators, B Chem. 108 (2005) 231–237. doi:10.1016/j.snb.2004.10.040.

[72] R. Oliveira Silva, J. Malzbender, F. Schulze-Küppers, S. Baumann, M. Krüger, O. Guillon, Microstructure and anisotropic mechanical properties of freeze dried SrTi0.75Fe0.25O3-δfor oxygen transport membrane substrates, J. Eur. Ceram. Soc. 38 (2018) 2774–2783. doi:10.1016/j.jeurceramsoc.2018.02.014.

[73] E.O. Filatova, Y. V. Egorova, K.A. Galdina, T. Scherb, G. Schumacher, H.J.M. Bouwmeester, S. Baumann, Effect of Fe content on atomic and electronic structure of complex oxides Sr(Ti,Fe)O3 − δ, Solid State Ionics. 308 (2017) 27–33. doi:10.1016/j.ssi.2017.05.016.

[74] R. Merkle, J. Maier, Oxygen incorporation into Fe-doped SrTiO3: Mechanistic interpretation of the surface reaction, Phys. Chem. Chem. Phys. 4 (2002) 4140–4148. doi:10.1039/b204032h.

[75] S. STEINSVIK, R. BUGGE, J.O.N. GJØNNES, J. TAFTØ, T. NORBY, THE

DEFECT STRUCTUFE OF SrTi1−xFexO3−y (x = 0–0.8) INVESTIGATED BY ELECTRICAL CONDUCTIVITY MEASUREMENTS AND ELECTRON ENERGY LOSS SPECTROSCOPY (EELS), J. Phys. Chem. Solids. 58 (1997) 969–976. doi:https://doi.org/10.1016/S0022-3697(96)00200-4.

[76] A. Mroziński, S. Molin, J. Karczewski, B. Kamecki, P. Jasiński, The influence of Iron Doping on Performance of SrTi1-xFexO3-δ Perovskite Oxygen Electrode for SOFC, ECS Trans. 91 (2019) 1299–1307. doi:doi: 10.1149/09101.1299ecst.

[77] S. Koch, Elchemea Analytical, (n.d.). https://www.elchemea.com.

[78] F. Yadollahi Farsani, M. Jafari, E. Shahsavari, H. Shakeripour, H. Salamati, Investigation of structural, electrical and electrochemical properties of La0.6Sr0.4Fe0.8Mn0.2O3-δ as an intermediate temperature solid oxide fuel cell cathode, Int. J. Hydrogen Energy. 45 (2020) 8915–8929. doi:10.1016/j.ijhydene.2020.01.030.

[79] S.L. Zhang, H. Wang, M.Y. Lu, A.P. Zhang, L. V. Mogni, Q. Liu, C.X. Li, C.J. Li, S.A. Barnett, Cobalt-substituted SrTi0.3Fe0.7O3-: δ a stable high-performance oxygen electrode material for intermediate-temperature solid oxide electrochemical cells, Energy Environ. Sci. 11 (2018) 1870–1879. doi:10.1039/c8ee00449h.

CRediT author statement terms definitions

Conceptualisation	Ideas; formulation or evolution of overarching research goals and aims
Methodology	Development or design of methodology; creation of models
Software	Programming, software development; designing computer programs; implementation of the computer code and supporting algorithms; testing of existing code components
Validation	Verification, whether as a part of the activity or separately, of the overall replication/reproducibility of results/experiments and other research outputs
Formal analysis	Application of statistical, mathematical, computational, or other formal techniques to analyse or synthesise study data
Investigation	Conducting a research and investigation process, specifically performing experiments, or data/evidence collection
Resources	Provision of study materials, reagents, materials, patients, laboratory samples, animals, instrumentation, computing resources, or other analysis tools
Data Curation	Management activities to annotate (produce metadata), scrub data and maintain research data (including software code, where it is necessary for interpreting the data itself) for initial use and later reuse
Writing – Original Draft	Preparation, creation and/or presentation of the published work, specifically writing the initial draft (including substantive translation)
Writing – Review & Editing	Preparation, creation and/or presentation of the published work by those from the original research group, specifically critical review, commentary or revision – including pre- or post-publication stages
Visualisation	Preparation, creation and/or presentation of the published work, specifically visualisation/data presentation
Supervision	Oversight and leadership responsibility for the research activity planning and execution, including mentorship external to the core team
Project administration	Management and coordination responsibility for the research activity planning and execution
Funding acquisition	Acquisition of the financial support for the project leading to this publication

Personal Information

Publications in international peer-reviewed journals

A. Mroziński, S. Molin, J. Karczewski, T. Miruszewski, P. Jasiński, Electrochemical properties of porous $Sr_{0.86}Ti_{0.65}Fe_{0.35}O_3$ oxygen electrodes in solid oxide cells: Impedance study of symmetrical electrodes, Int. J. Hydrogen Energy. 44 (2019) 1827–1838. doi:10.1016/j.ijhydene.2018.11.203.

A. Mroziński, S. Molin, P. Jasiński, Effect of sintering temperature on electrochemical performance of porous $SrTi_{1-x}Fe_xO_{3-\delta}$ (x = 0.35, 0.5, 0.7) oxygen electrodes for solid oxide cells, J. Solid State Electrochem. 24 (2020) 873–882. doi:10.1007/s10008-020-04534-0.

A. Mroziński, S. Molin, P. Jasiński, Study of oxygen electrode reactions on symmetrical porous $SrTi_{0.30}Fe_{0.70}O_{3-\delta}$ electrodes on $Ce_{0.8}Gd_{0.2}O_{1.9}$ electrolyte at 800 °C–500 °C, Electrochim. Acta. 346 (2020) 136285. doi:10.1016/j.electacta.2020.136285. **(special issue)**

S. Molin, J. Karczewski, B. Kamecki, **A. Mroziński**, S.F. Wang, P. Jasiński, Processing of $Ce_{0.8}Gd_{0.2}O_{2-\delta}$ barrier layers for solid oxide cells: The effect of preparation method and thickness on the interdiffusion and electrochemical performance, J. Eur. Ceram. Soc. 40 (2020) 5626–5633. doi:10.1016/j.jeurceramsoc.2020.06.006.

K. Lankauf, **A. Mroziński**, P. Błaszczak, K. Górnicka, J. Ignaczak, M. Łapiński, J. Karczewski, G. Cempura, P. Jasiński, S. Molin, The effect of Fe on chemical stability and oxygen evolution performance of high surface area $SrTi_{x-1}Fe_xO_{3-\delta}$ mixed ionic-electronic conductors in alkaline media, Int. J. Hydrogen Energy. 46 (2021) 28575–28590. doi:10.1016/j.ijhydene.2021.06.088.

A. Mroziński, S. Molin, P. Błaszczak, K. Górnicka, T. Miruszewski, J. Karczewski, P. Jasiński, Impact of Strontium Non-Stoichiometry of $Sr_xTi_{0.3}Fe_{0.7}O_{3-\delta}$ on Structural, Electrical, and Electrochemical Properties for Potential Oxygen Electrode of Intermediate Temperature Solid Oxide Cells, Int. J. Hydrogen Energy. (2023) In Press. doi.org/10.1016/j.ijhydene.2023.05.323.

Publications in proceedings of international conferences

J. Bartoszek, Y.-X. Liu, J. Karczewski, S.-F. Wang, **A. Mrozinski**, P. Jasinski, Distribution of relaxation times as a method of separation and identification of complex processes measured by impedance spectroscopy, in: EMPC 2017 – 21st Eur. Microelectron. Packag. Conf. Exhib., 2018. doi:10.23919/EMPC.2017.8346901.

A. Mroziński, S. Molin, J. Karczewski, P. Jasiński, Badania tytanianu strontu podstawianego żelazem jako potencjalnego materiału katodowego dla tlenkowych ogniw paliwowych, Biul. Pol. Stowarzyszenia Wodoru i Ogniw Paliw. 12 (2019) 35–39.

A. Mroziński, S. Molin, J. Karczewski, B. Kamecki, P. Jasiński, The influence of Iron Doping on Performance of $SrTi_{1-x}Fe_xO_{3-\delta}$ Perovskite Oxygen Electrode for SOFC, ECS Trans. 91 (2019) 1299–1307. doi:doi: 10.1149/09101.1299ecst.

Lectures at international conferences

A. Mroziński, J. Karczewski, S. Molin, P. Jasiński, Investigation of $SrTi_{0.65}Fe_{0.35}O_{3-\delta}$ as an oxygen electrode of solid oxide fuel cells, 13th International Symposium on Systems with Fast Ionic Transport (ISSFIT-13), July 03-07, 2018, Minsk, Belarus

J. Karczewski, B. Kamecki, **A. Mroziński,** B. Hołówko, S.-F.Wang, S. Molin, P. Jasiński, Effect of CGO thickness and preparation on the electrochemical performance of SOFC/SOEC cells, 13th International Symposium on Systems with Fast Ionic Transport (ISSFIT-13), July 03-07, 2018, Minsk, Belarus

A. Mroziński, S. Molin, J. Karczewski, B. Kamecki, P. Jasiński, Influence of the iron doping on performance of $SrTi_{1-x}Fe_xO_{3-\delta}$ perovskite oxygen electrode for SOFC, 16th International Symposium on Solid Oxide Fuel Cells (SOFC-XVI), September 08–13, 2019, Kyoto, Japan

A. Mroziński, P. Błaszczak, S. Molin, T. Miruszewski, J. Karczewski, P. Jasiński, The electrochemical performance of the infiltrated $Sr_{1-x}Ti_{0.3}Fe_{0.7}O_{3-\delta}$ perovskite oxygen electrode for Solid Oxide Cells, 14th International Symposium on Systems with Fast Ionic Transport (ISSFIT 14th), July 07–09, 2021, Ljubljana, Slovenia (online)

A. Mroziński, S. Molin, J. Karczewski, B. Kamecki, P. Jasiński, The impact of catalyst infiltration on the electrochemical performance of the cobalt free $Sr_{1-x}Ti_{0.3}Fe_{0.7}O_{3-\delta}$ (STF) perovskite oxygen electrode for Solid Oxide Cells, ACers 14th Pacific Rim Conference on Ceramic and Glass Technology (PACRIM 14), December 12-17, 2021, Vancouver, Canada (online)

A. Mroziński, P. Krajewski, A. Wałek, The context as much important as the content – the Bridge of Knowledge platform as a comprehensive ecosystem for research information, 16th International Open Repositories Conference, June 07–10, 2021, (online)

A. Mroziński, S. Molin, T. Miruszewski, J. Karczewski, P. Jasiński, Application of the DRT technique to identify electrochemical processes during the development of a $Sr_{1-x}Ti_{1-y}Fe_yO_{3-\delta}$ oxygen electrode materials, The distribution of relaxation times, an application of machine learning in electrochemistry, July 27–28, 2022, Honk-Kong, China (online) **Invited**

Lectures at national conferences

M. Szuflita-Żurawska, R. Szczodruch, **A. Mroziński**, Centrum Kompetencji MOST DANYCH i jego zadania, III Pomeranian Open Science Conference (III PKOS), October 8–9, 2019, Gdańsk, Poland

P. Krajewski, **A. Mroziński**, Rola data stewarda w realizacji zadań Centrum Kompetencji Biblioteki Politechniki Gdańskiej, IV Pomeranian Open Science Conference (IV PKOS), April 14–16, 2021, Gdańsk, Poland

A. Mroziński, Analiza doświadczeń zebranych podczas pracy jako Data Steward na Politechnice Gdańskiej, V Pomeranian Open Science Conference (V PKOS), December 1–3, 2021, Gdańsk, Poland

Posters presentations at conferences

A. Mroziński, J. Karczewski, S. Molin, P. Jasiński, Effect of infiltration of highly catalytic nanoparticles on polarization resistance of porous $SrTi_{0.65}Fe_{0.35}O_{3-\delta}$ for solid oxide fuel cells, 13th International Conference on Surfaces, Coatings and Nanostructured Materials (NANOSMAT), September 11–14, 2018, Gdańsk, Poland

B. Hołówko, **A. Mroziński**, J. Karczewski, S. Molin, P. Jasiński, Nanocrystalline hydrogen electrodes for solid oxide cells obtained by infiltration, 13th International Conference on Surfaces, Coatings and Nanostructured Materials (NANOSMAT), September 11–14, 2018, Gdańsk, Poland

S. Molin, B. Hołówko, **A. Mroziński**, B. Kamecki, J. Karczewski, P. Jasiński, Spray Pyrolysis Fabrication and Characterization of Diffusion Barrier Layers for Solid Oxide Fuel Cells, 13th International Conference on Surfaces, Coatings and Nanostructured Materials (NANOSMAT), September 11–14, 2018, Gdańsk, Poland

A. Mroziński, J. Karczewski, S. Molin, P. Jasiński, Badanie rezystancji polaryzacyjnej $SrTi_{1-x}Fe_xO_{3-\delta}$ dla potrzeb tlenkowych ogniw paliwowych, XV Sympozjum Przewodniki Szybkich Jonów (XV PSJ), September 26–29, 2018, Gdańsk, Poland

A. Mroziński, S. Molin, J. Karczewski, P. Jasiński, $SrTi_{1-x}Fe_xO_{3-\delta}$ perovskite oxygen electrode for Solid Oxide Fuel Cells infiltrated by highly catalytic nanoparticles, 22nd International Conference on Solid State Ionics (SSI 2019), June 16–21, 2019, PyeongChang, Korea

P. Krajewski, **A. Mroziński**, A comprehensive study of the metadata standards for implementation of multidisciplinary open data repository, Research Data Alliance 17th Plenary Meeting (RDA 17th), April 20–23, 2021, Edinburgh, Scotland (online)

A. Mroziński, P. Krajewski, Semantic network as a means of ensuring data quality – the Bridge of Knowledge platform example, 16th International Digital Curation Conference (IDCC21), April 19–20, 2021, Edinburgh, Scotland (online)

A. Mroziński, P. Krajewski, How to prepare for Plan S at the individual, institutional, and national levels – an example of actions taken at Gdańsk University of Technology, The Geneva Workshop on Innovations in Scholarly Communication (OAI12), September 06–10, 2021, CERN, Geneva, Switzerland (online)

A. Mroziński, The impact of the BRIDGE of DATA project on scientists' awareness in the research data management – Gdańsk Tech case study, Research Data Alliance 18th Plenary Meeting (RDA 18th), November 03–11, 2021, (online)

Involvement in scientific projects

National Science Center Poland, OPUS13, Understanding and minimization of ohmic and polarization losses in solid oxide cells by nanocrystalline ceramic and cermet functional layers, 2017/25/B/ST8/02275, project leader Piotr Jasiński

European Social Fund – Operational Program Knowledge Education Development, Development of an interdisciplinary doctoral program with an international dimension "InterPhD II", POWR.03.02.00-IP.08-00-DOK/16, project leader Maciej Bagiński

Polish National Agency for Academic Exchange, International scholarship exchange for doctoral students and academic staff "PROM", PPI/PRO/2018/1/00009/U/00, project leader Arkadiusz Żak

European Regional Development Fund – the Operational Program Digital Poland for 2014–2020, BRIDGE OF DATA – Multidisciplinary Open Knowledge Transfer System – stage II: Open Research Data, POPC.02.03.01-00-0033/17-00, project leader Paweł Lubomski